ÉCOLE POLYTECHNIQUE

École Polytechnique
Laboratoire d'Hydrodynamique

THÈSE

présentée pour obtenir le grade de
Docteur de l'École Polytechnique
Spécialité : Mécanique

par

Arnaud COUAIRON

Sujet :

Modes globaux fortement non-linéaires dans les écoulements ouverts

Soutenue le **7 janvier 1997** devant le jury composé de :

J.-M.	Chomaz	
P.	Coullet	
S.	Fauve	Rapporteur
V.	Hakim	Rapporteur
P.	Manneville	
R.T.	Pierrehumbert	
M.	Provansal	Président

ÉCOLE POLYTECHNIQUE

École Polytechnique
Laboratoire d'Hydrodynamique

THÈSE

présentée pour obtenir le grade de
Docteur de l'École Polytechnique
Spécialité : Mécanique

par

Arnaud COUAIRON

Sujet :

Modes globaux fortement non-linéaires dans les écoulements ouverts

Soutenue le **7 janvier 1997** devant le jury composé de :

J.-M.	Chomaz	
P.	Coullet	
S.	Fauve	Rapporteur
V.	Hakim	Rapporteur
P.	Manneville	
R.T.	Pierrehumbert	
M.	Provansal	Président

Remerciements

Les travaux présentés dans ce mémoire ont été effectués au laboratoire d'Hydrodynamique de l'École Polytechnique (LadHyX, CNRS UMR 156).

Je souhaite remercier vivement Patrick Huerre pour l'accueil chaleureux qu'il m'a réservé et son soutien permanent. Ses conseils nombreux et enrichissants lors de nos discussions informelles ont été des éléments importants qui ont contribué au bon déroulement de cette thèse.

Jean-Marc Chomaz a dirigé mes recherches avec enthousiasme et dynamisme. Il m'a accordée confiance et liberté pour développer ces travaux tout en dispensant conseils précieux et encouragements. Il a su me communiquer sa passion pour la recherche et n'a pas ménagé son temps pour améliorer la lisibilité de ce mémoire. Que ces quelques lignes soient l'occasion de lui exprimer ma plus grande reconnaissance.

Je tiens également à remercier Paul Manneville pour ses conseils éclairés lors de nombreuses discussions stimulantes. Sa grande disponibilité et sa patience m'ont aiguillé sur des pistes de recherche originales et je souhaite lui témoigner ma profonde reconnaissance pour ces interactions fructueuses.

Stephan Fauve m'a initié aux joies de la physique non-linéaire et des équations d'amplitude en DEA. Vincent Hakim et Stephan Fauve ont bien voulu s'intéresser à mes travaux et en être les rapporteurs. Je leur adresse tous mes remerciements pour leurs remarques qui ont contribuées à mettre ce travail en valeur.

Je remercie également Michel Provansal qui m'a fait l'honneur de présider le jury de soutenance, Pierre Coullet et Raymond Pierrehumbert, pour l'intérêt qu'ils ont porté à mes travaux et pour leur participation au jury.

Merci à l'ensemble des « gentils membres du LadHyX », permanents ou passagers, dont la bonne humeur a rendu l'ambiance du laboratoire tous les jours plus sympathique. Merci en particulier à Stéphane Le Dizès, Carlo Cossu, Benoît Pier, Thomas Loiseleux et Pierre Brancher, chacun à l'origine d'une étincelle qui a fait naître une partie de ces travaux. Merci à Olivier Pouliquen pour avoir bien voulu m'épauler dans l'organisation de séminaires. Merci à tous et en particulier à mes compagnons de bureau, Ivan Delbende, Paul Billant, Burt Tilley, Stéphanie Julien pour nos discussions quotidiennes sur la science, l'humour, l'art (c'est à dire la BD), la cuisine, le sport, ou la théologie. Merci à Jacques Webert pour sa patience à résoudre mes problèmes informatiques divers (il a bien voulu démonter mon terminal pour en libérer une mouche emprisonnée). Merci à Thérese Lescuyer pour son extrême obligeance et ses crumbles. Merci à tous ceux qui ne sont pas cités mais qui n'en ont pas moins contribué amicalement à l'aboutissement de ces recherches.

Je ne saurais oublier famille et amis qui m'ont soutenus par leur compréhension et leurs encouragements tout au long de ces travaux.

à Béatrice,
Guillaume.

Contents

Introduction

La majorité des écoulements rencontrés dans la nature sont des écoulements ouverts dans lesquels les particules fluides entrent continument puis quittent le domaine d'observation (jets, couches limites, sillages). Lorsqu'un paramètre de contrôle est augmenté au delà d'une valeur critique, un écoulement laminaire peut se déstabiliser et bifurquer vers un autre régime plus complexe où apparaissent des structures tourbillonnaires à grande échelle. L'apparition du désordre dans les écoulements hydrodynamiques nécessite la brisure des symétries du problème initial, ce qui se traduit par plusieurs bifurcations successives associées à ces brisures. Pour les systèmes fermés (convection, Taylor–Couette, physique de petites boites) les scénarios des premières bifurcations sont bien identifiés [64]. La dynamique des écoulements ouverts est moins bien connue; d'après des observations expérimentales, elle semble pouvoir être décrite également par une séquence de bifurcations mais qui ont lieu successivement dans l'espace. Par exemple l'évolution spatiale d'une couche de mélange implique une instabilité bidimensionnelle initiale qui sature en une ligne de rouleaux de Kelvin-Helmholtz. Plus loin en aval, cette allée de vortex est déstabilisée par l'appariement des structures, associé à la croissance spatiale du premier sous-harmonique. Ensuite, ce mode secondaire sature en une nouvelle rangée de vortex plus larges, deux fois plus espacés. Cette séquence spatiale d'instabilités et de saturations se répète jusqu'à l'apparition d'instabilités secondaires tridimensionnelles.

En ce qui concerne la première bifurcation des systèmes ouverts, les structures tourbillonnaires peuvent simplement résulter de l'amplification des perturbations à l'entrée de l'écoulement, présentes dans tout système expérimental ou numérique. Dans ce cas la dynamique de l'écoulement est sensible au bruit extérieur et le système se comporte comme un amplificateur spatial du bruit d'entrée. À l'inverse, les structures tourbillonnaires peuvent être très bien ordonnées avec une dynamique très peu sensible au bruit extérieur et une fréquence d'oscillation bien définie. Dans ce cas la dynamique est intrinsèque à l'écoulement et le système se comporte comme un oscillateur auto-entretenu. Les écoulements ouverts peuvent ainsi être classés en deux catégories selon qu'ils se comportent plutôt comme des amplificateurs de bruit ou plutôt comme des oscillateurs.

Un problème qui se pose pour décrire les écoulements de type oscillateur, est l'identification des mécanismes qui peuvent entretenir les oscillations : si une boucle de rétro-

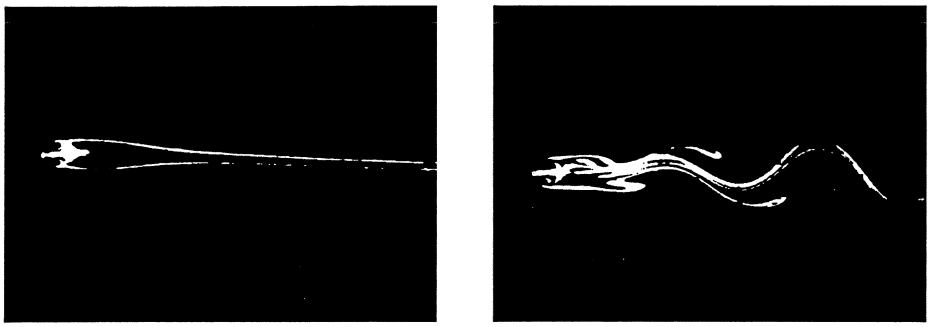

(a) (b)

FIG. 0.1 - Sillage derrière un cylindre. (a) Régime laminaire, $Re - Re_c = -0.4$. (b) Régime oscillatoire $Re - Re_c = 5.2$. D'après Mathis et Provansal, tiré de Guyon *et al.* [38]

action est présente et réinjecte les perturbations à l'entrée de l'écoulement, par exemple par un effet acoustique sur la pression, un effet de résonance peut être ainsi crée par l'intéraction entre l'écoulement hydrodynamique et une frontière [83]. Au contraire, depuis plus d'une dizaine d'années, certains écoulement ouverts se sont révélés être le siège d'oscillations auto-entretenues bien qu'aucune boucle de rétroaction extérieure ne soit présente [46, 68, 87, 89] ; le mécanisme d'amplification est purement hydrodynamique. La description théorique de cette dernière classe d'écoulements ouverts du type oscillateur à l'aide de modèles d'équations d'amplitude constitue le sujet de cette thèse.

L'exemple le plus classique d'écoulement ouvert se comportant comme un oscillateur auto-entretenu est le sillage derrière un cylindre (Figure 0.1). Lorsque le nombre de Reynolds dépasse la valeur critique de 45, l'écoulement laminaire stationnaire se déstabilise globalement et devient oscillatoire ; des tourbillons se forment de part et d'autre du cylindre et s'en éloignent pour former la double allée de Bénard–Kármán. Ce régime est très peu sensible au bruit extérieur et possède une fréquence bien définie, caractéristique de l'écoulement. La distribution spatiotemporelle des fluctuations associées représente cette oscillation auto-entretenue et constitue ce que l'on appelle un mode global de l'écoulement.

Mathis *et al.* [65] ont montré expérimentalement que la bifurcation globale vers le régime oscillatoire est du type Hopf et suit la théorie de Landau [58]. Mais des études ultérieures de la forme du mode global [35, 97] ont montré que cette première «bifurcation» ne suit pas exactement un scénario de système dynamique à la Landau [58], car le mode se déforme au premier ordre dès le seuil de bifurcation, et la position de son maximum varie comme l'inverse de la racine de l'écart au seuil (ce qui est en contradiction avec l'idée d'un seul mode propre excité au seuil).

D'autres exemples d'écoulement globalement instable ont été identifiés expérimentalement comme les jets chauds [68, 87] lorsque le rapport de densité entre le jet et le fluide extérieur est abaissé en dessous d'un seuil critique, ou les couches de mélange avec contre courant [89] lorsque l'intensité du cisaillement entre contre courant et courant dépasse un seuil critique. Les comportements intrinsèques de ces derniers écoulements

ont été mis en évidence aussi bien par des mesure spectrales d'une quantité fluctuante par rapport à l'écoulement de base, qui montrent un pic de fréquence plus énergétique au dessus du seuil d'instabilité globale, que par la réponse à un forçage localisé qui montre que le système n'est sensible à ce forçage que sous le seuil d'instabilité globale.

L'étude des écoulements ouverts (en particulier ceux qui se comportent comme des oscillateurs) a été effectuée par l'analyse des ondes d'instabilités hydrodynamiques qui peuvent se développer autour d'un état de base [45] (et mener ensuite le système à saturation à cause des non linéarités). La difficulté de cette approche est double: la plupart des écoulements considérés sont inhomogènes, c'est à dire qu'ils s'étendent spatialement dans la direction transverse et ce non parallélisme implique que l'état de base de ces écoulement n'est pas uniforme dans la direction de l'écoulement. D'autre part, une description en terme d'ondes d'instabilités hydrodynamiques est une description linéaire dont la validité est limitée par les fortes non linéarités des systèmes étudiés. Néanmoins, bien qu'au stade linéaire, la description du développement spatiotemporel des ondes d'instabilités ne puisse donner des informations sur la nature non linéaire des solutions bifurquées, l'idée de différencier les écoulements ouverts de type amplificateurs spatiaux du bruit d'entrée de ceux qui se comportent comme des oscillateurs, en associant ces différents comportements à un changement de nature de l'instabilité de l'état de base, a permis d'apporter des résultats qualitatifs et quantitatifs importants en ce qui concerne les seuils d'instabilité et les mécanismes de déstabilisation. En particulier, les notions d'instabilités absolues et convectives développées initialement dans le contexte de la physique des plasmas [12, 14, 62], ont été appliquées par Huerre et Monkewitz [45] aux écoulements cisaillés ouverts tels que les jets, les couches de mélanges ou les sillages dans le but de comprendre leur développement spatiotemporel et d'établir des scénarios possibles qui autorisent un comportement intrinsèque. Pour des écoulement idéalisés (parallèles et infinis), ces notions d'instabilités absolues et convectives sont définies par la réponse du système à une impulsion initiale localisée. Un système *convectivement instable* est tel qu'une perturbation localisée croît tout en étant emportée par l'écoulement. Dans un tel système, les perturbations liées aux conditions d'entrée sont simplement amplifiées par l'écoulement qui se comporte comme un amplificateur spatial du bruit d'entrée. La fréquence spécifique de ces écoulements est alors au mieux définie en moyenne seulement. Les jets, les couches de mélange ou les couches limites font partie de cette classe d'écoulements. À l'inverse, un système *absolument instable* est tel qu'une perturbation localisée croît et est de plus capable de remonter l'écoulement et de le contaminer tout entier, influençant en particulier les conditions à l'entrée. Un phénomène de résonance peut alors se mettre en place et le système acquiert une dynamique intrinsèque. Il se comporte comme un oscillateur avec une fréquence propre bien définie.

Le changement de nature de l'instabilité de l'écoulement de base avec transition d'instable convectif à instable absolu permet de déterminer théoriquement un seuil d'instabilité pour ces écoulements parallèles. Ce seuil correspond pour certains écoulements cisaillés [45] assez précisément au seuil d'instabilité globale observé expérimentalement ou dans des simulations numériques. Par contre ces notions linéaires ne décrivent pas l'état spatiotemporel de l'écoulement au dessus du seuil de bifurcation.

Pour les écoulements non parallèles, ces notions d'instabilités absolues et convectives ne sont définies que localement. Afin de relier les caractéristiques globales des

écoulements du type oscillateurs aux propriétés locales de l'instabilité de l'état de base, les notions d'instabilités absolue et convectives ont été étendues aux écoulement faiblement non parallèles d'abord par une analyse théorique [69] sur des équations modèles, puis les scénarios de transition vers une instabilité globale établis sur ces modèles ont finalement été confirmés pour des écoulements réels, soit expérimentalement [84], soit par des études numériques [42, 90, 96, 41]. Théoriquement, cette extension a été réalisée par une approche WKBJ sous l'hypothèse de faible inhomogénéité du milieu, traduisant que l'état de base du système varie lentement sur l'échelle d'une longueur d'onde typique de l'instabilité. La notion de *mode global linéaire* a été introduite à cette occasion pour désigner un mode d'oscillation auto-entretenue, c'est à dire la distribution spatiotemporelle des fluctuations par rapport à un état de base lorsque l'écoulement est globalement instable. Plus précisément, les modes globaux linéaires sont des solutions d'un problème aux valeurs propres pour lequel la direction x de l'écoulement est aussi une «direction propre» du système, c'est à dire que l'équation qui régit l'évolution des perturbations par rapport à l'état de base est linéarisée et non uniforme en x.

Afin d'illustrer ces notions d'instabilités absolues et convectives et de modes globaux linéaires par un exemple simple tiré de [19, 20], considérons l'équation de Ginzburg–Landau d'amplitude réelle A,

$$\frac{\partial A}{\partial t} + U_0 \frac{\partial A}{\partial x} = \frac{\partial^2 A}{\partial x^2} + \mu(x) A - A^3, \tag{0.1}$$

qui est supposée décrire l'évolution non linéaire des perturbations par rapport à l'état de base uniforme $A = 0$. L'inhomogénéité du milieu est représenté par une variation lente et linéaire du paramètre de bifurcation dans la direction de l'écoulement

$$\mu(x) = \mu_0 - \mu_1 x \tag{0.2}$$

et le milieu est supposé infiniment stable à l'infini. Le terme $U_0 \frac{\partial A}{\partial x}$ représente l'advection moyenne dans l'écoulement. Un domaine semi-infini modélise l'écoulement ouvert étudié et les conditions aux limites sont

$$A(0) = 0, \tag{0.3}$$

qui modélise l'obstacle ou l'entrée de l'écoulement, et

$$A(+\infty) = 0 \tag{0.4}$$

associée à la stabilité du milieu à l'infini.

Dans un premier temps, les caractéristiques locales de l'instabilité de l'état de base sont déterminées à partir de la relation de dispersion associée aux ondes d'instabilités $\exp(-i\omega t + ikx)$ pouvant se développer sur l'état de base uniforme $A = 0$:

$$\omega = U_0 k + i(\mu - k^2). \tag{0.5}$$

Le changement de nature (transition convectif/absolu) de l'instabilité de l'état de base a lieu lorsque, pour le nombre d'onde k_0 tel que la vitesse de groupe $d\omega/dk(k_0)$ soit nulle, le taux de croissance des ondes d'instabilités $\omega_i(k_0)$ s'annule, ce qui se traduit par

$$\frac{d\omega}{dk}(k_0) = U_0 - 2ik_0 = 0 \qquad \text{soit} \qquad k_0 = -i\frac{U_0}{2}, \tag{0.6}$$

et

$$\omega(k_0) = i\left(\mu - \frac{U_0^2}{4}\right). \tag{0.7}$$

L'état de base $A = 0$ est localement instable absolu lorsque $\omega_i(k_0) > 0$, soit $\mu(x) > U_0^2/4$ et localement instable convectif lorsque $\omega_i(k_0) < 0$, soit $\mu(x) < U_0^2/4$.

Pour ce modèle, le développement spatiotemporel linéaire des ondes d'instabilités peut être entièrement déterminé. Les modes globaux linéaires sont les solutions propres amplifiées de l'équation (0.1) linéarisée autour de l'état de base uniforme $A = 0$,

$$\frac{\partial A}{\partial t} + U_0\frac{\partial A}{\partial x} = \frac{\partial^2 A}{\partial x^2} + \mu(x)A \tag{0.8}$$

et soumise aux conditions aux limites (0.3) et (0.4). Parmi l'ensemble des solutions propres de (0.8, 0.3, 0.4),

$$A(x) = \exp(-i\omega_n t + U_0 x/2)\mathrm{Ai}\left[\mu_1^{1/3}x + \zeta_n)\right], \tag{0.9}$$

où les fréquences complexes ω_n sont donnés par

$$\omega_n = i(\mu_0 - U_0^2/4 + \mu_1^{2/3}\zeta_n), \tag{0.10}$$

et ζ_n désignent les zéros de la fonction d'Airy, les solutions amplifiées sont celles pour lesquelles le signe de la partie imaginaire de ω_n est positif et un mode global linéaire est donc obtenu lorsque la valeur de μ_0 est supérieure au seuil μ_g^l défini par

$$\mu_g^l = U_0^2/4 + (-\zeta_1)\mu_1^{2/3}, \tag{0.11}$$

La croissance des modes globaux linéaires est limitée par les non linéarités du modèle (0.1). Pour ce modèle, le seuil d'instabilité globale linéaire μ_g^l (équation 0.11) est donc décalé par rapport au seuil d'instabilité absolue $U_0^2/4$ d'une quantité qui varie comme une puissance 2/3 de l'inhomogénéité. Ce seuil traduit la présence d'une zone d'instabilité absolue locale au voisinage de l'origine du domaine et un résultat important de la théorie des modes globaux linéaires est la nécessité de cette zone d'instabilité absolue locale dans l'écoulement pour obtenir un mode global linéaire. Ce scénario a été étendu par Monkewitz, Huerre et Chomaz [69] au cas d'écoulement réels et des simulations numériques dans le cas des sillages [41] ont confirmé sa validité. Le seuil d'instabilité globale linéaire est prédit de façon précise par cette théorie et la fréquence d'oscillation est également bien prédite au premier ordre (pour le modèle réel (0.1), l'équation (0.10) donne une fréquence nulle). En revanche, le régime d'oscillations non linéaires (l'allée de von Karman pour les sillages) est un état saturé dont les caractéristiques spatiales ne sont pas obtenues par cette approche et dans le but de décrire ce régime, la théorie des modes globaux linéaires a été étendue dans le domaine faiblement non linéaire par Le Dizès *et al.* [61]. Un des objectif de cette extension a été d'étudier sous quelles conditions un mode global linéairement instable peut avoir une amplitude décrite par une équation de Landau. Il a été montré que cette théorie faiblement non linéaire possède des limites de validité : l'écart au seuil d'instabilité globale linéaire doit

être exponentiellement petit par rapport au paramètre d'inhomogénéité pour que l'amplitude des modes globaux linéaires reste d'ordre un et soit décrite par une équation de Landau.

Dans le but de s'affranchir de ces limites de la théorie faiblement non linéaire, une approche fortement non linéaire est nécessaire et constitue une des principales motivation de cette thèse. La description des non linéarités fortes qui interviennent dans les écoulements ouverts est effectuée dans toute cette étude en considérant la structure transverse de l'écoulement comme passive dans le mécanisme de déstabilisation globale, ce qui permet l'utilisation de modèles d'équations d'amplitude unidimensionnels de type Ginzburg–Landau. La distinction entre les écoulements possédant la dynamique d'un oscillateur et ceux qui se comportent comme des amplificateurs de bruit s'appuie sur l'existence de *modes globaux non linéaires*: ce terme désigne comme dans le cas linéaire la distribution spatiotemporelle des fluctuations par rapport à l'écoulement de base mais c'est maintenant une solution saturée oscillante de l'équation non linéaire d'évolution des ondes d'instabilités (et non plus d'une équation linéarisée autour de l'état de base). Cette approche fortement non linéaire s'appuie sur la théorie des systèmes dynamiques et les notions linéaires d'instabilités absolues et convectives sont utilisées afin de déterminer si elles gardent leur pouvoir prédictif pour les caractéristiques globales de l'écoulement. Dans le cadre de la théorie des modes globaux linéaires, ces notions ont permis de trouver avec succès le seuil d'instabilité globale au premier ordre. Pour les modes globaux fortement non linéaires, le seuil d'instabilité globale est parfois encore bien décrit par ces notions linéaires. Mais le cas contraire où le seuil d'instabilité globale est très différent du seuil d'instabilité absolu, est également possible. Dans les deux cas la théorie fortement non linéaire apporte des informations supplémentaires sur la structure spatiale des solutions bifurquées au dessus du seuil.

À l'inverse de la démarche effectuée habituellement pour les modes globaux linéaires qui consiste à décrire les milieux faiblement inhomogènes par une approche WKBJ puis à étendre l'analyse linéaire à une théorie faiblement non linéaire, la démarche éffectuée dans cette étude consiste à décrire les modes globaux fortement non linéaires d'abord pour les milieux homogènes puis à considérer que les modes globaux pour les milieux faiblement inhomogènes peuvent être décrits en perturbation de ces modes globaux homogènes.

Cette démarche est appuyée par le fait que recemment, des simulations numériques ont été effectuées pour des écoulements habituellement fermé, en les rendant ouvert par l'addition d'un écoulement moyen. Ces simulations concernent les systèmes de Rayleigh–Bénard par Müller *et al.* [71] et Taylor–Couette par Büchel *et al.* [15] pour lesquels des comportements de type oscillateur intrinsèque ont été mis en évidence. L'avantage de ces écoulement est du à leur uniformité dans la direction de l'écoulement et les résultats numériques obtenus par Müller *et al.* et Büchel *et al.* ont pu jouer le rôle de test dans le cas des écoulements homogènes pour les résultats obtenus dans cette étude pour les modes globaux fortement non linéaires.

L'expérience de convection de Rayleigh–Bénard décrit l'écoulement d'un fluide confiné entre deux plaques chauffé par le bas. Lorsque l'écart de température entre les deux plaques mesuré par le nombre de Rayleigh dépasse une valeur critique, l'état purement conductif du système devient instable et des rouleaux de convection d'axe transverse

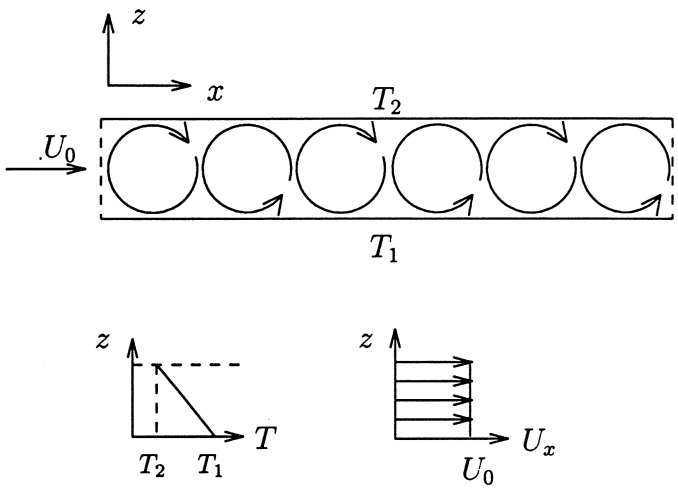

FIG. 0.2 - Expérience de convection de Rayleigh–Bénard en présence d'un écoulement transverse

apparaissent. Ce système fermé peut être rendu ouvert par l'addition d'un écoulement transverse (Figure 0.2). L'addition de cet écoulement transverse dont l'intensité est mesurée par le nombre de Reynolds, restabilise le système et le nombre de Rayleigh critique au delà duquel les rouleaux convectifs sont observés augmente avec le nombre de Reynolds.

Des simulations numériques des équations de Navier–Stokes pour ce problème effectuées par Müller *et al.* [71] montrent que les rouleaux de convection se propagent dans la direction de l'écoulement mais la structure spatiale de l'amplitude de ces rouleaux est stationnaire et constitue un mode global non linéaire (Figure 0.3), c'est à dire la solution d'une équation d'amplitude du type (0.1) avec $\mu(x) = \mu_0$ constant dans tout l'écoulement et des conditions aux limites adaptées : $A(0) = 0$ et $A(L) = 0$ qui traduisent que l'écoulement est imposé (parallèle à Ox) à l'entrée $x = 0$ et à la sortie $x = L$. La taille caractéristique de ces solutions, définie comme la distance à laquelle une amplitude de référence est atteinte est d'autant plus grande que l'advection est grande et l'un des buts de cette étude est d'obtenir des lois d'échelles pour cette taille en fonction de l'écart au seuil d'instabilité globale. Les modèles développés dans cette thèse, s'appliquent dans le cas de grandes tailles de boite et la condition à la limite en $x = L$ est remplacée par une condition à l'infini traduisant qu'une amplitude de saturation est atteinte. Ils montrent que l'écoulement de Rayleigh–Bénard avec advection latérale décrit ci-dessus se comporte comme un système semi-infini en ce qui concerne la sélection de l'état saturé.

De même, dans l'expérience de Taylor–Couette, un fluide est confiné entre deux cylindres, le cylindre extérieur étant fixe et le cylindre intérieur tournant à vitesse constante ; l'intensité de la rotation est mesurée par le nombre de Taylor. Si ce nombre de Taylor dépasse une valeur critique, l'écoulement de base, (représenté par l'écoulement de Couette circulaire pour lequel le champ de vitesse est orthoradial), devient instable et des stuctures tourbillonaires apparaissent sous la forme de rouleaux toroï-

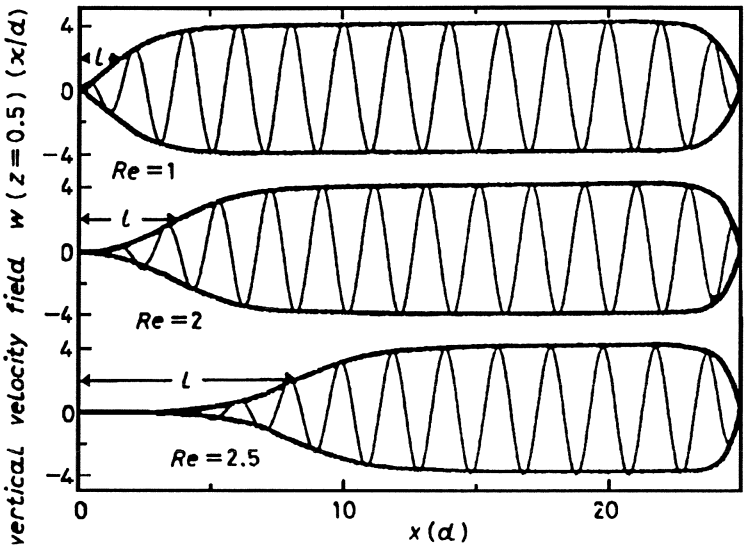

FIG. 0.3 - Vitesse verticale en fonction de la distance x à l'entrée de l'écoulement pour différent nombre de Reynolds, obtenue par simulation numérique des équations de Navier–Stokes pour le probème de Rayleigh–Bénard avec écoulement transverse par Müller *et al.* [71]. L'enveloppe de ces solutions représente un mode global non linéaire.

daux. Lorsqu'un écoulement axial est ajouté au système de Taylor–Couette (Figure 0.4), des simulations des équations de Navier–Stokes effectuées par Büchel *et al.* [15] pour ce problème montrent que le système est restabilisé, c'est à dire que le nombre de Taylor critique au delà duquel le système bifurque augmente avec le nombre de Reynolds (mesurant l'intensité de l'écoulement axial). Dans ce système, les rouleaux sont décrits par le champ des perturbations de vitesse par rapport à l'écoulement de base constitué de la superposition des écoulements de Couette circulaire et de Poiseuille annulaire; ils se propagent dans la direction axiale et leur structure spatiale constitue un mode global non linéaire du système. Deux types de conditions aux limites sont utilisées par Büchel *et al.* à l'entrée et à la sortie de l'écoulement : soit l'écoulement de base est imposé et dans ce cas, des solutions modes globaux non linéaires identiques à celles du problème de Rayleigh–Bénard avec advection sont obtenues pour l'écart de vitesse axiale par rapport à la composante de Poiseuille annulaire. Soit un écoulement parallèlle à l'axe (composante de Poiseuille uniquement) est imposé à l'entrée et à la sortie de l'écoulement; dans ce cas, une couche d'Ekman se développe au voisinage de $x = 0$ et la solution obtenue pour l'ecart de vitesse axiale par rapport à l'écoulement de base est semblable aux modes globaux non linéaires du problème de Rayleigh–Bénard avec advection sauf dans la couche d'Ekman. Nos modèles avec amplitude nulle imposée au bord représentent bien la première situation.

Ces modes globaux non linéaires ne sont pas sans rapport avec l'étude de la propagation des fronts en milieu infini. En effet, lorsque dans l'expérience de Rayleigh–Bénard, le nombre de Rayleigh est augmenté au delà de sa valeur critique, le système bifurque

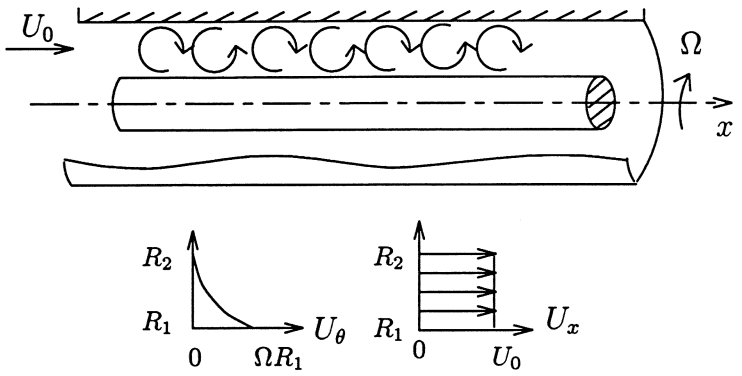

FIG. 0.4 - Expérience de Taylor–Couette en présence d'un écoulement axial.

de l'état conductif pur vers l'état convectif et l'apparition des rouleaux de vorticité a été décrite par Fineberg et Steinberg [33] comme un front de vortex reliant les deux états et se propageant dans l'état conductif instable. Les caractéristiques de ce front ainsi que la "texture" derrière le front, *i.e.* la longueur d'onde sélectionnée dans l'état convectif sont déterminées par un principe de sélection. Chaque solution de front possible reliant état conductif et état convectif se propage à une certaine vitesse et sélectionne une longueur d'onde particulière. Un seul front est dynamiquement sélectionné par le système et ce problème de sélection de vitesse de front a fait l'objet de nombreuses études théoriques [53, 6, 7, 22, 34, 51, 81, 30, 10, 93, 92]. Bien que ces problèmes de sélection soient encore non résolus dans le cas général, les critères de stabilité marginale [30, 10, 93] permettent d'apporter des éléments de réponse à la question des vitesses de front : le critère de stabilité marginale linéaire stipule que le front sélectionné est celui pour lequel l'état instable dans lequel se propage le front est marginalement stable (taux de croissance nul pour les ondes d'instabilités) dans le référentiel du front. Fineberg et Steinberg montrent que les mesures expérimentales de vitesse de front de vortex se propageant dans l'état conductif pour l'expérience de Rayleigh–Bénard correspondent au résultat théorique prévu par le critère de stabilité marginale linéaire. Ce critère peut cependant être mis en défaut ; il existe plusieurs exemples expérimentaux de fronts se propageant à une vitesse différente de celle prédite par ce critère, en particulier en cinétique chimique [43] ou dans les cristaux liquides nématiques [77]. Dans ce cas il faut se référer au critère de stabilité marginale non linéaire qui stipule que le front sélectionné est celui qui est marginalement stable dans son référentiel. Ces critères permettent donc de déterminer la vitesse d'un front se propageant vers un état instable ou métastable, pour un système considéré comme infini. Lorsqu'il y a une frontière, le référentiel du laboratoire est spécifié par cette frontière et l'invariance galiléenne est brisée. L'advection moyenne doit alors être prise en compte. Un mode global non linéaire peut être vu comme un front capable de remonter l'écoulement contre l'advection jusqu'à sentir l'effet du bord. Cette idée permet une description des modes globaux non linéaires en perturbation par rapport à des fronts stationnaires (fronts sélectionnés en milieu infini et équilibrés par l'advection). Le développement de cette description perturbative donne justement les lois d'échelle recherchées pour la taille des modes globaux non linéaires.

Plaza [79] a montré que le critère de stabilité marginale linéaire est équivalent à la détermination du changement de nature (transition convectif / absolu) de l'instabilité de l'état de base que le front envahit. Cette équivalence explique que l'addition d'un écoulement à un système dans lequel a été observé des fronts dont la vitesse correspond à la sélection par le critère de stabilité marginale linéaire, entraine une restabilisation du système telle que le seuil d'instabilité globale en présence d'advection soit obtenu par la détermination du changement de nature (absolu / convectif) de l'instabilité de l'état de base. Par exemple dans l'expérience de Taylor–Couette avec écoulement axial, Büchel *et al.* montrent que le seuil d'apparition des rouleaux toroïdaux coïncide avec la transition instable convectif / instable absolu de l'écoulement de base constitué par la superposition des écoulements de Poiseuille annulaire et Couette circulaire. Il en est de même pour le seuil d'apparition des rouleaux de convection dans l'expérience de Rayleigh Bénard avec écoulement latéral [71] qui correspond à un changement de nature d'instable convectif à instable absolu de l'écoulement de base constitué de l'écoulement de Poiseuille superposé à l'état purement conductif.

Plus généralement, les seuils d'instabilité globale en fonction de la vitesse d'advection pour les modèles développés dans cette étude coincident avec les vitesses des fronts sélectionnées en milieu infini par le critère de stabilité marginale (linéaire ou non linéaire) mais pas nécessairement avec le seuil d'instabilité absolu de l'écoulement de base. Les méthodes asymptotiques sur lesquelles reposent cette étude permettent de retrouver ce seuil et mettent également en évidence les caractéristiques spatiales des modes globaux non linéaires, solutions bifurquées au delà du seuil d'instabilité globale ; ces méthodes pourraient tout aussi bien s'appliquer à d'autres modèles, par exemple des modèles hamiltoniens ou bien des modèles où se propagent des solitons, pour lesquels les seuils ne correspondraient plus à des vitesses de fronts.

Les deux premiers chapitres se rapportent plus particulièrement aux milieux homogènes, tandis que les modifications entrainées par la faible inhomogénéité d'un milieu font l'objet du chapitre trois.

Dans le premier chapitre, l'influence des non linéarités fortes est décrite pour des systèmes dissipatifs qui admettent un potentiel. L'existence de modes globaux non linéaires est étudiée et ceux-ci sont caractérisés par des lois d'échelle près du seuil. L'accent est mis sur la comparaison entre propriétés locales et globales non linéaires. On montre en particulier que deux types de transitions peuvent avoir lieu vers une instabilité non linéaire globale appelées transition linéaire et transition non linéaire ; elles refletent les critères linéaire et non linéaire de stabilité marginale [93] dans l'étude de la propagation de fronts en milieux infinis. Chacune de ces transitions est associée à une loi d'échelle particulière pour la taille des modes globaux non linéaires. Une taille en $1/\sqrt{\epsilon}$ où ϵ désigne l'écart au seuil d'instabilité globale est obtenue dans le cas d'une transition linéaire vers l'instabilité globale alors qu'une taille en $\ln(1/\epsilon)$ est obtenue dans le cas d'une transition non linéaire. Ces lois d'échelles sont génériques comme le montre l'étude de plusieurs modèles d'équations d'amplitudes et peuvent donc être utilisées comme un critère pour déterminer le type de transition vers une instabilité globale dans un système expérimental.

Le deuxième chapitre étend ces résultats au cas de systèmes non potentiels. À nouveau, les modes globaux non linéaires sont obtenus par une approche de type système dynamique et leur existence est montrée par des développements asymptotiques rac-

cordés qui donnent également des lois d'échelle pour leur taille caractéristique et leur fréquence en fonction de l'écart au seuil d'instabilité globale. L'analyse en terme de système dynamique donne un critère de sélection de fréquence non linéaire. Les expériences numériques récentes de Büchel *et al.* [15] pour le système de Taylor–Couette avec advection et de Müller*et al.* [71] pour le système de Rayleigh–Bénard avec écoulement axial sont bien décrites par l'analyse de ces modèles. En particulier les mesures numériques de la taille des modes globaux effectuées par ces auteurs sont en très bon accord avec les lois d'échelle obtenues théoriquement, dans lesquelles n'intervient aucun paramètre ajustable.

Le troisième chapitre est consacré à l'extension aux milieux faiblement inhomogènes de la théorie des modes globaux fortement non linéaires décrits dans le premier chapitre. Nous montrons que les résultats numériques de Zielinska et Wesfreid [97] et expérimentaux de Goujon-Durand *et al.* [35], obtenus pour les sillages d'objets anguleux correspondent qualitativement à l'analyse que nous avons menée sur ces modèles simples. En particulier, leurs lois d'échelle obtenues expérimentalement sont bien décrites.

L'ensemble des résultats obtenus est résumé dans la conclusion où sont également proposées des extensions possibles de ce travail. Une idée qui a été un peu plus développée à la fin du chapitre deux concerne la stabilité secondaire des modes globaux non linéaires. Dans le cadre du modèle développé au chapitre deux, l'instabilité globale des modes globaux coincide avec la transition d'instable convectif à instable absolu de l'onde plane à laquelle le mode global est asymptotique à l'infini. Cette transition a été déterminée numériquement par l'analyse de la relation de dispersion des ondes d'instabilités autour de l'onde plane de base étendue en milieu infini, et l'instabilité globale secondaire du mode global a été vérifiée numériquement pour quelques valeurs des paramètres. Il est montré en particulier que cette bifurcation secondaire peut avoir lieu directement dès le seuil d'instabilité primaire. La dynamique obtenu au dela du seuil de bifurcation secondaire reste à analyser pour déterminer si elle est multipériodique ou directement chaotique. La description de ces deux premières bifurcations pourrait conduire à une ébauche d'un scénario de la transition vers le désordre dans les écoulements ouverts.

Chapitre 1

Modes globaux non-linéaires homogènes dans le cas potentiel

Global Instability in Fully Nonlinear Systems

A. Couairon and J. M. Chomaz
LadHyX, CNRS UMR 156, École Polytechnique, 91128 Palaiseau Cedex, France
(Received 12 April 1996)

Existence of a saturated steady solution of a nonlinear evolution equation subject to a boundary condition at $x = 0$, called a nonlinear global mode, is illustrated on the real subcritical Ginzburg-Landau model. Such a nonlinear global mode is shown to exist whereas the flow is linearly stable, convectively unstable, or absolutely unstable. If the linearized evolution operator is absolutely unstable, then a global mode exists but the converse is false. This result relies only on the existence of a structurally unstable heteroclinic orbit in the phase space and is likely to be generic as demonstrated by the supercritical Ginzburg-Landau and the van der Pol-Duffing equations. [S0031-9007(96)01599-2]

PACS numbers: 47.20.Ft, 47.20.Ky

Wakes behind bluff bodies [1], mixing layers with back flow [2], and helium or heated jets [3] constitute examples of open flows where self-sustained oscillations at a specific intrinsic frequency develop when varying the control parameter (the Reynolds number, the velocity ratio, or the density ratio, respectively) and give rise to saturated amplitude states. In such open flows, Galilean invariance is broken by the boundary conditions (the body, the splitter plate, the nozzle, respectively) and the effect of the advection velocity cannot be removed. Therefore, one has to deal, not only with the growth of disturbances, but also with their propagation. This leads us to distinguish between absolute (A) and convective (C) linearly unstable flows. These concepts have been initially developed in the context of plasma physics [4]. They refer to the asymptotic behavior of the impulse response of the flow in the frame singled out by the boundary condition (hereafter named "laboratory frame"): a system is said to be linearly stable (S) when its linear response to an initial localized impulse decays asymptotically in any moving frame, and linearly unstable otherwise: it is absolutely unstable (A) if, at any fixed location, the response grows in time and convectively unstable if it decays (C). The exponential growth of initial disturbances when the flow is absolutely unstable will ultimately be compensated by nonlinearities to give rise to an intrinsic self-sustained resonance. On the other hand, a convectively unstable flow is supposed to relax to the basic flow but will strongly respond to any continuously applied forcing and therefore behaves as a spatial amplifier.

These concepts apply as soon as instability waves propagate in the laboratory frame. They have been successfully used to interpret the dynamics of binary convection [5], lasers [6], and the dynamo theory of disklike objects [7].

Recently, one of us proposed to extend these ideas to take into account nonlinearity by simply replacing the impulse linear wave packet, used in the standard definition, by any saturated wave packet of finite size in an infinite domain [8]. He shows that, for nonlinearly unstable systems, distinction between nonlinearly convective or absolute instability depends only on whether the trailing front, separating the basic state from a bifurcated state, moves downstream or upstream in the laboratory frame. The determination of the nonlinear absolute or nonlinear convective nature of the instability is therefore straightforward once the front velocity is determined [9].

But as noticed in Ref. [8], this definition based on front velocity is quite formal as the laboratory frame is artificially defined and no specific physical behavior is associated with one or the other type of instability.

When the dynamics of real open flows is of interest, one should take into account "entrance" conditions at the origin of the domain and determine the nonlinear global (NG) instability. This new concept is more physical as it refers to the existence of nonlinear solutions in semi-infinite domains with a boundary condition at $x = 0$. Since the laboratory frame is singled out, the advection velocity is now externally imposed and the selection problem, encountered to determine the front speed in an infinite domain, is replaced by the simpler problem of existence of a solution in $x \in [0, +\infty)$. As we shall demonstrate elsewhere [10], properties of the phase space which determine the occurrence of NG instability and those which prelude the front selection are remarkably connected although the physical considerations leading to one or the other are different. In the following, we focus on the determination of the NG region and its links to A and C. For clarity, it is worth insisting that the term "nonlinear global mode" refers to the solution of a nonlinear homogeneous eigenproblem involving the whole streamwise domain and therefore corresponds to the dynamical system terminology. In the global mode literature [11], the "linear global mode" term refers to the solution of an eigenproblem which also involves the whole streamwise domain but which is nonhomogeneous and linear. These notions of global and NG modes should overlap when nonlinear effects will be considered on the linear global mode dynamics and when inhomogeneous

0031-9007/96/77(19)/4015(4)$10.00

(nonparallel) effects will be taken into account in the structure of the presently studied nonlinear global mode.

The purpose of this Letter is to illustrate the relationship between NG and A/C instability using a one dimensional real Ginzburg-Landau equation in a semi-infinite domain which accounts for an extended subcritical pitchfork bifurcation:

$$\frac{\partial A}{\partial t} + U_0 \frac{\partial A}{\partial x} = \frac{\partial^2 A}{\partial x^2} + \mu A + A^3 - A^5, \quad (1)$$

with the entrance condition $A(0) = 0$. Equation (1) depends on two control parameters (μ, U_0) independent of x. $U_0 \partial A/\partial x$ represents the effect of advection at the velocity $U_0 > 0$. Because of the symmetry $A \to -A$, only half of the solutions will be described. If the domain is made doubly infinite and the boundary condition $A(0) = 0$ is dropped, U_0 may be set to zero and classical results [12] are recovered: for $\mu < 0$, two linearly stable steady positive uniform states exist: $A_0 \equiv 0$ and $A_2 \equiv (1/2 + \sqrt{\mu + 1/4})^{1/2}$; for $\mu > 0$, A_0 becomes linearly unstable and A_2 remains the only stable state. Moreover, A_0 is linearly convectively unstable [13] (C) for $0 < \mu < U_0^2/4$ and linearly absolutely unstable (A) for $\mu > U_0^2/4$.

A nonlinear global mode is defined as a steady (or more generally an oscillatory) solution of (1) subject to the "entrance condition" (3) which therefore satisfies

$$U_0 dA/dx = d^2A/dx^2 + \mu A + A^3 - A^5, \quad (2)$$

$$A(0) = 0, \quad (3)$$

$$A(+\infty) = A_2. \quad (4)$$

As discussed in [8], this asymptotic behavior (4) is imposed by the existence of a Lyapunov functional with a minimum in A_2. In the phase space $(A, dA/dx)$, each trajectory of (2) not ending at A_2 or A_0 is associated with an infinite Lyapunov energy and hence is not physical. Conditions (3) and (4) imply that a NG mode is represented by a trajectory linking a point where $A = 0$ but with $dA/dx \neq 0$, to A_2. A solution linking $(A = 0, dA/dx = 0)$ to A_2 is not a global mode because it corresponds to a front solution with $A(-\infty) = 0$ which cannot be renormalized in $A(0) = 0$.

For convenience, let us consider that the advection velocity U_0 is fixed and that we study the topological changes in the phase portrait while increasing the control parameter μ. For a fixed advection velocity, let us define $\mu_A(U_0)$ as the threshold of NG instability. Using a perturbative asymptotic expansion, we have rigorously determined the onset of a global mode which corresponds to the emergence of an intersection between the stable manifold of A_2 with the dA/dx axis at finite dA/dx:

$$\mu_A(U_0) = 3/16(U_0^2 + 2U_0/\sqrt{3} - 1) \quad \text{for } U_0 < \sqrt{3}, \quad (5)$$

$$\mu_A(U_0) = U_0^2/4 \quad \text{for } U_0 > \sqrt{3}. \quad (6)$$

For simplicity, only the topological demonstration on which the rigorous proof is based is given here. As shown graphically in [8] for the case $\mu_A < 0$ and in Fig. 1 for the other cases, the emergence of an intersection between the stable manifold of A_2 and the dA/dx axis implies the existence at threshold of a structurally unstable heteroclinic trajectory between A_0 and A_2. When $U_0 < 1/\sqrt{3}$, [8] has shown the structure of the heteroclinic orbit and its perturbations. In this case, $\mu_A(U_0)$ is negative; therefore, A_0 is a saddle and a heteroclinic orbit connecting A_0 to A_2 exists for a single value of $\mu = \mu_A(U_0)$. This orbit is structurally unstable as it departs from A_0 along the unstable eigendirection. Its perturbation for $\mu > \mu_A(U_0)$ give rise to an intersection between the stable manifold of A_2 and the axis dA/dx

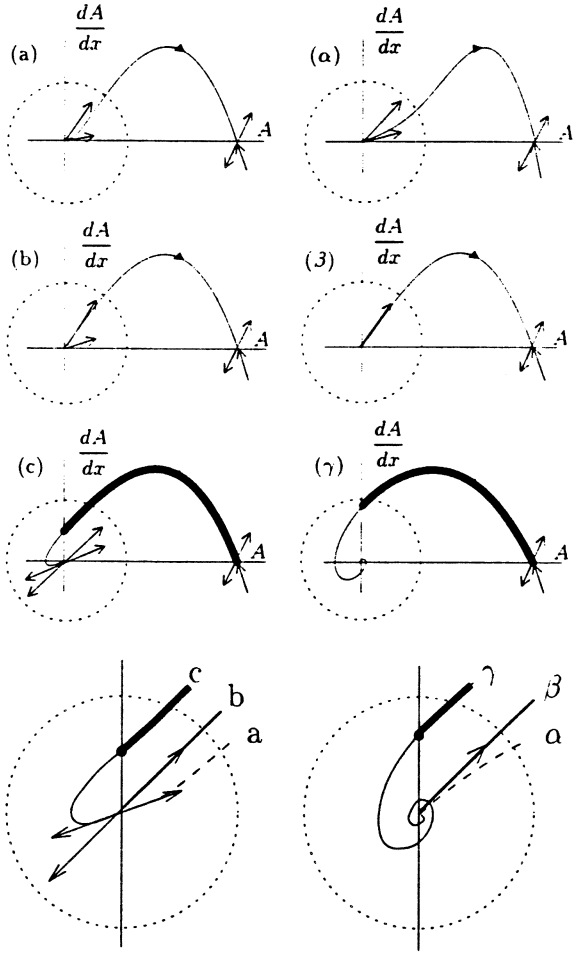

FIG. 1. Topological changes in the structure of the stable manifold of A_2 leading to the NG instability when keeping U_0 constant and increasing μ through the NG threshold $\mu_A(U_0)$. Left column: "global" instability case $1/\sqrt{3} < U_0 < \sqrt{3}$: (a) $0 < \mu < \mu_A$; (b) $\mu = \mu_A$; (c) $\mu > \mu_A$; right column: "local" instability case $U_0 > \sqrt{3}$; (α) $0 < \mu < \mu_A$; (β) $\mu = \mu_A$; (γ) $\mu > \mu_A$. The solution drawn by a *continuous heavy line* is the NG mode. In each case, the bottom figure presents the close up of the modifications which take place around A_0, a, b, c, α, β, γ referring to the labels in the figure.

(see Ref. [8]). When $U_0 > 1/\sqrt{3}$, the problem is less simple since the transition occurs for $\mu_A(U_0) > 0$, while A_0 is an unstable node. As shown in Fig. 1 where all possible cases obtained by numerical solutions of (2)–(4) are reproduced, whatever the value of μ positive, a heteroclinic orbit connecting A_0 to A_2 exists. For $1/\sqrt{3} < U_0 < \sqrt{3}$, and $\mu < \mu_A(U_0)$, the heteroclinic orbit always departs from A_0 to the right along its least unstable eigendirection (as it should generically [14]) [Fig. 1(a)]; at $\mu = \mu_A(U_0)$, an exceptional connection along the most unstable direction of A_0 appears [Fig. 1(b)]; when $\mu > \mu_A(U_0)$ the connection returns to the least unstable direction of A_0 [Fig. 1(c)] but from the other side of the dA/dx axis. In this case, the stable manifold of A_2 possesses a portion in $A < 0$ and therefore must cross the dA/dx axis giving rise to a NG mode plotted by a heavy line in Fig. 1(c). As for the former case ($U_0 < 1/\sqrt{3}$), an apparition of a global mode is linked to the crossing of a control parameter value for which a heteroclinic orbit between A_0 and A_2 exists and is structurally unstable because it departs from A_0 along its most unstable eigendirection. In this case, the transition is not associated to a local change around A_0 but to the global structure of the phase space and therefore cannot be detected by a linear analysis.

For $U_0 > \sqrt{3}$ and $\mu < \mu_A(U_0)$, the heteroclinic orbit always departs from A_0 to the right along its least unstable eigendirection [Fig. 1(α)] but for $\mu = \mu_A(U_0)$, the two eigendirections coincide [Fig. 1(β)]. For $\mu > \mu_A(U_0)$, the heteroclinic orbit spirals out of A_0 to A_2 [Fig. 1(γ)] giving rise to infinitely many global modes, only the first one being represented by heavy lines in Fig. 1(γ)]. At the bifurcation, the heteroclinic orbit is therefore structurally unstable but this time "locally" because the nature of the A_0 fixed point changes from node to focus. This local change occurs when two eigendirections near A_0 coincide, i.e., when the linear instability changes from linear convective to absolute (at $\mu = U_0^2/4$). Following the value of U_0, the threshold $\mu_A(U_0)$ has been determined by the global or local structural instabilities, depending which one occurs first. Only in the latter case does the NG threshold coincide with the A threshold.

These results have been demonstrated analytically by seeking the heteroclinic trajectory linking A_0 and A_2 as a polynomial or a series expansion in A. For each system, the existence of a NG mode for $\mu > \mu_A$ is then rigorously proved by matched asymptotic expansions with an inner linear region close to A_0 and a nonlinear region outside (the principle sketched in Fig. 1).

These results are synthesized in Fig. 2: In the shaded region (light or dark), the system is NG unstable. The dark shading corresponds to the A region whereas the light shaded region corresponds to a NG bifurcation which occurs while the basic state A_0 is linearly stable $\mu < 0$ or linearly convectively unstable $\mu > 0$. As we have shown, the NG threshold precedes the A threshold as

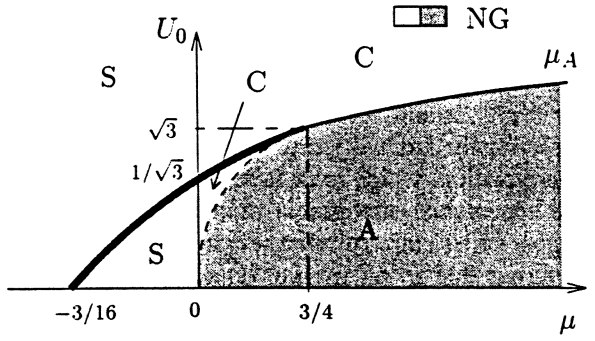

FIG. 2. NG domain in parameter space for the model (1). The dark gray region represents the absolutely (A) unstable region which is totally embedded in the NG region. In the light gray region, a NG exists whereas the system is not absolutely unstable. In this case, resonances are not predicted from a linear analysis but from a fully nonlinear one.

soon as a structurally unstable heteroclinic orbit appears in the phase space. This appearance involves the nonlinear solution of the system along the whole x domain and therefore cannot be obtained from a linearized approach. For $U_0 < \sqrt{3}$, the NG threshold (heavy line) always precedes the A threshold (discontinuous line) whereas for $U_0 > \sqrt{3}$, the system becomes NG unstable and A unstable simultaneously.

This result is likely to be general and does not seem to depend on the particular choice of a model equation. In the classical supercritical model

$$\frac{\partial A}{\partial t} + U_0 \frac{\partial A}{\partial x} = \frac{\partial^2 A}{\partial x^2} + \mu A - A^3, \qquad (7)$$

only one parameter μ or U_0 is necessary to describe the system, since one of them can be set to unity by rescaling A, x, and t. As a result, only one kind of transition should be observed by lack of degrees of freedom: we have found that the system becomes NG unstable and A unstable at the same time for $\mu_A = U_0^2/4$. But as soon as an extraterm is added to (7), for example, a nonlinear contribution to the advection [Eq. (8)], the NG region starts extending beyond the A domain. This system is known as the van der Pol-Duffing model:

$$\frac{\partial A}{\partial t} + (U_0 - A^2)\frac{\partial A}{\partial x} = \frac{\partial^2 A}{\partial x^2} + \mu A - A^3. \qquad (8)$$

The region of NG instability for model (8) in a semi-infinite domain with the condition (3) is bounded by the curves $\mu_A(U_0) = U_0^2/4$ for $U_0 < 6$, $\mu_A(U_0) = 3U_0 - 9$ for $U_0 > 6$. By contrast with model (1), the system becomes NG unstable and A unstable at the same value of the bifurcation parameter only for $U_0 < 6$, i.e., for small advection velocities. For $U_0 > 6$, the system is NG while being C unstable showing that this property arises even in the supercritical bifurcation case.

As already noted, the threshold of NG instability, which has been rigorously linked to the existence of

a structurally unstable heteroclinic orbit linking A_0 to A_2, is closely related to the selection of front velocity in infinite domains. van Saarloos and Hohenberg [9] have recently established on physical grounds a selection principle for the front velocity in the complex Ginzburg-Landau equation, which is in fact similar to our criterion for the appearance of a global mode. We are now able to propose an alternative interpretation of their results by conjecturing that in an infinite domain, the velocity v_f of the selected front between the basic state to the left and the bifurcated state to the right will be such that in the semi-infinite domain, a NG mode exists for advection velocities $U_0 < -v_f$ (v_f is counted positive to the right). If $-v_f$ is larger than U_0, a front initially imposed far downstream in a semi-infinite domain will move upstream without "feeling" at first the boundary condition at $x = 0$ and stop close to the boundary where it is "caught" at $x = 0$.

In conclusion, we have presented results concerning the nonlinear global (NG) instability vs the absolute (A) or convective (C) nature of the instability of a basic state using very simple models. NG are nonzero steady (or oscillatory) solutions of a well-posed, nonlinear system with a boundary condition at the origin. The existence of such a solution, which depends not only on the instability parameter, but also on the advection velocity, has been determined rigorously by matched asymptotic expansions. This solution appears while increasing μ as soon as a heteroclinic orbit linking the basic solution to the bifurcated solution in the phase space $(A, dA/dx)$ is structurally unstable. This structural instability may be either local, because it involves a change in the nature of the basic fixed point A_0 (the transition then corresponds to the linear absolute instability threshold), or global because the stable manifold of A_2 connects to the most unstable direction of A_0. In the latter case, the NG transition occurs while the system is either locally stable or locally convectively unstable. This implies immediately that a system is always NG unstable before being A unstable. We conjecture that the precedence of the NG instability over the A instability is general and therefore holds for any kind of instability in fluid mechanics, in plasma physics, in chemical reactions, or in nonlinear optics. An experimental confirmation of these results could be attempted by adding a mean flow to a chemical reaction. For example, Hanna *et al.* have studied propagating fronts in the iodate oxidation of arsenous acid [15] and have computed the velocity of a front appearing as a narrow blue band propagating through a colorless solution. This velocity seems nonlinearly selected. By rendering their experimental system open and setting an advection velocity in the solution, the emergence of NG modes should be observed as a steady blue narrow band surrounded by a colorless solution which, following the advection velocity magnitude, may happen while the solution is stable or convectively unstable.

We thank P. Manneville, P. Huerre, C. H. K. Williamson, and B. Tilley for many helpful comments and stimulating discussions.

[1] P. A. Monkewitz, Phys. Fluids **31**, 999–1006 (1988).
[2] (a) P. Huerre and P. A. Monkewitz, J. Fluid Mech. **159**, 151 (1985); (b) P. J. Strykowski and D. L. Niccum, Phys. Fluids A **4**, 770 (1992).
[3] (a) K. R. Sreenivasan, S. Raghu, and D. Kyle, Exp. Fluids **7**, 309 (1989); (b) P. A. Monkewitz, D. W. Bechert, B. Lehmann, and B. Barsikow, J. Fluid Mech. **213**, 611 (1990).
[4] (a) R. J. Briggs, *Electron-Stream Interaction with Plasmas* (MIT Press, Cambridge, MA, 1964); (b) E. M. Lifshitz and L. P. Pitaevskii, Physical Kinetics (Pergamon, London, 1981).
[5] G. Ahlers, D. Cannell, and R. Heinrichs, Phys. Rev. A **35**, 2757 (1987).
[6] (a) C. Z. Ning and H. Haken, Phys. Rev. A **41**, 3826 (1990); (b) P. Coullet, L. Gil, and F. Rocca, Opt. Commun. **73**, 403 (1989).
[7] A. Soward, Geophys. Astrophys. Fluid Phys. **64**, 201 (1992).
[8] J. M. Chomaz, Phys. Rev. Lett. **69**, 1931 (1992).
[9] (a) M. van Hecke, W. van Saarloos, and P. C. Hohenberg, Phys. Rev. Lett. **71**, 2162 (1993); (b) W. van Saarloos and P. C. Hohenberg, Physica (Amsterdam) **56D**, 303 (1992).
[10] A. Couairon and J. M. Chomaz, Physica D (to be published).
[11] (a) P. Huerre and P. A. Monkewitz, Annu. Rev. Fluid Mech. **22**, 473 (1990); (b) J. M. Chomaz, P. Huerre, and L. G. Redekopp, Phys. Rev. Lett. **60**, 25 (1988); (c) Stud. Appl. Math. **84**, 119 (1991); (d) P. A. Monkewitz, P. Huerre, and J. M. Chomaz, J. Fluid Mech. **251**, 1 (1993); (e) S. Le Dizès, P. Huerre, J. M. Chomaz, and P. A. Monkewitz, Philos. Trans. R. Soc. Lond. A **354**, 169 (1996).
[12] J. D. Gunton, M. San Miguel, and Paramdeep S. Sahni, in *Phase Transitions and Critical Phenomena*, edited by C. Domb and J. L. Lebowitz (Academic Press, New York, 1983), Vol. 8.
[13] R. J. Deissler, Physica (Amsterdam) **25D**, 233 (1987).
[14] J. Guckenheimer and P. Holmes, *Nonlinear Oscillations, Dynamical Systems, and Bifurcations of Vector Fields* (Springer-Verlag, Berlin, 1983).
[15] A. Hanna, A. Saul, and K. Showalter, J. Am. Chem. Soc. **104**, 3838 (1982).

Absolute and convective instabilities, front velocities and global modes in nonlinear systems

Arnaud Couairon and Jean–Marc Chomaz

LadHyX, CNRS UMR 156, Laboratoire d'Hydrodynamique,
École Polytechnique, 91 128 Palaiseau CEDEX, France

Abstract

We study the existence of self-sustained saturated solutions of the real Ginzburg–Landau equation subject to a boundary condition at $x = 0$; such solutions are called nonlinear global (NG) modes. The nonlinear global instability referring to the existence of these solutions is rigorously determined and the scaling behavior of the nonlinear global modes close to threshold is derived. The NG instability is first compared to the linear concept of convective/absolute (LC/LA) instability characterizing whether the impulse response of an unstable flow in an infinite domain is asymptotically damped or amplified at a fixed location. NG modes are shown to exist while at the same time the flow may be linearly stable, convectively unstable, or absolutely unstable. The growth size of the NG modes is shown to be proportional to $\epsilon^{-1/2}$ when NG and LA instabilities exist simultaneous, ϵ being the criticality parameter, whereas a $\ln(1/\epsilon)$ scaling is found when the NG instability occurs while the flow is LC unstable or linearly stable.

The nonlinear convective/absolute (NC/NA) instability defined [1] by considering, in infinite homogeneous domains, whether the front separating a bifurcated state from the basic state moves downstream or upstream, is determined using van Saarloos and Hohenberg results [2] for the selected front velocity. Remarkably, the NA domain and the NG domain are shown to coincide. Similar results are presented for supercritical bifurcating systems, for the "van der Pol–Duffing" system, and for a transcritical model. In all the cases, the LA instability is only a sufficient condition for the existence of a NG mode, and these simple models demonstrate that a system may be nonlinearly absolutely unstable whereas it is linearly convectively unstable. This property should be generic if one accepts the conjecture that the selected front velocity is always larger than the linear front velocity.

Response to a constant forcing applied at the origin is also studied. It is shown that in the NG region, the system possesses intrinsic dynamics which cannot be removed by the forcing. By contrast, the behavior of a nonlinear spatial amplifier is observed in a domain larger than the NC region. NC instability is only a sufficient condition to trigger the system with forcing.

Preprint submitted to Elsevier Science *October 21, 1996*

1 Introduction

The concepts of linear absolute (LA) and convective (LC) instabilities have recently been applied to understand the spatiotemporal development of open flows such as mixing layers, jets, or wakes [3, 4, 5]. In these flows fluid particles continuously enter and leave the experimental domain of interest. Therefore, the input perturbations and the mean advection have to be taken into account explicitly. The concepts of linear absolute or convective instability are usually defined with respect to the linear response to an initially localized impulse perturbation. If the wave packet, representing the Green function, asymptotically decays in any uniformly translating frame, the system is said to be linearly stable (LS) (Fig. 1(a)). If this is not the case, it is linearly unstable. Moreover, it is linearly absolutely (LA) unstable if, at any fixed location, the response grows in time (Fig. 1(c)) and linearly convectively (LC) unstable if it decays (Fig. 1(b)). In a LC unstable system, perturbations grow as they are advected away and the system acts as a spatial amplifier of incoming turbulence. On the contrary, in a LA unstable system, perturbations viewed at a fixed location keep growing and the system is thought to ultimately exhibit an intrinsic self-sustained oscillation.

In the linear approximation, such a self sustained oscillation has been analyzed by Chomaz *et al.* [6, 7, 8], Huerre and Monkewitz [3], Monkewitz *et al.* [9], le Dizès *et al.* [10], Hunt and Crighton [12, 13]. It has been called a linear global mode because it develops over the whole spatial domain, requiring the resolution of an eigenproblem, not only in the transverse direction, but also in the direction of the flow (x). Inhomogeneity in x (variation of the basic flow in x or boundary condition) is a necessary condition for the existence of linear global modes. When the inhomogeneity is weak (slow variation of the length scale λ, i.e. $d\log\lambda/dx \equiv \epsilon \ll 1$), a WKBJ approximation may be used to show that the existence of a local absolute region in the flow is a necessary condition for the occurrence of an unstable linear global mode. In fact, resonances observed in real experiments such as a flow past a cylinder, a helium hot jet [14], or a mixing layer with a back flow [15] are likely to result from the nonlinear saturation of a global mode. The weakly nonlinear theory has been applied to linear global modes [8, 10, 11] but, despite the already strong but inherent limitation that the amplitude must be exponentially smaller that the inhomogeneity parameter ϵ for the theory to be valid, it has been shown (Le Dizès *et al.* [10]) to

be ill-posed and the determination of the nonlinear nature of the bifurcation is in general impossible as ϵ goes to zero. The physical explanation of this mathematical breakdown is that, for an order-one advection velocity, the nonlinear modification of the basic flow occurs far downstream of the region which determines the growth rate of the linear global mode. Technically, this corresponds to the fact that, at the global instability threshold, the eigenfunctions of the linearized inhomogeneous operator and its adjoint do not overlap. This failure of the weakly nonlinear route signals the need for a strongly nonlinear analysis of the absolute and convective instability concepts.

In this spirit, Chomaz [1] has extended the notions of absolute and convective instabilities to nonlinearly unstable systems. This notion may be important not only for the description of nonlinearly unstable open flows such as boundary layers or Poiseuille flow, but also for linearly unstable flows with order-one advection for which the absolute instability occurs far from "the" threshold. For these systems where Galilean invariance is broken and the laboratory frame is unambiguously specified, nonlinear absolute and convective instabilities have been defined as follows: "The basic state of a system is *nonlinearly stable* (NS) if for all initial perturbations of finite extent and amplitude, the system relaxes to the basic state everywhere in any moving frame. The system is unstable if it is not stable in the above sense. The instability is *nonlinearly convective* (NC) if, for all initial perturbations of finite extent and finite amplitude, the system relaxes to the basic state everywhere in the laboratory frame. It is *nonlinearly absolute* (NA) if, for some initial condition of finite extent and amplitude, the system does not relax to the basic state everywhere in the laboratory frame." In the above definition, the "laboratory frame" refers to an experimental situation and is used to point out the frame specified by boundary conditions, forcing, *etc.*

A more convenient definition has been given in [1] for a one-dimensional bifurcating system **in an infinite domain**. The nonlinear nature of the instability may be determined by referring to the evolution of an initial "droplet" of bifurcating state surrounded by the basic state. When all initial droplets shrink (Fig. 1(d)) the system is stable; when at least one droplet expands (Figs. 1(e), 1(f)) the system is nonlinearly unstable. In this case, the distinction between absolute and convective

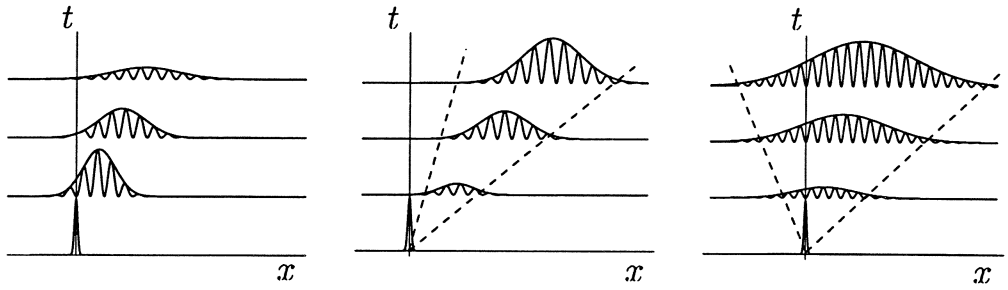

(a) Linearly stable (LS)

(b) Linearly convectively (LC) unstable

(c) Linearly absolutely (LA) unstable

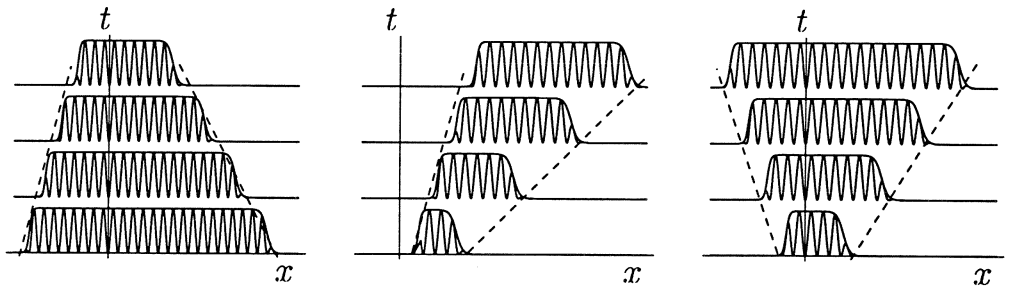

(d) Nonlinearly stable (NS)

(e) Nonlinearly convectively (NC) unstable

(f) Nonlinearly absolutely (NA) unstable

Figure 1: Sketches of the typical response of the system in the (x, t) plane.

instability depends on the velocity of the fronts limiting the droplet "in the laboratory frame." When the two limiting fronts are moving in the same direction, the instability is NC (Fig. 1(e)) and it is NA when the fronts are moving in opposite directions (Fig. 1(f)).

If we keep the usual convention that the mean advection is directed to the right, the convective or absolute instability is solely discriminated by the direction of propagation of the trailing front. In the abundant literature about fronts, the front velocity V_f is usually oriented from the bifurcated region to the basic state. Here V_f is thus positive when front moves to the left and negative when it moves to the right (V_f being oriented from right to left). Using this convention, the nonlinearly absolute or convective nature of the instability is determined by the sign V_f as follows: when $V_f > 0$ ($V_f < 0$), the front moves to the left (right) in the "laboratory"

frame, thus the flow is NA (NC) unstable. If the uniformly translating "front" solution is not unique, the determination of V_f implies the solution of a selection problem recently elucidated by Dee [19, 20], Ben Jacob *et al.* [21], and van Saarloos and Hohenberg [2, 22, 23] among others. In particular, van Saarloos and Hohenberg [2] have formulated the principle that the nonlinearly selected front velocity V_f is always greater than the velocity V_f^l of the linearly selected front. As pointed out by Huerre and Monkewitz [3], V_f^l is the velocity of the trailing edge of the Green function. Therefore, the sign of V_f^l determines whether the instability is **linearly absolute** ($V_f^l > 0$ with our orientation convention) **or linearly convective** ($V_f^l < 0$). van Saarloos and Hohenberg's principle essentially implies the extremely important property, illustrated by the present paper that LA instability is only a sufficient condition for NA instability. Indeed, if the system is LA unstable then $V_f^l > 0$, but as $V_f > V_f^l$, we immediately deduce that $V_f > 0$, which implies that the system is NA unstable. The converse is false since there may exist domains of the parameter space where the flow is linearly stable or linearly convectively unstable but nonlinearly absolutely unstable (see section 2).

The previous definitions pertain to the ideal case of an infinite domain with a somewhat artificial introduction of the laboratory frame. Dealing with real open flows, as argued by Huerre and Monkewitz [3] and Chomaz and coworkers [1, 6], the useful concept is the existence of a global mode of the flow which takes into account the upstream and downstream boundary conditions (eventually the lateral boundary conditions) and the nonparallelism of the flow. This global instability leads to self sustained dynamics characterizing the intrinsic behavior of the flow. In the linear approximation, the linear global instability corresponds to the emergence of a temporally growing solution occupying the whole spatial domain (the linear global mode). In a fully nonlinear study [16], the nonlinear global (NG) instability will correspond to the existence of a saturated solution of the original problem (the nonlinear global mode).

The physical significance of these notions will be illustrated by considering one-dimensional systems **in a semi-infinite domain**, with homogeneous left boundary conditions. A semi-infinite domain represents an idealized open flow, in which the perturbation level is supposed to be zero at the entrance of the test section. Galilean invariance is actually broken by the left boundary condition, which unambiguously

singles out the laboratory frame.

The aim of the present study is to establish the link between LA, NA, and NG instabilities for simple one-dimensional systems. For this purpose, we consider the one-dimensional real Ginzburg–Landau equation

$$\frac{\partial A}{\partial t} + U_0 \frac{\partial A}{\partial x} = \frac{\partial^2 A}{\partial x^2} - \frac{\delta \mathcal{V}(A)}{\delta A}, \tag{1}$$

where A stands for the real amplitude of the bifurcating mode. The operator $U_0 \partial A/\partial x$ represents the effect of advection at the mean velocity U_0 (taken positive). Except for the last section of our paper, the potential density $\mathcal{V}(A)$ is taken in the form

$$\mathcal{V}(A) = -\mu \frac{A^2}{2} - \frac{A^4}{4} + \frac{A^6}{6}, \tag{2}$$

which gives rise to a subcritical pitchfork bifurcation. In this case, equations (1) and (2) depend on two independent constant control parameters: the advection velocity U_0 and the bifurcation parameter μ.

The outline of the paper is as follows. In section 2, we give a brief review of the concepts ruling the propagation of fronts separating the bifurcating state from the basic state. This allows us to delineate the LS, LC, LA, NS, NC and NA regions of parameter space for model equation (1) with potential density (2). Although this section is a straightforward application of Chomaz's definition to van Saarloos and Hohenberg's results, the front solutions and the selection mechanism are presented because their phase-space interpretation also governs the existence of the NG mode. The latter problem is addressed in section 3 where the NG solutions of (1-2) in a semi-infinite domain with homogeneous boundary conditions at the origin ($x = 0$) are derived. Remarkably, we find that the existence region of such a NG mode, rigorously demonstrated by a perturbation argument, coincides with the NA region defined from the front velocity selection criterion. The NG mode existence demonstration gives us information which has no equivalent in the front selection problem. In particular, we obtain in this manner scaling laws for the growth size of the NG mode which appear to be remarkably different depending on whether the NG instability threshold precedes the LA instability threshold or coincides with it. The multiplicity of global modes is mentioned and the stability of all global modes is determined numerically. The response of (1) to an excitation of constant amplitude applied at the origin is examined in section 4 where it is demonstrated that the

system acts as a spatial nonlinear amplifier in the NC region. In section 5, we verify the genericity of the above results by examining two other potential densities $\mathcal{V}(A)$ corresponding to a supercritical bifurcation and to a transcritical bifurcation that breaks the $A \to -A$ symmetry, and by considering the case of the van der Pol–Duffing-like system with an additional nonlinear term $A^2 \partial A/\partial x$ in (1). In particular, we demonstrate that even for a supercritical bifurcation, the system may become NG unstable in regions of parameter space where the instability is LC.

We recall here the set of abbreviations we are going to use throughout this paper: LS, LC, LA denote linearly stable, linearly convective, and linearly absolute, respectively. NS, NC, NA denote nonlinearly stable, nonlinearly convective, and nonlinearly absolute, respectively. All these notions refer to an infinite domain and only NG, denoting nonlinear global, refers to the semi-infinite domain.

2 Front propagation and absolute instabilities

For the sake of clarity, it is convenient to emphasize once more the distinction between the **laboratory frame** in which the mean advection velocity is U_0, oriented to the right and the **advected frame** with no mean advection. We then describe the different possible fronts by their velocity v_f in the advected frame and V_f in the laboratory frame, oriented from right to the left. We recall that this somehow nonintuitive orientation is identical to the one classically adopted in the literature with v_f taken positive when pointing from the bifurcated region to the basic state region. In front studies, the bifurcated region is located to the left but in our case, the mean flow being taken to the right, the front we have to consider for the NC/NA instability determination separates the basic state on the left from the bifurcated state on the right. To preserve the mean flow classical orientation and the results from the front literature, we have decided to adopt this counter intuitive orientation for v_f and V_f. In the alternative, we would have been obliged to transform all the results from the front literature carrying unpractical minus sign in all the formulas. The velocity v_f is connected to its counterpart V_f in the laboratory frame, through the relation

$$v_f = U_0 + V_f \tag{3}$$

2.1 Front velocity selection criteria: a concise review

In the Rayleigh–Bénard experiment, when the temperature difference between the upper and the lower surface of the fluid layer is abruptly increased above threshold, the convection establishes itself by displacement of a convection front which is correctly determined by the theory developed below (Fineberg and Steinberg [25]). Similar phenomena occur in a Couette–Taylor flow. When the rotation rate is abruptly increased, the bifurcating state starts invading the diffusing state from the boundary forming a vortex front experimentally studied by Ahlers and Cannel [26] and numerically by Lücke *et al.* [27]. Front propagation also appears in chemical reactions as shown by Hanna *et al.* [28] or in population genetics (Aronson and Weinberger [30]). The determination of the front velocity in these various configurations and the analysis of the related pattern selection mechanism has motivated a whole group of theoretical studies. In particular, linear and nonlinear theories for front propagation have been developed [19, 20, 21, 22, 23]. The measurement of front velocities by Fineberg and Steinberg [25] and by Ahlers and Cannel [26] are in good agreement with the linear predictions. The nonlinear theory is not a pathological mathematical case and its validity has been experimentally illustrated in the work of Hanna *et al.* [28] on chemical waves in the iodate oxydation of arsenous acid systems. Their measurements of front velocities correspond to the nonlinear predictions of the transcritical model of section 5.3. Palffy-Muhoray *et al.* [31] also measured front velocities corresponding to the nonlinear predictions of the subcritical model in a nematic liquid crystal.

The mathematical analysis of equation (1) by Aronson and Weinberger [30] demonstrates that for a large class of potential functions $\mathcal{V}(A)$ and for sufficiently localized initial conditions the front velocity asymptotically approaches a constant value v_f. Dee [19, 20], Ben-Jacob *et al.* [21], and van Saarloos [22, 23] showed that this selected velocity corresponds to neutrally stable linear perturbations in the reference frame moving with the front. Huerre and Monkewitz [3] noticed that this problem is equivalent to the determination of the trailing edge velocity of the linear wave packet issuing from an impulsive initial perturbation (Green function). For a system invariant with respect to time translation and space translation in the

x-direction, the linear dynamics is described by a dispersion relation

$$D(\omega, k) = 0, \tag{4}$$

where ω and k are the complex frequency and complex wavenumber corresponding to a Fourier mode of the form $e^{i(kx-\omega t)}$. On each ray moving at velocity v to the left $x/t = -v$ in the (x,t) plane[1] (see Fig. 1), the asymptotically selected wave (k^v, ω^v) is such that[2]

$$D(\omega^v, k^v) = 0 \tag{5}$$

$$\frac{\partial D/\partial k}{\partial D/\partial \omega}(\omega^v, k^v) = v \tag{6}$$

On this ray, the growth rate equals

$$\sigma(v) = \omega_i^v + k_i^v v. \tag{7}$$

The trailing edge of the wave packet corresponds to the ray $x/t = -v^l$ on which the selected wave is neutral: $\sigma(v^l) = 0$. Therefore, the linearly selected front moves at velocity v^l.

Van Saarloos [22, 23] has noticed that for sufficiently localized initial conditions, "nonlinear" marginal stability may select a faster nonlinear front. van Saarloos and Hohenberg [2] have formulated the following conjecture: "*nonlinear selection occurs when there exists a discrete front with a velocity v^{nl} and a spatial decay rate*[3] *k_i^{nl} satisfying*

$$v^l < v^{nl} \quad \text{and} \quad k_i^l < k_i^{nl} \ . \tag{8}$$

When the above conditions are satisfied, it is indeed the front (v^{nl}, k_i^{nl}) that is selected over the linear front v^l, k_i^l. Moreover, this is consistent with an extended (nonlinear) marginal stability hypothesis since in that case the front v^{nl}, k_i^{nl} is still the stable one with the minimum velocity, i.e. fronts with $v > v^{nl}$ are linearly stable, while those with $v < v^{nl}$ are unstable."

Physically, this means that the front moving at speed v^{nl} will overtake all fronts moving at smaller velocity if it falls off faster toward $-\infty$ than the fronts with

[1] The minus sign comes from the convention for the sign of front velocity which is positive when the front moves toward the x negative.

[2] The supplementary pinching condition is not developed here (see [3]).

[3] k_i^{nl} is defined as $(1/A)dA/dx$ at $x \to -\infty$. Although its value may be determined by linearizing an amplitude equation around the basic state, k_i^{nl} depends on the properties of the front solution in the whole domain as illustrated in section 2.2, since the nonlinear selection involves the whole domain.

velocity v. "*The selected velocity is the one corresponding to the maximum value of k_i that describes the asymptotic spatial falloff of a front profile.*" This conjecture allows van Saarloos and Hohenberg to determine explicitly the front velocity of the complex Ginzburg–Landau equation.

2.2 Front solutions in the real Ginzburg–Landau equation

In this subsection, we describe uniformly translating fronts for the real Ginzburg–Landau equation. The profusion of details that follow might appear unnecessary as we only recover published results [18, 19, 20, 21, 22, 23, 24] in this section but the precise description of the phase space structure corresponding to the front solutions will be necessary for the determination of the global modes in section 3.

Let us recall some classical results [18] on the real Ginzburg–Landau model (1) and (2).

In the "advected" frame with $U_0 = 0$, equation (1) reads

$$\frac{\partial A}{\partial t} = \frac{\partial^2 A}{\partial x^2} - \frac{\delta \mathcal{V}(A)}{\delta A}, \tag{9}$$

and admits a Lyapunov functional $\mathcal{L}$

$$\mathcal{L}(A) = \int \left[\frac{1}{2} \left(\frac{\partial A}{\partial x} \right)^2 + \mathcal{V}(A) \right] dx. \tag{10}$$

One notes that $\mathcal{L}$ is minimum for uniform solutions that minimize the potential density $\mathcal{V}(A)$. The shape of the potential density given by (2) is displayed in Fig. 2 for different values of the bifurcation parameter μ. When $\mu < -1/4$, $A_0 \equiv 0$ is the single minimum. When $-1/4 < \mu < 0$, there exists three minima at $A_0 \equiv 0$ and $A_2 \equiv \pm(1/2+\sqrt{\mu+1/4})^{1/2}$. The amplitudes $A_1 \equiv \pm(1/2-\sqrt{\mu+1/4})^{1/2}$ correspond to a maximum of $\mathcal{V}(A)$ and therefore to a linearly unstable solution. The parameter value $\mu_M = -3/16$ defines the so-called Maxwell point at which the solutions A_0 and A_2 possess equal potential density. When $\mu_M < \mu < 0$, A_0 is said to be metastable (M) and A_2 is stable (S): a droplet of state A_2 embedded in an ocean of basic state A_0 expands. When μ passes 0, A_0 becomes a maximum of $\mathcal{V}(A)$, *i.e.* unstable, A_1 disappears, and A_2 becomes the only stable solution. This sequence of bifurcations is shown in Fig. 3.

A front represents a uniformly translating solution moving at velocity v of the

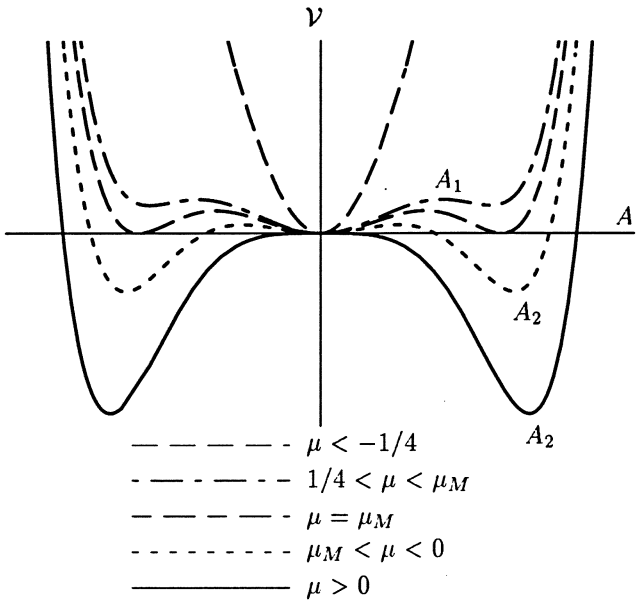

Figure 2: Shape of the potential $\mathcal{V}(A)$ versus the bifurcation parameter.

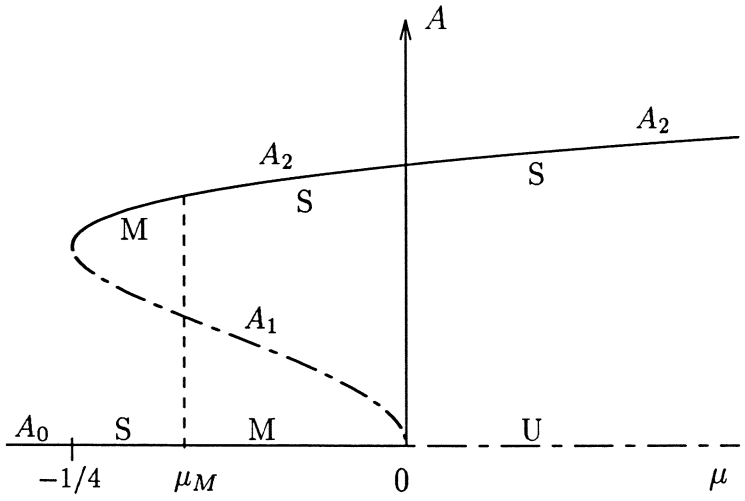

Figure 3: Bifurcation diagram of spatially uniform states. S: stable; U: unstable; M: metastable.

form[4] $A(x+vt)$. The front velocity satisfies the nonlinear eigenvalue problem

$$v\frac{dA}{dx} = -\frac{\delta \mathcal{V}}{\delta A} + \frac{d^2A}{dx^2} \tag{11}$$

with boundary conditions

$$A(-\infty) = A_0 = 0, \qquad A(+\infty) = A_2. \tag{12}$$

As noticed by many authors [19, 20, 21, 22, 23], for equation (11) with boundary conditions (12), the eigenvalue v is not unique and one has to determine which one is dynamically selected. In the phase space $(A, dA/dx)$, front solutions correspond to a heteroclinic orbit linking the basic state A_0 to the bifurcated state A_2. The front corresponding to the linear selection criterion [2] possesses the velocity $v^l(\mu)$ and a spatial decay rate $k_i^l(\mu)$ given by $\sigma(v^l) = 0$ where $\sigma(v)$ is given by (7) and $D(\omega, k) = -i\omega + k^2 - \mu$:

$$v^l(\mu) = 2\sqrt{\mu}; \qquad k_i^l(\mu) = -\sqrt{\mu}. \tag{13}$$

The linear front selection may only hold for $\mu > 0$. For the determination of nonlinear fronts, we have to describe the trajectories of (11) in the phase space. Phase portraits can be obtained by using a mechanical analogy. When x is formally interpreted as $-t$, equation (11) may be viewed as a dynamical system for a particle in a potential $-\mathcal{V}(A)$ with friction coefficient v. A detailed description of the phase portrait is given in Appendix A. Only general trends are discussed below, typical phase portraits being presented in Fig. 4. The arrows indicate increasing x and should be inverted according to the transformation $x \to -t$ when the particle analogy is used. The real orbits have been computed by a variable step Runge–Kutta integration of the associated first-order differential system

$$\frac{dA}{dx} = u, \tag{14a}$$

$$\frac{du}{dx} = vu + \frac{\delta \mathcal{V}}{\delta A}. \tag{14b}$$

Unstable manifolds are obtained using forward x-integration whereas stable manifolds are obtained by backward integration. The front solution exists when the stable manifold of A_2 (asymptotic to A_2 as $x \to +\infty$) connects to A_0 to form an

[4] By convention, the front velocity is oriented to the left whereas x is oriented to the right. This explains the unusual plus sign in $A(x+vt)$.

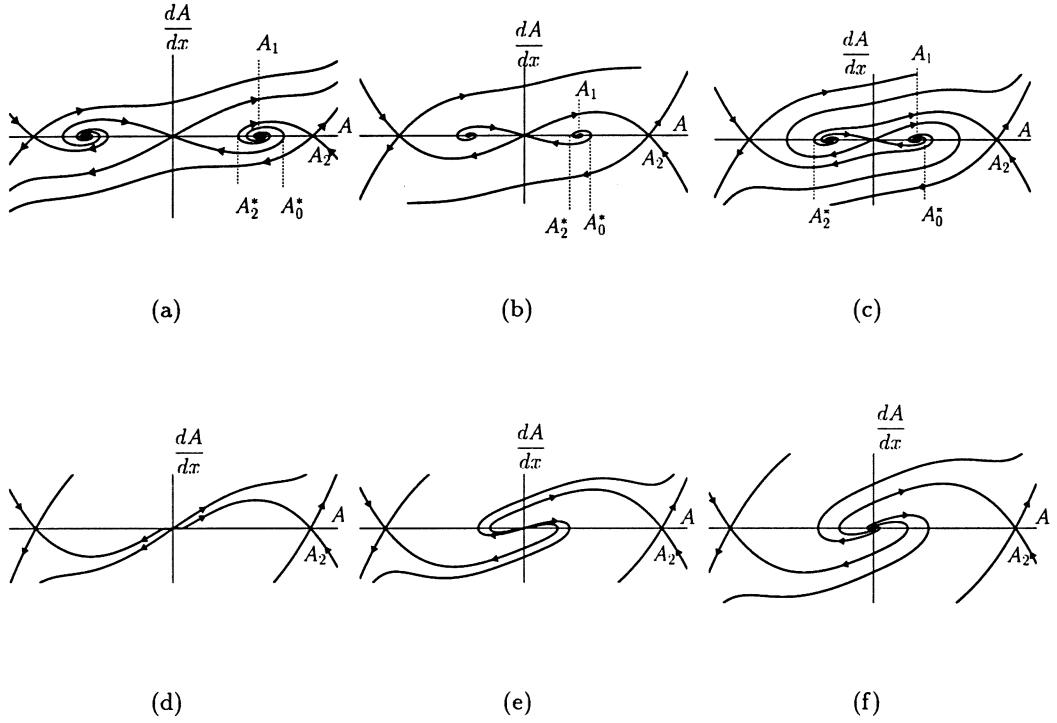

Figure 4: Phase portraits. See Fig. 5 for the region in the parameter space to which those phase portrait pertain.

heteroclinic orbit. In the following, the shape of this manifold in the phase space of dynamical system (14a-b) is discussed. Each phase portrait presented in Fig. 4 is typical of the region with the same label in parameter space (see Fig. 5).

Metastable region $\mu_M < \mu < 0$. At fixed μ, the stable manifold of A_2 issues from A_1 (Fig. 4(a)). For a particular value v_1 of v (Figs. 4(b) and 6(α)), the stable manifold of A_2 connects with the unstable manifold of A_0. Below v_1 (Figs. 4(c) and 6(β)), it comes spiraling out from $-A_1$. For a still lower particular value v_2, the stable manifold of A_2 connects from the $A < 0$ side to the unstable manifold of A_0 (Fig. 6(γ)); below v_2, the trajectory ending at A_2 comes from A_1 (Fig. 6(δ)). This sequence repeats itself indefinitely (Fig. 6(ϵ)), each change between an origin at $-A_1$ and A_1 being separated by a particular value v_n (dotted lines in Fig. 5) for which the stable manifold of A_2 connects with the unstable manifold of A_0, with $n-1$ about turns around A_0. This multiplicity of solutions may appear strange when considering the saddle structure of A_0. However, it may be easily checked by

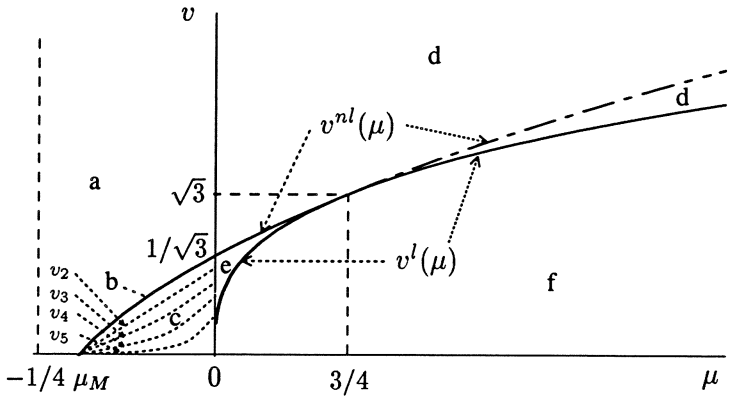

Figure 5: Front velocities versus the bifurcation parameter. Regions "a" to "f" correspond to the phase portraits similarly labeled on Fig. 4. The dotted lines represent discrete front velocities for $\mu < 0$. They persist when $\mu > 0$ but are not drawn since fronts exist continuously for all velocities. The scale on μ is not linear in order to make the picture clearer.

using the mechanical analogy. We leave it to the reader to transpose the discussion in terms of this mechanical analogy. Therefore, for $\mu_M < \mu < 0$, one has to solve a **discrete** selection problem (see Fig. 6(a)) since the heteroclinic orbits linking A_0 at $x = -\infty$ to A_2 at $x = +\infty$ exist for ordered discrete values v_n.

According to van Saarloos and Hohenberg's conjecture, the selected front **is the fastest front with the steepest fallout**: it corresponds to the heteroclinic orbit depicted in Figs. 4(b) and 6(α), associated with the velocity v_1 and therefore called v^{nl}. In Fig. 5, the selected front velocity is represented by the curve $v^{nl}(\mu)$ that separates domains "a" and "c". The corresponding particular solution may be sought in terms of a polynomial solution for $u(A) = dA/dx$, which satisfies

$$u\frac{du}{dA} - vu - \frac{\partial V}{\partial A} = 0, \tag{15}$$

with the boundary conditions

$$u(A_0) = 0, \quad u(A_2) = 0. \tag{16}$$

As found by van Saarloos and Hohenberg, this solution only exists for the particular value v^{nl}

$$v^{nl}(\mu) \equiv v_1(\mu) \equiv -\sqrt{3} + \frac{4}{\sqrt{3}}\left(A_2(\mu)\right)^2, \tag{17}$$

and it reads

$$u(A) = \frac{1}{\sqrt{3}}A(A_2^2 - A^2). \tag{18}$$

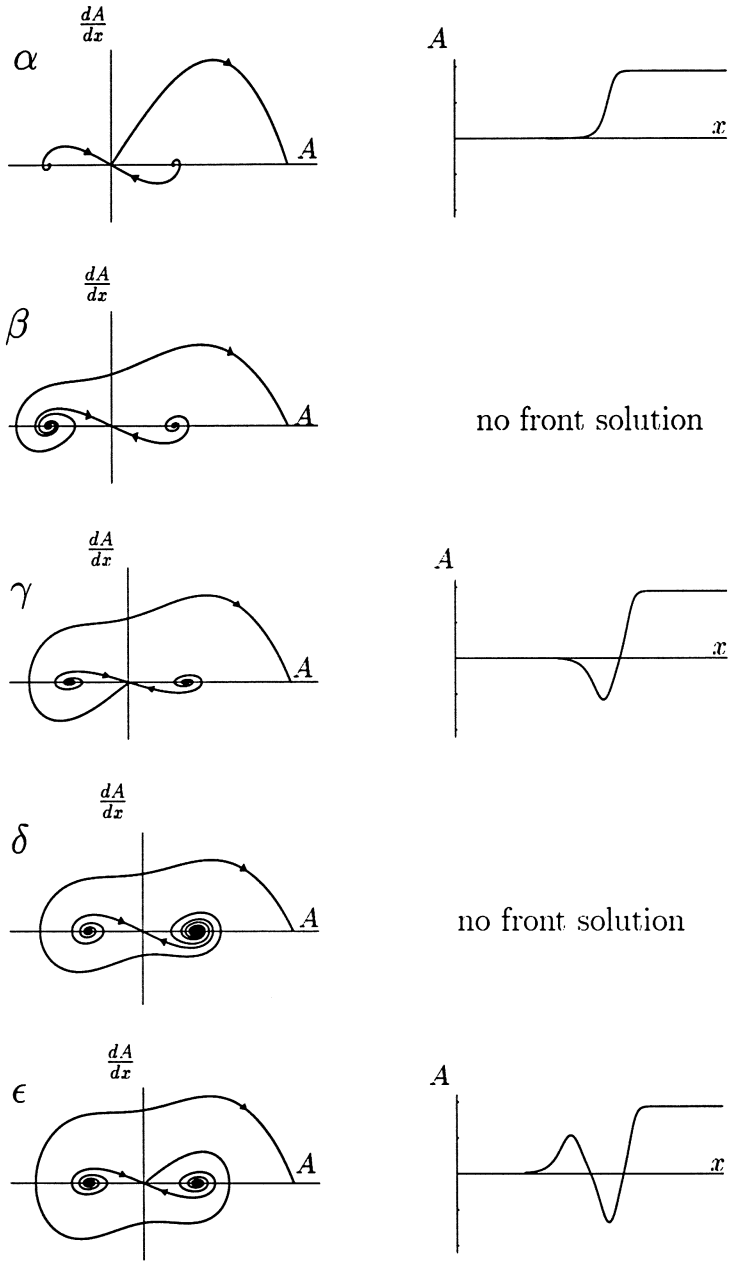

(a) $\mu_M < \mu < 0$

Figure 6: Front velocity selection: discrete selection for $\mu < 0$. α on line "b" in Fig. 5. β, γ, δ, ϵ are in domain "c". γ and ϵ corresponds to the dotted lines v_2 and v_3 of Fig. 5. β between v_1 and v_2. δ between v_2 and v_3.

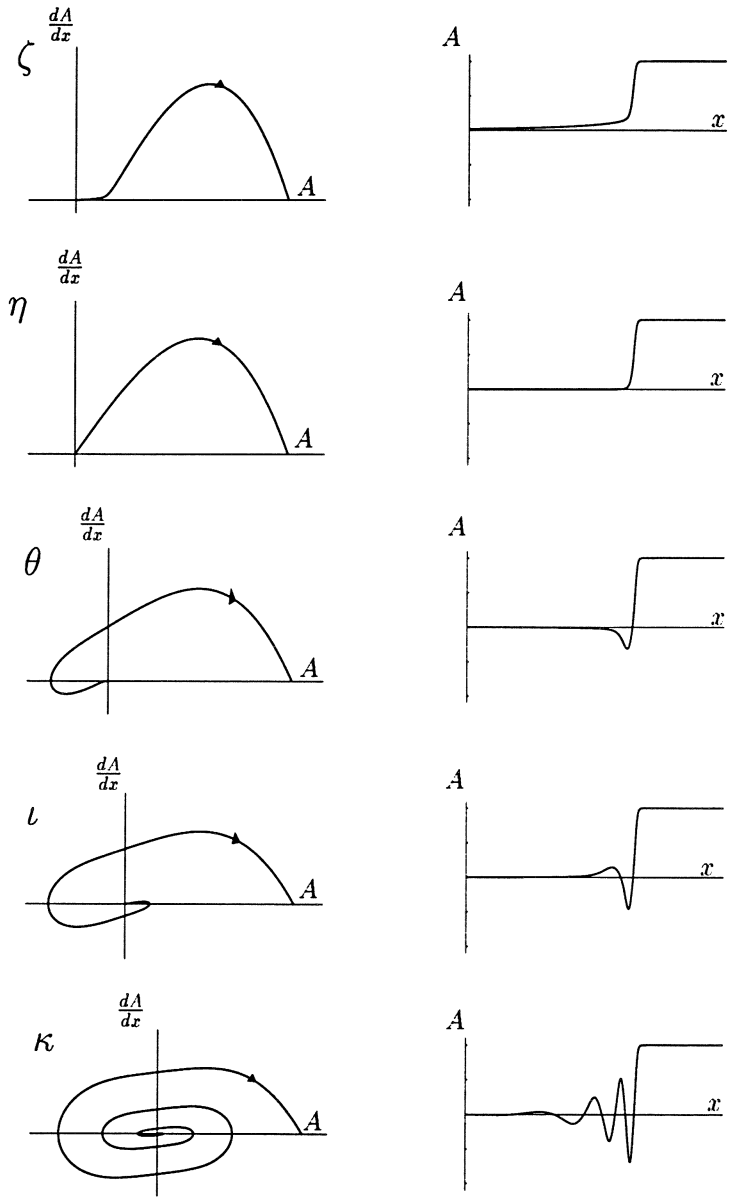

(b) $\mu > 0$

Figure 6: Front velocity selection: continuous selection for $\mu > 0$. ζ, η are in domain "d" in Fig 5. θ, ι are in domain "e" with half a turn and one turn around A_0 respectively. Between ι and κ, a sequence of front solutions with n half turns around the node A_0 exist, where n increases when approaching domain "f". κ is in domain "f" with an infinite number of turns around the spiral A_0.

This nonlinear front is associated with an asymptotic spatial decay rate given by

$$k_i^{nl}(\mu) \equiv -\left.\frac{du}{dA}\right|_{A_0} = -\frac{1}{\sqrt{3}}\left(A_2(\mu)\right)^2. \tag{19}$$

Linearly unstable region $\mu > 0$. It is quite remarkable that the above defined nonlinear front solution found for $\mu < 0$ persists for $\mu > 0$. The nonlinear and linear velocity curves $v^{nl}(\mu)$ and $v^l(\mu)$, plotted in Fig. 5, are tangent at $\mu = 3/4$. Therefore, we distinguish between three regions of (v, μ) space as defined in Fig. 5:

- region "d" where $v > v^{nl}(\mu)$ if $0 < \mu < 3/4$ and $v > v^l(\mu)$ if $\mu > 3/4$. In this region of parameter space, the corresponding stable manifold of A_2 issues, for any value of v, from A_0 without spiraling out (Figs. 4(d), 6(ζ) and 6(η)).

- region "e" where $v^l(\mu) < v < v^{nl}(\mu)$ in the range $0 < \mu < 3/4$. The heteroclinic orbit ending at A_2 comes from A_0 after **a finite number of turns** around A_0 (Figs. 4(e), 6(θ) and 6(ι)). Note that this number increases when parameters approach the curve $v^l(\mu)$ delineating the region "f". Again, this multiplicity may appear strange when considering the node structure of A_0, but it is easily checked with the mechanical analogy. The previously introduced dotted lines v_n in Fig. 5 persist in this region. In the part of region "d" between v_n and v_{n+1} fronts makes n half about turns around A_0. Since a front exists for all value of v, these lines are no longer significant and are not drawn in Fig. 5.

- region "f" where $v < v^l(\mu)$. The fixed point A_0 of equation (11) is an unstable focus and the heteroclinic orbit ending at A_2 comes from A_0 after **an infinite number of revolutions** around A_0 (Figs. 4(f) and 6(κ)).

Therefore, for $\mu > 0$, an heteroclinic orbit linking A_0 to A_2 is associated to a front solution for every value of v_f. The selection problem is **continuous** in contrast with the discrete selection problem prevailing in the range $\mu_M < \mu < 0$. Whatever μ, we have $v^{nl}(\mu) > v^l(\mu)$ but for $\mu < 3/4$, the nonlinear front falls off faster than its linear counterpart ($k_i^{nl}(\mu) > k_i^l(\mu)$) and the nonlinear front is selected following van Saarloos and Hohenberg's conjecture. On the contrary, for $\mu > 3/4$, the linear front is selected as $k_i^{nl}(\mu) < k_i^l(\mu)$

2.3 Linear absolute instability, nonlinear absolute instability and front velocities

Let us now introduce the laboratory frame characterized by a mean advection U_0 different from zero. As argued in the introduction, the sign of the linear front velocity in the laboratory frame $V^l = v^l - U_0$ determines whether the instability is linearly convective or absolute. Therefore, the curve $U_0 = v^l(\mu)$ delineates the linearly absolutely unstable region (in dark gray on Fig. 7). This curve corresponds to the NA instability threshold only when the linear front is selected, *i.e.* when $\mu > 3/4$. When $\mu_M < \mu < 3/4$, the nonlinear front is selected and the curve $U_0 = v^{nl}(\mu)$ defines the transition between NC and NA instability regions.

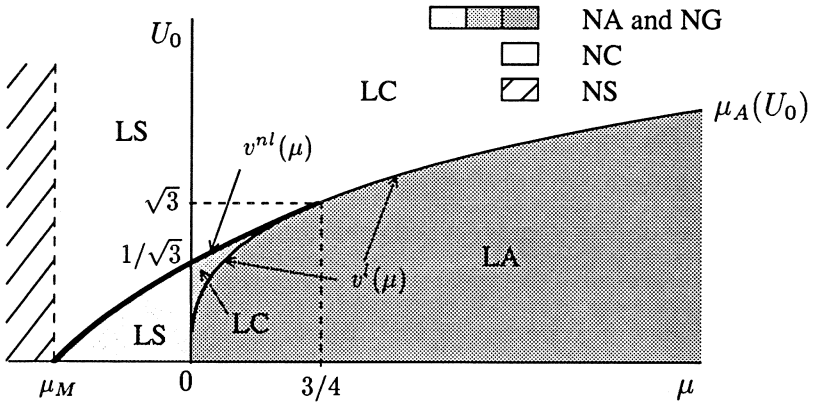

Figure 7: Parameter space. In the three shaded regions, the system is nonlinearly absolutely (NA) unstable. In the dark gray region, the system is linearly absolutely (LA) unstable. In the light gray region, the system is linearly stable (LS). In the medium gray region, the system is linearly convectively (LC) unstable. Section 3 will show that a NG mode exists in the three shaded regions. For fixed parameters, a finite number of NG modes exist in the light and medium gray regions and an infinite number of NG modes exist in the dark gray region.

Note that, in this NA region, the system is linearly stable when $\mu_M < \mu < 0$ (light gray region in Fig. 7), LC when $v^l(\mu) < U_0 < v^{nl}(\mu)$ (medium gray region in Fig. 7) and LA when $U_0 < v^l(\mu)$ (dark gray region in Fig. 7). For this model, we verify that the region LA is embedded within the NA region.

Up to now, we have fixed μ and determined the nature of the instability as a function of U_0, but as U_0 and μ may be viewed as two independent control parameters of the system, it may be more convenient to consider U_0 constant and determine the value $\mu_A(U_0)$ that defines the threshold between NC and NA. The expression

$\mu_A(U_0)$ obtained from the laws (13) and (17) for the selected front velocity reads

$$\text{if } U_0 < \sqrt{3}, \qquad \mu_A(U_0) = \mu^{nl}(U_0) = \frac{3}{16}\left(U_0^2 - \frac{2}{\sqrt{3}}U_0 - 1\right) \tag{20a}$$

$$\text{if } U_0 > \sqrt{3}, \qquad \mu_A(U_0) = \mu^{l}(U_0) = \frac{U_0^2}{4}. \tag{20b}$$

The curve $\mu^{nl}(U_0)$ defines the NC/NA transition for $U_0 < \sqrt{3}$ and has no specific significance for $U_0 > \sqrt{3}$. Whatever U_0, the curve $\mu^{l}(U_0)$ corresponds to the LC/LA transition but to the NC/NA transition only for $U_0 > \sqrt{3}$.

3 Nonlinear global modes in a semi-infinite domain

3.1 Nonlinear global modes and nonlinear absolute instability

We consider stationary solutions of (1) in a semi-infinite domain with $U_0 \neq 0$ and boundary condition $A(0) = 0$. As we have already noticed, this boundary condition breaks the Galilean invariance and unambiguously singles out the laboratory frame. Actually, it represents an idealized flow in which no disturbances are present at the entrance of the domain. For real flows, more realistic, but inevitably more complicated, boundary conditions should be studied case by case to see if our idealized solutions persist. An example will be given in section 4 for the signaling problem. Nontrivial stationary solutions satisfy the equation

$$\frac{d^2A}{dx^2} - U_0\frac{dA}{dx} + \mu A + A^3 - A^5 = 0, \tag{21}$$

with the boundary conditions

$$A(0) = 0, \qquad A(+\infty) = A_2. \tag{22}$$

If we replace U_0 by v, equation (21) becomes identical to equation (11) but with a different boundary condition. A nonlinear global mode is represented by a trajectory in phase space linking a point where $A(0) = 0$ with $dA/dx(0) \neq 0$ to A_2. Graphically, the existence of global modes for the system can be deduced from the phase portraits (Figs. 4 and 6). For fixed parameters μ and U_0, a global mode exists if the stable manifold of A_2 intersects the line $A = 0$ at a point different from A_0. We shall notice that, in contrast with the selection problem faced when determining the front velocity as a function of μ, the problem is here the existence or nonexistence of a solution with respect to both control parameters U_0 and μ.

In the range $\mu_M < \mu < 0$, a NG mode exists only when $U_0 < v^{nl}(\mu)$ (light gray region in Fig. 7) as the orbit asymptotic to A_2 crosses at least one time $A = 0$ with $dA/dx \neq 0$ (Fig. 4(c), region "c" in Fig. 5). When $v_{n+1} < U_0 < v_n$, n intersection points exist corresponding to n different NG solutions (Figs. 6(β) and 6(δ) for $n = 1$ and $n = 2$). When $U_0 > v^{nl}(\mu)$ (region "a" in Fig. 5), no NG mode exists since the stable manifold of A_2 comes from A_1 (Fig. 4(a)).

In the range $0 < \mu < 3/4$, the stable manifold of A_2 crosses at least one time the axis $A = 0$ with $dA/dx \neq 0$ for $U_0 < v^{nl}(\mu)$ (Figs. 4(e) and 4(f)) and the number of intersections increases when approaching the curve $U_0 = v^l(\mu)$. In the domain $v^l(\mu) < U_0 < v^{nl}(\mu)$, a finite number of NG modes exist, as the orbit ending at A_2 connect to A_0 with a finite number of revolutions around A_0 (Figs. 4(e), 6(θ) and 6(ι), medium gray region in Fig. 7). In the domain $0 < U_0 < v^l(\mu)$, an infinite discrete number of NG modes exists as the stable manifold of A_2 comes spiraling out from A_0 (Fig. 4(d), Fig. 6(κ), dark gray region in Fig. 7).

In the range $\mu > 3/4$, the orbit asymptotic to A_2 crosses $A = 0$ only for $U_0 < v^l(\mu)$ when the fixed point A_0 becomes an unstable focus (see Fig. 4(f)). In this case, an infinite number of global modes bifurcate at the same time (dark gray region in Fig. 7).

These results may also be expressed fixing U_0 and varying μ in which case a global mode exists when $\mu > \mu_A(U_0)$, where μ_A is defined by equations (20a-b). The number of NG modes is infinite above $\mu_A^l(U_0)$ (dark gray region in Fig. 7).

It is quite remarkable that the determination of the NA instability region based on the sign of the front velocities in an infinite domain coincides with the NG instability region in a semi-infinite domain. This allow us to propose a new criterion to determine the front velocity selection: The selected front may be viewed as the marginal global mode, *i.e.* the global mode with zero slope at the origin and, therefore, $v(\mu)$ is such that $\mu = \mu_A(v)$.

3.2 Existence of global modes and scaling laws

Whereas the front selection is based on a conjecture, the existence of a global mode can be demonstrated rigorously by matched asymptotic expansions corresponding to the perturbative arguments sketched in Figs. 8(b), 8(c) for $U_0 < \sqrt{3}$ and 8(d) for $U_0 > \sqrt{3}$. When $U_0 < \sqrt{3}$, at the NG threshold, the stable manifold of A_2 connects

with the most unstable manifold of A_0. This solution is known [24] to be structurally unstable. This is shown in Fig. 8(c): the heteroclinic trajectory emanates from the most unstable eigendirection corresponding to the largest eigenvalue of equation (21) linearized around origin. A small change in the control parameter μ around the value μ_A perturbs this orbit which can no longer be tangent to the most unstable eigendirection. For $U_0 < 1/\sqrt{3}$, the other direction is stable and the perturbed trajectories are shown in Fig. 8(b). For $1/\sqrt{3} < U_0 < \sqrt{3}$, A_0 is an unstable node, the perturbed trajectory emanates from the least unstable eigendirection and, when $\mu > \mu_A$, it makes one about turn around the origin in order to connect with A_2. It crosses the axis $A = 0$ at a point where $dA/dx \neq 0$, and corresponds to a global mode. When $U_0 > \sqrt{3}$, the particular solution existing at $\mu = \mu^{nl}(U_0)$ corresponds to an heteroclinic orbit tangent to the least unstable eigendirection at the origin which is structurally stable. Perturbation of this orbit through a variation of μ still leads to trajectories that remain tangent to the least unstable eigendirection (Fig. 8(e)). In such an instance, no NG mode is obtained.

In this subsection, we explicitly perturb the heteroclinic orbit prevailing at the bifurcation parameter $\mu = \mu_A(U_0)$ for a fixed advection velocity U_0. We demonstrate that a global mode exists as soon as $\mu > \mu_A$ (with $\mu_A = \mu^{nl}(U_0)$ when $U_0 < \sqrt{3}$, and $\mu_A = \mu^{l}(U_0)$ when $U_0 > \sqrt{3}$). Details of the calculations can be found in Appendix B.1.

This allows us to establish scaling laws with respect to a departure from the nonlinear absolute instability threshold $\epsilon = \mu - \mu_A$ for the slope at the origin $dA/dx(0)$ and for the characteristic size of the initial growth region of the global mode defined as the distance at which $A = 0.99A_2$.

In the parameter range $U_0 < \sqrt{3}$, the nonlinear selection criterion for the front velocity is expected to apply; the absolute instability threshold $\mu_A = \mu^{nl}(U_0)$, and the shape of the front at this value of the bifurcation parameter are known analytically (see Appendix B.1). We determine the perturbed solutions in the following way: For $\mu = \mu_A + \epsilon$ with $\epsilon \ll 1$, the solutions of equation (21) with boundary conditions (22) are the functions with $u(A) = dA/dx$ which satisfy

$$u\,u' - U_0\,u + \mu\,A + A^3 - A^5 = 0, \tag{23}$$

where the prime denotes differentiation with respect to A. Under this change of variable, the initially second-order equation (21) becomes first-order and the two boundary conditions (22) are transformed into

$$u'(A_0) = U_0, \qquad u\left(A_2(\mu)\right) = 0. \tag{24}$$

The first boundary condition $u'(A_0) = U_0$ results from writing (23) at $A = A_0$ and exploiting the original constraint $u(A_0) \neq 0$ on the existence of a global modes. One of the two boundary conditions has to be dropped in order to solve (23-24) in the singular limit $\epsilon \ll 1$ and an inner region of size ϵ^β has to be introduced in the neighborhood of the origin (see Figs. 8(a), 8(b) and 8(c)). The inner solution satisfies the condition $u'(A_0) = U_0$ whereas the outer solution satisfies the condition $u\left(A_2(\mu)\right) = 0$. The method of matched asymptotic expansions [32] is applied and the matching of inner and outer solutions imposes the size of the inner region to be ϵ^β with

$$\beta = \frac{\sqrt{3} + U_0}{2(\sqrt{3} - U_0)}. \tag{25}$$

This result is valid for $\beta > 0$, *i.e.* $U_0 < \sqrt{3}$. When $U_0 > \sqrt{3}$, the inner solution does not cross the axis $A = 0$ and no NG mode exists for $\mu = \mu^{nl}(U_0) + \epsilon$, $\epsilon \ll 1$. In Fig. 8(e) one sees that when $U_0 > \sqrt{3}$, matching of the inner and outer solutions is always possible but the inner solution remains tangent to the less unstable manifold at A_0 with no revolution around A_0 and never crosses the $A = 0$ axis. This confirms that the law for the global instability threshold μ_A changes as U_0 exceeds $\sqrt{3}$ since $\mu^{nl}(U_0)$ is no longer the threshold of NG instability when U_0 exceeds $\sqrt{3}$.

The slope $u(A_0)$ is given as a function of the departure ϵ from the absolute instability threshold by the expression

$$u(A_0) \simeq v_0 \epsilon^\beta, \tag{26}$$

where the constant v_0 is given by the matching (equation (B.19) of Appendix B.1).

The characteristic growth size of the global mode is defined as the distance Δx such that $A(\Delta x) = 0.99\, A_2$. It may be calculated by adding the x-thickness of the inner region and the size of the outer solution between the boundary of the inner layer ($A = \epsilon^\beta$) and the point at which the amplitude reaches the value $0.99\, A_2$.

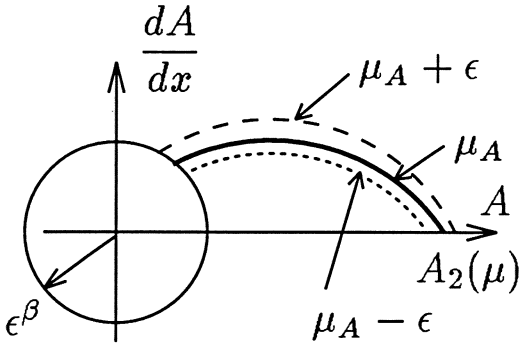

(a) Outer solution

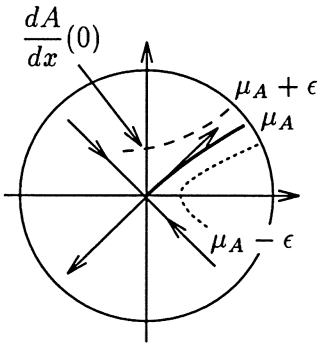

(b) A_0 saddle, $0 < U_0 < 1/\sqrt{3}$.

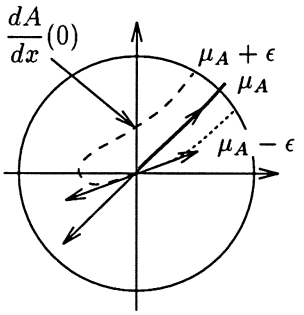

(c) A_0 unstable node, $1/\sqrt{3} < U_0 < \sqrt{3}$.

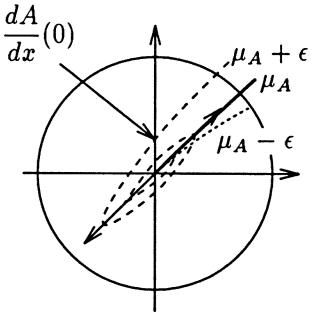

(d) A_0 unstable focus, $U_0 > \sqrt{3}$.

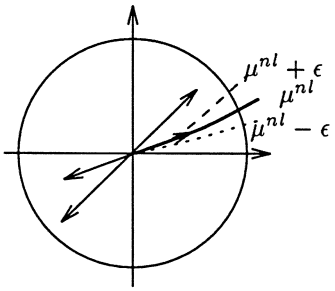

(e) A_0 unstable node, $U_0 > \sqrt{3}$, $\mu = \mu^{nl}$.

Figure 8: Matching of inner and outer solutions. The solution drawn in continuous line is the basic solution at the nonlinear instability threshold. The solution drawn in dashed lines is the perturbed solution above μ_A. The dotted line represents the solution for μ smaller than μ_A.

Details of the calculation are given in Appendix B.2. The scaling law so obtained is given by

$$\Delta x \simeq \frac{4}{\sqrt{3}+U_0}\left(-\beta \ln \epsilon + \ln \mathrm{K}\right) \tag{27}$$

where the constant K is found by the matching (equation (B.26) of Appendix B.2). If U_0 is set to zero and only the dominant term is taken into account, the result of Coullet *et al.* [34] valid for $U_0 = 0$ is recovered.

In the parameter range $U_0 > \sqrt{3}$, the system simultaneously becomes NG and LA unstable at the control parameter value $\mu^l = U_0^2/4$. The solution of equation (23) with boundary conditions (24) is known analytically as a series whose coefficients have to be determined numerically (see Appendix C). Except for the fact that we are now dealing with an infinite series[5] for the order zero external solution instead of a polynomial, the subsequent steps of the method are the same as in the previous case: for a bifurcation parameter setting $\mu = \mu^l + \epsilon, \quad \epsilon \ll 1$, equation (23) is solved subject to the boundary condition $u'(A_0) = U_0$ in the inner layer and the condition $u\left(A_2(\mu)\right) = 0$ in the outer layer (see Fig. 8(d)). The inner solution may be calculated explicitly; the outer solution takes the form of a numerically determined series. Matching of the two solutions again leads to the determination of the inner layer thickness, to the scaling laws for the slope of the solution at the origin $u(A_0)$ and for its growth size Δx, and to an additional solvability condition (equation (C.12) of Appendix C) which may be checked numerically. The scaling law for the slope at the origin is given by

$$u(A_0) \simeq v_0 \epsilon \exp\left(-\frac{U_0 \pi}{2\sqrt{\epsilon}}\right), \tag{28}$$

where the term v_0 represents the slope at the origin of the inner solution $d\xi/dx$ (ξ being the inner variable), as given in equation (C.14) of Appendix C. The growth size of the solution is given by

$$\Delta x \simeq \frac{\pi}{\sqrt{\epsilon}}. \tag{29}$$

The success of the matching procedure *a posteriori* proves that the NG instability threshold μ_A indeed follows the linear criterion when $U_0 > \sqrt{3}$. Numerically, we are able to perform the matching only for $U_0 > \sqrt{3}$ since for $U_0 < \sqrt{3}$, the additional solvability condition (equation (C.12) of Appendix C) cannot be fulfilled.

[5] which should be numerically estimated in each case

Each scaling law for the growth size of NG modes is characteristic of one kind of transition to a NG instability. Indeed, when the NG instability occurs while the system is convectively unstable ($U_0 < \sqrt{3}$), the growth size of NG modes scales as $\ln(1/\epsilon)$ (Eq. (27)), whereas it scales as $\epsilon^{-1/2}$ (Eq. (29)), when the NG instability occurs at the LC/LA transition ($U_0 > \sqrt{3}$).

The above scaling laws (26, 27, 28, 29) have been validated by direct numerical integration of system (14a-b). Numerical values of $u(A_0)$ and Δx for steady solutions are generated and compared with theoretical scaling predictions. The stable manifold of A_2 is obtained by backward variable step Runge–Kutta x-integration[6].

The numerically computed value of $\ln(dA/dx(x=0))$ are displayed in Fig. 9(a) as a function of the departure from criticality for four different advection velocities in the range $U_0 < \sqrt{3}$ ($U_0 = 0.1, 0.5, 1.0, 1.5$). The numerical values (dashed lines) of $\ln(dA/dx(x=0))$ are in excellent agreement with theoretical predictions (continuous lines) for small U_0. It can be seen that, as the advection velocity U_0 approaches $\sqrt{3}$, the domain of validity of scaling law (26) becomes restricted to a smaller neighborhood of the threshold μ^{nl}.

In order to validate scaling law (27) for the characteristic growth size Δx of global modes against the distance to the absolute instability threshold μ_A, all integration space steps between the amplitudes A_0 and $0.99\,A_2$ were added together. Predicted values given by the theoretical scaling law (27) (continuous lines in Fig. 9(b)) are in very good agreement with their numerical counterparts (dashed lines) for small advection velocities. As U_0 approaches $\sqrt{3}$, the agreement is restricted to small ϵ.

Scaling laws (28, 29) giving the slope of the global mode at the origin and its characteristic growing size in the range $U_0 > \sqrt{3}$ are checked numerically in the same way. Corresponding results are gathered in Fig. 10. We indeed verify that $\ln|\ln(dA/dx(x=0))|$ and $\ln \Delta x$ are linear as functions of $\ln \epsilon$ as long as ϵ remains sufficiently small. For higher ϵ, theoretical results and numerical values diverge in Fig. 10(a) due to the contribution of higher-order terms in ϵ. As detailed in Appendix C, v_0 is given by a series which converges very slowly. However, we do verify in Fig. 10 that the series is adequately converged.

[6] In order to validate the scaling laws completely, we have to check that the computed stable manifold of A_2 is indeed dynamically selected in a temporal simulation of (1). This will be done in section 4.

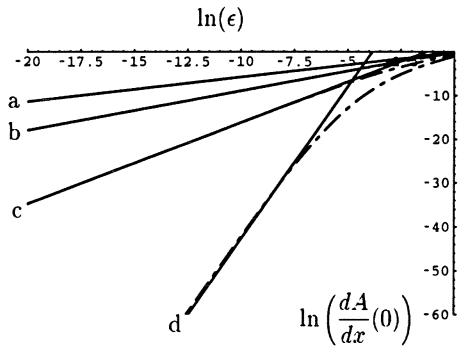

(a) $dA/dx(0)$ versus ϵ

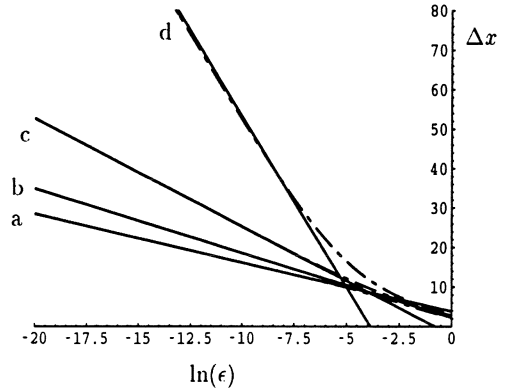

(b) Characteristic growth size Δx of the nonlinear global modes

Figure 9: Scaling laws for the subcritical model with $U_0 < \sqrt{3}$. a) $U_0 = 0.1$, b) $U_0 = 0.5$, c) $U_0 = 1.0$, d) $U_0 = 1.5$. The dashed lines represent the numerical values. The continuous lines represent the theoretical values. In a) b), numerical and theoretical values are almost identical.

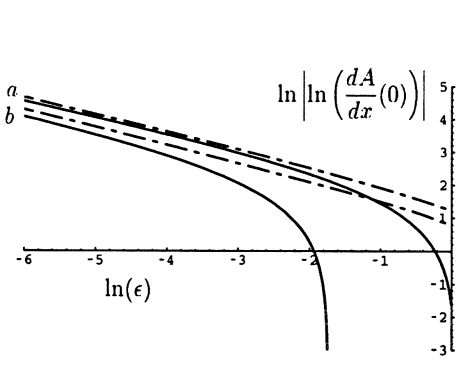

(a) $dA/dx(0)$ versus ϵ

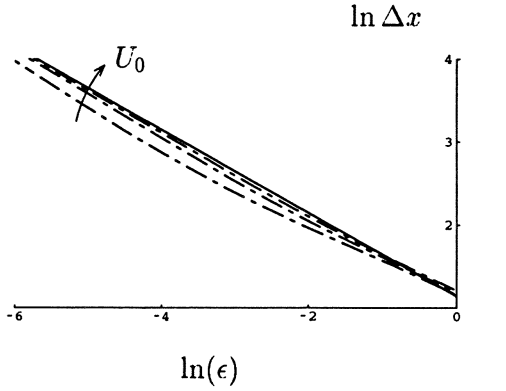

(b) Characteristic size Δx of the global modes

Figure 10: Scaling laws for the subcritical model with $U_0 > \sqrt{3}$. a) $U_0 = 3.0$, b) $U_0 = 2.0$. The dashed lines represent the numerical values. The continuous lines represent the theoretical values.

The solvability condition resulting from matching between inner and outer solutions takes the form

$$\sum_{0}^{\infty} w_k = 0 \quad \text{if} \quad U_0 > \sqrt{3}, \qquad \sum_{0}^{\infty} w_k \neq 0 \quad \text{otherwise} \tag{30}$$

where the numerically determined w_k depend on U_0 and $\mu_A(U_0)$ (see Appendix C). Fig. 11 indicates that $\sum_0^N w_k$ is different from zero for $U_0 < \sqrt{3}$ and zero for $U_0 > \sqrt{3}$. Note that e^{-15} nominally corresponds to zero in Fig. 11 as determined by numerical accuracy. The value of $\sum_0^N w_k$ approaches closer to zero for $U_0 > \sqrt{3}$ as the number of terms N in the series increases.

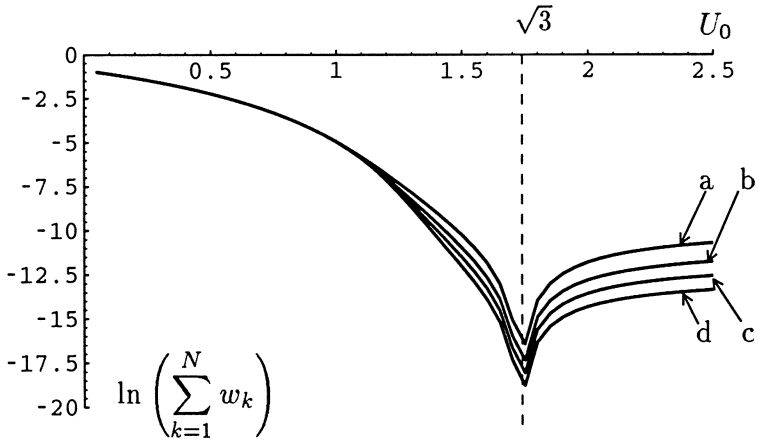

Figure 11: Zero-order term of the matching versus U_0. a) N=200 ; b) N=500 ; c) N=1000 ; d) N=2000.

This result is important since it validates the linear criterion for the existence of nonlinear global modes in the region $U_0 > \sqrt{3}$, $\mu > U_0^2/4$. It also demonstrates that in the range $U_0 < \sqrt{3}$, the curve $\mu^l = U_0^2/4$ does not signal the appearance of a nonlinear global mode since the matching cannot be done between an inner solution with $v_0 \neq 0$ and the series solution (C.2) at $\mu = \mu^l$. It is worth noting again that in the region $U_0 < \sqrt{3}$, $\mu < U_0^2/4$, a nonlinear global mode exists, despite the fact that the basic state is linearly convectively unstable or linearly stable.

3.3 Hysteresis loop in the control parameter space

The study of global modes has allowed us to predict the nonlinear solutions of the system as a function of the control parameters μ and U_0 but not which one

will be chosen. As pointed out by Chomaz [1], a hysteresis loop appears in the nonlinearly absolute range $\mu_A < \mu < 0$. The response of the system characterized by the amplitude at $x = +\infty$ (Fig. 12(a)) clearly shows the hysteresis loop between the unperturbed state and the NG mode. The hysteresis loop has been obtained numerically by computing the temporal solutions of partial differential equation (1) with potential density (2).

For $U_0 < \sqrt{3}$, let the system be in the initial uniform state A_0. The parameter μ is then increased in a quasistatic manner while maintaining U_0 constant in the range $U_0 < 1/\sqrt{3}$ (see Fig. 12). As long as $\mu < \mu_A$, a single solution exists (A_0

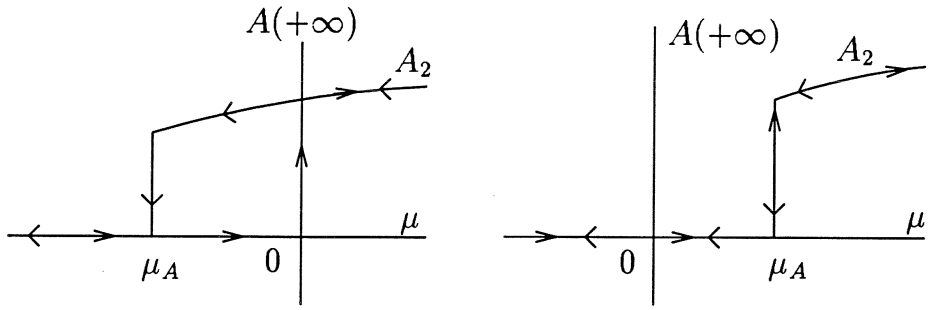

(a) $U_0 < 1/\sqrt{3}$ (b) $U_0 > 1/\sqrt{3}$

Figure 12: Numerically obtained values of A at $x \to +\infty$ and $t \to +\infty$ versus the bifurcation parameter.

everywhere). Above μ_A, a second global mode solution appears. In the absence of a large perturbation, the system is observed to remain in the uniform state A_0 until $\mu = 0$ because A_0 is linearly stable. Past $\mu = 0$, the uniform solution A_0 becomes linearly unstable, and the system tips over to the global mode which is now the unique stable solution. As μ is now decreased, the system remains on the global mode branch as long as $\mu > \mu_A$ and returns to the uniform state A_0 when the global mode solution disappears at $\mu = \mu_A$.

For $U_0 > 1/\sqrt{3}$, the hysteresis loop no longer exists. The transition between solutions takes place at $\mu = \mu_A$ now positive with no hysteresis but a jump in the value of $A(+\infty)$ from zero to its global mode value (see Fig. 12(b)).

3.4 Multiplicity of global modes

In the previous perturbative approach, we have not taken into account a possible multiplicity of global modes at given control parameter. In general, as mentioned in section 3.1 there exist several solutions satisfying equation (21) and associated boundary conditions (22).

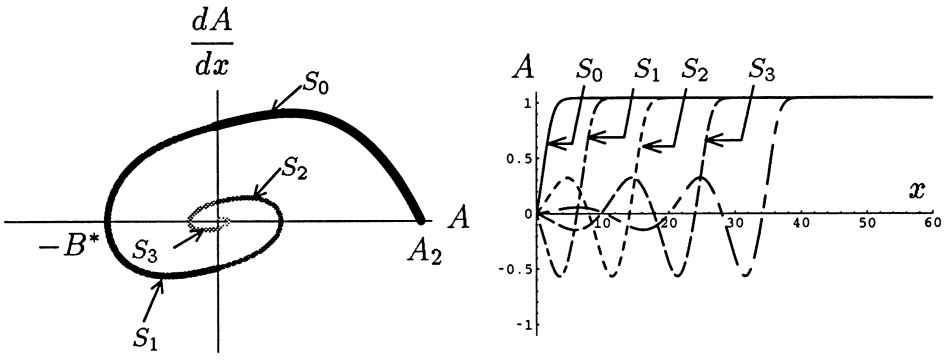

(a) Phase portrait

(b) NG solutions S_0, S_1, S_2 versus x

Figure 13: Multiplicity of global modes ($\mu > 0$ in this figure). Only S_0 verifies equation (21) with boundary conditions (22) without oscillating around A_0.

As seen from the phase portrait sketched in Fig. 13(a), the global mode multiplicity is related to the number of turns around the origin of the solution asymptotic to A_2. As already explained in section 3.1, when $\mu > \mu^l(U_0)$, the point A_0 is an unstable focus and there exists a discrete infinity of global modes linking the amplitude $A_0 = 0$ at $x = 0$ to A_2 at $x = +\infty$. In the domain of parameter space where the system is NG and LC unstable (light and medium gray regions in Fig. 7), a finite number of global modes exist as the stable manifold of A_2 makes a finite number of turns around A_0. This number increases when parameters are close to the curve $\mu = \mu^l(U_0)$.

The existence of a Lyapunov functional $\mathcal{L}(A)$ given by (10) trivially enables us to conclude that the steady solution with the smallest characteristic extent Δx, *i.e.* the solution with no oscillations around the origin, corresponds to the absolute

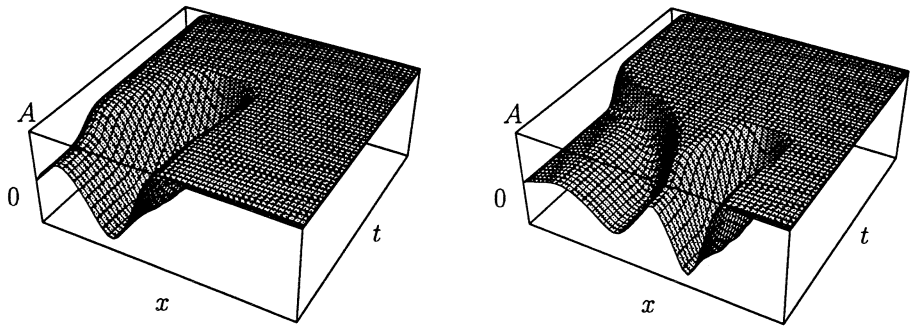

(a) (b)

Figure 14: (a) Simulation starting from the solution such that $A(0) = 0$, $A(+\infty) = A_2$ and crossing zero twice. $U_0 = 0.1$, $\mu = -0.01$. (b) Simulation starting from the solution crossing zero four times. $U_0 = 0.1$, $\mu = 0.001$.

minimum of $\mathcal{L}(A)$. However, the linear stability of the other solutions has to be determined.

We make the following conjecture, which has been numerically verified for a large set of temporal simulations: all the NG modes which oscillate around the origin before reaching A_2 are unstable. In other words, for fixed boundary conditions, the only stable steady solution is the one with the smallest characteristic extent Δx.

An example of temporal simulation is presented in Fig. 14(a). For $\mu = -0.01$ and $U_0 = 0.1$, the steady solution oscillating twice around the origin, (S_2 in Fig. 13) obtained by numerical integration of equation (21) in the phase space with associated boundary conditions (22), is used as the initial state at $t = 0$ for the temporal simulation. The solution is seen to evolve to the stable trajectory linking A_0 to A_2 with no oscillation. Similarly, a NG mode oscillating four times around A_0 freely evolves toward the NG mode with no oscillation in Fig. 14(b).

4 Signaling problems

In this section, we examine the response of the system to an external forcing at the origin. We therefore assume that the system is forced at a constant steady

amplitude $A(0) = B$ at the origin (because of the symmetry $A \to -A$, B is assumed to be positive). We look for steady solutions of (1) with potential density (2). As in the case of global modes, the existence of a Lyapunov functional implies that A reaches an extremum of $\mathcal{V}(A)$ at $+\infty$, *i.e.* $A(+\infty) = A_0$ or A_2. The procedure used to find these forced solutions is similar to the determination of NG modes. One may determine on the phase portraits (see Fig. 4) if the line $A = B$ intersects the stable manifold of either A_2 or A_0. In order to clarify the description of the possible solutions in parameter space, the reader may refer to Fig. 15 which summarizes the results obtained in the various regions of the (μ, U_0) space discussed below.

In the gray regions, solutions with $A(+\infty) = A_2$ for $A(0) = B$ exist but only for $B \neq 0$. In the light gray region, infinitely small B are sufficient whereas in the two darker gray zones, forcing has to exceed a threshold amplitude to obtain $A(+\infty) = A_2$. In the darkest gray region, the threshold is different if the forcing is increased or decreased.

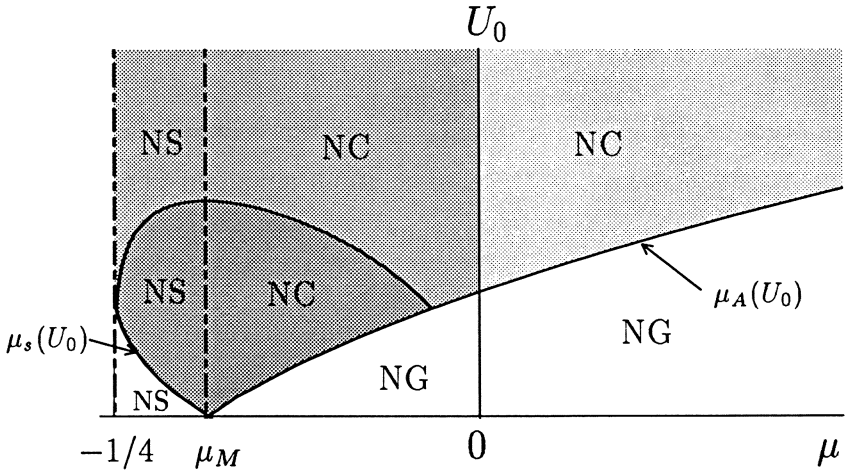

Figure 15: Regions of nonlinear global (NG) instability in the parameter space (white and $\mu > \mu_M$) and of NC instability (gray and $\mu > \mu_M$). The system acts as a nonlinear spatial amplifier in the gray regions. In the dark gray region, A_1 is an unstable spiral (Appendix A) and hysteretic behavior is obtained. In the medium gray region, forcing must exceed a critical threshold to be efficient. In the light gray region, even small forcing amplitudes are amplified. The nonlinearly stable (NS) region ($\mu < \mu_M$) contains a subdomain (gray) where the physical behavior of the system with respect to forcing is identical to the one in the NC region.

In the NG region ($\mu > \mu_A(U_0)$), when the NG mode is triggered once, the system

cannot relax back to A_0 even if the forcing is removed. This behavior reflects the intrinsic response of the system. In the NC region (gray regions with $\mu > \mu_M$), the system follows the variations of the forcing and returns back to A_0 when the forcing is removed (with hysteresis cycle in the dark gray region).

This nonlinear spatial amplifier behavior was expected in the NC region, but it surprisingly persists in the NS region when $\mu > \mu_s(U_0)$ (gray regions with $\mu < \mu_M$). The system relaxes toward A_0 for any forcing, only if $\mu < \mu_s(U_0)$. As a conclusion, the region of parameter space where the system acts as a nonlinear spatial amplifier contains not only the NC region but also part of the NS region. NC instability is only a sufficient condition to obtain a saturated response at infinity in the signaling problem.

4.1 Response to a forcing in the nonlinearly convective instability region

4.1.1 Evaluation of the hysteresis loop with the forcing parameter

When $\mu > 0$, A_0 is an unstable node (see Appendix A). Therefore, whatever μ and $B \neq 0$, the forced solution $A(0) = B$ will end up in A_2 and no hysteresis is possible (Fig. 16(c)). When $\mu < 0$, the stable manifold of A_2 possesses a point of minimum amplitude A_2^* (Figs. 16(a), 16(b)). A solution asymptotic to A_2 therefore exists if $B > A_2^*$ (see Figs. 16(α), (β)). The stable manifold of A_0 possesses a maximum amplitude A_0^*. Therefore, at least one solution asymptotic to A_0 exists for a forcing amplitude $B < A_0^*$.

When A_1 is an unstable spiral point (Fig. 16(β)) (see Appendix A), we have $A_2^* < A_1 < A_0^*$. Two solutions coexist for a forcing amplitude $A_2^* < B < A_0^*$: one relaxing toward A_0, the other toward A_2. When A_1 is an unstable node, we may have $A_2^* < A_1 < A_0^*$, but for high advection velocities, we have $A_2^* = A_1 = A_0^*$ and no multiple solution region exists (Fig. 16(α)).

In order to check numerically for hysteretic behavior with respect to forcing amplitude, we follow a procedure similar to that of section 3.3: The system is initially set to the uniform state A_0 and integrated in time while μ is kept fixed and the forcing is gradually increased from $B = 0$ in a quasistatic manner.

The system presents the response measured at $x = +\infty$ depicted in Figs. 16(a), 16(b): For $\mu < 0$ in the dark gray region in Fig. 15, when the forcing parameter

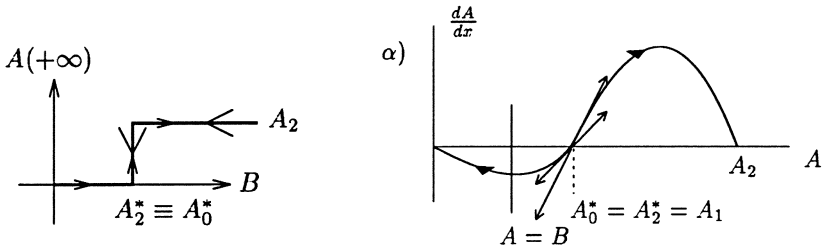

(a) $\mu_M < \mu < 0$ and A_1 is an unstable node (medium gray region on Fig. 15).

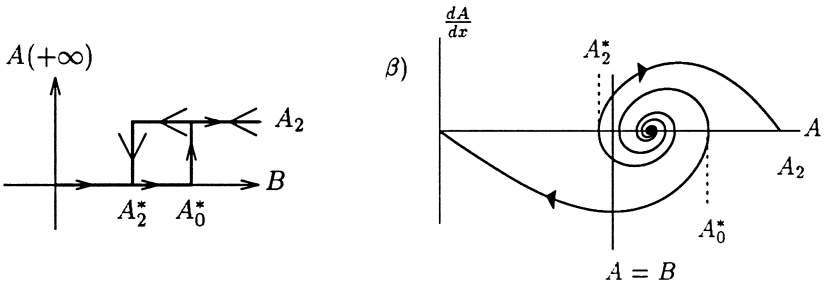

(b) $\mu_M < \mu < 0$ and A_1 is an unstable spiral (dark gray region of Fig. 15).

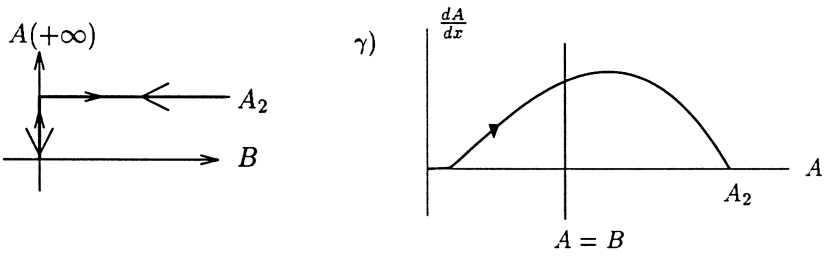

(c) $\mu > 0$ (light gray region of Fig. 15).

Figure 16: Response of the system versus the forcing parameter in the NC domain and the phase space corresponding to each case.

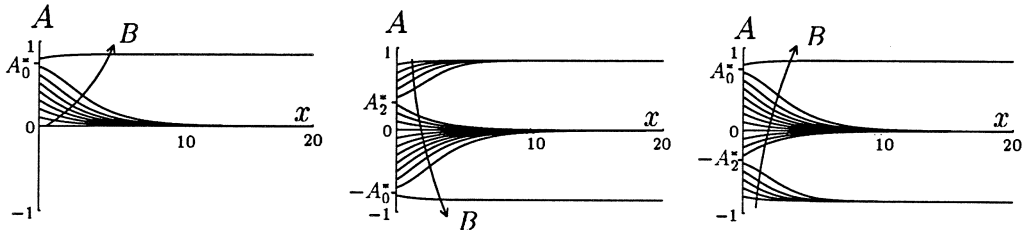

(a) Lower branch of the hysteresis

(b) Upper branch of the hysteresis

(c) Lower branch

Figure 17: Asymptotic response ($t \to \infty$) of the system versus the forcing parameter. Convective region $\mu < 0$

B remains below the threshold A_0^*, the system is locked to the solution asymptotic to A_0. When B exceeds A_0^*, the system tips over to the solution asymptotic to A_2 and remains locked to it as long as the forcing amplitude is kept above the lower threshold A_2^*.

The results of our numerical simulations are represented in Fig. 17 in order to illustrate this hysteretic behavior under forcing prevailing in the NC region when $\mu < 0$; initially, the solution is A_0 everywhere and B is increased quasistatically. In Fig. 17(a), the system travels along the lower branch of the hysteresis loop displayed in Fig. 16(b); in Fig. 17(b), it follows the upper branch. We indeed verify that the system tips over at the low and high threshold values A_0^* and A_2^* and therefore presents a clear hysteretic behavior to forcing.

4.1.2 Scaling law

A scaling law can be obtained for the minimum forcing amplitude A_2^* required to generate the bifurcated state A_2 at $x = +\infty$. The procedure is similar to the one followed for the determination of the scaling law for $dA/dx(x = 0)$ outlined in section 3.2. If $\epsilon = \mu^{nl} - \mu$ denotes the distance to the NG instability threshold, the corresponding scaling law reads (Appendix B.1)

$$A_2^* \simeq \mathrm{C}^* \epsilon^{\beta}, \tag{31}$$

where

$$\mathrm{C}^* = A_2(\mu_A)^{1-3\beta} (\beta - 1)^{\beta - 1} \left(\frac{\sqrt{3}}{2} \mathcal{B}\left(\frac{1}{2\beta}; 2 - \frac{1}{2\beta} \right) \right)^{\beta}, \tag{32}$$

β is the previously introduced constant (Eq. (25)) and $\mathcal{B}$ denotes the beta function [33].

The response of the system **in the NC region for $\mu > 0$** as a function of forcing amplitude is represented in Fig. 16(c). Either $B > 0$ and the system is locked to the mode asymptotic to A_2, or $B = 0$ and the system is locked to the trivial solution $A = 0$ for all x. The system does return to the uniform state A_0, as the forcing is suppressed.

4.2 Response to a forcing in the NG region

A **forced solution asymptotic to A_2** exists for all B (even $B = 0$) in the **NG region** since the line $A = B$ always intersects the stable manifold of A_2 (Figs. 18(α), 18(β)). This solution is obtained continuously from the global mode defined in the section 3 ($B = 0$) by shifting the origin to x_0 such that the amplitude of the NG mode at x_0 equals B. This weak effect of a forcing is in accordance with the fact that the NG mode may be interpreted as the intrinsic response of the system.

4.2.1 In the NG region for $\mu < 0$

In this region, forcing has an irreversible effect. If the system is initially set to the uniform state A_0 and the forcing is gradually increased from $B = 0$ in a quasistatic manner, the following sequence is obtained: the system keeps converging to A_0 at $x = +\infty$ until $B = A_0^*$ where it flips irreversibly to the NG branch (Fig. 19(a)). This first branch is similar to the first magnetization branch of ferromagnets. Then, even if B returns to zero, the system remains locked to A_2. It is not possible to unlock it by removing the forcing (Figs. 18(a) and 19(b)). The system remains locked to the global mode asymptotic to A_2 for all B.

If one allows B to change sign, the system tips over to the global mode such that $A(+\infty) = -A_2$ for $B = A_2^*$ (negative in the NG region), and remains locked to this mode as long as $B < |A_2^*|$. An hysteresis loop is therefore possible (dashed lines in Figs. 18(a) and 19(b), 19(c)) but the system never relaxes to the solution asymptotic to A_0.

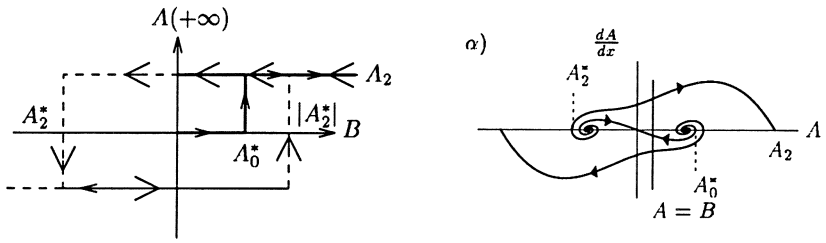

(a) NG domain $\mu_A < \mu < 0$.

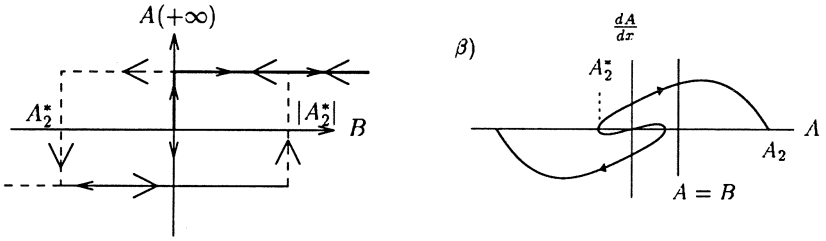

(b) NG domain $0 < \mu_A < \mu$.

Figure 18: Response of the system as a function of the forcing parameter and the corresponding solutions in the phase space (α),(β).

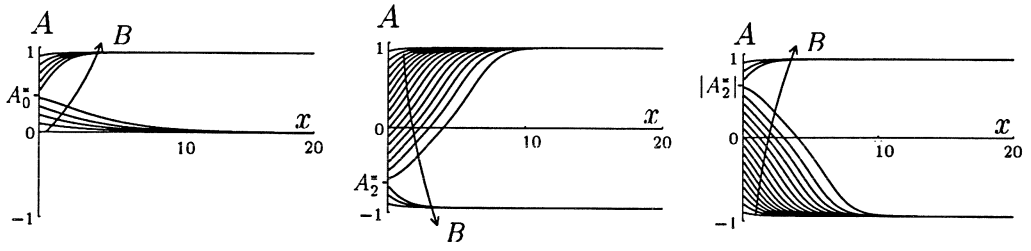

(a) The system becomes locked

(b) Upper branch of the hysteresis

(c) Lower branch

Figure 19: Asymptotic response $(t \to \infty)$ of the system versus the forcing parameter. NG region $\mu < 0$

4.2.2 In the NG region for $\mu > 0$

In the NG region for $\mu > 0$ (gray region in Fig. 15), the solution asymptotic to A_0 no longer exists (Fig. 18(β)). Therefore, the behavior of the system is similar to the case $\mu < 0$ in the NG region but the branch which locks the system on the solution asymptotic to A_2 coincides with the axis $B = 0$ (Fig. 18(b)).

By contrast with the NC region, in the whole NG region, a nontrivial intrinsic response obtained by forcing the system remains even when the forcing is suppressed. The system never relaxes back to A_0 when the forcing is removed. This behavior is in accordance with the interpretation of global modes as the intrinsic response of the system.

4.3 Response to a forcing in the NS region

In the NS region $\mu < \mu_M$, the stable manifold of A_2 possesses the same features as in the NC region for $\mu_M < \mu < 0$: either its minimum amplitude A_2^* is merged into A_1 (as in Fig. 16(α)) or $A_2^* < A_1$ (this happens if A_1 is a spiral; see Fig. 16(β)).

The stable manifold of A_0 may also possess the same features as in the NC region, *i.e.* its maximum amplitude A_0^* is either merged into A_1 (Fig. 16(α)) or $A_0^* > A_1$ (Fig. 16(β)). But there exists a new region embedded within the NS region (white region of Fig. 15 for $\mu < \mu_M$) where the stable manifold of A_0 possesses no maximum amplitude. This region is limited by a line

$$\mu = \mu_s(U_0) \equiv \begin{cases} \frac{\mu_M}{3}\left(4 - (1 - \sqrt{3}U_0)^2\right) & \text{if} \quad U_0 < \frac{1}{\sqrt{3}} \\ -\frac{1}{4} & \text{otherwise} \end{cases} \tag{33}$$

on which an heteroclinic orbit links A_2 to A_0 in the phase space (with $dA/dx < 0$). Note that such an orbit always exists for $\mu = -1/4$ if $U_0 > 1/\sqrt{3}$, since A_2 and A_1 merge one into another (saddle node bifurcation).

In consequence, the response of the system in the NS region is the same as in the NC region if $\mu > \mu_s(U_0)$ and corresponds to Fig. 16(a) if A_1 is a node or to Fig. 16(b)) if A_1 is a spiral. But if $\mu < \mu_s(U_0)$, the system cannot be forced regardless of the forcing amplitude and always relaxes back to A_0.

5 Genericity

In order to test the genericity of the previous scenarios, we successively examine a supercritical bifurcating mode, a van der Pol–Duffing-like model, and a transcritical

model. They all leave $A_0 = 0$ as a solution of the system. In the three cases, the formulation is chosen so that the linear absolute transition remains at the value $\mu^l(U_0) = U_0^2/4$. In particular, we wish to demonstrate that linear absolute instability is only a sufficient condition for nonlinear global instability and that, even in the case of a supercritical bifurcation, the system may be nonlinearly globally unstable while being locally convectively unstable.

5.1 Supercritical bifurcation

In the case of a supercritical bifurcation, the potential density is taken to be

$$\mathcal{V}(A) = -\mu A^2/2 + A^4/4 \tag{34}$$

and the classical bifurcation diagram involves the basic state $A_0 = 0$ and the bifurcated state $A_2(\mu) = \sqrt{\mu}$. Upon substituting the expression for the potential density in the equation (1), we obtain

$$\frac{\partial A}{\partial t} + U_0 \frac{\partial A}{\partial x} = \frac{\partial^2 A}{\partial x^2} + \mu A - A^3. \tag{35}$$

Note that the parameter U_0 is superfluous because the change of scale ($x \to x/U_0$, $t \to t/U_0^2$, $A \to U_0 A$, $\mu \to U_0^2 \mu$) rescales it to unity. Nevertheless, we keep it in the equation in order to draw a parallel with our previous study. In the supercritical case, there exists no domain of parameter space where the system becomes NG unstable while LC unstable (see Fig. 20). The phase portraits of steady solutions of (35) are strictly analogous to those pertaining to the density potential (2) when $U_0 > \sqrt{3}$.

In the range $\mu < \mu^l(U_0)$, the phase portraits are of type 21(a) while for $\mu > \mu^l(U_0)$ they are of type 21(b). The curve $\mu = \mu^l(U_0)$ signals a change in local behavior of the trajectories around A_0 (between an unstable node for $\mu < \mu^l$ and an unstable focus for $\mu > \mu^l$). It also coincides with the transition to NG instability.

Using matched asymptotic expansions, it is possible to show that the stable manifold of A_2 crosses the $A = 0$ axis with $dA/dx \neq 0$ only when $\mu > \mu^l$ (Appendix D). It is also possible to determine the scaling law for $dA/dx(x = 0)$ as a function of the distance to the NA instability threshold, as has been done in the case of a subcritical bifurcation with $U_0 > \sqrt{3}$. Details of the calculation are given in Appendix D. The final result is

$$\frac{dA}{dx}(0) \simeq v(0)\epsilon \exp\left(-\frac{U_0 \pi}{2\sqrt{\epsilon}}\right), \tag{36}$$

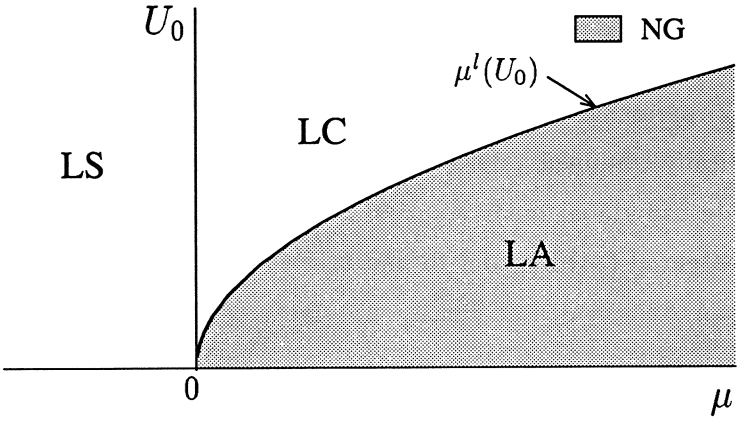

Figure 20: Parameter space for the supercritical model. NG modes exists in the gray region which corresponds to the region of linear absolute instability for this model.

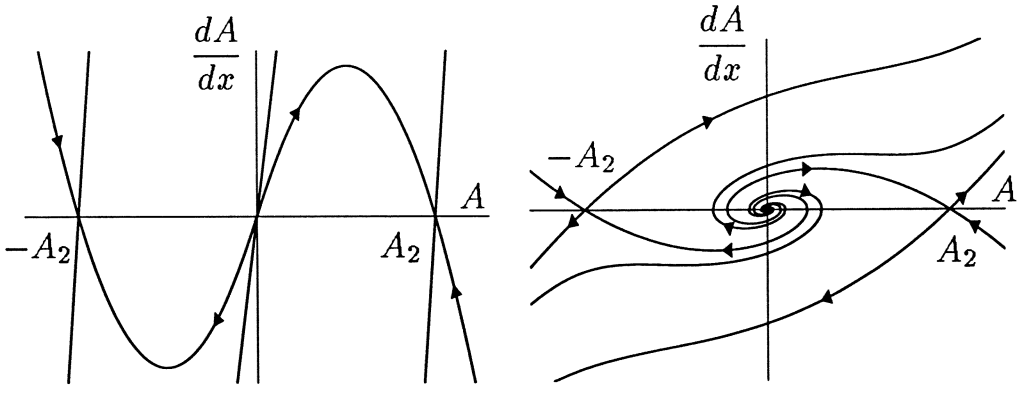

(a) LC unstable region

(b) LA unstable region

Figure 21: Phase portraits of the supercritical model.

with the slope of the inner solution $v(0) \equiv d\xi/dx$ given by equation (D.5) of Appendix D (ξ is the inner variable). The characteristic growth size of the solution is given by

$$\Delta x \simeq \frac{\pi}{\sqrt{\epsilon}}. \tag{37}$$

Fig. 22 represents the comparison of the theoretical scaling laws (36, 37) with the numerically obtained values of $\ln(dA/dx(x=0))$ and Δx. For μ close to μ_A, we compute the global mode solution by backward integration of the system (14a-b) with potential (34) in order to find the stable manifold of A_2. The predictions that $\ln|\ln(dA/dx(x=0))|$ and $\ln \Delta x$ are linear versus $\ln \epsilon$ for the small values of ϵ are well verified.

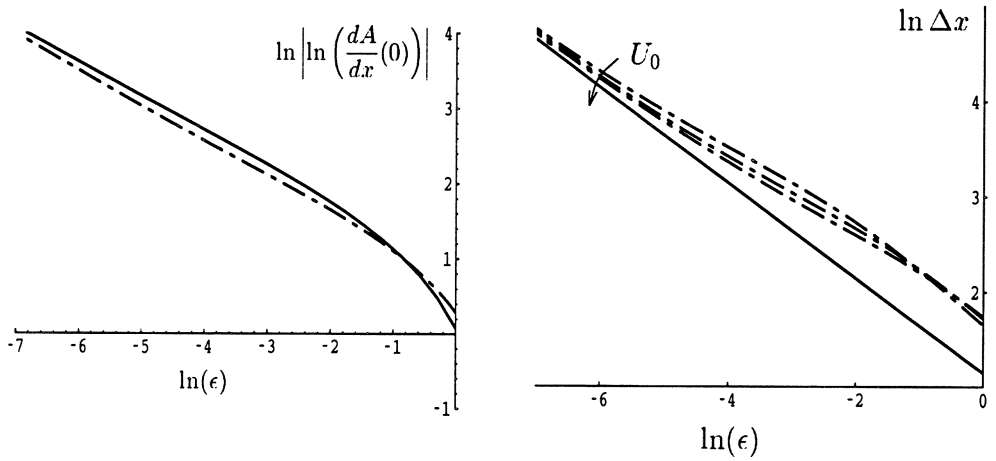

(a) $dA/dx(0)$ versus ϵ ; $U_0 = 1.0$.

(b) Characteristic growth size Δx of the global modes ; $U_0 = 1.0$, $U_0 = 1.5$,$U_0 = 2.0$

Figure 22: Scaling laws for the supercritical model. The dashed lines represent the numerical values. The continuous lines represent the theoretical values.

In phase space $(A, dA/dx)$, a particular trajectory $u(A) = -\frac{1}{\sqrt{2}}A(A-A_2)$ joining A_0 at $x = -\infty$ to A_2 at $x = +\infty$ exists for the specific value $\mu = 2U_0^2/9$. As in the case of the subcritical bifurcation for $U_0 > \sqrt{3}$, this solution does not correspond to a change of nature of the instability. The slope at the origin $\sqrt{\mu/2} = U_0/3$ of this particular solution is actually the smallest eigenvalue at $A = A_0$, whereas the largest eigenvalue is $2U_0/3$. As shown in Fig. 8(e), a perturbation of this particular solution remains tangent to the eigenvector with the smallest eigenvalue without

taking negative values.

5.2 "Van der Pol–Duffing" model

In this section, we add a nonlinear term $A^2\partial A/\partial x$ to equation (35). The amplitude equation is thus given by the two-parameter family known as the van der Pol–Duffing model

$$\frac{\partial A}{\partial t} + (U_0 - A^2)\frac{\partial A}{\partial x} = \frac{\partial^2 A}{\partial x^2} + \mu A - A^3. \tag{38}$$

The search procedure for particular steady solutions of equation (38) is carried out in the same way as before: we seek a polynomial solution $u(A)$ asymptotic to $A_2 = \sqrt{\mu}$ at $x = +\infty$ and to A_0 at $x = -\infty$ satisfying

$$uu' - (U_0 - A^2)u + \mu A - A^3 = 0. \tag{39}$$

This imposes $\mu = \mu^{nl}(U_0) \equiv 3(U_0 - 3)$, the solution being

$$u(A) = -\frac{1}{3}A(A^2 - A_2^2). \tag{40}$$

The straight line $\mu = \mu^{nl}(U_0)$ is tangent to the linear transition curve $\mu^l(U_0) = U_0^2/4$ for the parameters $\mu = 9, U_0 = 6$ (see Fig. 23). The heteroclinic orbit linking A_2

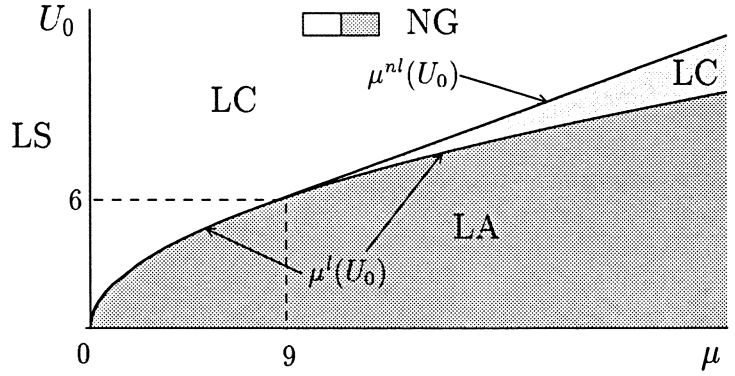

Figure 23: Parameter space for the van der Pol–Duffing model. NG modes exist not only in the region of LA instability but also in the region of LC instability.

from A_0 comes out therefore from the eigendirection[7] corresponding to the smallest eigenvalue when $\mu < 9$, whereas its outgoing direction corresponds to the highest eigenvalue if $\mu > 9$. Therefore, a NG mode exists when $\mu > \mu^{nl}(U_0)$ for $\mu > 9$,

[7]The slope at the origin of solution (40) is $A_2^2/3 = \mu^{nl}/3$ and the linear eigenvalues pertaining to equation (39) at $A = A_0$ are $\mu/3$ and 3 for $\mu = \mu^{nl}(U_0)$.

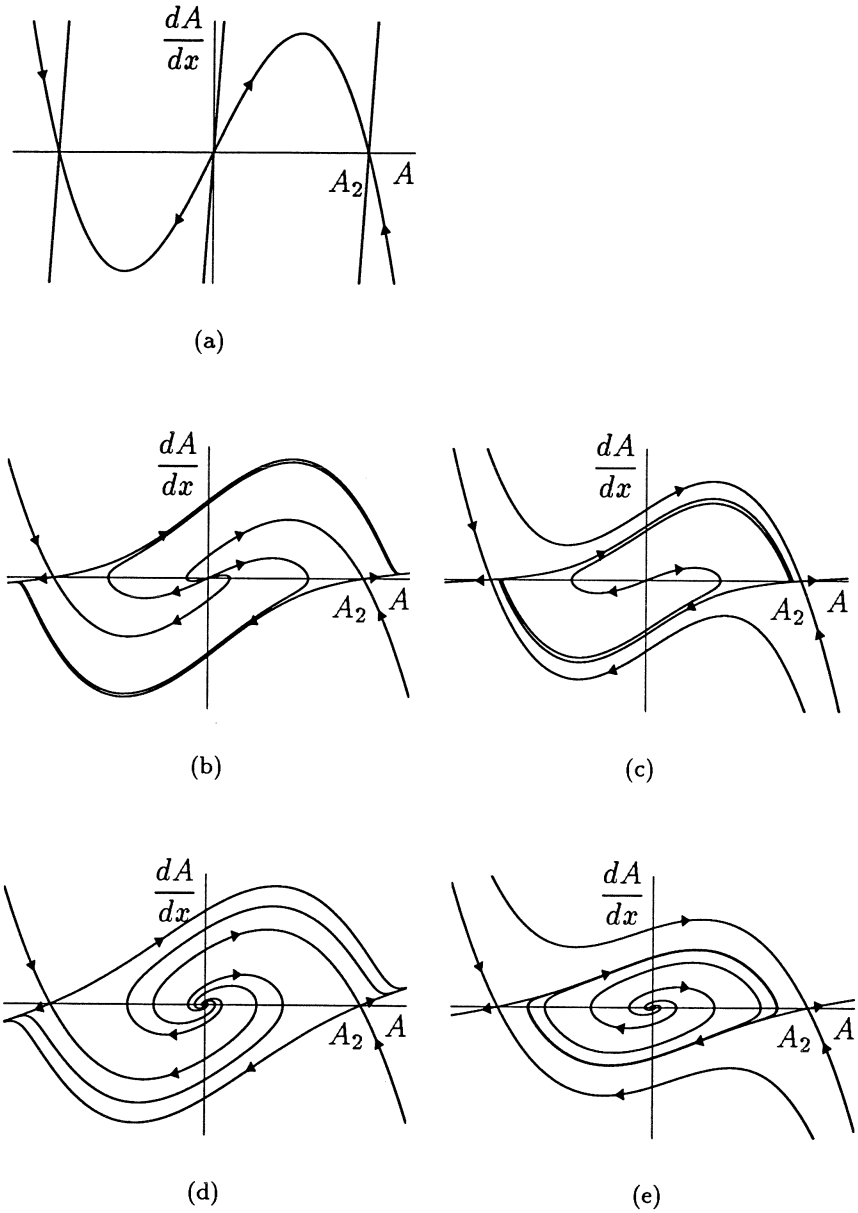

Figure 24: Phase portraits of the van der Pol–Duffing model. (a): white LC region in Fig. 23; (b) and (c): light gray LC region; (d) and (e): dark gray LA region. Phase portraits (c) and (e) are obtained for smaller advection velocities than (b) and (d), and display a limit cycle oscillation which do not alter the existence of NG modes.

whereas a NG mode exists only when $\mu > \mu^l(U_0)$ for $\mu < 9$. The numerically obtained phase portraits are shown on the Fig.s 24(a) to 24(e).

For $\mu > 9$, the system becomes thus NG unstable in a region where it is LC unstable. The existence of NG modes could also de demonstrated by a matched asymptotic expansion for $\mu > \mu^l(U_0)$ when $\mu < 9$ and $\mu > \mu^{nl}(U_0)$ when $\mu > 9$.

5.3 Transcritical bifurcation

In the present section we examine the case of a supercritical bifurcation perturbed by a cubic term breaking the symmetry $A \to -A$ in the potential. We keep the restabilizing order-4 term so that our model can be viewed as a perturbed supercritical case. This last model is similar to the model used by Ben-Jacob *et al.* [21] and Hakim [35] to illustrate the selection between linear and nonlinear front velocity. We choose the potential

$$\mathcal{V}(A) = -\mu\frac{A^2}{2} - \frac{A^3}{3} + \frac{A^4}{4} \tag{41}$$

which, upon substitution into equation (1) yields

$$\frac{\partial A}{\partial t} + U_0\frac{\partial A}{\partial x} = \frac{\partial^2 A}{\partial x^2} + \mu A + A^2 - A^3 \tag{42}$$

where μ and U_0 are the two control parameters as in the previous examples. The homogeneous steady solutions are $A_0 = 0$ for all μ and $A_1 = 1/2 - (\mu + 1/4)^{1/2}$ and $A_2 = 1/2 + (\mu + 1/4)^{1/2}$ for $\mu > -1/4$.

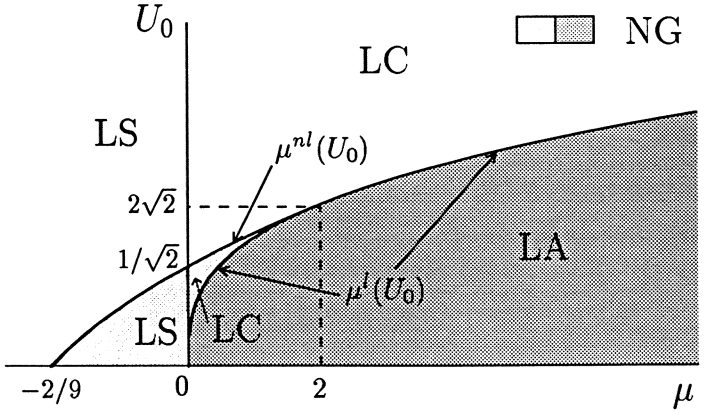

Figure 25: Parameter space for the transcritical model.

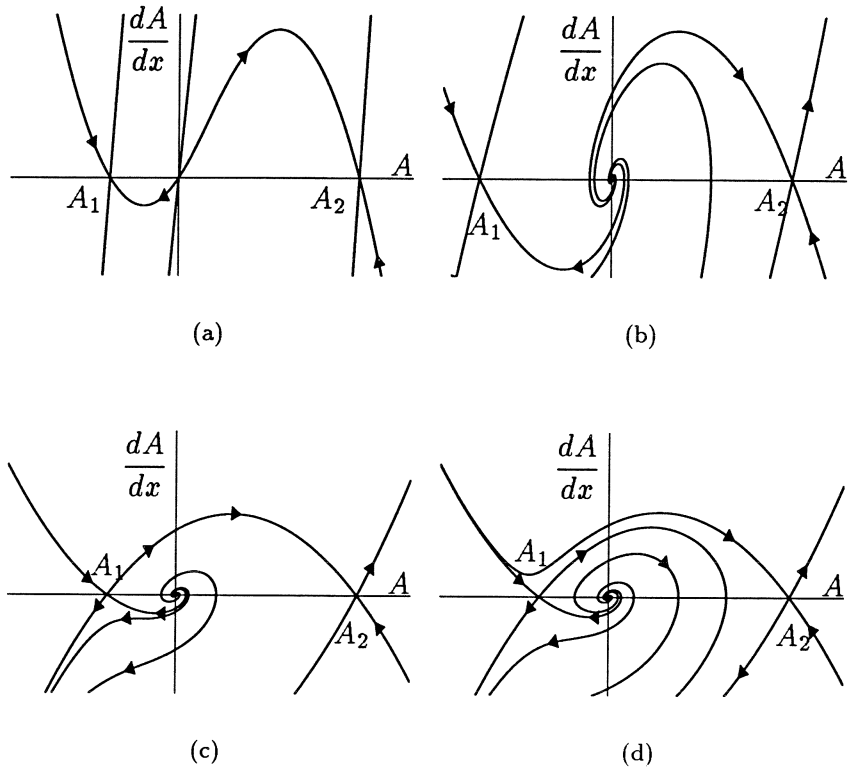

Figure 26: Phase portraits of the transcritical model. (a) corresponds to the white LC region in figure 25 whereas (b) to (d) correspond to the dark gray LA region. Phase portraits similar to (b), (c) and (d) with a node behavior around the origin are obtained in the light gray LC region.

A steady particular solution of the equation (42) linking the point A_0 to A_2 is sought as a polynomial function $u(A)$ which solves the equation

$$uu' - U_0 u + \mu A + A^2 - A^3 = 0. \tag{43}$$

This imposes $\mu = \mu^{nl}(U_0) \equiv -1/4 + \left(1/6 + \sqrt{2}U_0/3\right)^2$ (see Fig. 25). The corresponding solution reads

$$u(A) = -\frac{1}{\sqrt{2}}A^2 + \frac{U_0 + \sqrt{2}}{3}A \tag{44}$$

and represents the heteroclinic orbit[8,9] linking $A = A_0$ at $x = -\infty$ to $A = A_2$ at $x = +\infty$.

The polynomial solution (44) originates from the eigendirection corresponding to the largest eigenvalue for $\mu < 2$ and to the smallest eigenvalue for $\mu > 2$. As in the previous case a global mode exists in the parameter space where $0 < \mu < 2$ and $U_0^l(\mu) < U_0 < U_0^{nl}(\mu)$. We verify with phase portrait 26(b) that the system is NG unstable in this domain. For $\mu > 2$, the NG and LA instability thresholds coincide.

6 Conclusion

First we have identified, using published results, the NC/NA nature of the instability as a function of the advection velocity and the control parameter of the subcritical Ginzburg–Landau model. This determination only relies on the front velocity of a bifurcating state invading a basic state, the selection of which has been the object of recent studies. The NA/NC definition based on the existence and selection of a front in an infinite domain is somehow formal as the laboratory is artificially singled out. For this reason, we next considered nonlinear global instability in a semi-infinite homogeneous domain with zero-amplitude upstream boundary condition. This nonlinear global instability corresponds to the existence of a nontrivial nonlinear steady solution for which the direction of the advection has now to be considered as an eigendirection. The nonlinear global instability has been determined for the subcritical Ginzburg–Landau model and for three other variations on this theme: the supercritical Ginzburg–Landau model, the "van der Pol–Duffing" model, and the transcritical model.

For these cases that are homogeneous everywhere except at the origin, the domain of existence of a NG mode is rigorously determined from matched asymptotic

[8]This solution admits a slope at the origin $(U_0 + \sqrt{2})/3 = \left(1/2 + (\mu + 1/4)^{1/2}\right)/\sqrt{2}$ which has to be compared with the eigenvalues of equation (43) linearized at $A = A_0$:

$$-1/\sqrt{2} - \sqrt{2}\,(\mu + 1/4)^{1/2} \quad \text{and} \quad \left(1/2 + (\mu + 1/4)^{1/2}\right)/\sqrt{2}.$$

[9]Another polynomial solution exists for $U_0 = 1/\sqrt{2}$ and for all $\mu > 0$

$$u(A) = -\frac{1}{\sqrt{2}}(A^2 - A - \mu) \tag{45}$$

actually represents an heteroclinic orbit linking $A = A_2$ from $A = A_1$. This orbit brings no information as it is just a nonlinear global mode linking A_2 from $A = 0$ but $dA/dx \neq 0$ in a semi-infinite domain.

expansions, and is shown to coincide with the NA region determined from front velocity selection consideration. As predicted from the conjecture that a nonlinear front at least propagates at the linear front velocity, the NG instability (or equivalently here the NA) domain totally overlaps the LA region. Thus, LA instability is only a sufficient condition for NG instability and cases where the system is simultaneously LS or LC and NG unstable have been exhibited.

Studying the signaling problem, *i.e.* the effect of adding a steady forcing at the origin, allows us to show how the NC and NA instability manifests itself by a particular behavior. We have shown that once triggered, the NG mode sustains itself forever and therefore represents the intrinsic behavior of the system in the NG region. On the contrary, a study of the signaling problem in the NC region demonstrates that the flow behaves as a nonlinear spatial amplifier of the incoming perturbation, exhibiting hysteretic behavior in some cases, but returning to zero when the forcing is removed. Surprisingly, the same behavior is observed in the NS region too. In this subcritical system, the advection associated with a strong forcing at the origin is able to lock on to a bifurcated solution. Therefore NC instability is only a sufficient condition for the flow to behave as a nonlinear spatial amplifier.

The absolute or convective nature of a flow may be experimentally determined by investigating the response of the system to a forcing at the origin. It seems to us that an experimental quantitative confirmation of the theory could be made for example by adding a mean flow to a chemical reaction which exhibits nonlinear front selection (for example the one of Hanna *et al.* [28]). Plane Poiseuille flow, Couette flow between rotating cylinders, or swirling jet experiments are systems where these experimental validation could also be achieved. In an experimental setup, a comparison of the growth size of the NG modes with the two generic scalings ($\ln(1/\epsilon)$ and $\epsilon^{-1/2}$) should allow a determination of whether the NG instability occurs while the system is LC unstable or stable, or whether it occurs simultaneously at the LC/LA transition.

The very remarkable feature given by the proof of existence of a NG mode by matched asymptotic expansions is that the scaling laws as functions of the departure from the NG instability threshold are radically different when the NG threshold is linearly or nonlinearly determined. When the NG threshold coincides with the LA threshold, the growth size Δx (a kind of downstream correlation scale) has been

shown to vary as $\epsilon^{-1/2}$, ϵ being the departure from criticality. This power law contrasts sharply with the much stronger $\ln(1/\epsilon)$ variation of Δx obtained when the NG mode is nonlinearly determined and thus arises while the system is LC unstable or LS. Extension of the present study to the complex Ginzburg–Landau equation [36] shows that the same scaling holds and the theoretically derived law (with no free parameter) is shown to coincide exactly with the law observed by Büchel et al. [37] for the Taylor–Couette problem with throughflow and by Müller et al. [38] for the Rayleigh–Bénard problem with an added Poiseuille flow.

The authors are grateful to P. Manneville, P. Huerre and P. Weidman for their helpful comments on the manuscript.

A Local behavior of solutions of equation (21) near the fixed points A_0, A_1, A_2

The study is restricted to the case $\mu > -1/4$.

At $A = A_0$, the linearized equation (21) gives

$$\frac{d^2A}{dx^2} - U_0\frac{dA}{dx} + \mu A = 0 \tag{A.1}$$

The eigenvalues $k^{\pm}$ are thus given by the expression

$$k^{\pm} = \frac{U_0}{2} \pm \frac{1}{2}\left(U_0^2 - 4\mu\right)^{\frac{1}{2}}. \tag{A.2}$$

They are

- complex conjugate with positive real part for $\mu > \mu^l = U_0^2/4$ (A_0 is an unstable focus).
- real positive for $0 < \mu < \mu^l$ (A_0 is an unstable node).
- real and of opposite signs for $-1/4 < \mu < 0$ (A_0 is a saddle).

For $\mu = \mu^l$, A_0 is an improper node.

At $A = A_1$, we find the two eigenvalues $k_1^{\pm}$ in the same way

$$k_1^{\pm} = \frac{U_0}{2} \pm \frac{1}{2}\left(U_0^2 - 8\sqrt{\mu + \frac{1}{4}} + 16\mu + 4\right)^{\frac{1}{2}}. \tag{A.3}$$

They take the same value for $\mu = \mu_M\left(1 \pm \frac{2}{3}\left(1 - U_0^2\right)^{1/2} - \frac{1}{3}(1 - U_0^2)\right)$. This equation bounds a domain of the parameter space (μ, U_0) in which A_1 is an unstable

spiral point, whereas it is an unstable node out of this domain. On the boundary of this domain, A_1 is an improper node.

At $A = A_2$, The two eigenvalues $k_2^{\pm}$ are given by the expression

$$k_2^{\pm} = \frac{U_0}{2} \pm \frac{1}{2}\left(U_0^2 + 8\sqrt{\mu + \frac{1}{4}} + 16\mu + 4\right)^{\frac{1}{2}}. \tag{A.4}$$

They are always real and of opposite signs (A_2 is always a saddle).

These results are reported on the figure 27.

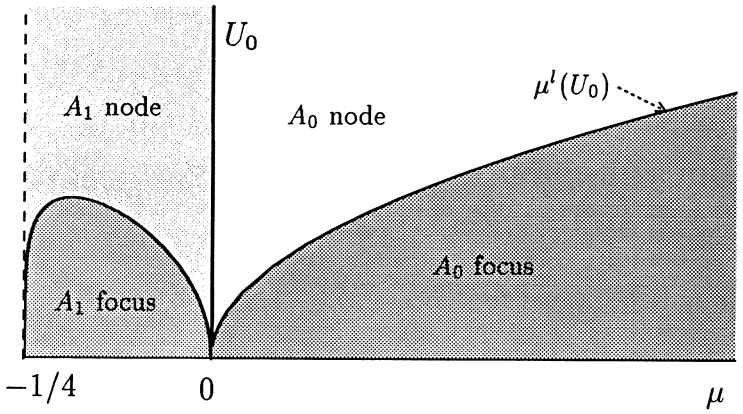

Figure 27: Nature of the fixed points A_0, A_1, A_2 versus the parameters μ and U_0. A_0 is an unstable focus in the dark gray domain, an unstable node in the white domain and a saddle for $\mu < 0$ (light and medium gray domain). A_1 is an unstable focus in the medium gray domain and an unstable node in the light gray domain. A_2 is a saddle everywhere.

B Singular perturbation analysis of the subcritical Ginzburg–Landau equation in the vicinity of the curve $\mu = \mu^{nl}(U_0)$ for $U_0 < \sqrt{3}$

B.1 Scaling law $dA/dx(x = 0) = f(\epsilon)$ with $\epsilon = \mu - \mu^{nl}$

The absolute instability threshold is given by

$$\mu_A = \mu^{nl} = \mu_M\left(1 - \frac{2}{\sqrt{3}}U_0 - U_0^2\right). \tag{B.1}$$

Throughout Appendix B we precise the dependence $A_2(\mu)$ only if necessary. Otherwise we use the notations $A_2 \equiv A_2(\mu^{nl})$ and $A_{2,\mu} \equiv dA_2/d\mu(\mu^{nl})$.

We seek a solution $u(A)$ of the equation (23) verifying boundary conditions (24). This function $u(A)$ is known for the value $\mu = \mu^{nl}$ (see equation (18)).

The order one equation (23) is compatible with a single boundary condition. We also assume the existence of an ϵ^β sized boundary layer in the neighborhood of A_0 in which an inner solution of the linearized equation (23) at $A = 0$ satisfies the boundary condition $u'(A_0) = U_0$ and out of which an outer solution of the equation (23) satisfies the boundary condition $u\left(A_2(\mu)\right) = 0$.

Outer solution:

Assuming that the solution $u(A)$ takes the following form

$$u(A) \simeq u_0(A) + \epsilon u_1(A), \tag{B.2}$$

and expanding the second boundary condition $u\left(A_2(\mu^{nl} + \epsilon)\right) = 0$ and the equation (23) in powers of ϵ, by comparison at each order we obtain:

- order 0:

$$u_0 u_0' - U_0 u_0 + \mu^{nl} A + A^3 - A^5 = 0 \tag{B.3a}$$

$$u_0(A_2) = 0 \tag{B.3b}$$

- order 1:

$$u_0 u_1' + u_0' u_1 - U_0 u_1 + A = 0 \tag{B.4a}$$

$$A_{2,\mu}\, u_0'(A_2) + u_1(A_2) = 0 \tag{B.4b}$$

The solution $u_0(A)$ is given by (see equation (18)):

$$u_0(A) = \frac{1}{\sqrt{3}} A(A_2^2 - A^2) \tag{B.5}$$

Upon substituting this solution in the system (B.4a, B.4b), and solving a first-order differential equation, we find:

$$u_1(A) = A^{\lambda_1}(A_2^2 - A^2)^{\lambda_2}\sqrt{3}\int_{A_2}^{A} a^{-\lambda_1}(A_2^2 - a^2)^{-\lambda_2 - 1} da\,, \tag{B.6}$$

where

$$\lambda_1 = \frac{-1 + \sqrt{3}U_0}{1 + U_0/\sqrt{3}} \quad \text{and} \quad \lambda_2 = \frac{-1 - \sqrt{3}U_0}{1 + U_0/\sqrt{3}} \tag{B.7}$$

Inner solution

The inner variable ξ is connected to the outer variable A through the relation

$$\xi = \frac{A}{\epsilon^\beta} \tag{B.8}$$

with β as yet unknown. At the first order ϵ^β, the linearized Ginzburg–Landau equation at $A = A_0$ yields the equation for the inner solution $\xi(x)$.

$$\frac{d^2\xi}{dx^2} - U_0\frac{d\xi}{dx} + \mu^{nl}\xi = 0 \tag{B.9}$$

Using the notation $v(\xi) = d\xi/dx$, the condition $u'(A_0) = U_0$ yields

$$v'(0) = U_0 \tag{B.10}$$

and the solution of the equation (B.9) takes the form

$$\xi(x) = \frac{2v_0}{\sqrt{3} - U_0}\left(\mathrm{e}^{r^+x} - \mathrm{e}^{r^-x}\right) \tag{B.11}$$

where $r^+ = (U_0 + \sqrt{3})/4$, $r^- = (3U_0 - \sqrt{3})/4$ and v_0 remains unknown since the second order equation (B.9) is to be solved with only one boundary condition.

The next step is the matching of the outer and inner solutions. Let us introduce

$$\eta = \frac{A}{\epsilon^\alpha} = \xi\epsilon^{\beta-\alpha} \tag{B.12}$$

into both solutions and expand the solutions in powers of ϵ in order to make the identification

$$u(A) \equiv \epsilon^\beta v(\xi). \tag{B.13}$$

The expansion of the inner solution reads

$$v(\xi) = \frac{U_0 + \sqrt{3}}{4}\eta\epsilon^{\alpha-\beta} + v_0^{1-\lambda_1}\left(\frac{\sqrt{3} - U_0}{2}\right)^{\lambda_1}\eta^{\lambda_1}\epsilon^{(\alpha-\beta)\lambda_1}. \tag{B.14}$$

The expansion of the outer solution yields

$$u(A) = \frac{A_2^2}{\sqrt{3}}\eta\epsilon^\alpha + \sqrt{3}A_2^{2\lambda_2}\eta^{\lambda_1}\epsilon^{\alpha\lambda_1+1}\int_0^{A_2} a^{-\lambda_1}(A_2^2 - a^2)^{-\lambda_2-1}da. \tag{B.15}$$

Since $A_2^2/\sqrt{3} = (U_0 + \sqrt{3})/4$, the comparison at the order ϵ^α gives no information. The comparison at the following order yields the size of the boundary layer

$$\beta = \frac{1}{1 - \lambda_1} = \frac{\sqrt{3} + U_0}{2(\sqrt{3} - U_0)} \tag{B.16}$$

and by insertion of the value v_0, the sought scaling law reads

$$u(A_0) = v_0\epsilon^\beta \tag{B.17}$$

where

$$v_0 = \left({A_2}^{-1-\lambda_1} \sqrt{3} \left(\frac{\sqrt{3} - U_0}{2} \right)^{-\lambda_1} \int_0^1 a^{-\lambda_1} (1-a^2)^{-\lambda_2 - 1} da \right)^{\beta}. \tag{B.18}$$

Using the beta function [33], this expression may be succinctly written

$$v_0 = \frac{3^{\beta - \frac{1}{2}}}{2^{\beta}} A_2^{3-4\beta} \mathcal{B}^{\beta} \left(2 - \frac{1}{2\beta}; \frac{1}{2\beta} \right). \tag{B.19}$$

B.2 Scaling law $\Delta x = f(\epsilon)$ with $\epsilon = \mu - \mu^{nl}$

The characteristic size of the front linking A_0 to A_2 for $\mu = \mu^{nl} + \epsilon$ is calculated in two parts: in the first part Δx_i is related to the inner solution; one has to calculate x_i such as $\xi(x_i) = 1$; in the second part Δx_o is related to the outer solution and verifies $\Delta x_o = x_o - x_i$ where

$$A(x_i) = \epsilon^{\beta} \quad \text{and} \quad A(x_o) = 0.99 A_2(\mu). \tag{B.20}$$

The inner solution is given by the expression (B.11). Thus, the first approximation of the inner characteristic size is given by the equation

$$\Delta x_i = x_i = \frac{4}{\sqrt{3} + U_0} \ln \left(\frac{\sqrt{3} - U_0}{2 v_0} \right). \tag{B.21}$$

The value v_0 is given by solution of equations (B.19) and (B.16).

The outer solution is given by the expression

$$\frac{dA}{dx} = u(A) = u_0(A) + \epsilon u_1(A). \tag{B.22}$$

Integrating the equation

$$\frac{dA}{u_0(A) + \epsilon u_1(A)} \simeq \frac{dA}{u_0(A)} - \epsilon \frac{u_1(A) dA}{u_0^2(A)} = dx \tag{B.23}$$

and neglecting terms of order ϵ, we obtain

$$\begin{aligned} \Delta x_o &= \int_{\epsilon^{\beta}}^{0.99 A_2(\mu)} \frac{\sqrt{3}}{A_2^2} \left(\frac{1}{A} + \frac{1}{2(A_2 - A)} - \frac{1}{2(A_2 + A)} \right) dA \\ &= \frac{\sqrt{3}}{A_2^2} \log \left(\frac{0.99 A_2}{\epsilon^{\beta} \left| 1 - (0.99)^2 - 2\epsilon (0.99)^2 A_{2,\mu} / A_2 \right|^{\frac{1}{2}}} \right), \end{aligned} \tag{B.24}$$

which yields the scaling law for the characteristic size by adding expressions (B.21) and (B.24), *viz.*,

$$\Delta x = \Delta x_i + \Delta x_o = \frac{\sqrt{3}}{A_2^2} \left(-\beta \log \epsilon + \log K \right) \tag{B.25}$$

where

$$K = \frac{0.992^{\beta} A_2^{4\beta} \mathcal{B}^{-\beta}\left(2 - \frac{1}{2\beta}; \frac{1}{2\beta}\right)}{\beta 3^{\beta} |1 - (0.99)^2 - 2\epsilon(0.99)^2 A_{2,\mu}/A_2|^{1/2}}. \tag{B.26}$$

$\mathcal{B}$ is again the beta function.

C Singular perturbation analysis of the subcritical Ginzburg–Landau equation in the vicinity of $\mu = \mu^l(U_0)$ for $U_0 > \sqrt{3}$

Scaling laws $dA/dx(0) = f(\epsilon)$ and $\Delta x = f(\epsilon)$ with $\epsilon = \mu - \mu^l$ and $U_0 > \sqrt{3}$

The absolute instability threshold is given by

$$\mu_A = \mu^l = \frac{U_0^2}{4}. \tag{C.1}$$

Throughout Appendix C we precise the dependence $A_2(\mu)$ only if necessary. Otherwise we use the notations $A_2 \equiv A_2(\mu^l)$ and $A_{2,\mu} \equiv dA_2/d\mu(\mu^l)$.

We seek a solution of equation (23) representing the stable manifold of A_2 as a series in the form

$$u(A) = -\sum_{k=1}^{+\infty} \nu_k(\mu)\,(A_2(\mu) - A)^k. \tag{C.2}$$

The boundary condition $u(A_2(\mu)) = 0$ is automatically verified since there is no zero order term in the series. In order to calculate the coefficients ν_k, one has to satisfy equation (23) at each order. The coefficients ν_k are thus calculated from ν_1 by the following recurrence formulas

$$\nu_1 = \frac{U_0}{2} - \frac{1}{2}\left(U_0^2 - 4\Gamma_1\right)^{\frac{1}{2}} \tag{C.3a}$$

$$\nu_{2k} = \frac{(2k+1)\left(\sum_{n=2}^{k} \nu_n \nu_{2k+1-n}\right) + \Gamma_{2k}}{U_0 - (2k+1)\nu_1} \tag{C.3b}$$

$$\nu_{2k-1} = \frac{2k\left(\sum_{n=2}^{k-1} \nu_n \nu_{2k-n} + \nu_k^2/2\right) + \Gamma_{2k-1}}{U_0 - 2k\nu_1}. \tag{C.3c}$$

The coefficients Γ_k depend on the shape of the potential and are given by

$$\Gamma_k = \frac{(-1)^k}{k!} \frac{d^{k+1}\mathcal{V}}{dA^{k+1}}(A_2(\mu)). \tag{C.4}$$

For the particular value $\mu^l = U_0^2/4$, the equation (C.2) represents the outer solution displayed by the continuous line in figures 8(a) and 8(d) at the absolute instability

threshold. Therefore, we do not apply the boundary condition at $A = A_0$. In the inner layer, the inner variable is ξ and the inner solution is calculated as a function of the departure from the criticality $\epsilon = \mu - \mu^l$, as a solution of equation (23) linearized about $A = A_0$ with the boundary condition $\xi(0) = 0$:

$$\xi(x) = \frac{v_0}{\sqrt{\epsilon}} \exp\left(\frac{U_0}{2}x\right) \sin\left(\sqrt{\epsilon}x\right). \tag{C.5}$$

v_0 is the slope at the origin of this solution $v(\xi) = d\xi/dx$ and is not yet determined since only one boundary condition has been applied to a second order equation. The matching between the inner solution $v(\xi) = d\xi/dx$ and the outer solution $u(A) = dA/dx$ allows a determination of v_0. One has to choose the following scaling between the inner variable and the outer variable in order to make the matching tractable

$$\xi = \epsilon^{-1} \exp\left(\frac{U_0\pi}{2\sqrt{\epsilon}} - \frac{U_0 A}{2v_0\epsilon}\right) A. \tag{C.6}$$

In other words, the inner solution (C.5) reaches its maximum at a value x_i close to $\pi/\sqrt{\epsilon}$ and both inner and outer solutions overlap for $x \simeq x_i$. Since the contribution of the outer solution (C.2) to the growth size scales like $\log \epsilon$, the dominant term for the characteristic size is given by

$$\Delta x \simeq \frac{\pi}{\sqrt{\epsilon}}. \tag{C.7}$$

We also choose an intermediate variable η such that

$$A = \eta\epsilon^{\alpha} \quad \text{with} \quad \frac{1}{2} < \alpha \leq 1. \tag{C.8}$$

Expanding the inner and outer solutions in increasing powers of ϵ, we obtain the inner solution as

$$v(\xi) = \left(\frac{U_0}{2}\eta\epsilon^{\alpha} - v_0\epsilon\right)\epsilon^{-1} \exp\left(\frac{U_0\pi}{2\sqrt{\epsilon}} - \frac{U_0\eta\epsilon^{\alpha-1}}{2v_0}\right), \tag{C.9}$$

and for the outer solution one finds

$$\begin{aligned} u(A) \;=\; & -\sum_{k=1}^{+\infty} \nu_k(\mu^l) A_2^k + \left(\sum_{k=1}^{+\infty} \nu_k(\mu^l) k A_2^{k-1}\right) \eta\epsilon^{\alpha} \\ & - \sum_{k=1}^{+\infty} \left(\frac{d\nu_k}{d\mu}(\mu^l) A_2^k + k\nu_k(\mu^l) A_{2,\mu} A_2^{k-1}\right) \epsilon. \end{aligned} \tag{C.10}$$

We use the following notations

$$w_k = \nu_k(\mu^l) A_2^{k-3} \qquad \text{and} \qquad z_k = \frac{d\nu_k}{d\mu}(\mu^l) A_2^k. \tag{C.11}$$

The term-by-term identification of the coefficients of the expansion in ϵ gives

- first solvability condition (order 0):

$$\sum_{k=1}^{+\infty} w_k = 0 \quad \text{if } U_0 > \sqrt{3}, \qquad \sum_{k=1}^{+\infty} w_k \neq 0 \quad \text{otherwise} \tag{C.12}$$

- second solvability condition (order ϵ^α):

$$\sum_{k=1}^{+\infty} k w_k = \frac{U_0}{2A_2^2} \tag{C.13}$$

- sought after value of v_0 (order ϵ):

$$v_0 = \sum_{k=1}^{+\infty} \left(z_k + k w_k A_2^2 A_{2,\mu\cdot} \right) \tag{C.14}$$

The scaling law for $u(0) = dA/dx(x = 0)$ then reads

$$u(0) = v_0 \epsilon \exp\left(-\frac{U_0 \pi}{2\sqrt{\epsilon}} \right). \tag{C.15}$$

The numerical values obtained for the equations (C.12), (C.13), and (C.14) are shown in the following table as functions of the number of terms in the series for $U_0 = 2$. The convergence of the series is relatively slow. We find $\sum_1^N w_k \simeq 10^{-8}$ and $(2A_2^2/U_0) \sum_1^N k w_k \simeq 0.96$ for $N = 40,000$ terms. The solvability conditions seem however to be verified.

N	$-\sum_{k=1}^{N} w_k$	$\frac{2A_2^2}{U_0} \sum_{k=1}^{N} k w_k$	$\sum_{k=1}^{N} \left(z_k + k w_k A_2^2 A_{2,\mu} \right)$
200	$7.551\,10^{-6}$	0.9492	$3.828\,10^{-3}$
400	$3.519\,10^{-6}$	0.9510	$1.831\,10^{-3}$
600	$2.254\,10^{-6}$	0.9520	$1.192\,10^{-3}$
800	$1.644\,10^{-6}$	0.9526	$8.798\,10^{-4}$
1000	$1.287\,10^{-6}$	0.9531	$6.953\,10^{-4}$
2000	$6.035\,10^{-7}$	0.9547	$3.356\,10^{-4}$
4000	$2.834\,10^{-7}$	0.9561	$1.625\,10^{-4}$
6000	$1.823\,10^{-7}$	0.9569	$1.064\,10^{-4}$
8000	$1.333\,10^{-7}$	0.9575	$7.891\,10^{-5}$
10000	$1.046\,10^{-7}$	0.9579	$6.257\,10^{-5}$
20000	$4.938\,10^{-8}$	0.9591	$3.048\,10^{-5}$
40000	$2.333\,10^{-8}$	0.9603	$1.488\,10^{-5}$

D Singular perturbation analysis of the supercritical Ginzburg–Landau equation in the vicinity of $\mu = \mu^l(U_0)$

Scaling law $dA/dx(0) = f(\epsilon)$ with $\epsilon = \mu - \mu^l$

The absolute instability threshold is given by $\mu_A = \mu^l = U_0^2/4$. The calculation of the scaling law is the same as in the subcritical case with $U_0 > \sqrt{3}$. We follow the same approach. We seek a solution of the equation

$$uu' - U_0 u + \mu A - A^3 = 0 \tag{D.1}$$

as a series similar to (C.2). The coefficients ν_k are calculated using formulas (C.3a-c). The inner solution takes the same form as in equation (C.5). In order to do the matching, the scaling law between the inner and outer variable has to be chosen in the form (C.6) The matching between the solutions is done by expanding the inner and outer solutions at orders 0, ϵ^α, and ϵ (with $A = \eta\epsilon^\alpha$). Here we use the notations

$$w_k = \nu_k(\mu^l)A_2^{k-2}(\mu^l) \qquad \text{and} \qquad z_k = \frac{d\nu_k}{d\mu}(\mu^l)A_2^k(\mu^l), \tag{D.2}$$

and by identifying the expansions of inner and outer solutions at each order, we obtain

- at the order zero
$$\sum_{k=1}^{+\infty} w_k = 0, \tag{D.3}$$
- at the order ϵ^α
$$\sum_{k=1}^{+\infty} k w_k = 1, \tag{D.4}$$
- at the order ϵ
$$v_0 = \sum_{k=1}^{+\infty} \left(z_k + \frac{k w_k}{2} \right). \tag{D.5}$$

Equations (D.3 and D.4) are solvability conditions and equation (D.5) then yields v_0. The sought scaling law takes exactly the same form as in the subcritical case, *viz.*

$$u(0) = v_0 \epsilon \exp\left(-\frac{U_0 \pi}{2\sqrt{\epsilon}} \right). \tag{D.6}$$

The following table shows the numerical values obtained for the solvability conditions and the calculation of v_0 as functions of the number of terms in the series

for the advection velocity $U_0 = 1$. The convergence of the series is relatively slow. For $N = 40,000$ terms, we find $\sum_1^N w_k \simeq 10^{-7}$ and $\sum_1^N k w_k \simeq 0.92$. The solvability conditions seem however to be verified.

N	$-\sum_{k=1}^{N} w_k$	$\sum_{k=1}^{N} k w_k$	$\sum_{k=1}^{N} \left(z_k + \frac{k w_k}{2} \right)$
200	$8.117\,10^{-5}$	0.860	2.895
400	$3.419\,10^{-5}$	0.873	2.946
600	$2.072\,10^{-5}$	0.879	2.971
800	$1.456\,10^{-5}$	0.884	2.987
1000	$1.109\,10^{-5}$	0.887	2.998
2000	$4.789\,10^{-6}$	0.895	3.029
4000	$2.087\,10^{-6}$	0.903	3.055
6000	$1.289\,10^{-6}$	0.907	3.068
8000	$9.178\,10^{-7}$	0.909	3.077
10000	$7.056\,10^{-7}$	0.911	3.083
20000	$3.133\,10^{-7}$	0.917	3.102
40000	$1.400\,10^{-7}$	0.921	3.118

E Multiplicity of solutions

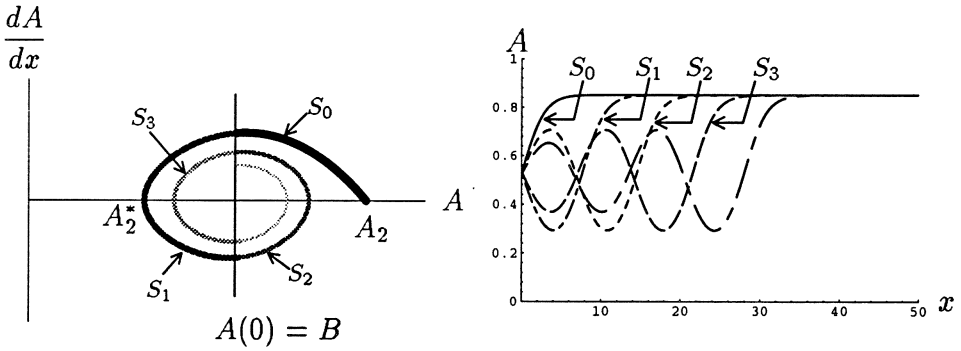

(a) Phase portrait.

(b) Forced solutions S_0, S_1, S_2 versus x.

Figure 28: Multiplicity of forced solutions in the NC region for $\mu < 0$. Only S_0 verifies steady Ginzburg–Landau equation with boundary conditions $A(0) = B$ and $A(+\infty) = A_2$ without oscillating around A_1.

Note that **in the NC region and in the NS region**, there may exist several steady solutions of equation (1) with potential density (2) satisfying the required

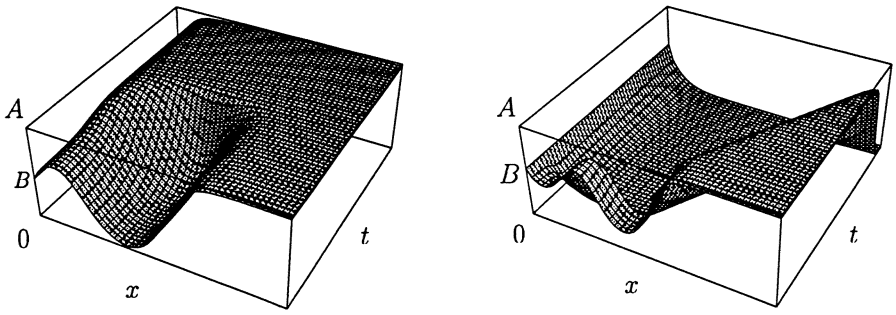

(a) (b)

Figure 29: Simulation in the NC region. (a) The starting solution crosses twice zero. $B = A_1$; $U_0 = 0.1$; $\mu = \mu_A - 0.01 = -0.164$. The system relaxes to the solution S_0 of Fig. 28 asymptotic to A_2. (b) The starting solution crosses three times zero. $B = A_1$; $U_0 = 0.1$; $\mu = -0.164$. The system relaxes to the solution asymptotic to A_0 which does not oscillate around A_1.

boundary conditions $A(0) = B$ with either $A(+\infty) = A_2$ or $A(+\infty) = A_0$, and oscillating around $A = B$. An example of multiplicity of solutions is shown in Fig. 28. A necessary condition for multiple solutions is that the stable manifold of A_2 (or A_0) oscillates around the amplitude B. For example, if $\mu < 0$, in the region of parameter space where A_1 is an unstable focus (see Appendix A) multiple solutions asymptotic to A_2 (or A_0) exist if $B > A_2^*$ (or $B < A_0^*$); when A_1 is an unstable node or when $\mu > 0$, there exists only one solution asymptotic to A_2 (or A_0) at $+\infty$. In the simulation displayed in Fig. 29, an oscillating solution of equation (21) such that $A(0) = B$ and $A(+\infty) = A_2$ becomes unstable and evolves to the steady solution without oscillation, that verifies the same boundary conditions. All numerical simulations we have undertaken indicate that oscillating forced solutions are unstable. Depending on the initial solution, they evolve either to the steady solution satisfying $A(+\infty) = A_2$ with no oscillations (Fig. 29(a)), or to the steady solution satisfying $A(+\infty) = A_0$ but still without oscillation (Fig. 29(b)).

In the NG region, there may also exist several steady solutions of equation (1) with potential density (2) such that $A(0) = B$ and $A(+\infty) = A_2$ as sketched in Fig. 30.

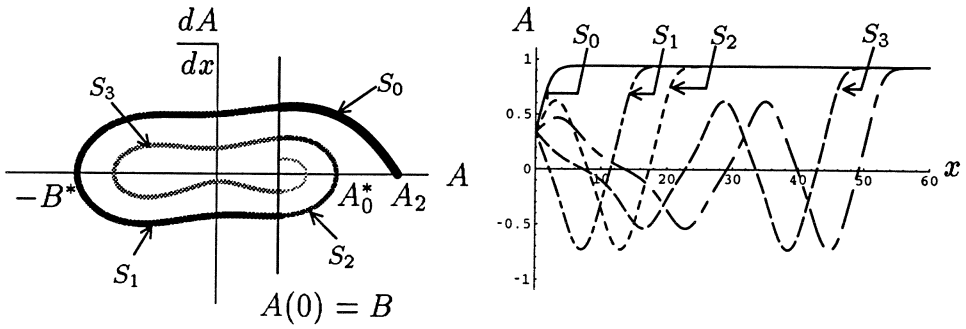

(a) Phase portrait.

(b) Forced solutions S_0, S_1, S_2 versus x.

Figure 30: Multiplicity of forced solutions in the NG region for $\mu < 0$. Only S_0 verifies steady Ginzburg–Landau equation with boundary conditions $A(0) = B$ and $A(+\infty) = A_2$ without oscillating around B.

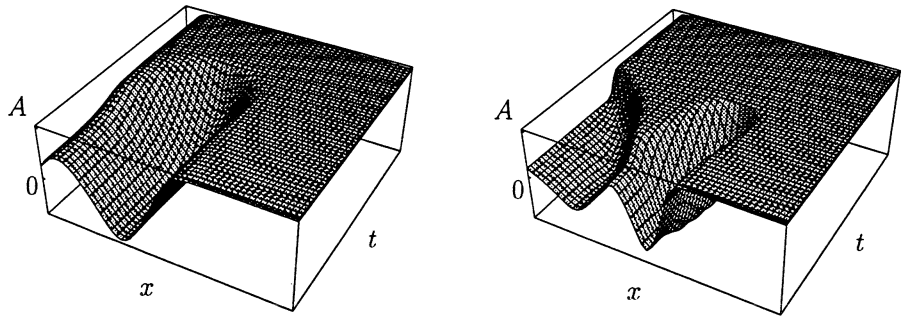

(a)

(b)

Figure 31: Simulation in the NG region. (a) The starting solution crosses twice zero. $B = 0.25$; $U_0 = 0.1$; $\mu = 0.001$. (b) The starting solution crosses three times zero. $B = 0.2$; $U_0 = 0.1$; $\mu = -0.05$. In (a) and (b), the system relaxes to the solution S_0 of Fig. 30(b) asymptotic to A_2.

All temporal simulations indicate that only the non-oscillating solutions are stable (Fig. 31): For the parameter setting $U_0 = 0.1$ and $\mu = 0.001$ ($\mu = -0.05$), the solution S_2 (S_3) oscillating twice in Fig. 30(a) (three times in Fig. 30(b)) evolves to the solution S_0 with no oscillation.

References

[1] J.M. Chomaz, *Absolute and convective instabilities in nonlinear systems*, Phys. Rev. Lett., **69**, (1992) 1931.

[2] W. van Saarloos and P.C. Hohenberg, *Fronts, pulses, sources and sinks in generalized complex Ginzburg-Landau equations*, Physica **D56**, (1992) 303.

[3] P. Huerre and P.A. Monkewitz, *Local and global instabilities in spatially developing flows*, Annu. Rev. Fluid Mech. **22**, (1990) 473.

[4] A. Bers, in *Physique des Plasmas*, edited by C. DeWitt and J. Peyraud (Gordon and Breach, New York, 1975).

[5] M.C. Cross, P.C. Hohenberg, *Pattern formation outside of equilibrium*, Rev. Mod. Phys. **65**, (1993) 851.

[6] J.M. Chomaz, P. Huerre, L.G. Redekopp, *Bifurcations to local and global modes in spatially developing flows*, Phys. Rev. Lett., **60**, (1988) 25.

[7] J.M. Chomaz, P. Huerre, L.G. Redekopp, *The effect of nonlinearity and forcing on global modes*, in *New Trends in Nonlinear Dynamics and Pattern-Forming Phenomena*, edited by P. Coullet and P. Huerre, (Plenum Press, New York, 1990).

[8] J.M. Chomaz, P. Huerre, L.G. Redekopp, *A frequency selection criterion in spatially developing flows*, Stud. Appl. Math. **84**, (1991) 119.

[9] P.A. Monkewitz, P. Huerre, J.M. Chomaz, *Global linear stability analysis of weakly non parallel shear flows*, J. Fluid Mech., **251**, (1993) 1.

[10] S. Le Dizès, P. Huerre, J.M. Chomaz, P.A. Monkewitz, *Linear global modes in spatially-developing media*, Phil. Trans. R. Soc. Lond. A **354**, (1996) 169.

[11] S. Le Dizès, P. Huerre, J.M. Chomaz, P.A. Monkewitz, *Nonlinear stability analysis of slowly diverging flows: Limitations of the weakly nonlinear approach*, in *Proceedings of the IUTAM Symposium on bluff-body wakes, dynamics and instabilities* (ed. H. Eckelmann, J. M. R. Graham, P. Huerre, P. A. Monkewitz), Berlin : Springer-Verlag, 147.

[12] R.E. Hunt, *Spatially Varying Flows with localized forcing*, Ph. D. Thesis (1995).

[13] R.E. Hunt, D.G. Crighton, *Instability of flows in spatially developing media*, R. Soc. Lond. A **435**, 109.

[14] K.R. Sreenivasan, S. Raghu, D. Kyle, *Absolute instability in variable density round jets*, Exp. Fluids **7**, (1989) 309.

[15] P.J. Strykowski, D.L. Niccum, *The influence of velocity and density ratio on the dynamics of spatially developing mixing layers*, Phys. Fluids A **4**, (1992) 770.

[16] A. Couairon, J.M. Chomaz, *Global Instability in fully nonlinear systems*, accepted in Phys. Rev. Lett.

[17] J. Guckenheimer, P. Holmes, *Nonlinear Oscillations, Dynamical Systems, and Bifurcations of Vector Fields*, (Springer Verlag, 1983)

[18] J.D. Gunton, M. San Miguel, Paramdeep S. Sahni, *The dynamics of first-order phase transitions*, in *Phase transitions and critical phenomena*, edited by C. Domb and J.L. Lebowitz, Vol. 8 (Academic Press, 1983).

[19] G. Dee, *Dynamical properties of propagating front solutions of the amplitude equations*, Physica **15D**, (1985) 295.

[20] G. Dee, *Propagation into an unstable state*, J. Stat. Phys. **39**, (1985) 705.

[21] E. Ben-Jacob, H. Brand, G. Dee, L. Kramer, J.S. Langer, *Pattern propagation in nonlinear dissipative systems*, Physica **14D**, (1985) 348.

[22] W. van Saarloos, *Front propagation into unstable states: Marginal stability as a dynamical mechanism for velocity selection*, Phys. Rev. A, **37**, (1988) 211.

[23] W. van Saarloos, *Front propagation into unstable states. II. Linear versus nonlinear marginal stability and rate of convergence*, Phys. Rev. A, **39**, (1989) 6367.

[24] J.A. Powell, A.C. Newell, C.K.R.T. Jones, *Competition between generic and nongeneric fronts in envelope equations* Phys. Rev. A, **44**, (1991) 3636.

[25] J. Fineberg and V. Steinberg, *Vortex-front propagation in Rayleigh–Benard convection*, Phys. Rev. Lett., **58**, (1987) 1332.

[26] G. Ahlers and D.S. Cannel, *Vortex-front propagation in rotating Couette–Taylor flow*, Phys. Rev. Lett., **50**, (1983) 1583.

[27] M. Lücke, M. Mihelcic and K. Wingerath, *Front propagation and pattern formation of Taylor vortices growing into unstable circular Couette flow*, Phys. Rev. A, **31**, (1985) 396.

[28] A. Hanna, A. Saul and K. Showalter, *Detailed studies of propagating fronts in the iodate oxydation of arsenous acid*, J. Am. Chem. Soc. **104**, (1982) 3838.

[29] D.G. Aronson and H.F. Weinberger, *1975 Nonlinear diffusion in population genetics, combustion, and nerve propagation*, in *Partial Differential Equations and Related Topics, Lecture Notes in Mathematics*, Vol. 446, pp 5–49, springer, New-York 1975.

[30] D.G. Aronson and H.F. Weinberger, *1978 Multidimensional nonlinear diffusion arising in population genetics*,Adv. Math. **30** (1978) 33.

[31] P. Palffy-Muhoray, H.J. Yuan, B.J. Frisken and W. van Saarloos, in *Nonlinear evolution of spatio-temporal structures in dissipative continuous systems*, edited by F.H. Busse and L. Kramer, Plenum Press, New-York 1990.

[32] C.M. Bender and S.A. Orszag, *Advanced Mathematical Methods for Scientists and Engineers*, Mc Graw Hill 1978.

[33] M. Abramowitz, I.A. Stegun, *Handbook of mathematical functions*, Dover.

[34] P. Coullet, L. Gil and D. Repaux, *Defects and subcritical bifurcations*, Phys. Rev. Lett. **62**, (1989), 2957.

[35] V. Hakim, in *Hydrodynamics and nonlinear instabilities*, Cambridge University Press, to be published.

[36] A. Couairon, J.M. Chomaz, *Pattern selection in the presence of a cross flow*, submitted to Phys. Rev. Lett.

[37] P. Büchel, M. Lücke, D. Roth, R. Schmitz, *Pattern selection in the absolutely unstable regime as a nonlinear eigenvalue problem: Taylor vortices in axial flow*, Phys. Rev. E. **53**, (1996) 4764.

[38] H.W. Müller, M. Lücke, M. Kamps, *Convective Patterns in Horizontal flow*, Europhys. Lett. **10**, (1989) 451; *Transversal convection patterns in horizontal shear flow*, Phys. Rev. A **45**, (1992) 3714.

Chapitre 2

Modes globaux non-linéaires homogènes dans le cas non potentiel

Pattern selection in the presence of a cross flow

A. Couairon, J. M. Chomaz
LadHyx, CNRS UMR 156, École Polytechnique, 91128 Palaiseau cedex, France
(October 31, 1996)

We study the pattern selection and the dynamics of a bifurcating system such as Taylor–Couette flow or Rayleigh–Bénard convection, subject to an externally imposed cross flow using the complex Ginzburg–Landau equation as a qualitative model. We show that the bifurcation scenario is radically modified by the introduction of a cross flow. For this model, we determine analytically the existence of nonlinear global modes (NG), *i.e.* nonlinear oscillating solution in a semi-infinite domain $[0, +\infty)$, with an homogeneous condition at $x = 0$. We show for this self similar equation that a NG mode exists only when the basic state is linearly absolutely unstable. The characteristic growth size varies as $\epsilon^{-1/2}$ because it is given by the beating of two linear waves with wave number difference of order $\sqrt{\epsilon}$ (ϵ being the criticality parameter). This law, never derived before, compares satisfactorily with numerical and experimental results from the literature on Taylor–Couette flow and on Rayleigh–Bénard convection.

47.20.Ft,47.20.Ky

It is now well established that the dynamics of closed flows such as flow between rotating coaxial cylinders (Taylor–Couette flow) or between horizontal plates heated from below (Rayleigh–Bénard convection) is reasonably described close to threshold by amplitude equations derived for an infinite system [1]. For a one-dimensional system, the effect of lateral boundaries have been shown to weakly stabilize the primary bifurcation by an order $1/L^2$ term (L being the size of the box). In these cases, for supercriticality small but larger than $\mathcal{O}(1/L^2)$, the condition at the lateral boundaries influences the flow in a diffusive manner and, except in small boundary layers, the solution has reached a local nonlinear equilibrium as if the domain were infinite [2]. If an externally imposed cross flow is added [3–5] (or equivalently if traveling waves are destabilized such as in binary convection [6,7]), the diffusion effects near boundaries are now convected in the direction of the cross flow and may determine the pattern selection in the whole domain. Intuitively, the addition of a cross flow increases the stability of the system as an initial perturbation which is advected downstream while being amplified and may ultimately leave the domain unperturbed. For the same cross flow but at a higher value of the bifurcation parameter (stronger instability), instabilities should be able to withstand the advection and saturate, forming a self-sustained mode (the so-called global mode). On a linear basis, this change of behavior has been associated with a notion first developed in plasma physics [9] of convective or absolute instability which relies on the direction of motion of the trailing edge of a wave packet in the boundary's reference frame. If the trailing edge moves downstream, the flow is convective and if it moves upstream, the flow is absolute [8].

In previous studies [10,11] we have proposed a nonlinear generalization of these definitions by directly solving the nonlinear global stability, considering the problem of the existence of a nonlinear solution in a semi-infinite domain with a homogeneous upstream boundary condition. The major result illustrated up to now only on potential systems (real Ginzburg–Landau type equation) was that absolute instability is a sufficient but not necessary condition for nonlinear global instability (*i.e.* nonlinearity may counterbalance the advection).

The present study generalizes these considerations to the more generic case of the complex Ginzburg–Landau equation which offers a physically more realistic but higher-dimensional problem. It establishes analytically, for the first time, the link between absolute instability and nonlinear pattern selection in a semi-infinite domain for the non potential case of the complex Ginzburg–Landau equation. This model is believed to describe the dynamics of the amplitude of Taylor–Couette [3,4] vortices or Rayleigh–Bénard [5] rolls close to the threshold with a cross flow [12]

$$\frac{\partial A}{\partial t}+U_0\frac{\partial A}{\partial x}=(1+ic_1)\frac{\partial^2 A}{\partial x^2}+\mu A-(1-ic_3)|A|^2A. \quad (1)$$

$U_0\partial A/\partial x$ represents the effect of advection with $U_0 > 0$. The bifurcation parameter is μ and c_1 and c_3 are real coefficients [13]. A rescaling of A, x, and t would allow us to set U_0 to unity while leaving the other parameters in Eq. (1) unchanged, but we will keep this redundance in parameter in order to facilitate comparison with experiments. This self similarity of (1) will imply that the global instability will occur identically for every U_0.

In an infinite domain, $A_0 \equiv 0$ is linearly convectively unstable [14] for $0 < \mu < \mu_A \equiv U_0^2/4(1+c_1^2)$ and linearly absolutely unstable for $\mu > \mu_A$, the associated absolute frequency being $\omega_A \equiv -c_1\mu_A$.

Eq. (1) is known [15] to exhibit a family of saturated traveling wave solutions parametrized by ω (defined up to an arbitrary phase):

$$A_2 \equiv a_N e^{iq_N x-\omega t}, \quad (2)$$

where $a_N^2 = \mu - q_N^2$, $\omega = U_0 q_N + c_1 q_N^2 - c_3 a_N^2$. Please note that once ω is specified, two solutions exist for $\mu > U_0^2/4(c_1+c_3)$: $q_N^{\pm} = \left(-1 \pm \sqrt{1+4(c_1+c_3)(\omega+c_3\mu)/U_0^2}\right) U_0/2(c_1+c_3)$, but that only q_N^+ exists for $0 \le \mu \le U_0^2/4(c_1+c_3)$.

In a semi-infinite domain, nonlinear global (NG) modes are defined as oscillatory solutions of Eq. (1) with the boundary condition at the origin $A(0) = 0$. At infinity, the NG mode is asymptotic to a plane wave of the type (2). The solution q_N^- when it exists is shown in [22] to be unphysical as it corresponds to a negative "group velocity" $d\omega/dq_N$.

Therefore, in the sequal only q_N^+ is considered and the + sign is dropped for simplicity of notations. Furthermore, only solutions asymptotic to a stable nonlinear wave will be considered here. This imposes two conditions: firstly $1-c_1c_3 > 0$ (Benjamin–Feir stable domain); secondly ω belongs to the white parabolic zone [16] depicted on Fig. 1 (the stability condition on q_N may be found in [15]).

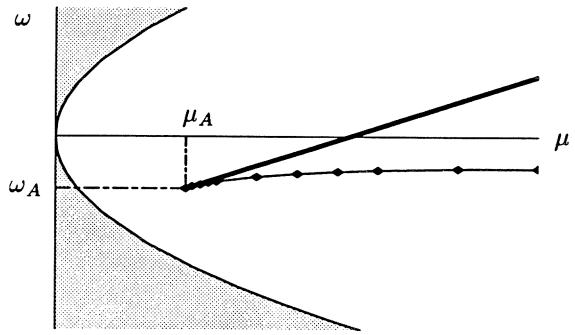

FIG. 1. Region of (μ, ω) space where saturated traveling waves (a_N, q_N) are stable (white region). NG modes exist for $\mu > \mu_A$ with a frequency $\omega_G(\mu)$ obtained numerically represented by the thin continuous curve. We predict that $\omega_G(\mu_A) = \omega_A$ and its slope (heavy continuous line) by a perturbation analysis aroud the threshold.

We are now faced with first considering the existence of a NG mode and then solving the frequency selection problem. Because of the rotational invariance ($A \to Ae^{i\theta}$), a NG mode may be sought in the form

$$A(x,t) = a(x)e^{i\int^x q(x')dx'}e^{-i\omega t}, \qquad (3)$$

with $a(x)$, $q(x)$, and ω real. This transformation which absorbs the phase invariance into the spatial origin is often associated [17–19] with the singular change of variable $k = \dot{a}/a$ (the dot denotes differentiation with respect to x), called the σ-process by Arnol'd [20]. Here we use $u = \dot{a}$ since a NG mode which satisfies $a(0) = 0$, would be a singular solution if we were using the variable k. Under the change of variable (3), the initially second-order equation (1) becomes first-order and is reduced to the dynamical system (4,5,6) in the three variables a, q, and $u = \dot{a}$:

$$\dot{a} = u \qquad (4)$$

$$a\dot{q} = -2uq - C(\omega - U_0 q)a - Cc_1(\mu a - U_0 u) - I_3 a^3 \qquad (5)$$

$$\dot{u} = aq^2 - C(\mu a - U_0 u) + Cc_1(\omega - U_0 q)a + R_3 a^3 \qquad (6)$$

with $C = (1+c_1^2)^{-1}$, $I_3 = C(c_1+c_3)$ and $R_3 = C(1-c_1c_3)$.

To different ω correspond different dynamical systems that we are going to describe. The interesting fixed points of this dynamical system are the point $A_2(\omega) \equiv (a_N, q_N, 0)$ which possesses a unique stable eigendirection when ω belongs to the unshaded region of Fig. 1 and represents the previously introduced saturated traveling wave, and the points $A_0^\pm(\omega) \equiv (0, q_0^\pm, 0)$ where $q_0^\pm = q_0 \mp \mathrm{sgn}(\sigma)\sqrt{(|\kappa + i\sigma| + \kappa)/2}$ and $q_0 = -Cc_1U_0/2$; κ,σ are reals and $\kappa + i\sigma \equiv C(1-ic_1)(\mu + i\omega - C(1-ic_1)U_0^2/4$. $A_0^-(\omega)$ is an unstable node and $A_0^+(\omega)$ is a saddle, the q direction being an unstable eigendirection for A_0^- but a stable one for A_0^+. In the phase space (a, q, u) a NG mode is represented by a trajectory linking a point of the plane $a = 0$ with u different from zero to A_2. In other words, a NG mode exists when the stable manifold of A_2 intersects the plane $a = 0$ at a point where $u \neq 0$. Introduction of this condition in Eq. (5) leads necessarily to $q = q_0$ at the intersection point if it exists. The stable manifold of A_2 can cross the plane $a = 0$ only on the axis $(q = q_0, a = 0)$.

For a given μ, we shall consider the two-dimensional surface formed by the union of all the stable manifolds of $A_2(\omega)$ generated by varying ω. From numerous numerical solutions of (4,5,6) we have found that, for all μ and ω, the stable manifold of A_2 emanates from A_0^- along the q-direction. Crossing of the axis $q = q_0, a = 0$ only occurs when $\mu > \mu_A(U_0, c_1, c_3)$ which therefore defines the global instability threshold. As in the real coefficient case, the emergence of the global mode is linked to the local changes around A_0^+ and A_0^-. When increasing μ through μ_A, those two points collide at $\mu = \mu_A$ and shift to opposite sides of the plane $q = q_0$ allowing a heteroclinic orbit for a particular frequency $\omega_G(\mu)$ to cross the $q = q_0, a = 0$ axis. The numerically selected values of $\omega_G(\mu)$ for which the axis $a = 0, q = q_0$ is crossed are plotted in Figure 1.

These observations are confirmed using a matched asymptotic expansion close to the threshold $\mu = \mu_A$ which shows that whatever U_0, a NG mode exists only for $\mu > \mu_A$ and predicts the frequency selection plotted in heavy line on the Fig. 1.

The perturbation analysis is carried on analytically except for matching conditions expressed as series which have to be evaluated numerically.

The heteroclinic trajectory $q_f(a), u_f(a)$ at $\mu = \mu_A$ and $\omega = \omega_A$ represents the Kolmogorov front [21,22] linking $A_0 = (0, q_0, 0)$ to A_2 (note that in this case $q_0^+ = q_0^- = q_0$). In the phase space all trajectories are described as functions of a; $q_f(a)$ and $u_f(a)$ are expanded in powers of a with general terms $\rho_j(a_N - a)^j$ and $\nu_j(a_N - a)^j$. When setting the bifurcation parameter value to $\mu = \mu_A + \epsilon$, the stable manifold of A_2 considered as a perturbation of the front $q_f(a), u_f(a)$ (the perturbation is also taken in the form of series expansions with general terms $\epsilon\eta_j(a_N - a)^j$ and $\epsilon\lambda_j(a_N - a)^j$) gives rise to a NG mode (intersection of the axis $a = 0, q = q_0$) cor-

responding to a single frequency of the form $\omega_A + \epsilon\omega_1$.

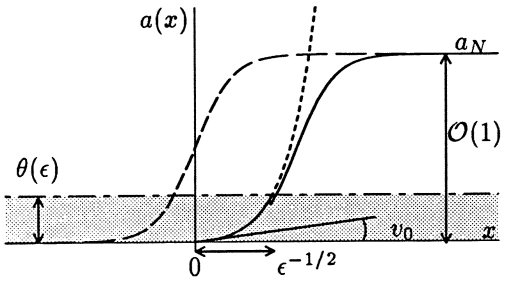

FIG. 2. Matching principle used to determine the frequency of a NG mode. The front at the threshold (long dashed line) is perturbed and shifted (continuous line) in order to match with the inner solution in the gray region.

Although the entire analysis has been carried out in the phase space, Fig. 2 displays its basic principle in physical space. The long dashed line represents the Kolmogorov front $q_f(a), u_f(a)$ at the threshold $\mu = \mu_A$ with frequency ω_A. When increasing μ, the front shape is slightly perturbed (continuous line). In the singular limit $\epsilon \ll 1$ an inner region of size $\theta(\epsilon) = \epsilon \exp(-CU_0\pi/2\beta\sqrt{\epsilon})$ determined by the matching has to be introduced in the neighborhood of the origin (gray region of Fig. 2) in order to take into account the boundary condition $a(0) = 0$. An inner solution is found analytically as a linear solution of (4–6) in the vicinity of $a = 0$. Application of the method of matched asymptotic expansions [23] between the inner and the outer solution leads to the determination of the slope v_0 at the origin of the inner solution and of the departure $\epsilon\omega_1$ of the NG mode frequency from ω_A.

The matching condition reads

$$\alpha + i\beta = \frac{|\zeta_1|^{\frac{1}{2}}}{v_0} \sum_{j=0}^{+\infty} \lambda_j - i \frac{v_0}{|\zeta_1|^{\frac{1}{2}}} \sinh^2\left(\frac{\alpha\pi}{\beta}\right) \sum_{j=1}^{+\infty} j\rho_j, \quad (7)$$

with $|\zeta_1| = \sqrt{C(1+\omega_1^2)}$, $\alpha = \sqrt{(|\zeta_1| - \kappa_1)/2}$, $\beta = \sqrt{(|\zeta_1| + \kappa_1)/2}$, and $\kappa_1 = C(1 + c_1\omega_1)$. The coefficients λ_j are linear in ω_1. Modulus and phase identification allow a numerical evaluation of Eq. (7) to determine v_0 and ω_1. Then the selected frequency $\omega_G \simeq \omega_A + \epsilon\omega_1$ is determined (heavy continuous line in Fig. 1). We are now able to find scaling laws for the characteristic growth size of NG modes and for their slope $|da/dx(0)|$ at the origin of the domain as a function of the departure from the NG threshold $\epsilon = \mu - \mu_A$.

The slope of NG modes is the slope v_0 rescaled by the size of the inner region:

$$\log\left|\frac{dA}{dx}(0)\right| \simeq -\frac{CU_0\pi}{2\beta\sqrt{\epsilon}} + \ln\epsilon + \ln v_0. \quad (8)$$

The dominant contribution as $\epsilon \to 0$ is $\epsilon^{-\frac{1}{2}}$ and this result is analytic although the coefficient β may be numerically computed only after having solved (7).

The characteristic growth size of the global mode is defined as the distance Δx such that $a(\Delta x) = 0.5\, a_N$. It may be calculated by adding the x-thickness of the inner region and the size of the outer solution between the boundary of the inner layer and the point at which the amplitude reaches the value $0.5\, a_N$. When keeping only the dominant contribution, the following scaling law is obtained:

$$\Delta x \simeq \pi/\beta\sqrt{\epsilon} \quad (9)$$

Note again, that the $\epsilon^{-1/2}$ dependence comes out naturally from the singular perturbation analysis.

These results allow us to interpret the pattern selection occurring in open flow systems in the globally unstable regime. For example Büchel *et al.* [3] describe propagating vortex structures in the rotating Taylor–Couette system with an externally imposed axial throughflow. Their simulations of the Navier–Stokes equations show that the bifurcation occurs for $\mu = \mu_A$. In the absolutely unstable regime, a unique spatiotemporal pattern is selected, the associated oscillation frequency and the spatial variation of the vortex flow intensity depending only on the control parameters and on the boundary conditions. They interpret the frequency and bulk wavelength selection as a nonlinear eigenvalue problem, the frequency being the eigenvalue, and show numerically that when approaching the absolute instability threshold, the selection mechanism is identical to the linear selection mechanism for front propagation described by Eq. (1) in an infinite domain. The numerical shape of the vortex flow intensity of Büchel *et al.* may be reinterpreted in terms of nonlinear global modes. In particular, they present a plot of the scaled growth length $L \equiv \sqrt{\mu}\Delta x$ of the vortex flow intensity versus the scaled advection velocity $V_g \equiv U_0\sqrt{C/\mu}$ which is in quite good qualitative agreement with our scaling law (9) rewritten in the form

$$\sqrt{\mu}\Delta x \simeq \pi\beta^{-1}\left(1 - V_g^2/4\right)^{-1/2}, \quad (10)$$

where $(1 - V_g^2/4)$ is the rescaled departure from criticality. In order to obtain a quantitative comparison, we have used in equation (10) the same values of the Reynolds number Re and Taylor T number as those plotted in Fig. 1 of [3] to generate for each combination (Re, T), the same set of Ginzburg–Landau coefficients U_0, c_1, c_3 as in [3], thereby allowing computation of our series coefficients and solution of equation (7). Values of c_1 and c_3 are, respectively, $\mathcal{O}(10^{-2})$ and $\mathcal{O}(10^{-3})$. U_0 varies from 0.12 to 0.65 and ω_1 obtained from (7) varies from -0.06 to -0.98. Please note that in our analysis β is a function of ω_1, but as c_1, c_3 are small, β stays so close to 1 that the theoretical predictions for the three sets are identical. Our theoretical results are superposed on those obtained by Büchel *et al.* [3] in Fig. 3(a). The good quantitative agreement, especially in the vicinity of the threshold $V_g = 2$, confirms the validity of our analysis

to describe the dynamics of Taylor–Couette system with throughflow.

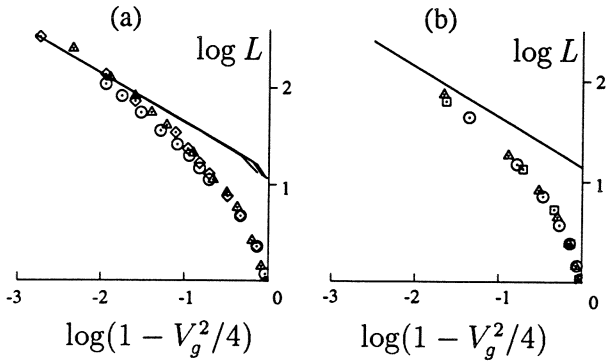

FIG. 3. (a) The scaled growth length of NG modes predicted by (10) (continuous lines) are superposed on the results of [3]. For Taylor–Couette problem with throughflow, the three sets of open symbols represent values computed in [3] for three different Taylor number. (b) The same quantities for the Rayleigh Bénard problem with throughflow. Symbols represent values computed in [5] for three different Rayleigh numbers. The continuous line is our theoretical $\epsilon^{-1/2}$ law with $\beta = 1$.

The same quantitative agreement is observed when we compare our theoretical analysis with the numerical results of Müller *et al.* [5] for the Rayleigh–Bénard problem with a Poiseuille flow (Fig. 3(b)). Moreover, the spatial structure of the NG mode (Fig. 4) analytically obtained in the present study for parameters values given in [5] and without additional free parameter is in good agreement with the one obtained in [5] by integration of Navier–Stokes equations.

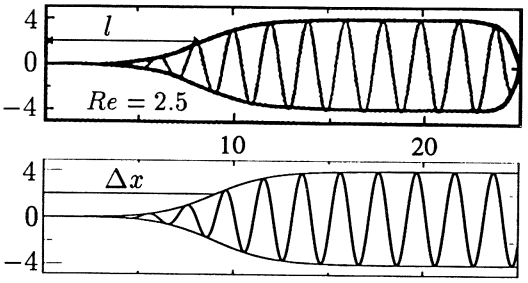

FIG. 4. (a) Vertical velocity field computed in [5] for the Rayleigh–Bénard problem with Poiseuille flow by numerical simulation of Navier–Stokes equations. (b) NG mode entirely analytically obtained in the present study without any adjustable parameter.

Finally, it is worth noting that the dependence in $\epsilon^{-1/2}$ of the typical growth length of the flow cannot be interpreted as the classical correlation length because it comes here from linear branches switching at the absolute instability threshold (two unstable linear waves with the same ω and wavenumber nearly equal with a phase shift proportional to $\epsilon^{1/2}$). The condition $a = 0$ is realized by the destructive interaction of these two waves and a distance of order $\epsilon^{-1/2}$ is required to reach order one amplitudes.

The authors wish to thank P. Weidman for his careful reading of the manuscript.

[1] P. Manneville, *Dissipative structures and weak turbulence*, (Academic Press, Boston, 1990).
[2] Y. Pomeau, S. Zaleski, P. Manneville, Journal of Applied Mathematics and Physics (ZAMP), **36**, 367 (1985).
[3] P. Büchel, M. Lücke, D. Roth, R. Schmitz, Phys. Rev. E. **53**, 4764 (1996).
[4] K.L. Babcock, G. Ahlers, D.S. Cannel, Phys. Rev. Lett. **67**, 3388 (1991); Physica D **61**, 40 (1992).
[5] H.W. Müller, M. Lücke, M. Kamps, Europhys. Lett. **10**, 451 (1989); Phys. Rev. A **45**, 3714 (1992).
[6] D. Bensimon, P. Kolodner, C.M. Surko, H. Williams, V. Croquette, J.Fluid Mech. **217**, 441 (1990).
[7] C. Cross, Phys. Rev. A, **38**, 3593 (1988).
[8] in many respect, absolute and convective instability are extension of elliptic and hyperbolic classification of linear problems.
[9] A. Bers, in *Physique des Plasmas*, edited by C. DeWitt and J. Peyraud (Gordon and Breach, New York, 1975).
[10] J.M. Chomaz, Phys. Rev. Lett., **69**, 1931 (1992).
[11] A. Couairon, J.M. Chomaz, submitted to Physica **D**; Phys. Rev. Lett. **77**, 4015 (1996).
[12] Note that c_1 and c_3 are no more zero when a cross flow is added, see [3] and [5].
[13] with $c_1 > 0$ (because of the symmetry $c_i \to -c_i, A \to \overline{A}$).
[14] P. Huerre, P.A. Monkewitz, Annu. Rev. Fluid Mech. **22**, 473 (1990).
[15] B.J. Matkowski, V. Volpert, Quart. Appl. Math. **51**, 265 (1993).
[16] In the Benjamin–Feir stable domain $1 - c_1 c_3 > 0$, there exists an upper bound $q_N^*(\mu, c_1, c_3)$ such that traveling waves (2) are linearly stable if $q_N < q_N^*(\mu, c_1, c_3)$ and linearly unstable otherwise. An explicit expression of $q_N^*(\mu, c_1, c_3)$ when the loss of stability is due either to long waves or to finite wavelength perturbations is derived in [15], the condition $q_N < q_N^*(\mu, c_1, c_3)$ being equivalently represented by the white parabola in Fig. 1.
[17] M.J. Landman, Stud. Appl. Math. **76**, 187 (1987).
[18] C.K.R.T. Jones, T.M. Kapitula, J.A. Powell, Proc. Roy. Soc. Edinburgh, **116A**, 193 (1990).
[19] N. Koppel, L.N. Howard, Stud. Appl. Math. **56**, 291 (1973).
[20] V.I. Arnol'd, *Geometrical methods in the theory of ordinary differential equations*, (Springer, Heidelberg, 1983).
[21] A. Kolmogorov, I. Petrovsky, N. Piskunov, Bull. Univ. Moscow, Ser. Int. Sec. A **1**, 1 (1937).
[22] W. van Saarloos, P.C. Hohenberg, Physica **D56**, 303 (1992).
[23] C.M. Bender, S.A. Orszag, *Advanced Mathematical Methods for Scientists and Engineers*, (Mc Graw Hill, 1978).

Primary and secondary nonlinear global instability

Arnaud Couairon and Jean–Marc Chomaz

LadHyX, CNRS UMR 156, Laboratoire d'Hydrodynamique,
École Polytechnique, 91 128 Palaiseau CEDEX, France

Abstract

In the present paper, we study oscillating solutions of the complex Ginzburg–Landau equation in a semi infinite domain asymptotic to a saturated traveling wave at $+\infty$ and subject to a homogeneous upstream boundary condition at $x = 0$. This condition breaks the Galilean invariance and therefore, the advection velocity has to be viewed as a control parameter. In the phase space, we give a criterion to determine the existence of a nontrivial solution called a nonlinear global mode or a self sustained resonance, and to obtain the selected frequency. The threshold and the frequency are shown to be determined by the linear absolute instability transition. We undertake a singular perturbation analysis which first proves the validity of the criterion and second yields scaling laws for the frequency, the growth size and the slope at the origin of the nonlinear global modes as functions of the criticality parameter. Those predictions are validated comparing with direct numerical simulation of the Ginzburg–Landau model. Furthermore, the results are in excellent agreement with numerical simulation of the Taylor–Couette problem with throughflow by Büchel *et al.* [27] and of the Rayleigh–Bénard flow with an added Poiseuille flow by Müller *et al.* [28]. The numerical simulations indicate that the NG modes are stable til the parameter value for which the saturated traveling waves, the asymptotic downstream part of the global modes, is itself absolutely unstable to perturbation as determined by the analysis of the dispersion relation of this secondary instability.

1 introduction

A first step toward understanding complex dynamics in spatially extended non equilibrium systems is to find solutions describing a basic pattern which plays a crucial role in the long time behavior. Typical examples of these solutions are the so called "coherent structures" [1] which are localized states or consists of domains with regular patterns separated by interfaces; for example in one-dimensional systems, these interfaces may be fronts, pulses, sources or sinks. These one-dimensional coherent structures have been recognized to play an important role in many problems of physical interest. Experimentally, they have been observed in various systems as binary

fluid mixtures [4], Taylor–Couette flow between rotating cylinders [26,27], chemical reactions [3], flames stabilized on a burner [5]. To describe these structures, Ginzburg–Landau models are extensively used as they are able to exhibit a very large spectrum of dynamical behavior when the parameters are varied. Ginzburg–Landau equations with real coefficients were first derived by Newell & Whitehead [6] and Segel [7] as long wave amplitude equations for Navier–Stokes equations close to an instability threshold. Complex Ginzburg–Landau equations were derived by Stewartson & Stuart [8] who studied Plane Poiseuille flow, among others.

Actually, complex Ginzburg–Landau equations describe the evolution of the amplitudes of unstable modes for any process exhibiting a Hopf bifurcation, for which the continuous band of wave number is destabilized. More generally, complex Ginzburg–Landau equations are relevant to describe spatially-extended systems when oscillations or waves are present [2].

When studying open flows, the fluid particles enter and leave continuously the domain of interest. Since a reference frame is usually singled out (the laboratory frame), upstream conditions and advection velocity have to be taken into account explicitly . For one-dimensional systems, this broken Galilean invariance introduces a new parameter of the system, the advection velocity, and severely limits the multiplicity of solutions "observable" in a semi-infinite domain. Indeed, each propagating coherent structure observed in a doubly open geometry usually possesses a specific velocity and frequency; moreover, it is usually dynamically selected among a continuous family as the long time asymptotic solution of the system. In particular, a front solution invades a region in an unstable or metastable state and leaves a stable pattern behind it, which is the one observable in an experimental setup. In the open flow case, the advection velocity is a fixed parameter and a "coherent structure" propagating at a velocity v may either be advected away if its velocity is not sufficiently high to withstand the advection or move upstream until it feels the boundary and stops at a fixed position. This idea is somewhat schematic because the introduction of a boundary condition at the origin of the domain may destroy the propagating structure existing in an infinite domain. For example the propagating Bekki–Nozaki hole [19] should be able to withstand an advection opposite to its velocity; However, as soon as its velocity is non zero, its amplitude too is never zero. As a result, in a semi infinite domain subject to the homogeneous upstream boundary condition $A(0) = 0$, which represents the ideal case of a medium with zero level noise at the entrance, the propagating Bekki–Nozaki hole should be destroyed when approaching the boundary. In such a *Gedanken* experiment, we expect that in a semi-infinite domain, only coherent structures compatible with the boundary condition (here $A(0) = 0$) can describe the pattern observed in a real experimental setup. Therefore, two conditions are required to stop a coherent structure by a boundary: firstly, the coherent structure should be member of a family indexed by its velocity and secondly, if it is viewed in the reference frame where it is stationary,

the coherent structure should posses a zero amplitude at some location (more generally should be compatible with the boundary conditions). Then, for the problem of pattern selection in a semi-infinite domain with advection U_0 the member of the family which propagates at a velocity exactly opposite to the advection should be a good candidate as steady or time oscillating state of the problem if it also possesses a point of zero amplitude.

When seeking the primary bifurcation of the flow, one usually increases a parameter and determines the threshold of instability when a non trivial state is obtained. The first non trivial state which may be observed should be a coherent structure propagating at a velocity which counterbalances exactly the mean advection.

These coherent structures caught by one boundary give rise to nonlinear global modes since they represent the nonlinear solution of a well posed problem with specific boundary condition, which appears when the trivial solution becomes globally unstable. To be more specific, the term "nonlinear global" (NG) mode refers throughout this paper to a time oscillating solution of a one dimensional system which links a state imposed by the upstream condition ($A(0) = 0$) and a finite amplitude state at infinity represented by a traveling wave. A NG mode oscillates at a characteristic frequency in the whole domain and constitutes a good candidate to describe self sustained oscillators such as wakes [9], Taylor–Couette flow with throughflow [27] or Rayleigh–Bénard problem with an added Poiseuille flow [28].

In the present study, we will illustrate these ideas by describing NG modes for the Ginzburg–Landau equation. These NG modes may be viewed as fronts pushed against one boundary. However, the usual problem of selection of velocity and frequency selection for the fronts is here advantageously replaced by a problem of existence of solutions, since the advection velocity is a fixed parameter and the frequency will naturally come out of the existence criterion. In particular, we seek the threshold of existence of the NG modes, hereafter denoted the NG threshold. Classically, transition to disorder is obtained by creation, competition and annihilation of coherent structures. But in an open system, the advection velocity has a strong regulating effect and above the primary bifurcation, NG modes represents the nonlinear spatial distribution of fluctuations. We address the question of stability of the NG modes and the secondary bifurcation is shown to coincide with the secondary absolute instability threshold. These successive bifurcations constitute a scenario for the transition to disorder in open systems.

The outline of this paper is as follows. In section 2, we present the model and set the existence problem. A phase space analysis allows us to solve this existence problem and in particular, to give a straightforward frequency selection criterion. In section 3, a singular perturbation analysis near the NG threshold allows us to derive scaling laws for the frequency and the spatial growth size of the NG modes. These laws compare satisfactorily with numerical measurements for the Taylor–Couette problem with throughflow by Büchel *et al.* [27] and for the Rayleigh–Bénard flow with an added Poiseuille flow by Müller *et al.* [28]. In section 4, some numerical

simulations are presented and give another validation of the scaling laws in the region of parameter space where no data are available.

These temporal simulations allow us to determine the stability of a NG mode. We establish numerically that the region of parameter space where a NG mode may be observed depends on the stability of the asymptotic traveling wave. A nonlinear global mode will be unstable if the traveling wave is absolutely unstable. In this case, only the structure close to the origin is not affected by instability. This secondary absolute or convective instability is determined by the analysis of the dispersion relation of linear perturbation waves on the nonlinearly saturated basic traveling wave state. We propose this two successive bifurcations as the basis of a scenario for the transition to disorder in open systems.

2 The Ginzburg–Landau model

We consider the complex Ginzburg–Landau equation giving rise to a supercritical bifurcation

$$\frac{\partial A}{\partial t} + U_0 \frac{\partial A}{\partial x} = (1 + ic_1)\frac{\partial^2 A}{\partial x^2} + \mu A - (1 - ic_3)|A|^2 A, \tag{1}$$

where U_0 denotes the advection velocity ($U_0 > 0$ by choice). A rescaling of A, x and t would allow to set to unity either U_0 or the bifurcation parameter μ but we will keep both parameters till section 4 in order to facilitate comparison with experiments. The coefficients c_1 and c_3 are real and c_1 is assumed to be positive since equation (1) possesses the symmetry ($A \to \overline{A}, c_i \to -c_i$), where $\overline{A}$ denotes the complex conjugation.

For the evolution of infinitely small perturbations in an infinite domain, we shall refer to the linear absolute instability theory initially developed in the context of plasma physics [29–31]. The laminar state $A = 0$ is said to be *convectively unstable* if disturbances propagate away from the localized initial source region and *absolutely unstable* if they spread upstream and downstream and contaminate the whole medium. In the present case, the nature of the linear instability of the laminar uniform state $A_0 \equiv 0$ is defined by

$$\mu_A \equiv \frac{U_0^2}{4(1 + c_1^2)} \tag{2}$$

and the flow is linearly convectively unstable [13] for $0 < \mu < \mu_A$ and linearly absolutely unstable for $\mu > \mu_A$. The absolute frequency at threshold $\mu = \mu_A$ is

$$\omega_A \equiv -c_1 \mu_A = -\frac{c_1 U_0^2}{4(1 + c_1^2)}. \tag{3}$$

Of course, the above introduced distinction between absolute and convective instability make sense only when the Galilean invariance is broken and a particular frame is singled out. This will be the case when a boundary condition is introduced at $x = 0$ to mimic the entrance condition of a real open flow. As we are going to show, the μ_A threshold will play a role in the existence of a finite amplitude solution of (1), a nonlinear global mode (NG), able to withstand the wind U_0 at the same time it accommodates the boundary condition. This global mode will involve traveling wave solution and we shall address the problem of existence, multiplicity and nature of the traveling wave solution before going any further.

Throughout the paper, we consider that the parameters U_0, c_1, c_3 are fixed and will describe the solutions in the μ, ω plane, ω being also considered as a parameter until we address the problem of its selection. Because of the symmetry $A \to A\,\mathrm{e}^{i\theta}$, we always describe the solutions of equation (1) up to an arbitrary phase.

2.1 Traveling waves

Equation (1) exhibits [10] a family of saturated traveling waves solutions parametrized by ω:

$$A_2 \equiv a_N\,\mathrm{e}^{iq_N x-\omega t}, \tag{4}$$

a_N, q_N and ω are real and shall respect the equations

$$a_N^2 = \mu - q_N^2, \tag{5}$$
$$\omega = U_0 q_N + c_1 q_N^2 - c_3 a_N^2. \tag{6}$$

Equations (5,6) posses two solutions $q_N^{\pm}$, the dissymmetry between q_N^+ and q_N^- being due to the Doppler effect introduced by the advection which breaks the $x \to -x$ symmetry:

$$q_N^{\pm} = -\frac{U_0}{2(c_1+c_3)} \pm \frac{1}{2(c_1+c_3)}\sqrt{U_0^2 + 4(c_1+c_3)(\omega + c_3\mu)}. \tag{7}$$

But the condition that a_N^2 is positive (5) restricts the domain of existence of each solution.

For fixed U_0, c_1, c_3, the region of existence of the solution (a_N^+, q_N^+) in the plane (μ, ω) is bounded by the heavy continuous lines in Figure 1(a) and corresponds to the white and light gray zone. Solutions (a_N^+, q_N^+) exist as soon as $A = 0$ is linearly unstable (*i.e.* for $\mu > 0$). In Fig 1(b), we represent the region of existence of the

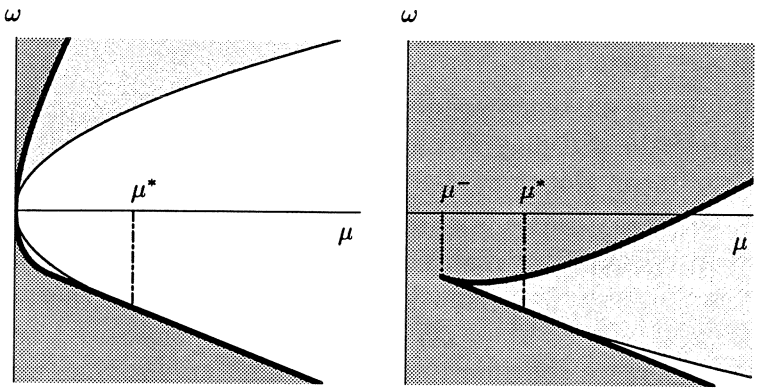

(a) (b)

Fig. 1. Domain of existence of (a) the traveling wave (a_N^+, q_N^+) and (b) the traveling wave (a_N^-, q_N^-). For both plot, the solution is linearly unstable in the light gray region and stable in the white region. In the dark gray region, the solution considered does not exist. Traveling wave (a_N^+, q_N^+) exists and may be stable for $\mu = 0$ whereas (a_N^-, q_N^-) exists for $\mu > \mu^-$ and is stable only for $\mu > \mu^*$ in the white region in (b).

solution (a_N^-, q_N^-) in the same manner. (a_N^-, q_N^-) only exists for $\mu > \mu^-$, with

$$\mu^- \equiv \frac{U_0^2}{4(c_1 + c_3)^2}. \tag{8}$$

It should be emphasized that for $0 < \mu < \mu^-$, the system (5,6) possesses a single solution (a_N^+, q_N^+).

A linear stability analysis of the traveling waves (4) has been given by Matkowski and Volpert [10] for long waves and finite wavelength perturbations. Their results may be recalled using q_N (standing for q_N^+ or q_N^-) as a parameter for the family of solutions that exist at (μ, c_1, c_3) given. They have found that in the Benjamin–Feir stable domain $1 - c_1 c_3 > 0$, the traveling waves of type (4) are linearly stable if their wavenumber satisfies $q_N^2 < {q_E}^2$, (denoted below as the Eckhaus stable band). The neutral Eckhaus wavenumber $q_E(\mu, c_1, c_3)$ is shown in [10] to be a different function of parameters when the loss of stability is due to long waves perturbations, in which case the neutral Eckhaus wavenumber is given by

$$q_E^2 = \mu \frac{1 - c_1 c_3}{3 + 2c_3^2 - c_1 c_3}, \tag{9}$$

or when it is due to finite wavelength perturbations[1]. These functions explicitly derived in [10] allow us to plot for each set of coefficients (U_0, c_1, c_3) the range of

[1] in which case the reader is referred to [10] for an explicit expression of the neutral Eckhaus wavenumber and of the boundaries of the region in the plane (c_1, c_3) to which it pertains.

frequencies as a function of μ in which the traveling waves are linearly stable (white regions in Figures 1(a) and 1(b)). The solution with the plus sign (a_N^+, q_N^+) is linearly stable in a parabolic region starting at $\mu = 0$ (Figure 1(a)) whereas the region of linear stability of (a_N^-, q_N^-) is only the sharp white wedge in Figure 1(b) for which $\mu > \mu^*$ where $\mu^* \equiv \mu^- {q_E^*}^2$, and $q_E^*(c_1, c_3) = q_E(\mu, c_1, c_3)/\sqrt{\mu}$.

2.2 Nonlinear global modes

In a semi-infinite domain, NG modes are defined [20] as time oscillating solutions of equation (1) with the boundary condition at the origin $A(0) = 0$ which breaks the Galilean invariance.

$$-i\omega A = (1 + ic_1)\frac{d^2A}{dx^2} - U_0\frac{dA}{dx} + \mu A - (1 - ic_3)|A|^2 A, \tag{10}$$

At infinity, the NG mode is asymptotic to a traveling wave of the type (4). As already stated for the great majority of cases, the values of μ, c_1, c_3 will be such that a single traveling wave will exist and in the reversed eventuality, only q_N^+ will be considered. For $-c_1 - \sqrt{1 + c_1^2} < c_3 < -c_1 + \sqrt{1 + c_1^2}$, we obtain $\mu_A < \mu^-$ and at the absolute instability threshold $\mu = \mu_A$, only the solution q_N^+ exists. By contrast, for $c_3 < -c_1 - \sqrt{1 + c_1^2}$, or $c_3 > -c_1 + \sqrt{1 + c_1^2}$, both solutions q_N^+ and q_N^- exist above μ_A, but the solution q_N^+ is shown in [12] to be the only physical solution as it corresponds to a positive "group velocity" $d\omega/dq_N$, allowing "information" to be propagated in the downstream direction whereas the q_N^- solution corresponds to a negative group velocity and propagates the "information" upstream. Therefore, only (a_N^+, q_N^+) will be considered below and the plus sign is dropped for clarity.

We also assume that the asymptotic traveling wave of a NG mode when $x \to +\infty$ is linearly stable (c_1 and c_3 belongs to the Benjamin–Feir stable region $1 - c_1 c_3 > 0$ and q_N to the Eckhaus stable band, *i.e.* μ, ω belong to the white region of Fig 1(a)). This condition is in fact a sufficient condition for the stability of NG modes but not a necessary condition and a weaker condition will be given in section 4 where a detailed analysis of the NG mode stability is presented.

To absorb the phase invariance ($A \to A\,\mathrm{e}^{i\theta}$), a NG mode may be written in the form

$$A(x,t) = a(x)\,\mathrm{e}^{i\int^x q(x')dx'}\,\mathrm{e}^{-i\omega t}, \tag{11}$$

with $a(x), q(x), \omega$ real. In [11,12,17,18], this transformation has been used for the study of front propagation in infinite domains and associated with the singular change of variable $k = \dot{a}/a$, called the σ-process by Arnol'd [14].

Under the change of variable (11), the initially second-order equation (1) in the complex variable A becomes first-order and is reduced to the dynamical system (12,13,14) in the 3 variables a, q, $k = \dot{a}/a$ (the dot denotes differentiation with respect to x):

$$\dot{a} = ka \tag{12}$$

$$\dot{q} = -c_0(\omega - c_1\mu) + c_0U_0(q - c_1k) - 2kq - I_3a^2 \tag{13}$$

$$\dot{k} = -c_0(c_1\omega + \mu) + c_0U_0(c_1q + k) + q^2 - k^2 - R_3a^2 \tag{14}$$

where $c_0 = 1/(1 + c_1^2)$, $R_3 = c_0(1 - c_1c_3)$ and $I_3 = c_0(c_3 + c_1)$.

This dynamical system is suited to study front solutions which do not become zero at some finite x-location. In the following, we describe the trajectories in the phase space (a, q, k), but since they have already been extensively described in previous studies concerning front propagation in infinite domains [11,12,17,18], we restrict ourselves to the particular features relevant for the understanding of the NG modes existence. If front solution are correctly described in the phase space (a, q, k), it is not the case for NG modes which correspond to singular trajectories in this space. A NG mode with $a(0) = 0$ and a non zero slope at the origin is necessarily represented by a singular trajectory in the phase space (a, q, k) as k becomes infinite when $a = 0$ and $\dot{a} \neq 0$ at some location. Below, we are led to use alternatively (a, q, k) but also a slightly different phase space with the variable a, q and $u = \dot{a}$ to represent NG modes as regular trajectories.

For the analysis of the dynamical system (12, 13, 14), the frequency ω is considered as a parameter, its selection being addressed later.

2.2.1 The fixed points

This dynamical system possesses three fixed points:

- $A_2 \equiv (a_N, q_N, 0)$ represents the previously introduced traveling wave (with the plus sign dropped); it stands depending on the context for the traveling wave of type (4) and for the fixed point $(a_N, q_N, 0)$ in the phase space as they are different representations of the homogeneous solution. In the phase space, A_2 is a saddle and possesses always a unique stable eigendirection, because it has been shown in [12] that the condition of positive "group velocity" for the traveling wave $A_2(\omega)$ (4) implies that the stable manifold of the fixed point $A_2(\omega)$ is one-dimensional.
- $A_0^+ \equiv (0, q_0 + \beta, k_0 + \alpha)$ where

$$\alpha = \sqrt{(|\kappa + i\sigma| - \kappa)/2}, \qquad \beta = -\mathrm{sgn}(\sigma)\sqrt{(|\kappa + i\sigma| + \kappa)/2} \tag{15}$$

and $q_0 = -c_0c_1U_0/2$, $k_0 = c_0U_0/2$;

$$\kappa = c_0(\mu + c_1\omega) - (1 - c_1^2)c_0^2U_0^2/4 \tag{16}$$

$$\sigma = c_0(\omega - c_1\mu) + c_1 c_0^2 U_0^2/2 \tag{17}$$

The stability of A_0^+ is determined from the eigenvalues of the system (12,13,14) linearized around A_0^+ which are $2(k_0+\alpha)$ in the a-direction and $-2(\alpha \pm i\beta)$ in the (q,k) direction, meaning that complex conjugate eigenvalues are associated with the eigenplane $a = 0$. Hence, A_0^+ is a stable spiral in the plane $a = 0$, whereas it is unstable in the a-direction.

- $A_0^- \equiv (0, q_0-\beta, k_0-\alpha)$ Similarly, A_0^- possesses the eigenvalues $2(k_0-\alpha)$ associated with the a-direction and $2(\alpha \pm i\beta)$ associated with the eigenplane $a = 0$. A_0^- is an unstable spiral in the plane $a = 0$, and the a-direction is unstable when A_0^- is in the $k > 0$ domain of the (q,k) plane or stable when A_0^- is in the $k < 0$ domain.

If we had not applied the change of variable (11), the laminar state $A = 0$ would have been represented by a single fixed point coinciding with the origin of the phase space $A = 0, \dot{A} = 0$. When using the phase space (a,q,k), this point $A = 0, \dot{A} = 0$ is split into two fixed points A_0^+ and A_0^-. Solutions increasing from (or decaying to) the laminar state $A = 0$ at minus (or plus) infinity must correspond to the orbits of the one-dimensional unstable or stable manifold of A_0^+ or A_0^-, which is not embedded in the subspace $a = 0$. A_0^+ and A_0^- may be physically interpreted only if the laminar state $A = 0$ is convectively unstable: A_0^+ represents the way to raise up from zero at $x \to -\infty$ and A_0^- represents the way to asymptote zero when $x \to +\infty$. The point A_0^- is associated with the complex quantity $q_0^- - ik_0^-$ which corresponds to the spatial branches propagating information downstream (usually denoted $k^+(\omega)$) [29–31]. Respectively, A_0^+ is associated with the upstream propagation of information. If the laminar state $A = 0$ becomes absolutely unstable, it is no longer possible to associate the different spatial branches with the propagation of information.

2.2.2 The plane $a = 0$

At this stage, it is necessary to describe in details the plane $a = 0$ which has been shown by Landman [11] to be an invariant subspace of the system (12–14) in which a set of bounded heteroclinic orbits linking A_0^- to A_0^+ exist. One of these bounded orbits is displayed in light line in each Figure 2(a) and 2(b). But an infinity of similar orbits exist between A_0^- and A_0^+, each of them crossing the $q = q_0$-axis at a different value of k. None of the trajectories in the plane $a = 0$ are physical but serve as a footprint of the trajectories slightly of the plane $a = 0$. Any point of the plane $a = 0$ with a finite value of k belongs to one of these trajectories which start from A_0^- and ends at A_0^+. We show below that only the unbounded orbits (called the separatrices) in the plane $a = 0$ (heavy lines in Figures 2) are relevant to describe NG modes as for a NG mode, $a = 0$ but $\dot{a} \neq 0$ at the origin; this implies $k \to \infty$. These separatrices on which k is singular when $x = 0$ are given by:

$$q = q_0 + \frac{\beta \sinh(2\alpha x) - \alpha \sin(2\beta x)}{\cosh(2\alpha x) - \cos(2\beta x)} \tag{18}$$

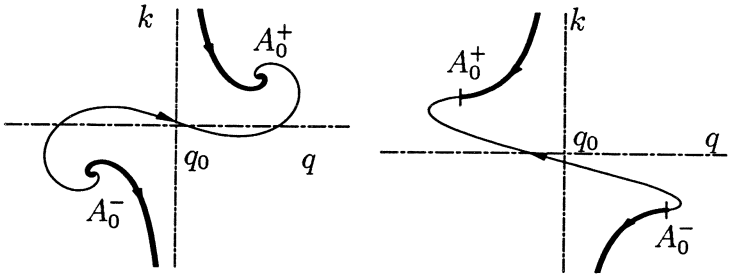

(a) $\sigma < 0$ (b) $\sigma > 0$

Fig. 2. Plane $a = 0$ of the phase space (a, q, k). One bounded heteroclinic orbit (light line) between A_0^- and A_0^+ is represented among the infinity which exist and fill the whole plane. The single unbounded trajectories (heavy lines) arriving to A_0^+ or starting from A_0^- are called the separatrices (18,19) and are asymptotic to $q = q_0$ at $k \to \infty$.

$$k = k_0 + \frac{\alpha \sinh(2\alpha\, x) + \beta \sin(2\beta\, x)}{\cosh(2\alpha\, x) - \cos(2\beta\, x)} \tag{19}$$

The singularity at $x = 0$ is removed when considering the variable u such that

$$u = \dot{a} = ka \tag{20}$$

Indeed, when equation (19) is introduced into equation (20) and after an integration of (20), we obtain

$$a = \frac{u_0}{\sqrt{2|\zeta|}} \exp\left(\frac{c_0 U_0}{2} x\right) (\cosh(2\alpha x) - \cos(2\beta x))^{\frac{1}{2}} \tag{21}$$

where u_0 is an integration constant. It may be seen that $u \to u_0$ when $x \to 0$. The separatrices (18,19) associated with equation (21) constitute a linear solution of the system (12–14) which departs from the plane $a = 0$ with a slope $u = \dot{a}$ different from zero;

2.2.3 Front solutions

In the phase space (a, q, k), a front is represented by an heteroclinic trajectory linking A_0^- to A_2 (or exceptionally A_0^+ to A_2). Such fronts exist when the stable manifold of $A_2(\omega)$ intersects the unstable manifold of $A_0^-(\omega)$ which is not embedded in the plane $a = 0$. The stable manifold of $A_2(\omega)$ departs from A_0^- for a continuous set of frequencies and this situation arises for a continuous set of velocities U_0. Therefore, a double family of fronts exists [12], parametrized by the frequency and the velocity,(which in the case of front propagation in an infinite domain represents the velocity of the front). Each bounded trajectory of the plane $a = 0$ departing from A_0^- is associated with a front trajectory since both orbits posses the same behavior near

A_0^-. Among the double family of fronts, a particular front is dynamically selected for fixed μ, c_1, c_3 and will represent the long time asymptotic of the system. For equation (1), the selected front has been shown to correspond to the Kolmogorov front [24] and its frequency is the absolute frequency ω_A (equation (3)); its velocity is linked to μ and c_1 by the same relation (equation (2)) which links U_0 and these parameters. In the phase space, the Kolmogorov fronts corresponds to the unique values of parameters defining the absolute threshold for which $A_0^+ = A_0^- = A_0$.

2.2.4 NG modes

In the phase space (a, q, k), a NG mode is represented by a trajectory linking a point of the plane $a = 0$ different from $A_0^\pm$ to A_2. In other words, a NG mode exists when the stable manifold of A_2 intersects the plane $a = 0$ at a point which is not a fixed point. Introduction of this condition in equations (12–14) leads necessarily to $q = q_0$ at the intersection point if it exists. The property $u = \dot{a}$ different from zero at the origin characterizes the existence of a NG mode, which is represented in the new (a, q, u) space by a regular trajectory linking a point of the axis $(a = 0, q = q_0)$ to A_2, instead of a singular trajectory departing from an infinite k on the axis $(a = 0, q = q_0)$ in the (a, q, k) space. To see if the stable manifold of a A_2 reaches such a point, it is convenient to use the phase space (a, q, u) and look for a crossing of the plane $a = 0$ by the stable manifold of A_2. Keeping the same notation for the fixed points under the change of variable (20), from the equations, it is obvious to see that crossing may only occur on the axis $(a = 0, q = q_0)$. Up to now, we have considered ω as a fixed parameter, and as the stable manifold of $A_2(\omega)$ is one-dimensional, it generically does not cross the axis $(a = 0, q = q_0)$ except eventually for discrete values of ω. Therefore, the existence of of a global mode is determined in the (a, q, u) phase space by the seek of an intersection between the axis $(a = 0, q = q_0)$ and the 2-dimensional surface formed by the union of each stable manifold of each $A_2(\omega)$ generated by varying ω. The intersection point belongs to a specific stable manifold of a particular $A_2(\omega)$ which defines the selected frequency.

Let us define $\mu_G(U_0, c_1, c_3)$ the threshold of emergence of a NG mode (*i.e.* the smallest value of μ for which the set of stable manifold of $A_2(\omega)$ intersects the axis $(a = 0, q = q_0)$. This NG instability threshold will be shown first numerically and then analytically to coincide with the absolute threshold μ_A (equation (2)), $\mu_A = c_0 U_0^2/4$, the frequency of the NG mode at the threshold being $\omega = \omega_A$. We first describe our observations of the numerically generated phase portraits.

2.3 Phase portraits

For fixed parameters U_0, c_1, c_3 and μ, when varying ω in the band of allowed frequencies (white domain in Figure 1(a)), the fixed point $A_2(\omega)$ describes an arc of a circle in the plane $u = 0$ of the phase space to which the union of the stable mani-

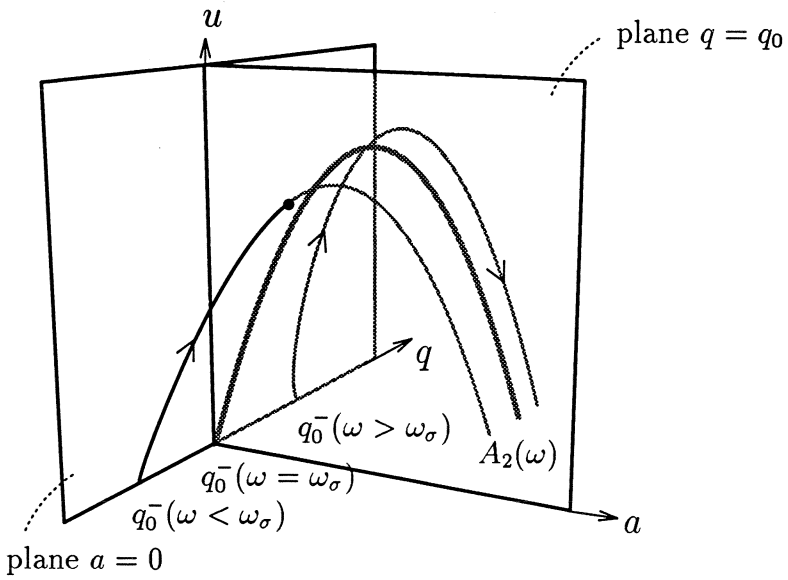

Fig. 3. Stable manifolds of $A_2(\omega)$ in the space (a, q, u) for $\mu = 0.15$ such that $\mu < \mu_A(U_0, c_1)$ with $U_0 = 0.9$, $c_1 = 0.5$, $c_3 = 0.2$. The axis $(q = q_0, a = 0)$ may be reached only asymptotically for a specific frequency corresponding to the value ω_σ such that $q_0^- = q_0$. The trajectory is then a heteroclinic orbit between $A_0^-(\omega_\sigma)$ and $A_2(\omega_\sigma)$ which does not represent a NG mode as $u = 0$ at the virtual intersection when $x = -\infty$. For any other frequency, the stable manifold of $A_2(\omega)$ emanates from $A_0^-(\omega)$ and either crosses the plane $q = q_0$ at a finite a when $\omega < \omega_\sigma$ (black point at the crossing) or remains embedded within one side of the plane $q = q_0$ when $\omega > \omega_\sigma$.

folds of $A_2(\omega)$ parametrized by ω is kond. But in the (a, q, u) space, the dynamical system (12–14) is transformed into

$$\dot{a} = u \tag{22}$$

$$a\dot{q} = -2uq - c_0(\omega - U_0 q)a - c_0 c_1 (\mu a - U_0 u) - I_3 a^3 \tag{23}$$

$$\dot{u} = aq^2 - c_0 (\mu a - U_0 u) + c_0 c_1 (\omega - U_0 q)\, a + R_3 a^3 \tag{24}$$

which is singular when $a \to 0$ although a NG mode is represented by a regular trajectory. Therefore, we are led to compute the trajectories in the four-dimensional phase space $(\Re(A), \Im(A), \Re(\dot{A}), \Im(\dot{A}))$ different from the phase space (a, q, u) in which they will be represented. The stable manifolds of $A_2(\omega)$ are computed for each value of ω by a backward numerical integration of (10) using variable step Runge–Kutta x-integration. When a NG mode exists, it should cross the axis $(a = 0, q = q_0)$ at a finite value of u representing its slope at the origin and the trajectory representing the NG mode in the (a, q, u) space turns out to be regular.

For $\mu < \mu_A$, when ω varies in the white stable band of Fig 1(a), no NG mode exists

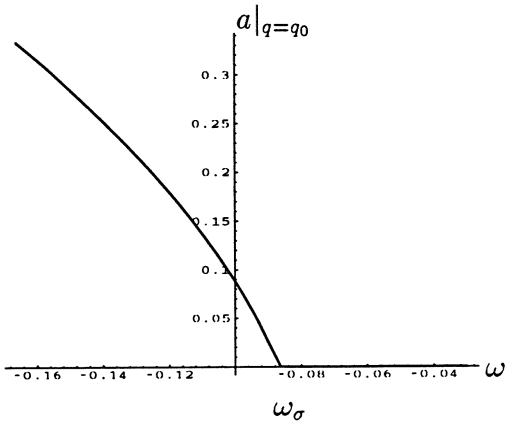

Fig. 4. Amplitude a of the stable manifold of $A_2(\omega)$ at the crossing of the plane $q = q_0$ as a function of ω for the same parameters as Fig. 3 ($c_1 = 0.5$, $c_3 = 0.2$, $U_0 = 0.9$, $\mu = 0.15$, for these values, the threshold is $\mu_A = 0.162$). No cusp is obtained showing that no GM exists for this value of the bifurcation parameter.

as the stable manifold of $A_2(\omega)$ never crosses the axis $(a = 0, q = q_0)$. Figure 3 shows three stable manifolds of $A_2(\omega)$ for three different values of the frequency. The values of the frequencies are chosen different enough such that the three entire manifolds are clearly distinct. To interpret the observations, let us define ω_σ the threshold value such that $\sigma = 0$ (equation (17))

$$\omega_\sigma \equiv c_1\mu - c_1c_0U_0^2/2. \tag{25}$$

For $\omega = \omega_\sigma$ (drawn in heavy line in Figure 3), we obtain (only when $\mu < \mu_A$) $q_0^-(\omega_\sigma) = q_0$. Therefore the heteroclinic orbit linking $A_0^-(\omega_\sigma)$ and $A_2(\omega_\sigma)$ does not cross the axis $(a = 0, q = q_0)$ but asymptotes the point A_0^- on this axis. Therefore, this orbit does not represent a NG mode as the crossing occurs at $u = 0$ when $x = -\infty$. When $\omega < \omega_\sigma$, the stable manifold of $A_2(\omega_\sigma^-)$ crosses the plane $q = q_0$ as $A_2(\omega)$ and $A_0^-(\omega)$ are on each side of the plane $q = q_0$ and the crossing amplitude is not zero

When $\omega > \omega_\sigma$, the stable manifold of $A_2(\omega)$ remains in the half space $q < q_0$ and does not cross the plane $q = q_0$. The fact that no NG mode is obtained for $\mu < \mu_A$ is determined by plotting in Figure 4 the amplitude a of the stable manifold of $A_2(\omega)$ when it crosses the plane $q = q_0$, as a function of the frequency. For $\omega < \omega_\sigma$, a nonzero value of a is found at the intersection. No cusp is obtained at $\omega = \omega_\sigma$ and for $\omega > \omega_\sigma$, $a|_{q=q_0}$ does not exist.

For $\mu > \mu_A$, the two-dimensional set of stable manifolds of $A_2(\omega)$ has been observed to intersect the axis $(a = 0, q = q_0)$ for a particular value of ω determining the selected frequency ω_G of a NG mode. Figure 5 presents the stable manifolds of three different $A_2(\omega)$ for three values of the frequency ($\omega < \omega_G$, $\omega = \omega_G$ and $\omega > \omega_G$). Since we have chosen three frequencies close to each other in order to show the differences in the three trajectories, the three distinct fixed points $A_2(\omega)$ appear so

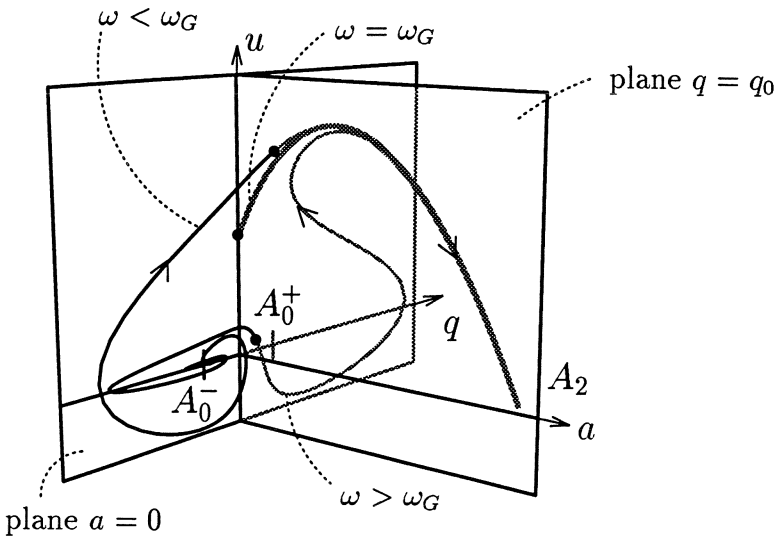

Fig. 5. In the space (a, q, u), three typical stable manifolds of three $A_2(\omega)$ for three different frequencies ω ($\omega < \omega_G$, $\omega = \omega_G$ (heavy line), $\omega > \omega_G$), above the NG threshold *i.e.* when $\mu > \mu_A(U_0, c_1)$ ($\mu = 0.6$, $U_0 = 0.9$, $c_1 = 0.5$, $c_3 = 0.2$). The crossing of the axis $(q = q_0, a = 0)$ occurs for a single value ω_G of the frequency ω. The black points denote the intersection with the plane $q = q_0$ used to construct Fig 6.

close to each other that they are presented by a single symbol $A_2(\omega)$ in Figure 5. For $\omega > \omega_G$, the stable manifold of $A_2(\omega)$ avoid the axis $(a = 0, q = q_0)$ and makes an about turn in the half space $q > q_0$ (shaded part in Figure 5) before crossing the plane $q = q_0$ at a finite value of a and then it reaches A_0^- spiralling in the half space $q < q_0$. For $\omega < \omega_G$, it crosses directly the plane $q = q_0$ at a finite value of a and goes directly to A_0^- in spiral. When ω equals exactly ω_G, the stable manifold of $A_2(\omega_G)$ crosses the $q = q_0$ plane exactly on the axis $(a = 0, q = q_0)$ at a finite value of u. It is quite remarkable that this singular trajectory insures a smooth transition between the two configurations described above.

To find the precise value ω_G for which the intersection with the axis $(a = 0, q = q_0)$ occurs, and to obtain a criterion for the existence of a NG mode, we have plotted systematically as in Figure 6 the amplitude a of the stable manifold of $A_2(\omega)$ when it crosses the plane $q = q_0$, as a function of the frequency ω. Around a single value $\omega_G(\mu, U_0, c_1, c_3)$, this amplitude can approach zero as close as wished depending only on the resolution we use to span the ω axis, as indicated by the cusp in Figure 6. We have verified that at the value ω_G given by the criterion sketched in Figure 6, the slope of the solution u at the origin is non zero.

The analysis of the phase portraits for all $\mu > \mu_A$ and the frequency selection criterion sketched in Figure 6 allow to find numerically for each set of parameters

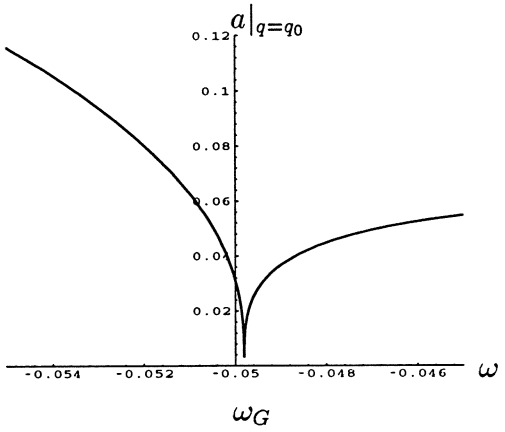

Fig. 6. Amplitude $a|_{q=q_0}$ of the stable manifold of $A_2(\omega)$ at the crossing of the plane $q = q_0$ as a function of ω for the parameters $c_1 = 0.5$, $c_3 = 0.2$, $U_0 = 0.9$, $\mu = 0.6$ (same as Fig. 5). For these values, a nonlinear global mode exists as μ is larger than the NG instability threshold $\mu_A = 0.162$. The cusp in the curve indicate the existence of this NG mode with $a = 0$.

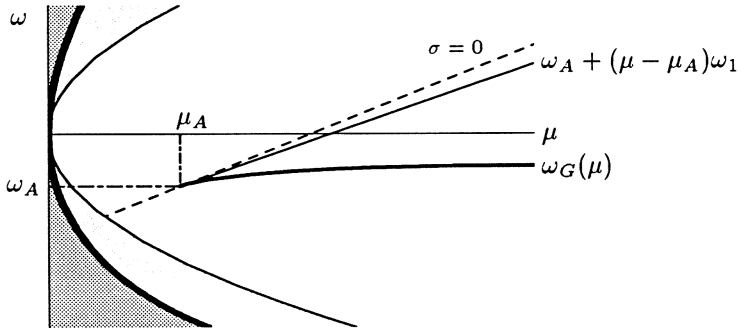

Fig. 7. Selected frequency of the NG modes as a function of μ obtained numerically by the method explained in Fig. 4 (heavy continuous line). Zoom of the zone close to 0 of Figure 1(a), see Fig. 1 caption for the explanation of the gray and white regions. NG modes are found to exist only for $\mu > \mu_A$ and their frequency equals $\omega_G(\mu)$, with $\omega_G(\mu_A) = \omega_A$. Parameters are $c_1 = 0.5$, $c_3 = 0.2$, $U_0 = 0.9$ (same as Figs. 5 and 6. We predict that $\omega_G(\mu_A) = \omega_A$ and the slope of $\omega_G(\mu)$ (light line) by a singular perturbation analysis around the threshold. The line $\sigma = 0$ is also plotted as a dotted line.

U_0, c_1, c_3 the curve ω_G as a function of μ represented in Figure 7. This selected frequency $\omega_G(\mu)$ shown in heavy continuous line in Figure 7 starts from ω_A at the threshold μ_A; The leading order and the next order of the frequency, *i.e.* the slope at μ_A (light continuous line) is the prediction of the perturbation analysis presented in section 3.

Numerical resolution of trajectory in the phase space indicates that the nonlinear global threshold coincides with the threshold of absolute instability μ_A. This observation will be proven by the perturbation analysis presented in the next section.

3 Proof of the existence of a global mode for $\mu > \mu_A$ and scaling laws

We propose here to turn the numerical and graphical observations for the occurrence of a NG mode into proof of the existence of a global mode for $\mu > \mu_A$, by performing a singular perturbation analysis near the threshold of global instability. The analysis predicts for fixed parameters, U_0, c_1, c_3 the leading and first order of the frequency $\omega_G(\mu)$ (see Figure 7) at the threshold and the growth size[2] of the NG modes as a function of the departure from the NG instability threshold. However, since the first order of the frequency will be given by the numerical estimate of an analytical matching condition (equation (44) below), a case by case calculation has to be done for each set of parameters to prove the existence of a NG mode for $\mu > \mu_A$.

In the phase space[3] (a, q, u), we are looking for the stable manifold of $A_2(\omega)$ which at $\omega, \mu, c_1, c_3, U_0$ fixed may be parametrized by a. The trajectory $q_f(a), u_f(a)$ at $\mu = \mu_A$ and $\omega = \omega_A$ represents the heteroclinic orbit linking $A_0^- = A_0 = (0, q_0, 0)$ to $A_2(\omega_A)$. It is similar to the orbit corresponding to ω_σ which has been geometrically interpreted on the phase portraits presented in Figure 3 in section 2. The parametric representation $q_f(a)$ and $u_f(a)$ are expanded in powers of a with general terms [4] $\rho_j(a_N - a)^j$ and $\nu_j(a_N - a)^j$. When setting the bifurcation parameter value to $\mu = \mu_A + \epsilon$, the stable manifold of $A_2(\omega)$ is considered as a perturbation of the solution $q_f(a), u_f(a)$ and the perturbation is also taken in the form of series expansions with general terms $\epsilon\eta_j(\omega)(a_N - a)^j$ and $\epsilon\lambda_j(\omega)(a_N - a)^j$. This perturbed solution satisfies the boundary conditions at infinity, *i.e.* it asymptotes $A_2(\omega)$ along its unique stable eigendirection. It constitutes the outer solution of the problem which should be matched with the proper inner solution valid around $a = 0$.

In the singular limit $\epsilon \ll 1$ an inner region of size $\theta(\epsilon)$, $\theta(\epsilon)$ being a jauge determined by the matching, has to be introduced in the neighborhood of the origin in order to take into account the boundary condition $a(0) = 0$. An inner solution is represented analytically as the linear solution (18,19,21) of system (12–14) in the vicinity of $a = 0$.

Application of the method of matched asymptotic expansions [15] between the inner and the outer solution should give rise to a NG mode determined by the intersection of the perturbed solution and of the axis $(a = 0, q = q_0)$. This mode corresponds to a single frequency of the form $\omega_A + \epsilon\omega_1$. The matching leads to the determination of the slope v_0 at the origin and growth size of the NG mode and of the departure $\epsilon\omega_1$ of the NG mode frequency from ω_A.

---

[2] defined as the distance at which the amplitude reaches 99 % of its maximum value.

[3] Reason for considering this phase space and not (a, q, k) as already discussed is that we wish to obtain regular trajectories near $a = 0$ for the global modes.

[4] For simplicity of notations, unless otherwise stated, a_N and q_N denotes in this section $a_N(\omega_A)$ and $q_N(\omega_A)$, evaluated at $\mu = \mu_A$.

We now proceed to a detailed analysis of the outer and inner solutions.

3.1 Outer solution

By setting the bifurcation parameter value to $\mu = \mu_A + \epsilon$ and the frequency to $\omega_A + \epsilon\omega_1$ with $\epsilon \ll 1$, and ω_1 to be determined, the outer solution of equations (22,23,24), representing the stable manifold of $A_2(\omega)$ just above the threshold and away from the origin, is sought in the form of perturbed series:

$$u_o(a) = \frac{da}{dx} = \sum_{j=0}^{+\infty} (\nu_j + \epsilon\lambda_j)(a_N - a)^j \ , \tag{26}$$

$$q_o(a) = \sum_{j=0}^{+\infty} (\rho_j + \epsilon\eta_j)(a_N - a)^j \ . \tag{27}$$

At the threshold ($\epsilon = 0$), the coefficients ν_j, ρ_j are those of the heteroclinic orbit $q_f(a), u_f(a)$ corresponding to the Kolmogorov front solution [24] and are computed recursively and numerically The coefficients λ_j, η_j are assumed to be linear functions of ω_1 *i.e.* $\lambda_j = \lambda_j^0 + \omega_1\lambda_j^1$, $\eta_j = \eta_j^0 + \omega_1\eta_j^1$ and represent the departure of the NG mode from the front solution. They are recursively and numerically computed in the same manner as ν_j and ρ_j by requiring that (26) and (27) satisfy equations (22,23,24) at each order in ϵ and j, and for each value of ω_1. To start the recurrence, we need to use the boundary condition at $x \to +\infty$ which reads:

$$u_o\left(a_N(\mu_A + \epsilon, \omega_A + \epsilon\omega_1)\right) = 0, \tag{28}$$

$$q_o\left(a_N(\mu_A + \epsilon, \omega_A + \epsilon\omega_1)\right) = q_N(\mu_A + \epsilon, \omega_A + \epsilon\omega_1). \tag{29}$$

For the outer solution, the boundary condition at $+\infty$ allows to obtain the leading order coefficients for u_0 and q_0 series: $\nu_0 = 0$, $\rho_0 = q_N(\omega_A)$, and at first order the equations (also given by equations (23,24) at first order):

$$2(q_N - q_0)\nu_1 - c_0U_0\rho_1 - \nu_1\rho_1 - 2I_3a_N^2 = 0 \ , \tag{30}$$

$$c_0U_0\nu_1 + 2(q_N - q_0)\rho_1 - \nu_1^2 + 2R_3a_N^2 = 0 \ . \tag{31}$$

Equations (30,31) give us ν_1 and ρ_1 by elimination of ρ_1:

$$\nu_1^3 + 4k_0\nu_1^2 + (4(q_N - q_0)^2 + 4k_0^2 - 2R_3a_N^2)\nu_1 - 4(q_N - q_0)I_3a_N^2 - 4R_3a_N^2k_0 = 0. \tag{32}$$

The positive root of equation (32) determines ν_1 which is unique as required by the condition that the front solution is unique. Once ν_1 and ρ_1 are determined, λ_0 and η_0 are computed by equations

$$(2(q_N - q_0) - \rho_1)\,\lambda_0 - c_0 U_0 \eta_0 = c_0(c_1 - \omega_1) \tag{33}$$
$$c_0 U_0 \lambda_0 + (2(q_N - q_0) - \nu_1)\,\lambda_0 = c_0(1 + c_1\omega_1) \tag{34}$$

which may be split into two parts according to the linear dependence of λ_0 and η_0 as functions of ω_1. Then all coefficients (ν_j, ρ_j), (λ_j, η_j) are computed recursively, each couple being solution of a linear system of equations for which the r.h.s. depends only on coefficients with smaller index. Once all coefficients have been computed, we obtain the asymptotic behavior of the outer solution close to the origin where the inner solution prevails

$$u_o(a) \overset{a\to 0}{\simeq} \sum_{j=0}^{+\infty} \nu_j a_N^j - a \sum_{j=0}^{+\infty} j\nu_j a_N^{j-1} + \epsilon \sum_{j=0}^{+\infty} \lambda_j a_N^j \tag{35}$$
$$q_o(a) \overset{a\to 0}{\simeq} \sum_{j=0}^{+\infty} \rho_j a_N^j - a \sum_{j=0}^{+\infty} j\rho_j a_N^{j-1} + \epsilon \sum_{j=0}^{+\infty} \eta_j a_N^j \tag{36}$$

Obviously $u_o(a)$ and $q_o(a)$ given by equations (35,36) cannot satisfy the boundary condition at $a = 0$.

3.2 Inner solution

To satisfy the boundary condition at the origin, we introduce an inner layer near $a = 0$ where the amplitude $a(x)$ of the inner solution remains small. Using the variable ξ such that $a = |A| = \theta(\epsilon)\xi$, where $\theta(\epsilon)$ denotes the size in amplitude of the inner layer, we linearize the dynamical system (22–24) around $a = 0$ and seek a solution of the linearized system satisfying the boundary condition $\xi(0) = 0$. All the bounded trajectories already described in section 2 which exist in the plane $a = 0$ and link A_0^- to A_0^+ [11] cannot be considered as valid inner solutions to find a NG mode since they do not allow to depart from the plane $a = 0$ with a finite slope at the origin. By contrast, the separatrices (18,19) which possess a singularity (infinite k when $x = 0$) are the only solutions departing from the plane $a = 0$ with a finite slope $u = \dot{a}$ at the origin and therefore will constitute the inner solution of the problem. Solutions (18,19) and (21) are rewritten using $\mu = \mu_A + \epsilon$ and $\omega = \omega_A + \epsilon$, after rescaling the previously introduced coefficients α and β representing the departures of the vawenumber q from q_0 and spatial growth rate k from k_0 at A_0^-: $\alpha = \alpha_1\epsilon^{1/2}$ and $\beta = \beta_1\epsilon^{1/2}$;

$$\xi = \frac{v_0}{\sqrt{2|\zeta_1|}}\, e^{k_0 x} \left(\cosh(2\alpha_1\epsilon^{1/2}x) - \cos(2\beta_1\epsilon^{1/2}x)\right)^{\frac{1}{2}} \tag{37}$$

$$q_i = q_0 + \epsilon^{1/2} \frac{\beta_1 \sinh(2\alpha_1\epsilon^{1/2}\,x) - \alpha_1 \sin(2\beta_1\epsilon^{1/2}\,x)}{\cosh(2\alpha_1\epsilon^{1/2}\,x) - \cos(2\beta_1\epsilon^{1/2}\,x)} \tag{38}$$

$$k_i = k_0 + \epsilon^{1/2} \frac{\alpha_1 \sinh(2\alpha_1 \epsilon^{1/2} x) + \beta_1 \sin(2\beta_1 \epsilon^{1/2} x)}{\cosh(2\alpha_1 \epsilon^{1/2} x) - \cos(2\beta_1 \epsilon^{1/2} x)} \tag{39}$$

with $|\zeta_1| = \sqrt{c_0(1+\omega_1^2)}$, $\alpha_1 = \sqrt{(|\zeta_1| - \kappa_1)/2}$, $\beta_1 = \sqrt{(|\zeta_1| + \kappa_1)/2}$, and $\kappa_1 = c_0(1 + c_1\omega_1)$. The $\epsilon^{1/2}$ rescaling comes from the beating of the two waves associated with A_0^+ and A_0^-. Solution (37) indeed satisfies the boundary condition $\xi(0) = 0$. When $x \to +\infty$, we seek the asymptotic behavior of the inner solution $\xi(x)$, $k_i + iq_i$ in order to do the matching with the outer solutions (35,36). The maximum of the function $\xi(x)$ may be obtained for a value close to $x = \pi/\beta_1\sqrt{\epsilon}$ and the matching must be done close to this value. Therefore, the asymptotic behavior of the inner solution reads when $x \sim \pi/\beta_1\sqrt{\epsilon}$

$$\xi(x) \simeq \frac{v_0 \epsilon^{-1/2}}{\sqrt{2|\zeta_1|}} e^{\frac{k_0 \pi}{\beta_1 \epsilon^{1/2}}} \sqrt{\cosh(2\alpha_1 \pi/\beta_1) - 1} \tag{40a}$$

$$k_i + iq_i \simeq k_0 + iq_0 + \epsilon^{1/2}(\alpha_1 + i\beta_1) \frac{\sinh(2\alpha_1 \pi/\beta_1)}{\cosh(2\alpha_1 \pi/\beta_1) - 1} \tag{40b}$$

3.3 Matching

In order to determine the unknown integration constant v_0 (the slope at the origin of the inner solution) and the departure $\epsilon\omega_1$ of the frequency of the NG mode from ω_A, we apply the method of matched asymptotic expansions [15] to the complex quantities $u_o(a)/a + iq_o(a)$ given by equations (35,36) and $k_i + iq_i$ given by equation (40b). At order zero, we obtain three solvability conditions which read

$$\sum_{j=0}^{+\infty} \nu_j a_N^j = 0, \quad \sum_{j=0}^{+\infty} \rho_j a_N^j = q_0, \quad -\sum_{j=0}^{+\infty} j\nu_j a_N^{j-1} = k_0 \tag{41}$$

At the next order ($\mathcal{O}(\epsilon^{1/2})$), we obtain the size of the inner layer

$$\theta(\epsilon) = \epsilon \exp\left(-\frac{c_0 U_0 \pi}{2\beta_1\sqrt{\epsilon}}\right), \tag{42}$$

and the matching condition

$$\alpha_1 + i\beta_1 = \frac{|\zeta_1|^{\frac{1}{2}}}{v_0} \sum_{j=0}^{+\infty} \lambda_j a_N^j - i \frac{v_0}{|\zeta_1|^{\frac{1}{2}}} \sinh^2\left(\frac{\alpha_1 \pi}{\beta_1}\right) \sum_{j=1}^{+\infty} j\rho_j a_N^{j-1}, \tag{43}$$

Let us recall that the coefficients λ_j are linear in ω_1: $\lambda_j = \lambda_j^0 + \omega_1 \lambda_j^1$. Modulus and phase identification allow a numerical evaluation of equation (43) to determine v_0

and ω_1. In particular, an equation involving only ω_1 is found by multiplying real and imaginary parts of l.h.s. and r.h.s. of equation (43) and reads

$$\alpha_1\beta_1 = -\sinh^2\left(\frac{\alpha_1\pi}{\beta_1}\right)\sum_{j=1}^{+\infty} j\rho_j a_N^{j-1}\sum_{j=1}^{+\infty}\left(\lambda_j^0+\omega_1\lambda_j^1\right)a_N^j\ . \tag{44}$$

The frequency shift ω_1 may be numerically evaluated as solution of equation (44). Then the selected frequency is evaluated as $\omega_G \simeq \omega_A + \epsilon\omega_1$. This second order prediction is plotted as the heavy continuous line in Figure 7). We are now able to find scaling laws for the characteristic growth size of NG modes and for their slope $|da/dx(0)|$ at the origin of the domain as a function of ϵ the departure from the NG threshold $\mu - \mu_A$.

The slope of NG modes is the slope v_0 determined by equation (43) and rescaled by the size of the inner region:

$$\log\left|\frac{da}{dx}(0)\right| \simeq -\frac{c_0U_0\pi}{2\beta_1\sqrt{\epsilon}} + \ln\epsilon + \ln v_0. \tag{45}$$

The dominant contribution as $\epsilon \to 0$ is $\epsilon^{-\frac{1}{2}}$ and this result is analytic although the coefficient β_1 depending on ω_1 may only be numerically computed after having solved (44);

The characteristic growth size of the global mode is defined as the distance Δx such that $a(\Delta x) = 0.5\,a_N$. It may be calculated by adding the x-thickness of the inner region and the size of the outer solution between the boundary of the inner layer and the point at which the amplitude reaches the value $0.5\,a_N$. Since at the upstream edge in the outer layer, the spatial growth of the NG mode is exponential, its outer contribution to the growth size is of order $\ln(1/\epsilon)$. Therefore, when keeping only the dominant contribution which comes from the inner layer, the following scaling law is obtained:

$$\Delta x \simeq \frac{\pi}{\beta_1\sqrt{\epsilon}} \tag{46}$$

Note again, that the $\epsilon^{-1/2}$ dependence comes out naturally from the singular perturbation analysis and may be physically interpreted as the beating of the two waves associated with the fixed points A_0^+ and A_0^-. The above scaling laws (45,46) have been validated in the real case ($c_1 = c_3 = 0$) by numerical integration in x of the trajectory in the phase space given by the ordinary differential equations (12,13,14) and are found in good agreement with theoretical predictions, as presented in [21]. We now proceed to the comparison of the scaling laws with results from numerical simulation of the partial differential equation (1) in regions of parameter space (U_0, c_1, c_3) where no numerical or experimental data are available.

4 Simulations

Up to this point in the present paper, only existence of steady solutions (nonlinear global modes) of equation (1) has been investigated numerically and theoretically. If numerical integrations of the system (12,13,14) confirm the validity of the matched asymptotic expansion analysis and show the essential results that a NG mode exists only when the basic state is linearly absolutely unstable, they tell us nothing on the time behavior of equation (1). Therefore, a direct numerical integration of the partial differential equation (1) is desirable in order to investigate the temporal behavior and test the basin of attraction of the NG mode we have determined and its stability.

In order to test the validity of our analysis, we first compare the results given by numerical simulations of equation (1) with those obtained in section 2 from the phase portrait analysis on the one hand, and with those obtained by the matching in section 3 on the other hand. This will confirm that the NG mode is indeed the attractor of the system when it exists. We determine next the region of parameter space in which a NG mode is found by simulations of equation (1) and show that this region is given by the change of nature of the instability of the asymptotic traveling

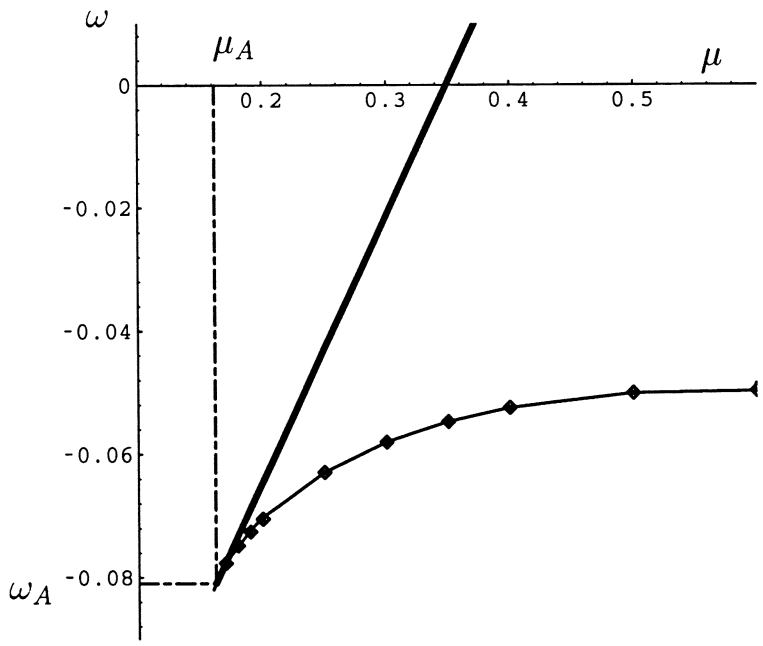

Fig. 8. Close up of the Figure 7 on which results from a temporal simulation have been added. The ligth curve is the frequency of NG modes found from the dynamical system integration (Eqs. (12, 13, 14), Fig. 6). The diamonds are frequency values found in numerical simulation of equation. (1) after transient behavior has disappeared. The straight heavy line represents the slope of $\omega_G(\mu)$ at the NG threshold given by the matched asymptotic expansion technique. Parameters are $U_0 = 0.9$, $c_1 = 0.5$, $c_3 = 0.2$.

wave of a NG mode selected for this parameter value, from convective to absolute.

4.1 Validation of the scaling laws

Figure 8 shows the frequency of the NG modes obtained by the above-mentioned three methods. For $U_0 = 0.9$, $c_1 = 0.5$, $c_3 = 0.2$, we vary μ from the threshold $\mu_A = 0.162$ to $\mu = 0.6$ and for each μ, we report the frequency $\omega_G(\mu)$ obtained as in Figure 6 by numerical integration of the ordinary differential equations (12,13,14) (light curve), for which the stable manifold of $A_2(\omega)$ crosses the axis ($a = 0, q = q_0$ but $u \neq 0$) of phase space, as found by the criterion presented in section 2. For the same values of μ, we undertake a temporal simulation of partial differential equation (1) with $A(0) = 0$ and the boundary condition at the outlet ensuring that the solution is asymptotic to any traveling wave (*i.e.* we impose equality between the ratio of the amplitudes $A(x+dx, t+dt)/A(x,t) = A(x,t)/A(x-dx, t-dt)$); the initial state of the system is $A(x) = 0$ for all x and an infinitely small perturbation is added (a Gaussian in amplitude located at the middle of the integration domain). The amplitude grows and evolves to a NG mode as shown in reference [21]. When the amplitude has become steady, we measure the frequency of the NG mode (which is found to correspond to the frequency of the selected asymptotic plane wave at infinity). These numerical measurements reported as diamonds in Figure 8 superpose exactly on the curve corresponding to the frequencies obtained by the phase portrait analysis. Finally, we compute the slope at the threshold of $\omega_G(\mu)$, by equation (44) as given by our singular perturbation analysis. The straight heavy line in Figure 8 represents this result for which we obtain $\omega_G = \omega_A + \omega_1 \epsilon$ with $\omega_1 = 0.433$. It is in excellent agreement with the results found numerically by the phase portraits analysis or by the temporal simulations.

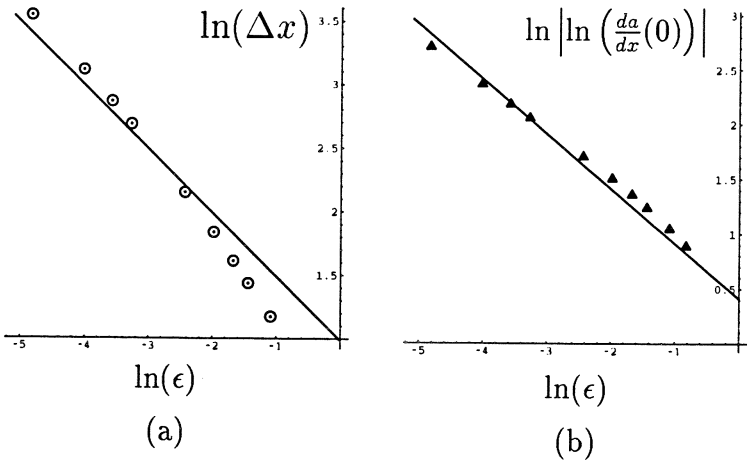

Fig. 9. Growth size (a) and slope at the origin (b) of the NG modes for different values of the criticality ϵ and $c_1 = 0.5$, $c_3 = 0.2$, $U_0 = 0.9$. The straight lines represent the scaling laws obtained fom the analytical matching and the dots results from a temporal simulation of Eq. (1).

In the temporal simulations, when the long time régime is reached, we also measure the growth size of the NG mode and its slope at the origin as a function of the departure ϵ from the NG instability threshold. The numerical values (dots in Figures 9(a) and 9(b)) are found in good agreement with the theoretical scalings $\Delta x \sim \epsilon^{-1/2}$ and $\ln|da/dx(0)| \sim \epsilon^{-1/2}$(equations (46) and (45)) represented by the straight lines. This threefold test not only confirms the validity of the singular perturbation analysis, but it also indicates that the NG mode is the attractor of the dynamics and by this fact it validates the frequency "selection" criterion of section 2 far from threshold. For fixed parameters U_0, c_1, c_3, μ, the phase portraits analysis is far easier and faster to handle than a temporal numerical simulation and predicts with a very good accuracy the NG mode frequency which will be "selected" in a temporal simulation. Let us emphasize again that for a given set of parameters, the frequency comes out naturally from the existence of the NG mode.

4.2 Comparison with results from the Rayleigh-Bénard and Taylor-Couette problems

It is not evident that the scaling laws derived analytically in section 3.3 and verified in section 4.1 by integration of the dynamical system (12, 13, 14) and by temporal simulation of equation (1) may apply to describe real flows. To test the relevance of the present model to describe experimental situations, we have interpreted in [23] the pattern selection occurring in two open flows. Büchel *et al.* [27] describe propagating vortex structures in the rotating Taylor–Couette system with an externally imposed axial throughflow. Müller *et al.* [28] have undertaken a similar description for the Rayleigh–Bénard problem with a Poiseuille flow. The power law (46) has been satisfactorily compared in [23] with numerical measurements of the growth size of NG modes obtained for the Taylor–Couette problem with throughflow by Büchel *et al.* [27] and for the Rayleigh–Bénard flow with an added Poiseuille flow by Müller *et al.* [28], by integration of Navier–Stokes equations. As shown in Figure 10, the growth length $L \equiv \sqrt{\mu}\Delta x$ of the vortex flow intensity versus the scaled advection velocity $V_g \equiv U_0\sqrt{c_0/\mu}$ is in quite good qualitative agreement with our scaling law (46) rewritten in the form

$$\sqrt{\mu}\Delta x \simeq \frac{\pi}{\beta_1}\left(1 - \frac{V_g^2}{4}\right)^{-1/2}, \tag{47}$$

where $(1 - V_g^2/4)$ is the rescaled departure from criticality. Our theoretical results are superposed on those obtained by Büchel *et al.* [27] in Fig. 10(a). The good quantitative agreement, especially in the vicinity of the threshold $V_g = 2$, confirms the validity of our analysis to describe the dynamics of Taylor–Couette system with throughflow. The same quantitative agreement is observed when we compare our theoretical analysis with the numerical results of Müller *et al.* [28] for the Rayleigh–Bénard problem with a Poiseuille flow (Fig. 10(b)). However, it is to be pointed out

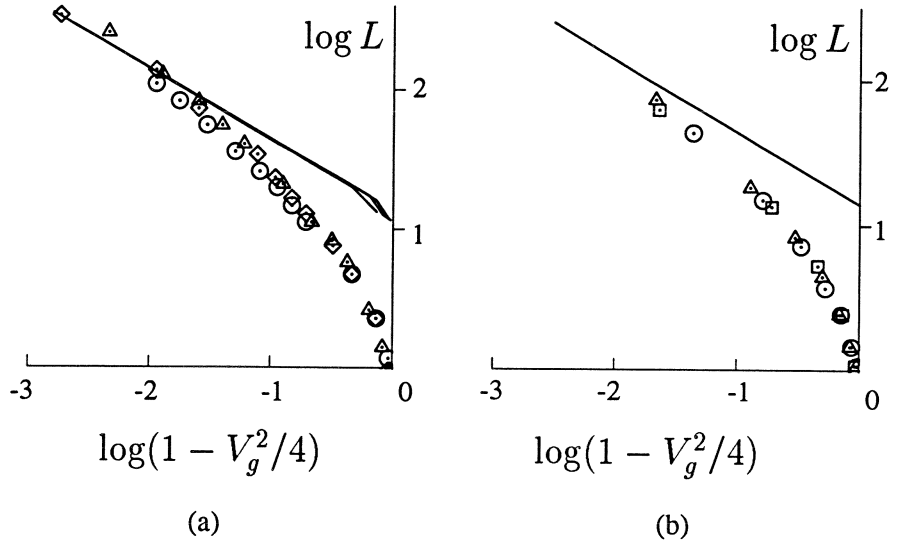

(a) (b)

Fig. 10. (a) The scaled growth length of NG modes predicted by (47) (continuous lines) are superposed on the results of [27]. For Taylor–Couette problem with throughflow, the three sets of open symbols represent values computed in [27] for three different Taylor number. (b) The same quantities for the Rayleigh Bénard problem with throughflow. Symbols represent values computed in [28] for three different Rayleigh numbers. The continuous line is our theoretical $\epsilon^{-1/2}$ law with $\beta_1 = 1$.

that the values of the coefficients c_1 and c_3 used by Büchel *et al.* and Müller *et al.* are small ($c_1 \sim \mathcal{O}(10^{-2})$ and $c_3 \sim \mathcal{O}(10^{-3})$. For this reason, a real model of amplitude equation would have been sufficient to obtain the same quantitative agreement.

4.3 Global instability of the nonlinear global modes and secondary convective and absolute instability of the asymptotic traveling waves

4.3.1 Stability of the NG modes at threshold $\mu = \mu_A$

In a temporal simulation, the NG modes are obtained as long time behavior of the impulse response associated with equation (1). They are asymptotic to a traveling wave as x goes to infinity. We assumed in section 2 that parameters were such that the asymptotic traveling waves were linearly stable when prolongated from x equals $-\infty$ to $+\infty$. We wish here to point out that this condition is too strong and may be relaxed by allowing convectively unstable traveling waves.

Throughout this section, we are going to use the term "wing" to denote the traveling wave to which a NG mode is asymptotic when $x \to +\infty$. Since we have fully determined the wing of the NG mode at the NG threshold, we are now able to precise if this traveling wave is a stable, a convectively or an absolutely unstable state of the system and then explore numerically the link of this result with the stability of the corresponding NG mode. When the parameters U_0, c_1, c_3 are fixed, the threshold of NG instability has been shown to coincide with the threshold of

absolute instability $\mu_A = U_0^2/4(1+c_1^2)$ of the basic state $A = 0$. At the threshold μ_A, the NG mode (and therefore its wing) oscillates at the selected frequency $\omega_A = -c_1\mu_A$. The corresponding wave number at $x \to +\infty$ (in the wing part) $q_N(\omega_A)$ is then a function of the parameters

$$q_N(\omega_A) = \sqrt{\mu_A}\left(\frac{\sqrt{1+c_3^2}-\sqrt{1+c_1^2}}{c_1+c_3}\right). \tag{48}$$

By testing if $q_N(\omega_A)$ is in the Eckhaus stable band, we have obtained in the plane (c_1, c_3), the region in which the traveling wave $A_2(\omega_A)$ is linearly stable. The reason for which the stability limits (using the wave numbers as parameters) depend only on c_1, c_3 and not on μ comes from the rescaling $q \to q/\sqrt{\mu}$, $a \to a/\sqrt{\mu}$, $U_0 \to U_0/\sqrt{\mu}$ which would have allowed to set μ to unity, but which has not been done in order to distinguish the effect of the advection velocity from the effect of the bifurcation parameter. Please note that this stability domain is also independent on U_0 as μ_A, U_0 and c_1 are linked by (2) at the threshold μ_A and the rescaling of μ_A to unity sets U_0 to $2\sqrt{1+c_1^2}$. Moreover, $q_N(\omega_A)$ and the Eckhaus neutral wavenumber $q_E(\mu_A, c_1, c_3)$ at the NG instability threshold μ_A are both proportional to $\sqrt{\mu_A}$. As a result the region of linear stability of $A_2(\mu_A)$, determined solely by the intersection of the surfaces $q_N(\mu_A, c_1, c_3)$ (equation 48) and $q_E(\mu_A, c_1, c_3)$ (equation 9) does not depend on μ_A.

Figure 11 shows the region of stability in the shape of a "balloon" plotted in heavy line and denoted by the S symbol. All numerical simulations undertaken in this region, setting the bifurcation parameter slightly above μ_A and starting from the initial state $A = 0$ everywhere excepted at the middle of the computation domain where a 10^{-3} Gaussian perturbation is added, show that the system indeed evolves to a stable NG mode. But a NG mode may still be obtained when parameters are chosen outside of this balloon of linear stability. Please note that even in the Benjamin–Feir unstable domain (BF region limited by the interrupted line), a NG mode may be obtained as the ultimate state of the system as shown in Figure 12 by the result of the simulation undertaken for $c_1 = 0.5$, $c_3 = 2.1$, $U_0 = 0.9$, $\mu = 0.2$. Initially, the system is in the state $A = 0$ for all x and small perturbations are added. It evolves to the NG mode corresponding to these parameters. Vizualisation starts when the system has reached the NG mode state and an extra perturbation with a gaussian envelope with a core size of 5 in the neighborhood of some x-location (here $x = 30$) is added. This perturbation grows but is advected and leaves the domain of observation. Ultimately, the system returns back to the NG mode. This behavior is fully coherent with a convectively unstable plane wave.

We make the conjecture that the relevant concept to determine the global instability of a NG mode (the secondary global bifurcation of the flow) is here the absolute or convective nature of the instability of its wing (the traveling wave $A_2(\omega_G(\mu))$). We are going to test this conjecture first by determining the boundary in the plane

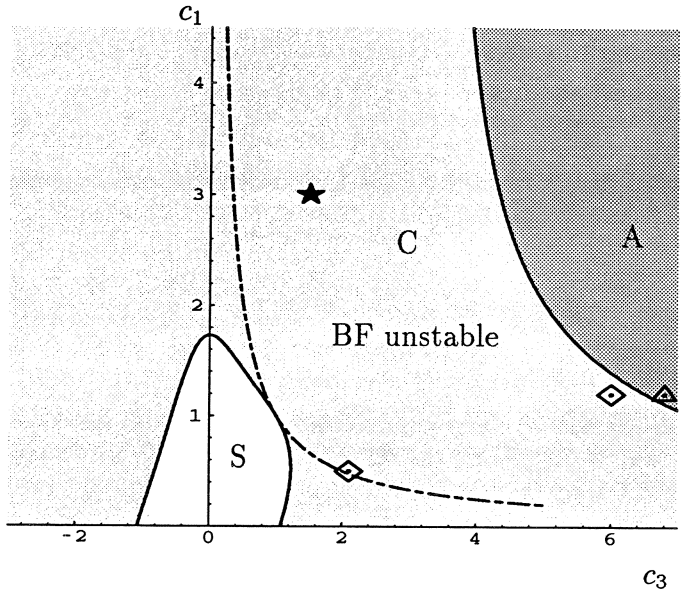

Fig. 11. Region of linear stability, convective instability and absolute instability of the "wing" $A_2(\omega_A)$ of the NG mode at the NG threshold. The "balloon" (S) is the region (in white) where $A_2(\omega_A)$ is linearly stable (limited by the heavy line, the intersection of $q_N(\omega_A)$ and $q_E(\mu_A, c_1, c_3)$. The loss of stability is always due to long waves perturbation [10]. The "wing" of the NG mode is convectively unstable at the NG threshold in the ligth gray region. The NG mode at the threshold μ_A is absolutely unstable to the right of the continuous line (dark gray region). The rigth of the dashed-dotted line defines the Benjamin–Feir limit. The points represents parameters values used in the simulations presented in Figs. 12 (left diamond), 13(a) (right diamond), 13(b) (triangle) and 15 (star)

.

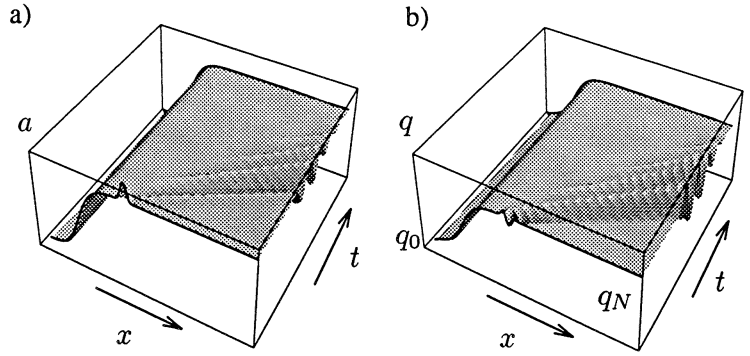

Fig. 12. a) Extended (3D) diagram of the spatiotemporal amplitude a and b) the phase gradient q resulting from a numerical simulation of the partial differential equation (1) in the Benjamin–Feir unstable domain with $c_1 = 0.5$, $c_3 = 2.1$ (left diamond in Figure 11), $U_0 = 0.9$, $\mu = 0.2$. For these values the traveling wave $A_2(\omega_A)$ is convectively unstable. Starting from $a = 0$ for all x, a NG mode is reached when $t \to +\infty$. The vizualization starts when a perturbation in amplitude (here a gaussian) at $x = 30$ is added. A wave packet grows but is advected away and the system returns back to the NG mode which is then stable when its asymptotic traveling wave is convectively unstable.

(c_1, c_3) for which the nature of the instability of the traveling wave $A_2(\omega_A)$ at $\mu = \mu_A$ changes from convective to absolute. Because of the self-similar symmetry of (1), this absolute instability region is independent of U_0. This allows us to determine the region of parameter space for which the NG mode is unstable at threshold *i.e.* as soon as it appears from the region for which the NG mode is stable at threshold. Then we present simulations which confirm that when c_1 and c_3 are in the gray domain of Figure 11 *i.e.* such that $A_2(\omega_A)$ is convectively unstable, we still obtain a stable NG mode, above threshold μ_A. By contrast, if c_1 and c_3 are such that $A_2(\omega_A)$ is absolutely unstable, an intricated dynamics is obtained at the bifurcation μ_A, displaying a quasi periodic behavior. In the latter case, the route to disorder seems to posses at least a second step.

The absolute or convective nature of the traveling wave is determined classically [32] by considering the dispersion relation for instability waves $\exp(-i\Omega t + iKx)$, obtained by the standard linearization of equation (1) around a traveling wave $A_2(\omega)$: amplitude and phase are written in the form

$$a(x,t) = a_N + a_1(x,t), \qquad \theta(x,t) = q_N x - \omega t + \theta_1(x,t) \tag{49}$$

with $a_1(x,t)$ and $\theta_1(x,t)$ proportional to $\exp(-i\Omega t + iKx)$. The dispersion relation reads:

$$\Omega(K) = -iK^2 + (U_0 + 2q_N c_1)K - ia_N^2 + i\sqrt{(1+c_3^2)a_N^2 - (c_1^2K^2 - 2iq_N K - c_3 a_N^2)^2}, \tag{50}$$

where a_N, q_N are given by equations (5, 6) and Ω, K are complex. Only the phase branch is considered, being the only one to turn unstable. It is quite remarkable that using the form (49) for the perturbations, one obtains a linear equation with constant coefficients and therefore avoids to use the Floquet analysis [33] which generically determines the secondary bifurcation of a periodic state.

We seek the neutral saddle points K_0, $d\Omega/dK(K_0) = 0$ such that $\Im(\Omega_{0,i}(K_0)) = 0$ by the "pinching" process (see [29,30,32] for details), which defines the boundary between absolute and convective instability for the traveling wave $A_2(\omega)$. Results are plotted in Figure 11: the light continuous line delineates the region of secondary absolute instability for the flow at threshold $\mu = \mu_A$, i.e. the change of nature from convective to absolute of the secondary instability of the plane wave $A_2(\omega_A)$ for $\mu = \mu_A$ (ω_A and μ_A given by equations (2,3)). It does not depend on U_0 because of the above-mentioned rescaling and does not depend on μ as only its threshold value is considered here. The simulations in Figure 13 reported in the form of spatiotemporal plots of the amplitude in gray level from zero (dark) to high values (white) have been undertaken for values of parameters indicated by the right diamond and the triangle in Figure 11, corresponding to $c_3 = 6.0$ (diamond) or $c_3 = 6.8$ (triangle) with $c_1 = 1.2$. For these simulations, we have chosen $\mu = 1$ and U_0 5% below the value

corresponding to the NG threshold. The system initially in the uniform state $A = 0$ (dark zone in the lower part of the diagram) evolves rapidly to a NG mode with a large growth size as indicated by the black part near the origin in Figure 13(a), which is due to the fact that parameters are close to the primary bifurcation threshold. In Figure 13(a) for which the "wing" of the NG mode is supposed to be convectively unstable (diamond in Figure 11), we observe that initial transient stand for a long time but finally are advected away. In the region where the amplitude has reached its saturation value, perturbations are amplified and develop a spatial oscillation of the amplitude $|A|$, but they are advected downstream as indicated by the inclined line network of iso amplitude on the right part of Figure 13(a). Ultimately, the system effectively evolves back to the stable NG mode. Transients leave slowly the medium because parameters are close from the boundary of secondary global instability.

By contrast, in the region of secondary absolute instability (triangle in Figure 11), the system never evolves to a stable NG mode (Figure 13(b)). The upstream part of the solution grows as a NG mode (black region near the origin) but at some location in the saturated region (gray), the amplitude starts to oscillate around its saturation value and never reaches a steady state, as indicated by the inclined line network which contaminate the right part of Figure 13(b). In this case, as soon as the flow is primarily globally unstable, it is also secondarily globally unstable.

Such simulations indicate that the secondary global instability threshold coincides with the threshold of absolute instability of the wing.

4.3.2 Secondary instability of a NG mode varying the control parameter

The preceding analysis which has been done at the NG threshold μ_A can been extended to any value of μ by conjecturing that the global secondary bifurcation coincide with the local absolute threshold for the secondary bifurcation of the traveling wave corresponding to the "wing" of the NG mode. For a given set of parameters (c_1, c_3, U_0), we have to determine the convective or absolute nature of the instability of the traveling wave of frequency $\omega_G(\mu)$, where $\omega_G(\mu)$ is selected by the phase space criterion of section 2, and then to check with a simulation if the corresponding NG mode is obtained when $A_2(\omega_G(\mu))$ is convectively unstable, the transient being advected away. Reciprocally, when the traveling wave of frequency $\omega_G(\mu)$ for parameters c_1, c_3, U_0, μ is absolutely unstable to secondary perturbations, we should obtain that the NG mode is linearly unstable as transient never dies out

In order to give a slightly more general result, we chose the alternative method of determining the convective or absolute nature of the instability of any traveling wave. Then we check in a simulation by increasing the bifurcation parameter if the secondary bifurcation is obtained when the wing becomes absolutely unstable.

In Figure 14, we have plotted the stability and convective instability boundaries of traveling waves $A_2(\omega)$ represented by the reduced wavenumber $q_N^* \equiv q_N/\sqrt{\mu}$

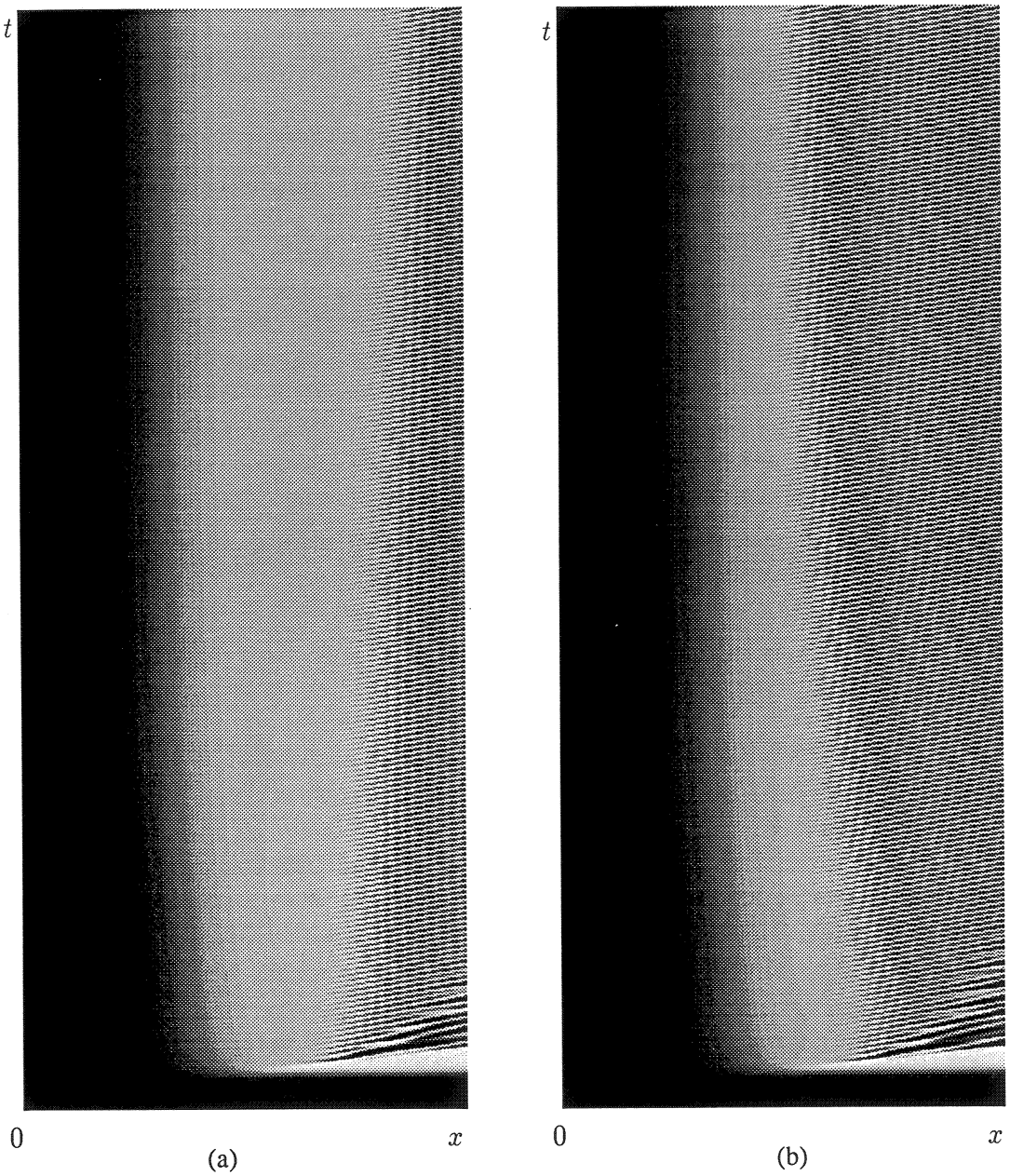

Fig. 13. Spatio-temporal diagram of the evolution of the amplitude in gray scale. $|A| = 0$ corresponds to black. The x-size is 50 and time goes from 0 to 200. (a) Simulation for the parameters indicated by the rightmost diamond in Figure 11 ($c_1 = 1.2$, $c_3 = 6$) and $\mu = 1$, U_0 is 5% below the value corresponding to the NG threshold. Ultimately, a pure NG mode is obtained (the transient being washed downstream) as expected in regard of convective instability of the wing. (b) Simulation for the parameters indicated by the triangle in Figure 11 ($c_1 = 1.2$, $c_3 = 6.8$) and identical values for μ and U_0. No NG mode is obtained as the transient does not die out since the threshold of absolute instability of the wing has been exceeded.

(which uses the rescaling allowing to set μ to unity) as a function of c_3, for the parameter $c_1 = 3$ and for different reduced velocities $U_0^* \equiv U_0/\sqrt{\mu}$ (corresponding to the values $U_0^* = 0.0$, 0.4, 0.8, 1.2, 1.6 and 2.0). The stability region (S) is bounded by the neutral Eckhaus wavenumber $q_E/\sqrt{\mu}$. For each reduced advection velocity, the boundary between convective and absolute instability is made up of a couple of lines bounding tongues in which the traveling wave corresponding to the reduced wavenumber q_N^* is convectively unstable (C). For $U_0^* = 0$ the tongues are symmetric in $q_N^* \to -q_N^*$ due to the $x \to -x$ symmetry of the problem and are obtained by Weber *et al.* [35]. When U_0 is non nil, the tongues are no longer symmetric and negative wave-numbers have to be considered. Please note that for $q_N^* > 0$, the size of the convective region decreases while increasing the advection velocity whereas for $q_N^* < 0$, the size of the convective region increases when the reduced velocity increases. For the chosen value of $c_1 = 3$, the reduced velocity at the primary bifurcation threshold given by $U_0^* = 2\sqrt{1 + c_1^2}$ equals $U_0^* \simeq 6.32$ and for c_3 between 0 and 2, the range of Figure 14, the NG mode is convectively unstable at threshold. The tongue of convective instability for $U_0^* \simeq 6.32$ covers the entire Figure 14. It is equivalent to increase the bifurcation parameter at fixed advection velocity or to decrease the advection velocity at fixed μ, each operation representing a decay of the reduced advection velocity. To compare the secondary global bifurcation of the flow with the secondary absolute instability of the wing of the NG mode, we fix c_3 (in the following examples, $c_3 = 1.5$), and U_0^* is decreased from its value at the primary bifurcation threshold til the second bifurcation is obtained (μ is set to unity). For each value U_0^*, we undertake a temporal simulation of equation (1) and when the amplitude of the system has reached a steady state, the wavenumber of the wing of the corresponding NG mode is measured and reported in Figure 14. The star, the cross and the circle in Figure 14 constitute three examples of such numerical experiments for reduced velocities $U_0^* = 2$ (star), $U_0^* = 1.6$ (cross) and $U_0^* = 1.2$ (circle). Our hypothesis of a secondary bifurcation given by the absolute instability of the wing is confirmed as the wavenumber measured in each stable case belongs to the corresponding tongue of convective instability of the wing. Above the secondary bifurcation threshold (Figure 14, circle), it is not possible to determine the wavenumber of the wing, because the system evolves toward a solution which is not asymptotic to a traveling wave in the wing. Instead, the wavenumber has been evaluated from the selected frequency close to the origin in the unstable NG mode case (circle) and corresponds to the crossing of the "operating point" (q_N^*, c_3) into the absolute instability region for the plane wave of the wing. At the secondary bifurcation, the wavenumber of the wing should be exactly on the boundary of absolute instability of the wing.

Figure 15 shows spatiotemporal plots of the amplitude resulting from, simulations of equation (1) for the parameter setting $c_1 = 3$ and $c_5 = 1.5$, and for reduced velocities $U_0^* = 1.6$ and $U_0^* = 1.2$. The amplitude $|A|$ is plotted in grayscale with zero values corresponding to black and maximum amplitude to white. When $U_0^* = 1.6$ (Figure 15(a)), the amplitude grows from the uniform initial state $A = 0$. Perturbations develop an oscillation in the amplitude as shown by the line network in the middle

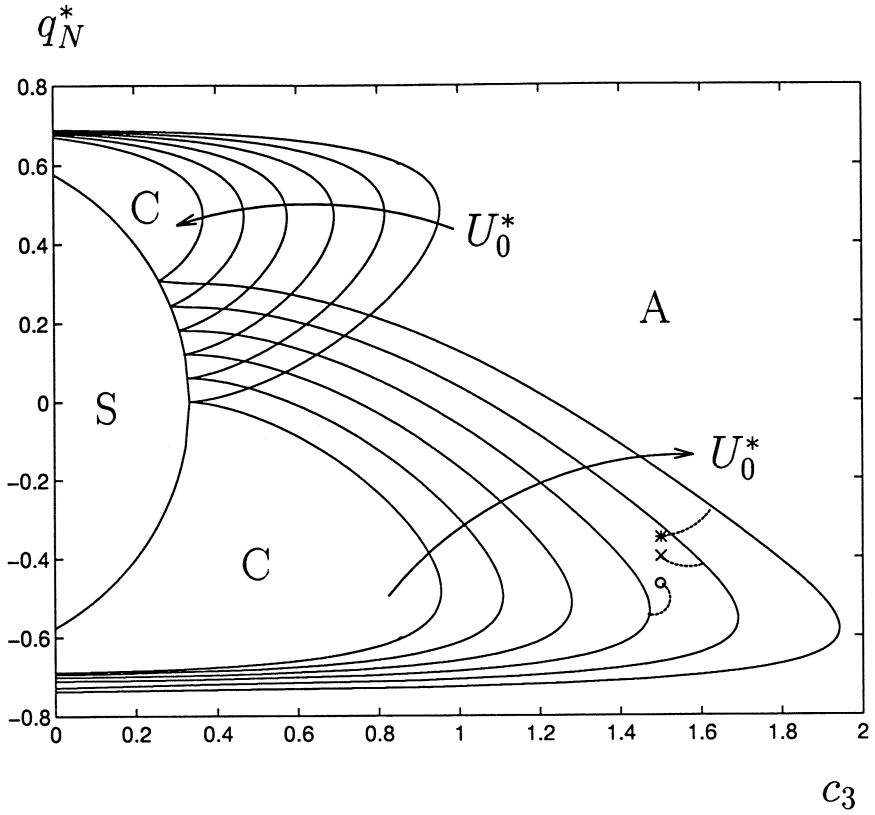

Fig. 14. Regions of stability, convective and absolute instability of traveling waves in the plane (q_N, c_3) for a fixed parameter $c_1 = 3$. The traveling wave with reduced wavenumber $q_N^* \equiv q_N/\sqrt{\mu}$ is linearly stable within the S region. Each couple of tongues refers to a reduced velocity $U_0^* \equiv U_0/\sqrt{\mu}$ (which equals 0.0, 0.4, 0.8, 1.2, 1.6 and 2.0) and bounds the region of convective instability of the traveling waves. The cross and the star refers to the simulations in the convective region for $c_3 = 1.5$, $U_0^* = 2$ (star) and $U_0^* = 1.6$ (cross referring to simulation in Figure 15(a)). The circle refers to simulation 15(b) with $U_0^* = 1.2$; in the latter case, the NG mode is unstable but q_N has still been measured from the oscillation frequency close to the origin.

right part, but they are advected as time runs and ultimately leave the medium. Since parameters are far from the primary bifurcation threshold, the growth size of the solution is small as shown by the small black band near $x = 0$. Transient has died out and the long time asymptotic state of the system is a NG mode as shown by the upper part of the plot which is black near $x = 0$ and uniformly gray in the upper right part. The wavenumber of its wing is measured and reported by the cross in Figure 14. We verify that it belongs to the tongue of convective instability of the wing corresponding to $U_0^* = 1.6$. In each simulation such as the one of Figure 15(a) for which a NG mode is reached, the wavenumber of its wing properly rescaled belongs to a tongue of convective instability. For example the star in Figure 14 which represents the results of a simulation similar to Figure 15(a) but for $U_0^* = 2$, belongs to the C tongue corresponding to $U_0^* = 2$.

By contrast, for $U_0^* = 1.2$ (Figure 15(b)) the long time asymptotic solution starts to

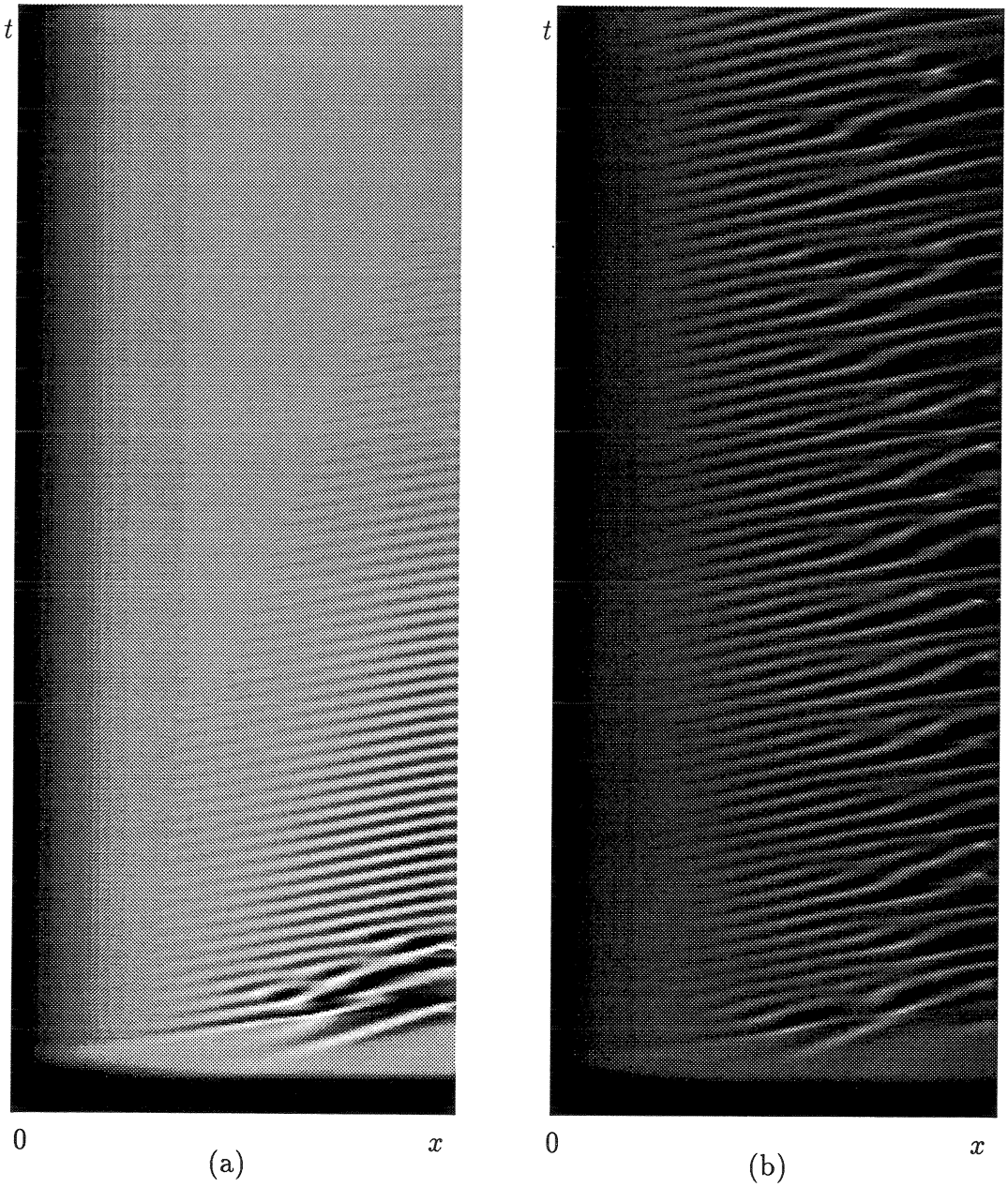

Fig. 15. Same as Figure 13. (a) Simulation for $c_1 = 3$, $c_3 = 1.5\, U_0^* = 1.6$ (cross in Figure 14). A NG mode is obtained and parameters are in the tongue of convective instability of the wing corresponding to $U_0^* = 1.6$. (b) Simulation above the secondary bifurcation for $c_1 = 3$, $c_3 = 1.5\, U_0^* = 1.2$. No NG mode is obtained. The system does not evolve to a time periodic state. Defects continuously appear and the nature (multiperiodic or chaotic) of this global secondary transition will be to be determined.

grow spatially as a NG mode but it neither reaches a traveling wave at $x \to +\infty$, nor becomes time periodic. A disordered régime appears in the long time behavior with defects where the amplitude is zero at some point. This is indicated by the greater contrast between the maxima of the amplitude, which reaches higher values than below the secondary bifurcation (white thin lines), and the minima which reach zero values (large black bands in the right part of Figure 15(b)). This régime may be reminiscent of the defect turbulence observed by Chaté and Manneville [2] among others. But its exact nature remains to be determined to precise if the transition to disorder possesses a single step or if multiperiodic states and chaotic régime are obtained via successive global bifurcations.

As a conclusion of this section, there is numerical evidence that the absolute instability of the wing of a NG mode determines the secondary bifurcation of the flow. It would be interesting to make a full linear instability analysis of the NG modes involving their entire spatial structure, in order to confirm this conjecture or by contrast to determine if a core instability as in the case of the Nozaki–Bekki [34] hole may occur, at least in some range of the (c_1, c_3) plane.

5 Conclusion

We have described for the one-dimensional Ginzburg–Landau equation the NG modes which are time oscillating solutions linking the state $A = 0$ (the boundary condition) to a saturated state represented by a traveling wave. We have shown that NG modes exist when the bifurcation parameter exceeds a critical value corresponding to the absolute/convective instability threshold of the basic state $A = 0$. We have proposed a frequency "selection" criterion for the NG modes relying only on numerical computation in the phase space, which comes out naturally from the existence condition of a NG mode and has been validated by numerical simulations. We have derived theoretically scaling laws for the frequency, the growth size and the slope at the origin of NG modes as functions of the departure from the NG threshold. These scaling laws, derived analytically for the first time, allow to explain the power law obtained numerically by simulation of Navier–Stokes equations for the NG modes in the Taylor–Couette problem with throughflow by Büchel *et al.* [27] and for the Rayleigh–Bénard flow with an added Poiseuille flow by Müller *et al.* [28]. We have addressed the question of the domain of parameter space in which a NG mode is stable, in order to give the validity region of our scaling laws. We have therefore studied the convective/absolute nature of the instability of the traveling wave to which a NG mode is asymptotic when $x \to +\infty$ (its wing). At the NG threshold, numerical simulations indicate that the region of convective instability of the wing corresponds to a region of global secondary instability of the NG modes. Our scaling should therefore describe the basic patterns observed in fluid flows in the (C) region of parameter depicted in Figure 11. When the wing of a NG mode at threshold μ_A becomes absolutely unstable, the bifurcated solution of the flow cannot

be a NG mode; the system must evolve to a more complicated solution in general not time-periodic or quasi-periodic. The primary bifurcation is hidden by the secondary bifurcation which appears simultaneously. To be more general, we have conjectured that further from the NG instability threshold (the primary global bifurcation), the loss of stability of a NG mode is due to the change of nature of the instability (from convective to absolute) of its wing. This conjecture has been tested by determining the absolute/convective instability of traveling waves and numerical temporal simulations in the globally unstable region are found in agreement with this hypothesis. A nonperiodic solution with defects continuously appearing, is obtained when for fixed parameters, the bifurcation parameter is increased above the secondary global bifurcation threshold. The nature of this global secondary transition remains to be determined.

References

[1] M.C. Cross, P.C. Hohenberg, *Pattern formation outside of equilibrium*, Rev. Mod. Phys. **65**, 851 (1993).

[2] H. Chaté, P. Manneville, *Phase diagram of the two-dimensional complex Ginzburg-Landau equation* Physica **224A**, 348 (1996).

[3] A. Hanna, A. Saul, K. Showalter, *Detailed studies of propagating fronts in the iodate oxydation of arsenous acid*, J. Am. Chem. Soc. **104**, 3838 (1982).

[4] P. Kolodner, J.A. Glazier, *Interaction of localized pulses of traveling-wave convection with propagating disturbances*, Phys. Rev. A, **42**, 7504 (1990).

[5] D.O. Olagunju, B.J. Matkowski, *Burned stabilized cellular flames*, Quart. Appl. Math. **48**, 645 (1990).

[6] A.C. Newell, J.A. Whitehead, *Finite bandwidth, finite amplitude convection*, J. Fluid. Mech. **38**, 279 (1969).

[7] L.A. Segel, *Distance side-walls cause slow amplitude modulation of cellular convection*, J. Fluid. Mech. **38**, 203 (1969).

[8] K. Stewartson, J.T. Stuart, *A nonlinear instability theory for a wave system in plane Poiseuille flow*, J. Fluid. Mech. **48**, 529 (1971).

[9] C. Mathis, M. Provansal, L. Boyer, *The Bénard von Kármán instability: an experimental study near the threshold*, J. Phys. (Paris) Lett. **45**, 483 (1984).

[10] B.J. Matkowski and V. Volpert, *Stability of plane wave solutions of complex Ginzburg-Landau equations*, Quart. Appl. Math. **51**, 265 (1993).

[11] M.J. Landman, *Solutions of the Ginzburg-Landau equation of interest in shear flow transition*, Stud. Appl. Math. **76**, 187 (1987).

[12] W. van Saarloos and P.C. Hohenberg, *Fronts, pulses, sources and sinks in generalized complex Ginzburg-Landau equations*, Physica **56D**, 303 (1992).

[13] P. Huerre, P.A. Monkewitz, *Local and global instabilities in spatially developing flows*, Annu. Rev. Fluid Mech. **22**, 473 (1990).

[14] V.I. Arnol'd, *Geometrical methods in the theory of ordinary differential equations*, (Heidelberg: Springer, 1983).

[15] C.M. Bender and S.A. Orszag, *Advanced Mathematical Methods for Scientists and Engineers*, (Mc Graw Hill, 1978).

[16] M. Abramowitz, I.A. Stegun, *Handbook of mathematical functions*, (Dover, 1972).

[17] C.K.R.T. Jones, T.M. Kapitula, J.A. Powell, *Nearly real fronts in a Ginzburg-Landau equation*, Proc. Roy. Soc. Edinburgh, **116A**, 193 (1990).

[18] N. Koppel, L. N. Howard, *Plane wave solutions to reaction-diffusion equations*, Stud. Appl. Math. **56**, 291 (1973).

[19] K. Nozaki, N. Bekki, (a) Phys. Rev. Lett. **51**, 2171 (1983); (b) J. Phys. Soc. Jpn. **53**, 1581 (1984).

[20] J.M. Chomaz, P. Huerre, L.G. Redekopp, *The effect of nonlinearity and forcing on global modes*, in *New Trends in Nonlinear Dynamics and Pattern-Forming Phenomena*, edited by P. Coullet and P. Huerre, (Plenum Press, New York, 1990).

[21] A. Couairon, J.M. Chomaz, *Absolute and convective instabilities, front velocities and global modes in nonlinear systems*, submitted to Physica **D**.

[22] A. Couairon, J.M. Chomaz, *Global instability in nonlinear systems*, Phys. Rev. Lett. **77**, 4015 (1996).

[23] A. Couairon, J.M. Chomaz, *Pattern selection in the presence of a cross flow*, submitted to Phys. Rev. Lett.

[24] A. Kolmogorov, I. Petrovsky, N. Piskunov, *Investigation of a diffusion equation connected to the growth of materials, and application to a problem in biology*, Bull. Univ. Moscow, Ser. Int. Sec. A **1**, 1 (1937).

[25] K.L. Babcock, G. Ahlers, D.S. Cannel, *Noise-sustained structure in Taylor–Couette flow with through flow*, Phys. Rev. Lett. **67**, 3388 (1991); *Stability and noise in Taylor–Couette flow with through-flow*, Physica **61D**, 40 (1992).

[26] G. Ahlers, D.S. Cannel, *Vortex-front propagation in rotating Couette–Taylor flow*, Phys. Rev. Lett., **50**, 1583 (1983).

[27] P. Büchel, M. Lücke, D. Roth, R. Schmitz, *Pattern selection in the absolutely unstable regime as a nonlinear eigenvalue problem: Taylor vortices in axial flow*, Phys. Rev. E. **53**, 4764 (1996).

[28] H.W. Müller, M. Lücke, M. Kamps, Europhys. Lett. **10**, 451 (1989); Phys. Rev. A **45**, 3714 (1992).

[29] R.J. Briggs, *Electron-Stream Interaction with Plasmas* (MIT Press, Cambridge, MA, 1964).

[30] A. Bers, in *Physique des Plasmas*, edited by C. DeWitt and J. Peyraud (Gordon and Breach, New York, 1975).

[31] E.M. Lifshitz, L.P. Pitaevskii, *Physical kinetics* (Pergamon, London, 1981).

[32] P. Huerre, M. Rossi in *Hydrodynamics and nonlinear instabilities*, Cambridge University Press, to be published.

[33] L. Brevdo, T.J. Bridges, *Absolute and convective instabilities of spatially periodic flows*, Phil. Trans. in print (1996).

[34] H. Chaté, P. Manneville, *Stability of the Bekki–Nozaki hole solutions to the one-dimensional complex Ginzburg–Landau equation* Phys. Lett. **A 171** 183, (1992).

[35] A. Weber, L. Kramer, I.S. Aranson, L. Aranson, *Stability limits of traveling waves and the transition to spatiotemporal chaos in the complex Ginzburg–Landau equation*, Physica **61D**, 279 (1992); *Stability limits of spirals and traveling waves in nonequilibrium media*, Phys. Rev. A **46**, R2992 (1992).

[36] A. Pumir, B.I. Shraiman, W. van Saarloos, P.C. Hohenberg, H. Chaté, M Holen, *Phase vs. defect turbulence in the 1-D complex Ginzburg–Landau equation*, in *Ordered and turbulent Patterns in Taylor–Couette flow* edited by C.D. Andereck and F. Hayot, (Plenum Press, New York 1992).

Chapitre 3

Modes globaux non-linéaires pour les milieux faiblement inhomogènes

Nonlinear global modes in slowly varying flows

Arnaud Couairon and Jean–Marc Chomaz

LadHyX, CNRS UMR 156, Laboratoire d'Hydrodynamique,
École Polytechnique,
91 128 Palaiseau CEDEX, France

Abstract

We study the existence of nonlinear solutions of the real Ginzburg–Landau amplitude equation, with varying coefficients when the solution is subject to a boundary condition at $x = 0$. These solutions, called nonlinear global modes, are explicitly obtained from a matched asymptotic expansion when nonlinear effect dominates the inhomogeneity. The dynamics of this model is believed to mimic the behavior of strongly nonlinear but weakly nonparallel basic flow (basic flow varying in the streamwise direction). For the model, we derive scaling laws for the amplitude of nonlinear global modes and for the position of the maximum that are in agreement with experimental observations of Goujon-Durand *et al.* [1] and numerical simulation of Zielinska & Wesfreid [2] on the wake behind bluff bodies.

1 Introduction

Most of the spatially extended open flows of interest may be classified according to their dynamical behavior. Either they may be easily manipulated by external excitations (for example a forcing fixed in space or upstream noise contaminating the entrance condition of the flow) and they behave as a noise amplifier. Mixing layers and boundary layers belong to this class. Or they display a self sustained saturated oscillation unaltered by external excitation. In this case, the flow becomes tuned at a specific intrinsic frequency everywhere in space and behaves as a single oscillator. The associated spatial distribution of fluctuations defines the global mode of the flow. The Kármán vortex street behind a cylinder constitutes a typical example of transition to a global mode régime. When the Reynolds number is increased above a critical value (~ 45), the laminar steady flow becomes globally unstable and ultimately exhibits a self sustained oscillation (a saturated limit cycle oscillation [1–3]). A global mode régime (also called a self-sustained oscillation régime or a resonant régime) also appears in jets [4], when the inner density is lightened, in mixing layer when suction is applied to one of the stream [5], in Rayleigh–Bénard with Poiseuille flow when the heating is high

enough [6] or in Taylor-Couette system with an added axial throughflow [7], when the rotation rate is increased.

If the existence of oscillator like behavior of the strongly unstable system are now well established, the relevant mechanism allowing to sustain the oscillations is yet controversial, especially for bluff body wakes. The problem may be formulated in term of feedback loop giving rise to an oscillator. If the moving downstream branch of the loop is similar between every model and is made of vortical instability wave growing downstream, the "upstream" branch closing the loop differs from one model to another.

One of the proposed mechanism is concerned with a feedback loop made up of a growing vortical instability wave [8] moving upstream, and has been associated with the notions of absolute and convective instability initially developed in the context of plasma physics [9–11]. They characterize the impulse response of a system within the parallel flow approximation at each streamwise station obtained by extending the flow that exists at a particular station x. If localized disturbances spread upstream and downstream and contaminate the entire flow, the system is said to be *locally absolutely unstable.* If by contrast disturbances are swept away from the source, the system is said to be *locally convectively unstable.*

Another proposed mechanism for wakes relies on hydroacoustic resonances occurring when there is a second blunt body at a finite distance downstream [12]. A feedback loop dominates the dynamics of the flow with a downstream branch consisting of rotational instability waves rolling up into vortices and an upstream branch consisting of global irrotational pressure disturbances generated by interaction between the vortical structures and the downstream body. This mechanism might also apply when no downstream body is present, the pressure wave being directly emitted by the growing and saturating vortices.

A third mechanism has been proposed by Villermaux [13] in the form of a nonlinear feedback which models the reintroduction of disturbances close to the bluff body by the counter flow which exists just behind the cylinder. But such a model is not generic as it is unable to predict the behavior of hot jets, convection cells with throughflow or Taylor–Couette rolls with an added Poiseuille flow in which no recirculation are present but which exhibit resonance and scaling laws similar to the wake instability.

Moreover, for none of these two last models, the acoustic feedback or the advection feedback have predicted precise threshold value or scaling laws generic to the class of self sustained resonance we consider.

In more complex geometry, all three feedback mechanism might be active and the ultimate goal will be to be able to precisely quantify each mechanism. But at present, it seems likely from numerous experimental and numerical evidencies [14] that the feedback through vortical instability wave that we are going to discuss

does apply to wakes, mixing layer, jets, Rayleigh–Bénard and Taylor–Couette flow.

In order to describe open flows, entrance condition, nonlinearity, as well as non-parallelism of the flow have to be taken into account. Using the notions of local absolute and convective instability most open shear flows have been recently investigated and the existence of a global mode has been associated with local linear instability of the flow (see [14] for a review). The term "global modes" usually refers to the exponentially growing in time solution of a nonhomogeneous linear eigenproblem involving the whole streamwise direction, and the "global instability" refers to its existence. The connection between global instability and local absolute nature of the instability has been first established on model equation and subsequently extended to real flows [15]. In the present paper, we will consider only amplitude equation models and compare directly results derived for these models to real experiments. But we have to keep in mind that these flow are far from local threshold, and that the real flow dynamics does not reduce exactly to the model.

For model equations, it has been shown by Chomaz *et al.* [16,17] that a necessary condition for the linear global instability is the existence of a finite region of absolute instability. Once the linear global stability solved and analyzed in the WKBJ framework, it was natural to study the weakly nonlinear behavior [18] as early experimental evidence shows that the global bifurcation was following the Landau equation. Unfortunately, the weakly nonlinear problem turns out to be ill posed in the sense that the approach was only valid when the departure from threshold is exponentially small in comparison with the inhomogeneity parameter [19]. This drastic limitation of the "easy nonlinear theory" [20] may be explained by the fact that for order one advection velocity, the second order modification of the basic flow due to the growth of the perturbation occurs far downstream the region determining the growth rate of the linear global instability. When small but not exponentially small departure from threshold are considered, a fully nonlinear study is necessary and is the aim of the present paper.

In a previous study, we have carried out a fully nonlinear study of the homogeneous and nonpotential case [26] which gives a good agreement with the numerical observations by Büchel *et al.* [7] for the Taylor–Couette problem with throughflow, or by Müller *et al.* [6] for the Rayleigh–Bénard problem with an added Poiseuille flow. We are going to present here extensions of the previous study to the inhomogeneous case and we assume that the bifurcation parameter varies linearly in x, the direction of the flow. This assumption does not restrict the generality of the study since the method could be applied to arbitrary $\mu(x)$. Moreover, we focus this study on the case of a real amplitude equation, but as for the homogeneous case, the nonhomogeneous global mode should have a similar structure for the real and complex amplitude [24,26].

We present the model in section 2. We assume that nonlinearities dominate inho-

mogeneity and we make a weakly non parallel assumption, using a small parameter μ_1 accounting for the inhomogeneity of the medium, ($\mu(x) = \mu_0 + \mu_1 x$). In the case of an order one advection velocity, this hypothesis allows us to derive in section 3, a matched solution exactly representing the saturated weakly nonparallel global mode with the upstream boundary condition that the flow is unperturbed at $x = 0$. In section 4, we derive scaling laws for the maximum amplitude of the global mode and its position versus the departure from instability threshold. In section 5, The analytical solution and the scaling laws found in section 4 allow a direct and quantitative comparison with the experimental results by Goujon–Durand *et al.* [1] and with the numerical results by Zielinska & Wesfreid [2] which concern the wake of angular obstacles. They observe the variations of the amplitude of the longitudinal velocity component in the streamwise direction similar to those obtained in our model. According to these observations, the nonlinear saturation of the amplitude occurs on a smaller scale than the scale of streamwise variation of the mean flow, allowing our weakly non parallel assumption to be at leading order correct. A discussion of this hypothesis is done in section 5. The scaling laws for the maximum amplitude and its position versus the departure from instability threshold predicted by the present theoretical approach are in good agreement with those observed by these authors.

2 The Ginzburg–Landau model

The Ginzburg–Landau model describes the evolution of the complex amplitude of instability waves which develop behind the cylinder. As for mixing layers [27], wakes are strongly unstable and evolves in space. Therefore, inhomogeneity of the flow modifies the local stability characteristics and has to be taken into account explicitly. In the model, this inhomogeneity is introduced in the local growth rate $\mu(x)$ which varies in the streamwise direction and is assumed for simplicity to be such that the flow is stable ar infinity *i.e.* such that $\mu(+\infty) < 0$. In a real flow, the laboratory frame is usually singled out by the conditions at the entrance of the flow; this breaks the Galilean invariance and leads to take into account the mean advection velocity of the flow explicitly. The objective of the present paper is to describe the spatial structure of nonlinear global modes, which in the present case are steady fully nonlinear solutions of the real Ginzburg–Landau equation with varying coefficient $\mu(x)$ and with a nonzero advection term $U_0 > 0$:

$$\frac{\partial A}{\partial t} + U_0 \frac{\partial A}{\partial x} = \frac{\partial^2 A}{\partial x^2} + \mu(x) A - A^3, \tag{1}$$

in a semi-infinite domain $[0, +\infty)$ with an "entrance" condition

$$A(0) = 0, \tag{2}$$

and an asymptotic behavior at $x = +\infty$ dictated by the fact that the system is stable at infinity with a single minimum of the potential when $A = 0$.

$$A(+\infty) = 0. \tag{3}$$

The bifurcation parameter is assumed to depend linearly on the space variable x

$$\mu(x) = \mu_0 - \mu_1 x \tag{4}$$

where μ_0 and μ_1 are positive constants. This choice of a linear dependence is similar to the one used in [16,21,22] to study the linear global stability. It allows to give a concrete and quantitative example but does not restrict the generality of the study which remains valid as long as $\mu(x)$ is any decreasing function depending on x only through a slow space variable $X = \mu_1 x$. Therefore, μ_1 defines the inhomogeneity length scale $L = \mu_1^{-1}$.

Throughout this study we are going to compare the effect of inhomogeneity and nonlinearity. A practical and physical way to do so will be to associate to nonlinearity and nonparallelism a specific length scale that we are going to express. Once each physical effect will be identified and quantified by an associate length scale, the structure of the global mode and the dominant effect will be obvious.

The variation of $\mu(x)$ defines the region where the flow is linearly stable as the distance $x_0 = \mu_0/\mu_1$ at which $\mu(x_0) = 0$. As for the advection velocity, we assume that μ_0 is of order one and the size of this linearly stable region scales as the inhomogeneity length $x_0 \sim L$. The linear theory of absolute and convective instability allows us to define the threshold of absolute instability as a function of the advection velocity, *i.e.* the value

$$\mu_A \equiv \frac{U_0^2}{4} \tag{5}$$

above which the basic uniform state $A = 0$ is linearly unstable with waves growing and contaminating the entire medium. At the origin of the semi-infinite domain, we assume that the bifurcation parameter is greater than μ_A: $\mu_0 = \mu_A + \epsilon$, *i.e.* we assume that a finite region of absolute instability exists near the origin. As for the linear stability, we define the size of the absolute region x_A as the distance at which $\mu(x_A) = \mu_A$. We may now deduce this boundary of the locally absolute domain x_A:

$$x_A = \frac{\epsilon}{\mu_1} \tag{6}$$

Throughout this study in the case $\mu_1 \neq 0$, we will not only use a weakly nonparallel hypothesis ($\mu_1 \ll 1$), but also a stronger condition ensuring that nonlinearities

dominates over nonparallelism in a sense that will be rigorously defined through the matching but that we are going to precise with physical arguments. The problem faced here is the nonuniform limit $\mu_1 \to 0$ and $\epsilon \to 0$ which imposes to define the range of variation for μ_1 compared to ϵ.

Let us denote by x_s the position of the maximum amplitude of the NG mode (see Figure 1). Actually, the scaling for x_s is unknown and part of this study is to determine this scaling by comparison with all the linear or nonlinear length scales which might play a role. When the nonlinearity are weak compared to inhomogeneity as in the study by Le Dizès *et al.* [19], The global mode may be described by a linear solution of Equation (1) with the required boundary conditions and its maximum simply determined by the root of its derivative is found to be located at a position wich scales like L. This exact result $x_s \sim L$ is sketched in Figure 2(a). To estimate the conjugated effect of nonlinearity, instability and advection in term of a length scale is in general not easy but in the present case, we will take advantage that when $\mu_1 = 0$ (parallel flow case), we know from the study of the homogeneous case [24] the spatial structure of steady solutions of (1) vanishing at the origin and saturating at a finite amplitude when $x \to +\infty$. In order to avoid confusion, these solutions for which the bifurcation parameter does not vary with respect to x, will be denoted "homogeneous" nonlinear global (HNG) modes throughout the study. Please note that they are asymptotic to $A_2 = \sqrt{\mu}$ at infinity. For Equation (1), their existence has been shown to be limited to the range $\mu > \mu_A$, where $\mu_A \equiv U_0^2/4$ represents the absolute instability threshold.

In this case, the linear absolute/convective transition and the nonlinear global instability are simultaneous. In [24], we have defined the characteristic growth size of HNG modes as the distance at which the solution reaches 99% of its maximum amplitude A_2, and we have determined the scaling of Δx as a function of the departure from global instability threshold $\epsilon = \mu - \mu_A$ has been shown to be such that

$$\Delta x \simeq \frac{1}{\sqrt{\epsilon}}. \tag{7}$$

When inhomogeneity describes at first order the departure of the NG mode from its homogeneous counterpart, we should obtain $x_s \gg \Delta x$ (Figure 2(b)). By contrast, when the departure of the NG mode from its homogeneous counterpart is described by the criticality parameter ϵ at first order, x_s should be of the same order of magnitude as Δx (Figure 2(a)).

To precise these two arguments, let us first assume that the growth size of HNG modes is sufficiently small in comparison with the inhomogeneity length scale $\Delta x \ll \mu_1^{-1}$. Intuitivelly, under this hypothesis, the solution will initially (in space) grow as if the flow was homogeneous and once the saturated amplitude reached, it will follow adiabatically the saturated amplitude $A_2 = \sqrt{\mu(x)}$ til $\mu(x) = 0$ where the flow will be stable and the amplitude almost nil. This typical evolution

is reported on Figure 1(c). Using the growth size scaling (7) for homogeneous NG modes, our hypothesis that Δx must be much smaller than the inhomogeneity length scale L reads

$$\Delta x \ll L \ (\sim x_0) \quad \Rightarrow \quad \frac{1}{\sqrt{\epsilon}} \ll \frac{1}{\mu_1} \quad \Rightarrow \quad \epsilon \gg \mu_1^2 \tag{8}$$

This assumption excludes the region below the line $\epsilon = \mu_1^2$, in the plane (ϵ, μ_1) (dashed-dotted line in Figure 2) but is not sufficient. Indeed, the length scale Δx should not only be compared to L but also to the size of the absolute region x_A.

Whether Δx is smaller or larger than x_A leads us to distinguish two regions of the parameter space (μ_1, ϵ). In the dark gray region in Figure 2, ϵ is sufficiently high so as to allow the mode to grow and saturate within the locally absolute region $\Delta x \ll x_A$ (Figure 1(c)). The description of its spatial growing part as the leading edge of an homogeneous NG mode is possible if condition (9) is satisfied:

$$\Delta x \ll x_A \quad \Longleftrightarrow \quad \frac{1}{\sqrt{\epsilon}} \ll \frac{\epsilon}{\mu_1} \quad \Rightarrow \quad \mu_1 \ll \epsilon^{3/2}, \tag{9}$$

This naive thought is fully confirmed by the analysis of section 3 where we will see that in the dark gray region in Figure 2, *i.e.* when $\mu_1 \ll \epsilon^{3/2}$, the spatial structure of the NG mode is at first order, the one of the Kolmogorov [30] front which describe the HNG mode at leading order, and the next order which has to be taken into account as long as the solution grows in space is the departure from global instability threshold $\epsilon = \mu_0 - \mu_A$, and not the inhomogeneity which acts far downstream.

In fact, condition (9) is overrestrictive and we will show that the weaker condition $\mu_1 \ll \epsilon$. is sufficient. In the region defined by $\epsilon^{3/2} \ll \mu_1 \ll \epsilon^{1/2}$ (or equivalently $x_A \ll \Delta x \ll x_0$ as shown in Figure 1(b)), inhomogeneity of the flow is no more negligible at the location where the solution saturates. As a result, a NG mode grows in space less rapidly than its homogeneous counterparts, as inhomogeneity counterbalances the departure from global instability threshold, and x_s the position of the maximum amplitude occurs far downstream than the location solely predicted by the homogeneous growth size Δx. It should be therefore possible to extend the analysis and maintain the hypothesis of scale separation between the growth size now measured by x_s and the inhomogeneity length scale as in Figure 1(b). But at this stage of the analysis scaling for x_s is unknown and the limit of validity cannot be determined. The analysis of section 3 will show that x_s scales as μ_1/ϵ^2 and therefore, the limit will be $\epsilon = \mu_1$. This result has been reported in Figure 2. Our description is therefore valid in the light as well as dark gray regions in (ϵ, μ_1) space. Relative scaling of the various length scales introduced are reported in Figure 3(a) as functions of ϵ. When the effect of the criticity ϵ dominates over the effect of inhomogeneity ($\epsilon \gg \mu_1^{2/3}$), the position x_s

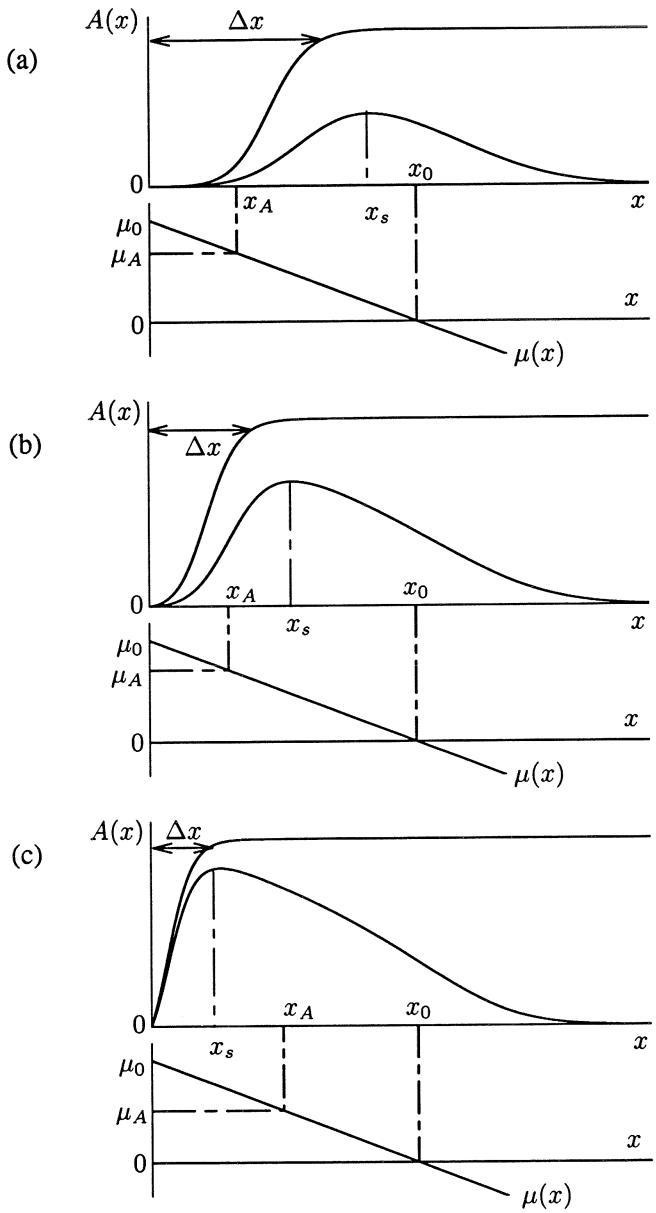

Fig. 1. Comparison of NG modes with their homogeneous counterparts. In the present study, we describe NG modes when their growing part is constituted at leading order by the leading edge of the corresponding homogeneous NG mode obtained with $\mu_1 = 0$. Their decreasing part is interpreted as the variation of the saturation amplitude $A_2(\mu)$ with respect to x, as μ is decreasing with x. $x_A \equiv (\mu_0 - \mu_A)/\mu_1$ denotes the size of the locally absolute domain. (a) When x_s approaches x_0, a linear or a WKBJ analysis [19] may describe the NG mode. (b) When Δx is greater than x_A (light gray region in Fig. 2) the inhomogeneity modify the HNG mode at first order. (c) When Δx is smaller than x_A (parameters in the dark gray region in Fig. 2), the inhomogeneity is expected to modify the HNG mode only at second order.

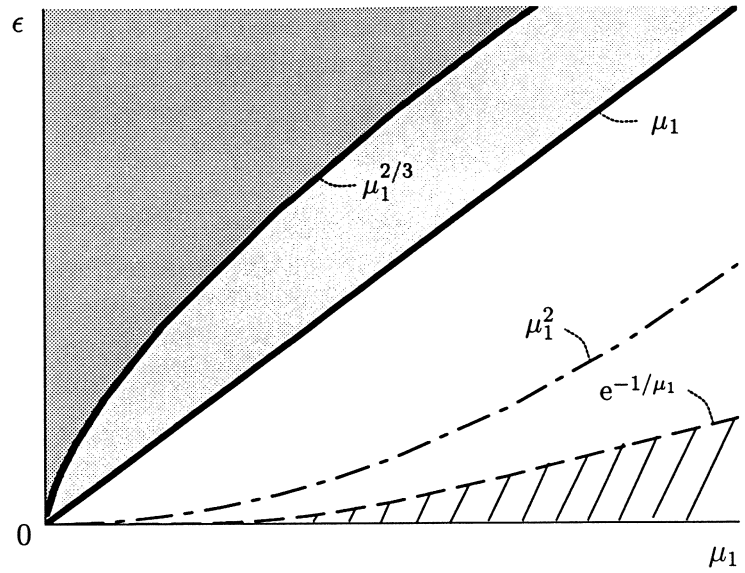

Fig. 2. Parameter space (μ_1, ϵ). Above the dashed-dotted line $\epsilon = \mu_1^2$, the growth length $\Delta x \simeq \epsilon^{-1/2}$ of homogeneous NG modes is smaller than the inhomogeneity length scale L. The gray regions indicate where the present fully nonlinear and weakly inhomogeneous description applies. In the dark gray region, the maximum amplitude position x_s of NG modes scales like the growth length $\Delta x \simeq \epsilon^{-1/2}$ of homogeneous NG modes (Figure 2(c)). In the light gray region, the present study will show that x_s is greater than Δx, scales as μ_1/ϵ^2 and remains smaller than the inhomogeneity length scale (Figure 2(b)). The whole analysis presented below shows that the fully nonlinear description cannot be done in the white region ($\epsilon \ll \mu_1$), (Figure 2(a)). In the hatched region, the weakly nonlinear theory on linear global modes described by a WKBJ approximation [19] is valid.

of the maximum amplitude scales like Δx (continuous line). Both length scales are smaller than x_A (dashed-dotted line). By contrast, inhomogeneity may bring a dominant contribution (if $\mu_1 x_s \gg \epsilon$) and when decreasing ϵ from $\mu_1^{2/3}$, x_s grows faster than Δx (Δx in dashed line). Both x_s and Δx are greater than x_A.

In order to cover the regions above the $\epsilon = \mu_1^2$ line in (ϵ, μ_1) space, the inhomogeneity parameter and the departure from global instability threshold ϵ are therefore assumed to be connected by the relation

$$\mu_1 = \epsilon^n \tag{10}$$

with $1/2 < n < 3/2$ between the dashed-dotted line and the heavy continuous line $\epsilon = \mu_1^{2/3}$ in Figure 2, and $n > 3/2$ in the dark gray region. The slope of the continuous straight line $\epsilon = \mu_1$ which corresponds to $n = 1$ will be obtained during the analysis.

Our goal is to obtain a uniform convergence in μ_1 and ϵ in both the dark and the light gray region and to describe the spatial structure of NG modes in each

of these regions. In particular, in the light gray region, for a given n, we seek a scaling law for the position of the maximum amplitude in the form

$$x_s \simeq \frac{s}{\mu_1^{\gamma}}, \tag{11}$$

where s is a constant to be precised later. As may be expected, in the dark gray domain, we will find that $x_s \simeq \epsilon^{-1/2} = \mu_1^{-1/2n}$ as for homogeneous NG modes, but in the light gray domain, x_s will be found to exceed $\epsilon^{-1/2}$. Figures 3(a) and 3(b) set out the main question we wish to answer: n is the power linking μ_1 and ϵ. What is the power γ (with respect to n) of the scaling law for x_s ? When μ_1 is fixed and ϵ is varied (equivalently n is varied), the position of the maximum x_s is represented as a function of ϵ in Figure 3(a); the power γ is represented as a function of n in Figure 3(b).

When $n > 3/2$, (dark region of Figure 2), inhomogeneity of the medium do not affect the position of the maximum amplitude which scales as $\epsilon^{-1/2}$ like the growth size of homogeneous NG mode (Figure 3(a)). Hence $\gamma = 1/2n$, as represented by the continuous line in Figure 3(b). This remains true until the maximum amplitude is reached in the locally convective region $x_s > x_A$ (Figure 3(a)), or equivalently $\gamma < 1 - 1/n$ (Figure 3(b)). The latter conditions are represented by the dotted-dashed lines, which intersect the continuous curves when $x_s = x_A$ at $\epsilon = \mu_1^{2/3}$ in Figure 3(a) and at $n = 3/2$ in Figure 3(b). Therefore, when $x_s > x_A$, the dashed line Δx in Figure 3(a) no longer represents the scaling of x_s. The present analysis will show that the new scaling for x_s is μ_1/ϵ^2 as long as it remains smaller than the inhomogeneity length scale, *i.e.* for $\epsilon \gg \mu_1$. Similarly in Figure 3(b), when $1/2 < n < 3/2$, the dashed line $\gamma = 1/2n$ no longer represents the appropriate power of the scaling law for x_s. Instead, we must find the new power law represented by the continuous part of curve for $n < 3/2$ in Figure 3(b). Since with this new γ, we must obtain an x_s (Equation 11) still smaller than the inhomogeneity length scale, this leads to a new limit which will turn to be $\gamma = 1$, for which our hypothesis breaks down.

3 Spatial structure of NG modes

Figure 4 represents an example of NG mode obtained by temporal numerical simulation of Equation (1) with (2) and (3). Initially, the system is in the uniform state $A = 0$ and an infinitely small perturbation is added at some location. The amplitude grows and saturates. When it has reached a steady state, the asymptotic solution obtained is a NG mode which satisfies

$$\frac{d^2A}{dx^2} - U_0\frac{dA}{dx} + (\mu_0 - \mu_1 x)A - A^3 = 0, \tag{12}$$

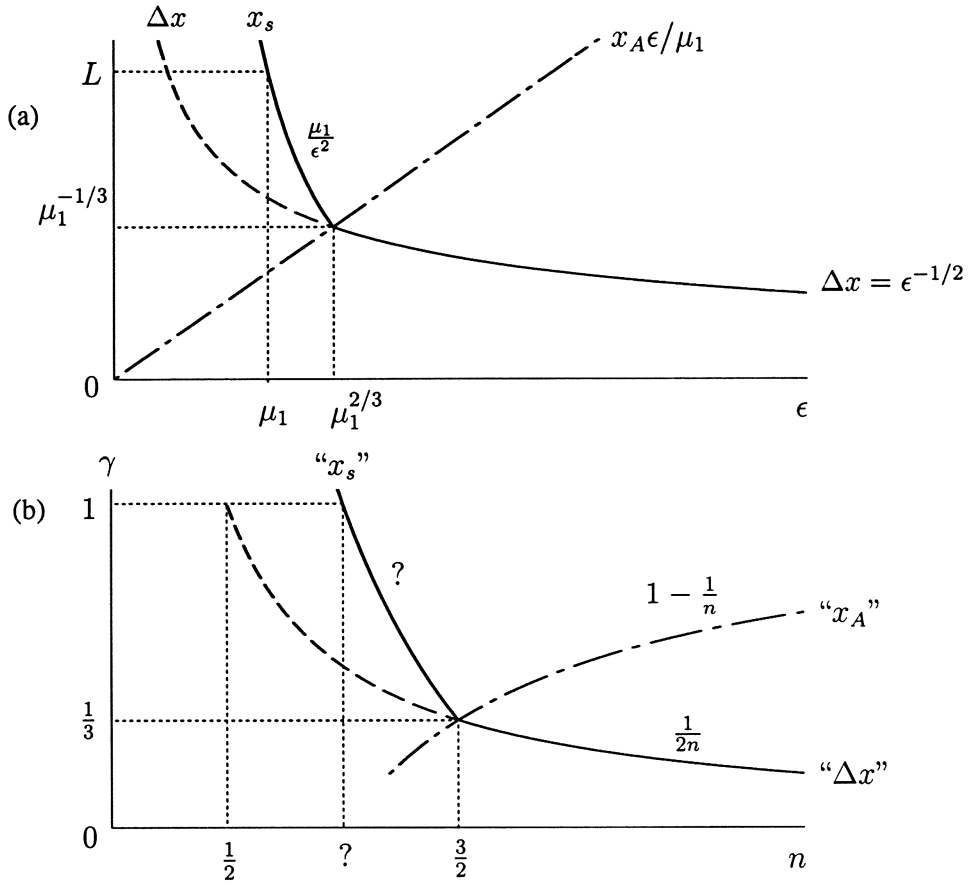

Fig. 3. (a) Position of the maximum x_s (continuous line) as a function of the departure from the NG instability threshold ϵ, for a fixed μ_1. (b) Critical exponent γ of the position of the maximum amplitude of NG modes x_s (Eq. (11)) versus the power n linking ϵ and μ_1 (Eq. (10)). In (a) and (b), the intersection of dotted dashed curves with the continuous curve represent the boundary between the dark gray and light gray regions in Fig. 2 and corresponds to $x_s = x_A$. Below the dashed–dotted line (dark gray domain in Fig. 2), $x_s \simeq \epsilon^{-1/2} = \mu_1^{-1/2n}$ as for homogeneous NG modes. Above the dashed–dotted line (light gray region in Fig. 2), x_s scales as μ_1/ϵ^2 and reflects the influence of the inhomogeneity in the medium. $\gamma < 1$ corresponds to the hypothesis $x_s \ll L$.

with vanishing amplitude at the origin and at infinity. The spatial structure of the NG modes will be described using the method of matched asymptotic expansions [31]. We distinguish six subdomains in the original semi-infinite domain represented on Figure 4.

In KF, the solution grows in space till it reaches its maximum amplitude. This subdomain has been already described for homogeneous global modes in [24] (parallel flow case) which are given at leading order by the Kolmogorov front solution [30]. The central nonlinear layer (CNL) denotes the subdomain where the solution is locally saturated *i.e.* equals the finite amplitude state A_2 and follows adiabatically the slow variation of the bifurcation parameter $\mu(x)$ (non-

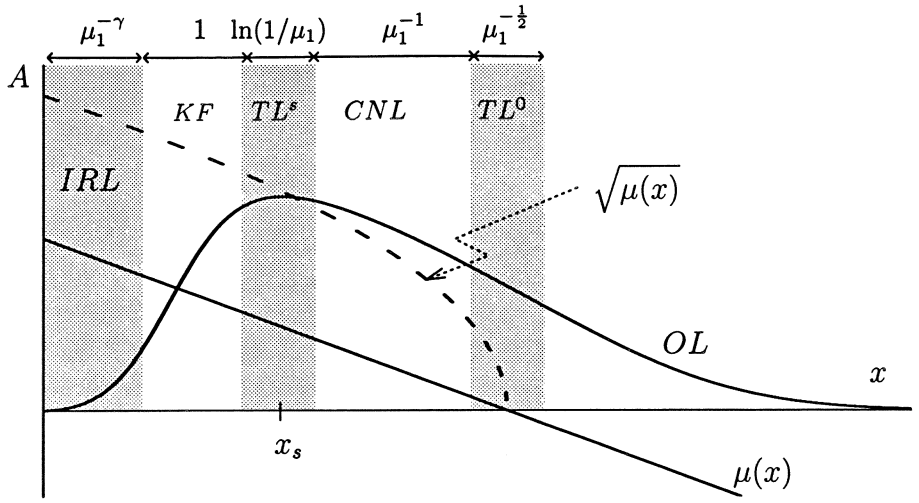

Fig. 4. Asymptotic solution of (1–3). The bifurcation parameter $\mu(x)$ is represented by the straight line. In the original semi-infinite domain, three transition layers (the inner resonant layer IRL at the origin, TL^s around the maximum amplitude and TL^0 near the point x_0 where $\mu(x_0) = 0$) allow to connect linear and nonlinear regions; CNL denotes central nonlinear regions and OL is an outer linear region.

linear WKBJ approximation with variation on the scale μ_1^{-1}). In the outer layer at $+\infty$ (OL), the amplitude is small since the flow is stable there. The linear theory applies and the linear WKBJ approximation applies as the wave follows the wavenumber spatially damped to the right, traditionally [10,9] called k^+.

In each subdomain, we need two boundary conditions in order to find the corresponding solution of (12). We only know the boundary conditions at the origin and at infinity of the whole domain. Introduction of the inner resonant layer IRL at the origin and of the transition layers TL^s around x_s, TL^0 around the point x_0 where $\mu = 0$, and matching between different layers allow to determine all integration constants. A specific name has been given to the initial layer at $x = 0$ as this layer is (at least partially) embedded in the absolutely unstable region and the corresponding degeneracy of wavenumber (for small ϵ) allows to fulfill the boundary condition at threshold. Only for $\mu > \mu_A$, the solution in the inner resonant layer allows the trajectory matched with the solution in the KF layer to cross the $A = 0$-axis with $dA/dx \neq 0$, as this requires the beating of "two waves" in this layer. In a way, this layer plays the role of the master oscillator and therefore should be partially embedded in the absolutely unstable region as already intuitively assumed. Let us start the matching from the central nonlinear layer CNL whose right boundary is located at x_0. Matching of the trailing edge of the NG mode in TL^0 and OL turns out to be not coupled to the rest of the matching. Therefore the spatial structure of NG modes will be described starting from CNL and proceeding towards TL^s, KF, IRL, the description of the trailing edge in TL^0 and OL being saved for appendix A.4, since these two layers are slaves of the structure of the NG mode in CNL. The detailed structure of the NG mode represented in Figure 4 will be described for each layer in the appendix A. In the

following, we indicate only briefly the nature of the solutions in each layers and we focus on the description of the NG mode in the transition layer IRL which is the key layer for this matching. Indeed, the matching between this layer and KF determines the dominant part in the scaling law for the position of the maximum amplitude x_s, which will be compared with experimental and numerical results of [1,2] in section 5.

3.1 Qualitative description of NG modes

For convenience, the structure of the layers and the principle of their matching will be described in the reversed order from $+\infty$ to 0, from the simplest to the hardest.

3.1.1 The downstream part: matching OL to CNL via TL^0

In OL, the solution is strongly linearly damped; nonlinear terms in Equation (12) are neglected and the solution reflects the interplay of advection and inhomogeneity as the product of a shifted Airy decreasing function with an exponential term (advection) (see Equation (A.21)). It may be also viewed as the linear WKBJ solution which follows adiabatically the variation of the linear wavenumber.

In the transition layer TL^0 of size $\mu_1^{-1/2}$, the basic state is nearly locally neutral; nonlinearities, advection and inhomogeneity possess the same order of magnitude ($\sim \mu_1^{1/4}$) in Equation (12) and the corresponding solution matches both solutions in CNL and OL. At this stage, note that the matching in TL^0 fixes the position of the layer TL^0 around the point x_0, but does not give any information about the position of the maximum x_s (which is two layers away).

3.1.2 The central part

In the central nonlinear layer CNL (of size μ_1^{-1}), the NG mode amplitude is saturated; it follows adiabatically the variation of μ and decreases slowly from its maximum at x_s to a small amplitude ($\sim \mu_1^{1/4}$) at which the solution must be matched with the linear outer solution of Equation (12) in OL. The amplitude in CNL is approximately the weakly decreasing function $A \sim \sqrt{\mu_0 - \mu_1 x} = \sqrt{\mu(x)}$, for which the slope remains small at each station. It reflects the interplay of nonlinearities and inhomogeneity and can be formulated as the nonlinear WKBJ solution of the problem.

At the upstream part of CNL, the amplitude is close to its maximum value. Since we assume that the distance from the origin to x_s the position of the maximum amplitude is much smaller than μ_1^{-1}, the maximum amplitude is at first order

$\sqrt{\mu_0} \simeq \sqrt{\mu_A}$. In the transition layer TL^s around x_s, the amplitude is then a linear solution of Equation (12) linearized around $A = \sqrt{\mu_A}$. Since Equation (12) is of second order, we must determine two integration constants. One is given by the matching with the solution in CNL, and the condition that x_s realizes a maximum of the amplitude yields the second one.

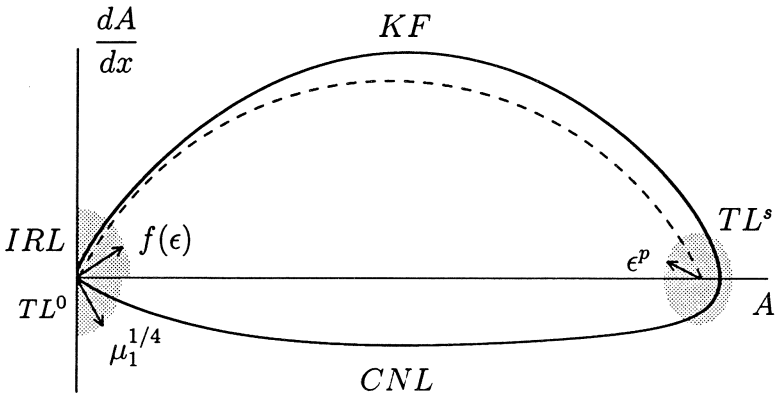

Fig. 5. The projection of the phase space in the plane $(A, dA/dx)$ shows the different layers (the transition layers being in gray). TL^1 (of size $f(\epsilon)$ given in Eq. (20,26)) and TL^s (of size ϵ^p) allow respectively to satisfy the boundary condition at the origin and to connect in the phase space the solution in CNL^- to the point of maximum amplitude. The decreasing part of the NG mode ($dA/dx < 0$) is close to the (A, x) plane of phase space and the matching of this part of the trajectory is then done in the physical space.

Up to now, matchings have been realized in the physical space as the variations in OL, TL^0, CNL, and TL^s were slow. But the phase space $(A, dA/dx)$ has to be invoked in order to realize the last matching and to represent the solution in a more physical way, as in the Kolmogorov front layer, the variations of A are fast. Figure 4 may be thought as the projection in the plane (A, x) of the three-dimensional trajectory representing the NG mode in the phase space $(A, dA/dx, x)$, whereas Figure 5 presents the same trajectory but projected on the plane $(A, dA/dx)$. The different scales on Figures 4 and 5 show that from x_s to $+\infty$ in the decreasing part of the trajectory, the NG mode evolves slowly; therefore dA/dx keeps being small and the trajectory lay nearly in the (A, x) plane of the phase space and the slow variable $X = \mu_1 x$ could have been used to present this part of the trajectory. But when considering the growing part of the NG mode ($x < x_s$), since $x_s \ll \mu_1^{-1}$ by assumption, x does not vary much on the scale μ_1^{-1} and the trajectory in the phase space is now close to the plane $(A, dA/dx)$, close meaning that the distance from the plane $(A, dA/dx)$ is small when measured in $X = \mu_1 x$ variable. The solution in KF then takes the form of a front linking a small amplitude to $\sqrt{\mu_A}$, which is reminiscent of the shape of homogeneous NG mode [24] in the parallel flow case, described in the phase space $(A, dA/dx)$ as the stable manifold of a saddle fixed point $(A_2, 0)$. This stable manifold is itself viewed as the perturbation of an heteroclinic trajectory linking the origin $(0, 0)$ of phase space to the point $(A_2 = \sqrt{\mu_A}, 0)$ and representing the

Kolmogorov front solution in an infinite homogeneous domain (presented in interrupted lign in Figure 5). When $\mu = \mu_A + \epsilon$, the perturbed trajectory defines an homogeneous NG mode which links in the phase space, a point of the dA/dx-axis to $(A_2, 0)$. When considering the effect of inhomogeneity, we must take into account a new perturbation in this trajectory by introducing corrective terms in μ_1 and $\mu_1 x$ in the basic front solution at threshold.

In our three dimensional phase space, the solution in KF is described as a series expansion of dA/dx in A with coefficients depending on x:

$$u(A) = \frac{dA}{dx} = \sum_{j=0}^{+\infty} \left(-\nu_j - \epsilon\lambda_j + \mu_1(\zeta_j + \eta_j x)\right)(A_2 - A)^j, \tag{13}$$

where ν_j, λ_j, ξ_j, η_j are constant. Terms of order ϵ may be larger than terms in $\mu_1 x$, but the contrary may also happen when $x > x_A = \epsilon/\mu_1$. This comparison of orders in the first correction of the basic front solution in KF leads to the distinction of the white and light gray regions in Figure 2. The matching between KF and TL^s (done in the phase space), determines the first coefficients in the series (13), allowing to compute other coefficients recursively. In practise, the coefficients expressed as an analytical formula have to be computed numerically. Note that when this matching is done, we obtain the result that x_s must be at least greater than the size $\ln(1/\mu_1)$ of TL^s. After having computed the set of coefficients in Equation (13), we know the asymptotic behavior of $u(A)$ when $A \to 0$:

$$\begin{aligned} u(A) \simeq & -\sum_{j=1}^{+\infty} \nu_j A_2^j + \sum_{j=1}^{+\infty} j\nu_j A_2^{j-1} A \\ & + \mu_1 x \sum_{j=0}^{+\infty} \eta_j A_2^j - \epsilon \sum_{j=0}^{+\infty} \lambda_j A_2^j + \mu_1 \sum_{j=0}^{+\infty} \zeta_j A_2^j. \end{aligned} \tag{14}$$

We now proceed to the detailed description of the solution in IRL.

3.2 Spatial structure of NG modes in the inner resonant layer IRL

In this layer, the amplitude is small since A vanishes at $x = 0$. Denoting ξ the inner variable which is connected to the amplitude by the relation $A = f(\epsilon)\xi$, where $f(\epsilon) \to 0$ as $\epsilon \to 0$, ξ satisfies the linearized Equation (12) around $A = 0$:

$$\xi'' - U_0 \xi' + \mu(x)\xi = 0. \tag{15}$$

Since $\xi(x)$ must vanish at the origin, the solution of Equation (15) may be written with one undetermined integration constant v_0, and using Airy functions [32]

$$\xi(x) = \frac{v_0 \pi}{\mu_1^{1/3}} \, \mathrm{e}^{\frac{U_0}{2}x} \left(a \, \mathrm{Bi}\left((x - x_A)\mu_1^{\frac{1}{3}} \right) - b \, \mathrm{Ai}\left((x - x_A)\mu_1^{\frac{1}{3}} \right) \right) \tag{16}$$

where $x_A = \epsilon/\mu_1$ denotes as previously the size of the absolute domain, $a = \mathrm{Ai}\left(-x_A \mu_1^{1/3}\right)$ and $b = \mathrm{Bi}\left(-x_A \mu_1^{1/3}\right)$. The slope v_0 at the origin of the inner solution (16) will be fixed by the matching.

3.2.1 Matching $IRL \to KF$ in the case $\mu_1 \ll \epsilon^{3/2}$

In the case $\mu_1 \ll \epsilon^{3/2}$ (or equivalently in the dark gray region in Figure 2, and $n > 3/2$ range of Figure 3), since $x_A {\mu_1}^{1/3} = \mu_1^{1/n-2/3} \to -\infty$ and $(x - x_A)\mu_1^{1/3} \to -\infty$, Airy functions may be expanded using their asymptotic behavior at $-\infty$. We find again the inner solution already found for homogeneous global modes [24]

$$\xi(x) = \frac{v_0}{\sqrt{\epsilon}} \, \mathrm{e}^{\frac{U_0}{2}x} \sin\left(\sqrt{\epsilon}\, x\right). \tag{17}$$

Keeping in mind the condition $\mu_1 \ll \epsilon^{3/2}$, *i.e.* that in this domain, the NG mode must reach its maximum before the boundary of the absolute domain ($x_s \ll x_A$), we obtain that order ϵ must be lower than order of terms in $\mu_1 x$ (and μ_1), (whatever the scaling law for the position of the maximum amplitude) and necessarily:

$$x_s \sim \mu_1^{-\gamma} < x_A = \mu_1^{1-1/n} \qquad \text{or} \qquad \gamma < 1 - \frac{1}{n}, \tag{18}$$

which is the domain below the dashed-dotted line in Figure 3. The matching may then proceed with the same scaling laws than for homogeneous NG modes. As $x \to \pi\epsilon^{-1/2}$, solution (17) admits in the phase space the asymptotic behavior: [1]

$$\frac{d\xi}{dx} \simeq \frac{U_0}{2}\xi - v_0 \, \mathrm{e}^{\frac{U_0}{2}\frac{\pi}{\sqrt{\epsilon}}}. \tag{19}$$

Introducing $A = f(\epsilon)\xi$ in the inner expansion (19) and identifying with the expansion (14) in KL leads to the choice of the size of IRL (in the phase space):

$$f(\epsilon) = \epsilon \, \mathrm{e}^{-\frac{U_0}{2}\frac{\pi}{\sqrt{\epsilon}}}, \tag{20}$$

[1] $\Delta x \simeq \pi\epsilon^{-1/2}$ is the characteristic growth size of homogeneous NG modes.

and to the following matching conditions:

$$\sum_{j=1}^{+\infty} \nu_j A_2^j = 0, \qquad \sum_{j=1}^{+\infty} j\nu_j A_2^{j-1} = \frac{U_0}{2}, \qquad \sum_{j=0}^{+\infty} \lambda_j A_2^j = v_0. \tag{21}$$

Terms in $\mu_1 x$ (and μ_1) have not to be matched since the whole matching is done at leading order, and as expected the spatial structure of NG modes is fully consistent with the one of homogeneous NG modes.

3.2.2 Matching $IRL \to KF$ in the case $\epsilon^{3/2} \ll \mu_1 \ll \epsilon^{1/2}$

In the case $\epsilon^{3/2} \ll \mu_1 \ll \epsilon^{1/2}$ (or equivalently in the light gray region in Figure 2, and in the white region above $\epsilon = \mu_1^2$, $1/2 < n < 3/2$), since $n < 3/2$, we obtain $x_A {\mu_1}^{1/3} = {\mu_1}^{1/n-2/3} \to 0$. In the upstream part of KF and downstream part of IRL where both solutions match, terms of order $\mu_1 x$ may be larger than order ϵ (above the dashed–dotted line $\gamma > 1 - 1/n$ of Figure 3(b)) and must be taken into account first. The matching will be done for $x \simeq s/\mu_1^\gamma$ at a greater distance[2] than the one obtained for $n > 3/2$. This condition equivalent to $\Delta x \ll x_s$ leads to

$$\frac{1}{\mu_1^\gamma} \gg \frac{1}{\sqrt{\epsilon}} = \frac{1}{\mu_1^{1/2n}}, \quad \text{or} \quad \gamma \geq \frac{1}{2n} > \frac{1}{3}. \tag{22}$$

Since $(x - x_A)\mu_1^{1/3} \simeq s\mu_1^{1/3-\gamma} \to +\infty$, the solution (16) admits the asymptotic expansion

$$\frac{d\xi}{dx} \simeq \frac{U_0}{2}\xi + v_0\sqrt{\pi}\, \mathrm{e}^{\frac{U_0}{2} s\mu_1^{-\gamma}}\, \mathrm{Ai}(0)\, \left(s\mu_1^{1/3-\gamma}\right)^{1/4} \mathrm{e}^{\frac{2}{3}\left(s\mu_1^{1/3-\gamma}\right)^{3/2}}\, \mathrm{E}(\mu_1) \tag{23}$$

where $\mathrm{E}(\mu_1)$ is the remaining of the expansion of (16) which may take different forms according to the relative position of γ and n, and reads

- if $\gamma > 1/2n$ and $\gamma \neq 2/n - 1$:

$$\mathrm{E}(\mu_1) = 1 - s^{1/2}\mu_1^{1/n-\gamma/2-1/2} \tag{24}$$

- if $\gamma > 1/2n$ and $\gamma = 2/n - 1$:

$$\mathrm{E}(\mu_1) = 1 - \left(\frac{1}{4s^{1/2}} + \frac{1}{4s} + \frac{7}{48s^{3/2}}\right)\mu_1^{3/n-2} \tag{25}$$

[2] which also represents the dominant contribution in the scaling law of the position of the maximum amplitude x_s. This point is explained in section 4.

- if $\gamma < 1/2n$, matching will not be possible since we required that $x > \epsilon^{-1/2}$, when both solutions in IRL and KF match.

Using again $A = f(\epsilon)\xi$ in the expansion (23,24,25), identification with the outer expansion (14) is only possible if

$$f(\epsilon) = \mu_1^{11/12-3\gamma/4} \, \mathrm{e}^{-\frac{2}{3}\left(s\mu_1^{1/3-\gamma}\right)^{3/2}} \, \mathrm{e}^{-\frac{U_0}{2} s\mu_1^{-\gamma}} \tag{26}$$

and

$$\gamma = \frac{2}{n} - 1. \tag{27}$$

The matching conditions give v_0 and s which satisfy

$$s = \left(\frac{1+4R}{2} + \frac{1}{2}\left((1+4R)^2 + \frac{7}{3} \right)^{1/2} \right)^2, \quad \text{with} \quad R = \frac{\sum_{j=0}^{+\infty} \lambda_j A_2^j}{\sum_{j=0}^{+\infty} \eta_j A_2^j} \tag{28}$$

$$v_0 = -\frac{s^{3/4}}{\pi^{1/2}\mathrm{Ai}(0)} \sum_{j=0}^{+\infty} \eta_j A_2^j. \tag{29}$$

The equation (27) is represented by the continuous line in Figure 3(b) for $n < 3/2$. When $n = 1$, we find $\gamma = 1$, and this restricts a posteriori the domain of validity of our analysis to the range $1 < n < 3/2$. When $n \to 1$, the position of the maximum $x_s \to s/\mu_1$ and becomes of the same order than the inhomogeneity length scale. This corresponds to the case shown in Figure 1(c) for which the structure we have postulated for the NG mode (dominated by nonlinearity) breaks down. Our analysis describing a fully NG mode in a weakly inhomogeneous medium as a perturbed front solution is therefore only valid when $n > 1$, i.e. for $\mu_1 \ll \epsilon$ in the gray regions in Figure 2. The conclusion of this section is that in Figure 2, we have distinguished the dark gray region for which inhomogeneity modifies only the tail of the homogeneous nonlinear global mode and not its leading edge, from the light gray region where inhomogeneity acts strongly on the leading edge as well as on the tail of the HNG mode. However, in the front region (KF), the variation of the amplitude remains dominated by nonlinearity. In both cases, the IRL layer is crucial as the particular form of the solution in this layer allows to respect the boundary condition by the beating of two waves.

4 Scaling laws for x_s and for the maximum amplitude

The matching has been shown to be possible when $\mu_1 \ll \epsilon$. We now proceed to the description of the scaling laws directly given by the matching for the maximum

amplitude and its position.

In the transition layer IRL, the solution grows til the inner amplitude becomes of order one, i.e. on a distance which scales like $\mu_1^{-\gamma}$ with $\gamma = 1/2n$ if $n > 3/2$ and $\gamma = 2/n - 1$ if $1 < n < 3/2$. In the Kolmogorov front region KF, the NG mode keeps growing till $A = A_2 - \epsilon^p$, (or til the upstream part of TL^s where the rescaled inner amplitude is of order one; see appendix A.2); The contribution of this layer TL^s in which the solution saturates, to the characteristic growth size scales like $\ln(1/\epsilon)$ (or equivalently $\ln(1/\mu_1)$) because of the exponential dependence of the amplitude (see Equation (A.9)). Thus, the total growth size is determined at the lowest order by the inner resonant layer and reads

$$x_s \simeq \frac{\pi}{\sqrt{\epsilon}} \quad \text{if} \quad \mu_1 \ll \epsilon^{3/2}, \quad \text{i.e.} \quad x_s \simeq \Delta x \ll x_A \ll L \tag{30}$$

$$x_s \simeq \frac{s\mu_1}{\epsilon^2} \quad \text{if} \quad \epsilon^{3/2} \ll \mu_1 \ll \epsilon, \quad \text{i.e.} \quad x_A \ll \Delta x \ll x_s \ll L, \tag{31}$$

where s is given by (28). The maximum amplitude is reached in TL^s. The detailed structure of the NG mode in this layer is given in appendix A.2 as a small correction to the saturation amplitude $A_2 \equiv \sqrt{\mu_A}$ of homogeneous NG modes. From Equation (A.11), we obtain immediately the maximum amplitude of the global modes which reads

$$A_s \simeq \sqrt{\mu_A} + \epsilon\frac{1}{2\sqrt{\mu_A}} - \frac{\mu_1}{\sqrt{\epsilon}}\frac{\pi}{2\sqrt{\mu_A}} \quad \text{if} \quad \mu_1 \ll \epsilon^{3/2}, \tag{32}$$

$$A_s \simeq \sqrt{\mu_A} - \frac{\mu_1^2}{\epsilon^2}\frac{s}{2\sqrt{\mu_A}} + \epsilon\frac{1}{2\sqrt{\mu_A}} \quad \text{if} \quad \epsilon^{3/2} \ll \mu_1 \ll \epsilon. \tag{33}$$

The maximum amplitude is only slightly modified with regard to the maximum amplitude $\sqrt{\mu_A + \epsilon}$ valid for HNG modes. This is not surprising since our fully nonlinear hypothesis implies that we have to remain sufficiently far from threshold in order for the inhomogeneity to act as a perturbation on the homogeneous fully nonlinear case. Moreover, Equations (32,33) are fully consistent with the extrapolation:

$$A_s \sim A_2(x_s) \simeq \sqrt{\mu_0 - \mu_1 x_s} \simeq \sqrt{\mu_A} + \frac{1}{2\sqrt{\mu_A}}(\epsilon - \mu_1 x_s) \tag{34}$$

and introduction of (30,31) into expansion of (34) in powers of ϵ yields exactly Equations (32,33).

5 Comparison with experimental and numerical results in wakes

In [1], Goujon-Durand *et al.* have studied experimentally the evolution of the global mode issued from the destabilization of the wake behind a trapezoidal bluff body. They have measured the streamwise and the crosswise velocity on the axis and at one diameter off the axis for a large region of streamwise location. Repeating this measurement for several Reynolds numbers R (*i.e.* increasing the mean flow velocity), they have shown the existence of a universal curve for the renormalized amplitude of the streamwise velocity profile. They have rescaled the amplitude by its maximum value and the streamwise coordinate by the position of the maximum and they have found that the data collapse to a single curve (Figure 8(a)). They have proposed the following scaling laws for the maximum amplitude value A_s and position x_s which fit their measurements:

$$A_s \simeq A_0 (R - R_c)^{1/2}, \tag{35}$$

$$x_s \simeq (R - R_c)^{-1/2}, \tag{36}$$

where $R - R_c$ denotes the departure from critical Reynolds number R_c for the occurrence of the global mode, R_c being experimentally determined by plotting A_s^2 versus R. In [2], Zielinska and Wesfreid have presented results from two dimensional numerical simulations of wake flow behind a triangular obstacle and confirmed the experimental results of Goujon-Durand *et al.* [1]. In particular, the form of global modes and their dependence on the Reynolds number found numerically were in agreement with the scaling laws (35), (36) given in [1]. The universality of these scaling laws is reinforced by the fact that a different body has been used in the two studies (triangular in [2] and trapezoidal in [1]). Only when the wake is confined by side boundaries at ± 5 diameters, the rescaled global mode shape appears to vary with R.

Direct comparison of those real two-dimensional flow dynamics with our oversimplified model might seem unrealistic but as for oblique shedding [28], the scenario and behavior obtained with our toy model applies amazingly well to the real world. Once the idea of a comparison between model and reality accepted, we still face the problem that the nonparallelism of the flow (measured in the model by μ_1) is finite and depends on the Reynolds number which itself defines the instability of the flow measured by ϵ in the model. Therefore, for the wake flow, μ_1 and ϵ are linked to a single control parameter R and the representative point corresponding to real experiment in the (μ_1, ϵ) plane (Figure 2) will move on a lign parametrized by R for which ϵ will go to zero while μ_1 will stay finite at threshold. For large enough ϵ, the representative point $(\mu_1(R), \epsilon(R))$ will always enter the gray domain of Figure 2 where the theory we have developed applies indeed uniformly, but only when (μ_1, ϵ) goes to zero! We shall therefore extrapolate the results we have derived using asymptotic theory (WKBJ) to finite value of (μ_1, ϵ) and compare to numerical simulation of (1) to test their range of validity

before comparison with experiments.

The experimentally and numerically obtained [1,2] scaling law (36) for the position of the maximum corresponds to the one found theoretically for the amplitude equation (Equation (30)). To compare with (35), the scaling laws for the maximum amplitude (32) or (33) have been extrapolated by considering that A_s is a function of the parameters ϵ and μ_1 which are no longer connected through the relation $\mu_1 = \epsilon^n$. In the expansions (32,33), we transform the sum $\sqrt{\mu_A}+\epsilon/2\sqrt{\mu_A}$ back into the unique term $\sqrt{\mu_0} = \sqrt{\mu_A + \epsilon}$. When μ_1 is kept constant and ϵ independently is brought to zero, Equations (32), (33) show that A_s becomes negative and even singular. The value of ϵ at which this extrapolated scaling laws predict a zero maximum amplitude is obtained by $A_s(\epsilon_i) = 0$ (with $i = 1,\ 3/2$) when:

$$\epsilon_{3/2} \simeq \left(\frac{\pi}{2\mu_A}\right)^2 \mu_1^2 \quad \text{if} \quad n > \frac{3}{2}, \qquad (\Delta x \ll x_A), \tag{37}$$

$$\epsilon_1 \simeq \left(\frac{s}{2\mu_A}\right)^{1/2} \mu_1 \quad \text{if} \quad 1 < n < \frac{3}{2}, \qquad (x_A \ll \Delta x \ll x_s \ll 1/\mu_1). \tag{38}$$

Keeping in mind that $\mu_1 \ll 1$, we find that $\epsilon_i \ll 1$. Therefore, as sketched on Figure 6, $A_s^2 \sim \mu_A+\epsilon-\mu_1 x_s$, with x_s given by Equations (30) or (31) (which yields (32) or (33), dashed and dotted-dashed lines) is extremely close to the scaling law (35) observed experimentally and numerically (continuous line) in [1,2].

Figure 6 has been plotted with a large value of the inhomogeneity parameter

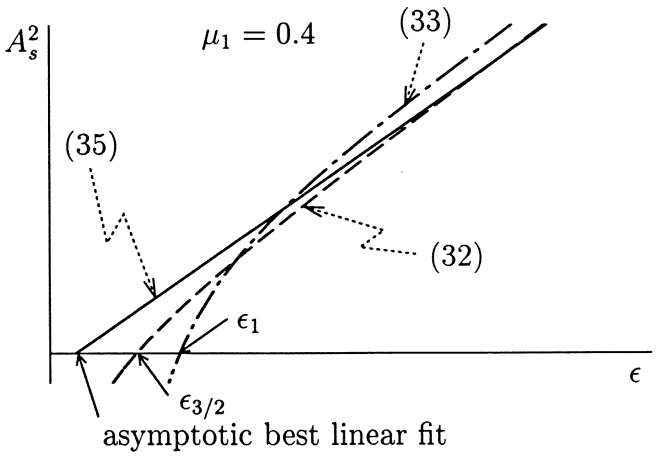

Fig. 6. Comparison of the "observed scaling law" (35) and of the scaling laws (32,33) predicted by the present theory. The continuous line represents schematically the best linear fit of the theoretical law for A_s^2 in the spirit of the studies [1,2]. The dashed line represents the theoretical result (32) and $\epsilon_{3/2}$ goes to zero when μ_1 is brought to zero. In this plot, a large value of μ_1 ($\mu_1 = 0.4$) has been used in order to show the difference, and the dashed curve is however very close to the continuous line. The dashed-dotted line represents (33) and approaches the dashed line too when $\mu_1 \ll 1$.

($\mu_1 = 0.4$) in order to show the differences between the scaling laws (32), (33) and (35). The experimentally observed scaling law (35) (continuous line) represents actually the best linear fit of the theoretical scaling laws Even with the large value of μ_1 used, the dashed curve (scaling law (32)) is close to the continuous curve.

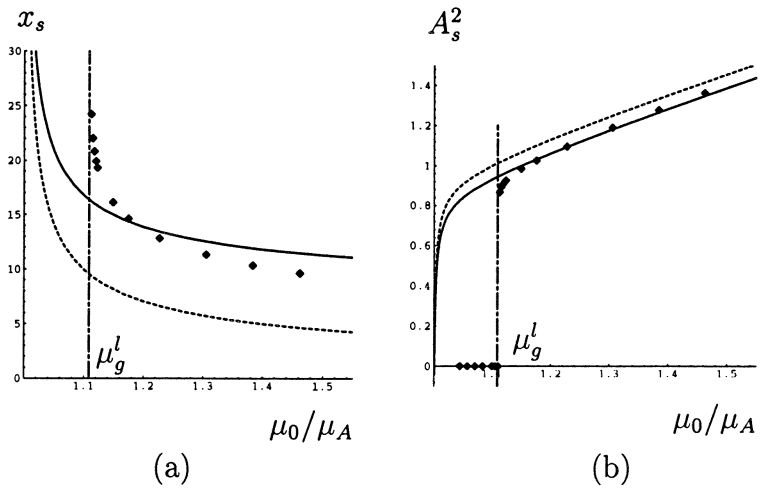

Fig. 7. (a) Comparison of the position of the maximum amplitude obtained by temporal numerical simulation of Equation (1) (dots) with the scaling law (30) (dashed line). The continuous line represents (30) with a second order contribution in $\ln(\mu_1)$ (b) Same as (a) with numerical data for the maximum amplitude compared to (32). We have used the value $\mu_1 = 0.01$ estimated from [29]. The interrupted line indicates the weakly nonlinear Landau theory with a Landau constant of 10^{-22}. It crosses the axis at the linear global threshold μ_g^l computed in [16] with respect to the local absolute threshold. When $\mu < \mu_g^l$, we have obtained that the flow relaxes to zero following the linear global mode theory [16] with $A_s = 0$ but $x_s = x_g^l \sim 106$ here.

To test the validity of the model, we have compared the scaling law (32) with results from numerical temporal simulations using a more realistic value of the inhomogeneity parameter $\mu_1 = 0.01$ which has been deduced as will be seen below from the work of Hammond & Redekopp [29]. Figure 7 shows the values of the maximum amplitude and its position as a function of the ratio of the bifurcation parameter to the threshold value μ_0/μ_A. The dots are computed in temporal simulations by the very long time behavior (up to a million time steps) of the real system (1) with 1500 points spaced by 0.1. The time marching is implicit allowing a great deal of efficiency. We have also reported the value of the shift on the linear global threshold ($\mu_g^l = \mu_A + \mu_1^{2/3}\zeta_0$, where $\zeta_0 = 2.338$ is the first zero of the Airy function) derived by Chomaz *et al* [16] using the linear theory. This threshold may be approached by the numerical data with less than 0.4 % error. Except for the shift on threshold, we obtain a good qualitative agreement between the scaling law (30) (dashed line in Figure 7(a)) and the numerical results obtained for the position of the maximum amplitude (dots). The continuous line represents the scaling law (30) with addition of the second order contribution to x_s in $\ln(\mu_1)$ computed from Equation (A.9). The scaling law (32) for the

maximum amplitude (dashed line in Figure 7(b)) is very close from the obtained numerical values and when using the second order contribution in $\ln(\mu_1)$ to x_s, the agreement is even closer (continuous line). Therefore, the results reported in Figure 7 show that scaling (30) and (32) derived theoretically using the uniform limits as ϵ and μ_1 simultaneously tends to zero, describe with good agreement the numerical solution obtained by integration of (1) using a fixed (small) value of μ_1, except in a small range above the linear global threshold. In this range simulations need a high number of time steps to reach equilibrium and therefore, the size of this range is difficult to quantify but for the value of inhomogeneity parameter used, it is less than 0.4 % and may grow when using higher values of μ_1. For this relatively small value of μ_1, the agreement of the computed location of the maximum x_s and the scaling law (theoretical in interrupted line and experimental) $x_s \simeq \epsilon^{-1/2}$ is approximately correct. On the contrary for the maximum amplitude, the linear scaling of A_s^2 with ϵ observed experimentally is not recovered as close to the threshold, the maximum is far from the origin where the linear scaling of μ in x is valid. The Landau constant given by the weakly nonlinear Landau theory developed in [18] has been computed and equals 10^{-22}. This extremely small value is represented by the interrupted line in Figure 7(a) which indicates that a departure of 10^{-22} above the linear global threshold μ_g^l is sufficient to reach order one amplitudes. This sharp transition predicted by the linear global mode theory is in agreement with the fast variation of A_s^2 shown in Figure 7(a) close to μ_g^l.

In order to show more clearly the quantitative agreement between the model (1) and the experimental observations by Goujon-Durand *et al.* and the numerical observations by Zielinska & Wesfreid [2], we have integrated Equation (1) numerically and we have now to show how one may be related to the other. We follow to that aim the derivation of Monkewitz *et al* [15]. We have used in the model (1) some scales on the amplitude, the time and the streamwise coordinate allowing to set to unity the coefficients of the diffusive term and the coefficient of nonlinearity; But if the model (1) had been derived from the full two dimensional Navier–Stokes equations, using weakly nonparallel assumption as in [15], the Ginzburg–Landau equation obtained would use dimensionless variables based on physical scales such as the size d of the body, the velocity U_∞ of the stream flow without body and the time scale d/U_∞. Using these units based only on physical scales, the local linear growth rate of instability waves is a function of the Reynolds number, the dimensionless streamwise slow coordinate X and may be written in the form of a Taylor expansion around the wavenumber k_0 corresponding to the maximum growth rate:

$$\sigma = \sigma_{\max}(X,R) + \frac{\sigma_{kk}(X,R)}{2}(k - k_0(X,R))^2, \tag{39}$$

where k_0 is the saddle point of the dispersion relation at X. This expansion represents the dispersion relation associated with the equation

$$\frac{\partial A}{\partial T} - i\sigma_{kk}(X,R)k_0\frac{\partial A}{\partial X} = -\frac{\sigma_{kk}(X,R)}{2}\frac{\partial^2 A}{\partial X^2} + \left(\sigma_{\max}(X,R) + \frac{\sigma_{kk}(X,R)}{2}k_0^2\right)A, \tag{40}$$

in which some nonparallelism effect have not been included. When including the leading order nonlinear term $|A|^2A$ compatible with translational invariance in time, and after expanding $\sigma_{\max}(X,R)$, $\sigma_{kk}(X,R)$ and $k_0(X,R)$ at first order in the variable X and assuming that $\sigma_{kk}(X,R)$ and $k_0(X,R)$ dependence on X are acting at higher order, we obtain

$$\frac{\partial A}{\partial T} - i\sigma_{kk,0}(R)k_0\frac{\partial A}{\partial X} = -\frac{\sigma_{kk,0}(R)}{2}\frac{\partial^2 A}{\partial X^2} - \gamma|A|^2A + \left(\sigma_{\max,0}(R) + \frac{\sigma_{kk,0}(R)}{2}k_0^2 - \left.\frac{d\sigma_{\max}}{dX}\right|_0 X\right)A \tag{41}$$

This model needs the evaluation of the complex coefficients $\sigma_{kk,0}(R)$, $\sigma_{\max,0}(R)$, $d\sigma_{\max}/dX|_0$, k_0 and γ. Finally, we assume that only $\sigma_{\max,0}(R)$ depends on the Reynolds number and is proportional to R.

The coefficients of Equation (41) may be all deduced from the work of Hammond & Redekopp [29], except from the nonlinear coefficient γ. They study numerically two-dimensional wake behind rectangular based body and compute the local growth rate $\sigma(X)$ as a function of the distance to the body. Their Figure 6 in [29](a) and Figure 13 in [29](b) exhibit a parabolic variation of $\sigma(X)$, by contrast with our assumption of a linear variation. Using the theoretical framework developed in [15] for an infinite domain, they have computed the complex coefficients of Equation (41) for a criticity of 33%. The complex coefficients we are going to use are estimated from theirs. Because of their quadratic variation of $\sigma_{\max}$ in X, they do not obtain directly a value for $d\sigma_{\max}/dX|_0$ but a coefficient of the quadratic term (which equals 0.0149) that we are going to identify to $d\sigma_{\max}/dX|_0$, as we just need an order of magnitude. This value of μ_1 evaluated by the computation of the coefficients corresponds approximatively to the mean slope of $\sigma(X)$ determined by Hammond & Redekopp (Figure 6 in [29](a) and Figure 13 in [29](b)). We might as well have chosen $d\sigma/dx|_0 \sim \sqrt{d^2\sigma/dx^2}$ identifying the typical size of the nonparallel effect; this would have led to an order of magnitude larger μ_1 for which departure from the asymptotic laws (30,32) affect a larger range of ϵ.

Let us first rewrite Equation (41) by rescaling the streamwise coordinate X (using the change of variable $X = x(-\Re\sigma_{kk,0}/2)^{1/2}$) in order to set the coefficient of the diffusive term to unity; the amplitude is also properly rescaled to eliminate the imaginary terms proportional to $\partial A/\partial x$ and A, and to set the real part of the nonlinear coefficient to unity. We obtain a complex version of Equation (1):

$$\frac{\partial A}{\partial T} + U_0 \frac{\partial A}{\partial x} = (1 + ic_1)\frac{\partial^2 A}{\partial x^2} + (\mu_A + \epsilon - \mu_1 x)A - (1 - ic_3)|A|^2 A \qquad (42)$$

where all coefficients are obtained from those of Equation (A.1) computed in [29] after applying the rescaling. Since the model (1) is real and since we use values of the coeficients obtained in [29] for a complex model, we therefore have a crude estimation, but only the order of magnitude is sufficient. The advection velocity is estimated to $U_0 \simeq 2$ and its link to the threshold value μ_A (Equation (5)) yields $\mu_A \simeq 1$. The inhomogeneity parameter is estimated to $\mu_1 \simeq 0.01$.

Once μ_1 has been estimated, the model (1) then depends on a single coefficient $\epsilon = \mu_0 - \mu_A$. Typical criticalities ϵ are obtained using the same values of the ratio $(\mu_0 - \mu_g^l)/\mu_g^l$ than in [2] for the ratio $(R - R_c)/R_c$, leading to a comparable departure from instability threshold $\epsilon \equiv (R - R_c)/R_c$.

The results obtained with this protocol are sketched in Figure 8(a), 8(b) and for the shape of the global mode in Figure 8(d) after having renormalized the amplitudes to set A_s and x_s to unity. Figure 8(d) from the model with a fixed $\mu_1 = 0.033$ and Figure 8(e) for which the parameter μ_1 has been varied as a function of ϵ to fit the tail of the global mode show that the growing part of the NG modes are superposed into one curve exactly as for the experimental results by Goujon-Durand *et al.* [1] (Figure 8(a)) or for the numerical results by Zielinska and Wesfreid [2] (Figures 8(b), 8(b)). But in Figure 8(d), the tails of the renormalized NG modes are not superposed into one curve, as in the numerical study [2] when different blockage have been used. This discrepancy in the tails may be due to the fact that the assumption of a linear variation of $\mu(x)$ with respect to x is crude; different profiles for the bifurcation parameter should be tried to describe more accurately the tails. Experimental or numerical data in [1] and [2] have been obtained in a fixed short domain $[0, x_M]$. Therefore, the rescaled NG modes plotted in Figures 8(a), 8(b), 8(c) seem to be shorter (in the rescaled coordinate x/x_s) when ϵ is small. This is an effect of the rescaling by x_s which is growing when ϵ is decreased. For consistency, we have represented in Figs 8(d) and 8(e) the NG modes of the toy model cut at the same fixed position than in Figs 8(a), 8(b), 8(c), *i.e.* viewed through a finite window of fixed size and rescaled by x_s. Tails appears shorter when ϵ is brought to zero as x_s increases. A better comparison but somehow more artificial may be obtained for the tail by letting the inhomogeneity coefficient μ_1 vary with the Reynolds number as in the experiments. We therefore wish to let μ_1 vary slightly with ϵ and test a new comparison with an estimation of μ_1 for each value of the criticity.

In this second set of simulations, the inhomogeneity parameter of our problem is estimated according to Figure 3(b) of [2] which shows the amplitude of the transverse velocity component on the axis against the streamwise position x/d (rescaled by the size of the bluff body), resulting from numerical integration of Navier–Stokes equations for the wake configuration. For each R, a value for μ_1

(a)

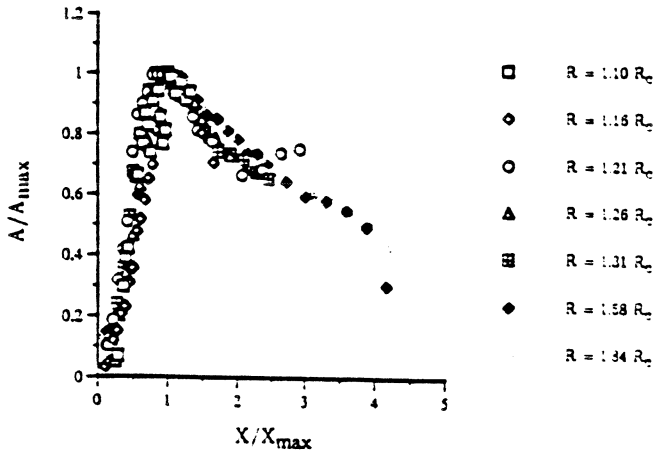

(b)

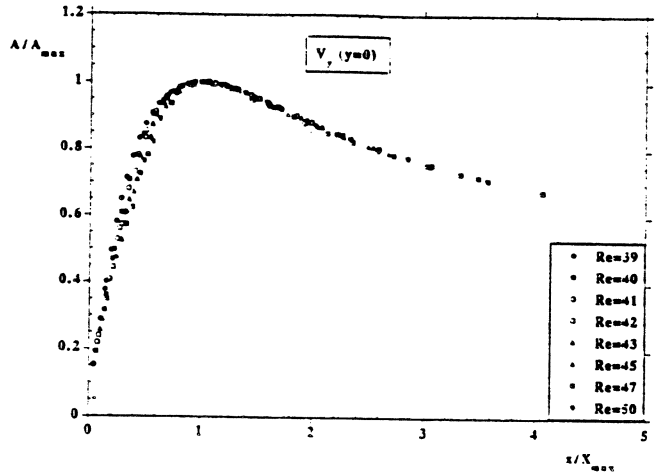

(c)

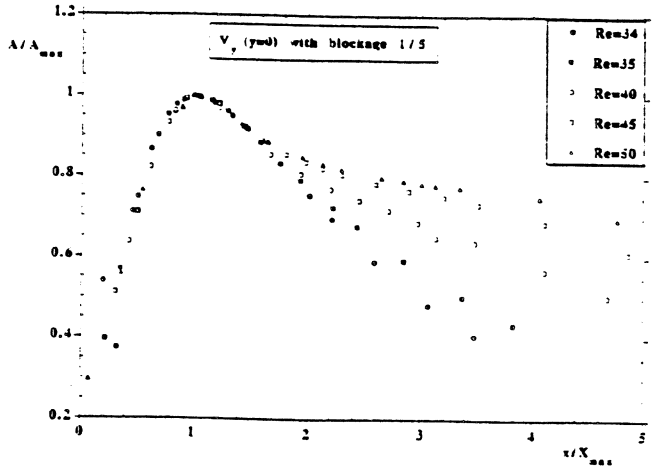

Fig. 8. Renormalized global modes scaled with A_s and x_s with the same departures from critical Reynolds number (38.3) than in [2], corresponding to R = 41, 42, 43, 45, 47, 50. (a) Experimental data for the NG mode associated with transversal velocity component of the wake from [1]. (b) Numerical data from [2]. (c) Numerical data from [2] with variation of the blockage. (d) Results of the present study using a constant inhomogeneity parameter $\mu_1 = 0.033$ (no free parameter). (e) Results of the present study for which the inhomogeneity parameter has been slightly varied with ϵ as estimated from Figure 3(b) in [2].

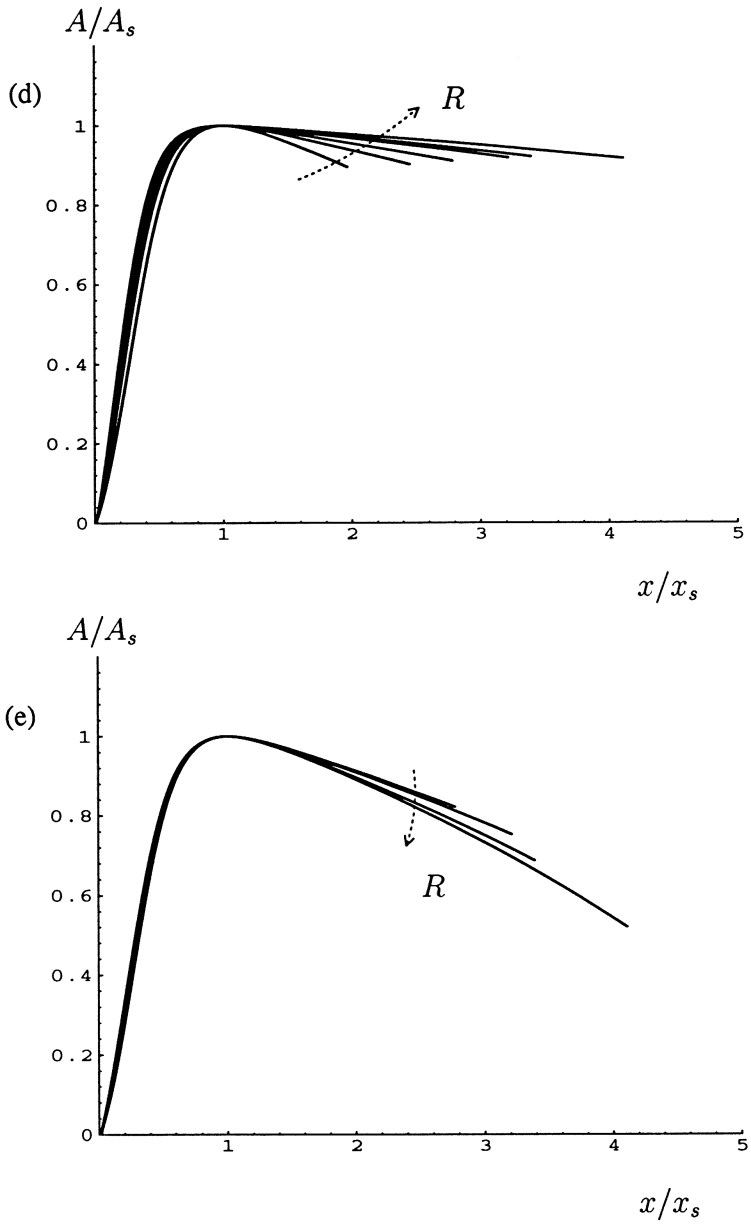

Fig. 8. See caption in previous page.

is computed by assuming that downstream of x_s, the amplitude follows adiabatically the weak variation of $\sqrt{\sigma(x)}$, $\sigma(x)$ being the local linear growth of the perturbation of the basic state $\sigma(x)/\sigma(x=0) \sim \mu(x)/\mu(x=0)$. We obtain this way an estimation of the inhomogeneity parameter μ_1 which satisfies $\mu_1 \ll \epsilon^{3/2}$. The values of μ_1 vary from 0.032 for $R = 41$ to 0.065 for $R = 50$. In our theoretical model, we have made the hypothesis of a linear variation of $\mu(x)$ with respect to x. However, Figure 3(b) of [2] shows that far downstream, the wake inhomogeneity is certainly weaker than linear. For this reason, we are loosing accuracy in the description of the tail of NG modes. Moreover, when the Reynolds number approaches its critical value, the estimation of μ_1 becomes unaccurate as the portion of the tail computed in [2] becomes too small. (for $R = 39$ it is even

impossible to estimate the inhomogeneity of the wake as the saturation in nearly reached within the plotted domain). Therefore we have used Reynolds values $41, 42, 43, 45, 47, 50$, (relative criticities from 7% to 30 %) rescaled our NG modes with A_s and x_s as in [2] and compared our results (Figure 8(e)) to Figure 8(a) of Goujon-Durand *et al* and 8(b) of Zielinska & Wesfreid.

Of course, the tail of NG modes is not accurately described by (1) (as in reality, μ is not linear in x) but we have already shown by the matching that a tail is just slave (being in a local WKBJ nonlinear equilibrium) of the frontal zone upstre and therefore depends adiabatically on the variation of the bifurcation parameter with respect to x. Therefore, the analysis should be easily modified to take into account more complex (quadratic,...) variation of $\mu(x)$ (*i.e.* $\sigma(X)$) and should then describe accurately the tail.

However, without going to these particular cases, the quantitative agreement is good since from the origin to twice the position of the maximum x_s, we see only slight differences between various results of Figure 8.

Early exploration of the global dynamics [3] have reported Landau like dynamics when the amplitude of the wake is measured at a fixed location. Zielinska & Wesfreid [2] have undertaken such measurements that we have reported as dashed lines in Figure 9; we have mimicked such measurements using the model (1) with the inhomogeneity parameter varying with ϵ as in Figure 8(e). Of course as the global scaling (35),(36) are not compatible with a local scaling of the amplitude in $A(x_{\text{fixed}}) \sim \sqrt{R - R_c}$, we should not observe this scaling but we want to quantify the departure of numerical results on model (1) for varying μ_1 from the classical Landau theory.

In Figure 9, we have measured the amplitude at three different fixed distances from results of Figure 8(e) and reported similar measurements by Zielinska &

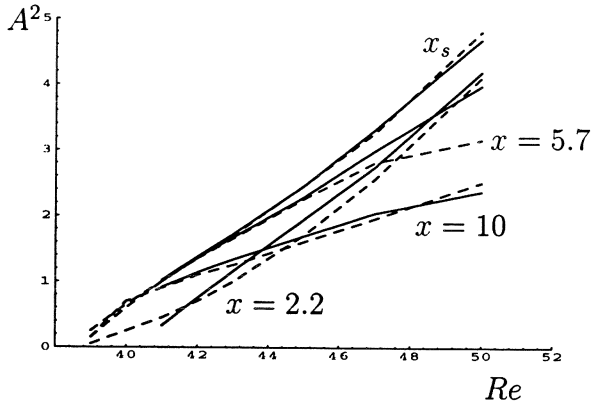

Fig. 9. A^2 at different spatial station chosen as in [2], i.e. variable $x = x_s$ and fixed $x = 2.2$, 5.7 and 10. The dotted lines represent the values reported from Figure 5 of [2]. The continuous lines represent our values computed from Equation (12). Arbitrary units are used in the ordinate scale.

Wesfreid (Figure 5(c) of [2]). At a fixed location close to the origin (to the body), ($x = 2.2$), the amplitude varies approximately linearly with x, the slope being proportional to $f(\epsilon)$ given by Equation (20), and therefore $A^2(x = 2.2)$ possesses a parabolic shape in Figure 9. By contrast, far enough from the origin, *i.e.* downstream of x_s for the ϵ reported in Figure 9, A^2 is approximately linear with respect to R (Figure 9 for $x = 5.7$ and $x = 10$) as for all the ϵ reported, those points belong to the tail where the amplitude is locally saturated and therefore, they follow $A^2(x_{\text{fixed}}) = \sigma_{\text{fixed}} = \mu_{\text{fixed}} = \mu_A + \epsilon - \mu_1 x_{\text{fixed}}$. Thus, if A^2 scales linearly with ϵ, the threshold value it points at is the local and not the global one: $\epsilon = \mu_1 x - \mu_A$. This analysis breaks down if the fixed position of the probe is too far in the tail. Again the quantitative agreement is fairly good, even for the highest Reynolds number ($R = 50$). For $x = x_s(R)$, A_s^2 is linear with respect to R in agreement with Zielinska & Wesfreid results and with our extrapolation. Similar measurements using a fixed value of μ_1 would have led to similar results while the probe is between the origin and the maximum, as in Figure 8(d) the difference from Figure 8(e) is to be seen in the tails.

6 Conclusion

In this paper we have shown that the spatial structure of nonlinear global modes in weakly inhomogeneous (non parallel) semi-infinite systems may be described by perturbing the global mode solution we have derived for an homogeneous (parallel) semi-infinite domain and which predicts exactly with no free parameter the behavior of Rayleigh–Bénard convection [6] and Taylor–Couette rolls [7] with throughflow. Our model takes into account only two small parameters: the criticity ϵ of the flow and the inhomogeneity parameter μ_1 . The nonlinear global modes are derived in the uniform limit where ϵ and μ_1 are brought to zero. The Landau theory based on a WKBJ approximation has been shown to be valid in an exponentially small domain of the plane (μ_1, ϵ). By contrast, this fully nonlinear theory which is essentially based on results for front propagation in homogeneous systems leads to the existence of nonlinear global modes in an entire algebraic domain of the plane (μ_1, ϵ). We have shown that the saturation may occur either within the locally absolutely unstable domain or downstream of the boundary x_A of this region. In the latter case, NG modes are described as fronts perturbed by the inhomogeneity at first order. But in both cases, the inner resonant layer plays the master role of the resonator. Our main result is the existence of critical exponents for the scaling law of the maximum amplitude position, which depend on the relative magnitude of the departure from global instability threshold ϵ and of the inhomogeneity length scale. When $\mu_1 \ll \epsilon^{3/2}$, the the NG mode is described at first order as a perturbed Kolmogorov front, the scaling law for maximum amplitude location is in $1/\sqrt{\epsilon}$ and is in agreement with experimental and numerical results in wakes. In light of this results we are able to interpret the fit used for the maximum amplitude in [1,2]. By contrast, when $\epsilon^{3/2} \ll \mu_1 \ll \epsilon$, the inho-

mogeneity modifies the front solution at leading order and the critical exponent should changes as two length scales appear in the scaling law for x_s: the length associated with the criticity parameter $\epsilon^{-1/2}$ and the inhomogeneity length scale μ_1^{-1}.

It is quite surprising that such a simple one-dimensional amplitude model may be found in agreement with experimental and numerical results since only the dynamics along the streamwise direction has been considered and simplified to the extrem. Another challenge is to explain why such a theory based on the hypothesis of a weak inhomogeneity of the medium (WKBJ type of assumption) which might appear unreasonable in the case of wakes, describes however successfully the spatial structure of the wake reported in the literature. A lot of reasons all reflecting the crudeness of the model may be pointed out to indicate that the model should not describe accurately the real experimental or numerical results. First, the spatial structure in the crosswise direction and the propagation of the perturbation in this crosswise direction has been neglected in the mechanism of global instability. This crosswise direction is considered to be slave to the dynamics in the streamwise direction. Secondly, our model is minimal in the sense that it takes into account only the leading order terms in x, k and R necessary to lead to a nonlinear global instability. The linear part of the model represents the simplest dispersion relation depicted to absolute to convective instability transition. The cubic nonlinearity is the leading order nonlinear term compatible with translational invariance in time. The reason of the ability of the present theoretical approach to describe real experiments, even if the parameters are driven far beyond the validity domain of the theory, is perhaps due to these essential ingredients which capture the main features of conserved symmetries or broken symmetries of the real flow.

In [1], it is suggested that the experimentally observed scaling laws could be explained by a model of Ginzburg–Landau equation with complex coefficients. We have studied in [26] the structure of homogeneous NG modes of the complex Ginzburg–Landau equation with cubic nonlinearities and we have shown that although the model is no more potential, they behave as the linear model and exhibit a growth size which scales like $\epsilon^{-1/2}$ as for the real Ginzburg–Landau model. As scaling laws for all the length scales introduced in section 2 keep being identical when the complex Ginzburg–Landau equation is considered, the structure of the NG mode should be similar in the real and in the complex case. The only novel results being the frequency selection which should be similar to the homogeneous case at leading order [26]. For the maximum amplitude value and location, the scaling laws should only differ by numerical factors depending upon the imaginary parts of the Ginzburg–Landau coefficients. Associated with the derivation of those coefficients for the experimental setup used in [1], this study should lead to a systematic quantitative comparison between our theory and the experiment. However, if the imaginary parts of the Ginzburg–Landau coefficients are small (as for the Rayleigh–Bénard or the Taylor–Couette experiment), the

real model should give very good quantitative agreement between theory and experiment (as it is already the case when the flow is parallel [26]).

A Detailed spatial structure of NG modes

A.1 Outer layer CNL

In this subdomain, the NG mode has saturated and its saturation amplitude follows the weak variation of the bifurcation parameter with respect to x. On using the change of variable

$$Z = \mu_1 x - \mu_0 \tag{A.1}$$

where $\mu_0 = \mu_A + \epsilon$ and $\mu_1 = \epsilon^n$, we can rewrite Equation (12) up to the second order in the form

$$ZA(Z) + A^3(Z) + \epsilon^n U_0 A'(Z) = 0 \tag{A.2}$$

where a prime denotes differentiation with respect to the argument. The solution of Equation (A.2) reads

$$A(Z) = \sqrt{-Z} + \epsilon^n \frac{U_0}{4(-Z)^{\frac{3}{2}}} \tag{A.3}$$

and represents the saturation amplitude which follows the weak variation of $\mu(x)$ with respect to x. By making use of (A.1), we obtain $Z = -\mu_A - \epsilon + \epsilon^n x$, and expansion of (A.3) in powers of ϵ yields

$$A \simeq \sqrt{\mu_A} - \epsilon^n \frac{1}{2\sqrt{\mu_A}} x + \epsilon \frac{1}{2\sqrt{\mu_A}} + \epsilon^n \frac{U_0}{4\mu_A^{3/2}}. \tag{A.4}$$

A.2 Transition layer TL^s

Around the saturation amplitude, $A = A_2(\mu_A) - \epsilon^p \phi(x)$, where $\phi(x)$ satisfies the equation obtained by linearizing (12) around $A_2 \equiv A_2(\mu_A)$:[3]

$$\frac{d^2\phi}{dx^2} - U_0 \frac{d\phi}{dx} + \mu_2 \phi = (\epsilon^{1-p} - \epsilon^{n-p} x) A_2, \tag{A.5}$$

[3] For clarity, we no longer explicitly mention the (μ_A) dependence of $A_2 \equiv A_2(\mu_A) = \sqrt{\mu_A}$.

where $\mu_2 = \mu_A - 3A_2^2 = -2\mu_A$. Using the notations

$$k_- = \frac{U_0(1-\sqrt{3})}{2} \qquad k_+ = \frac{U_0(1+\sqrt{3})}{2}, \tag{A.6}$$

the general solution of Equation (A.5) then reads

$$\phi(x) = c_1\, \mathrm{e}^{k_+(x-x_s)} + c_2\, \mathrm{e}^{k_-(x-x_s)} + \epsilon^{1-p}\frac{A_2}{\mu_2} - \epsilon^{n-p}\frac{A_2}{\mu_2}\left(x + \frac{U_0}{\mu_2}\right), \tag{A.7}$$

where the last non-exponential term represents a particular solution of (A.5) and c_1, c_2 are integration constants. A boundary condition will be imposed by the matching when $x - x_s \to +\infty$. The outer solution (A.4) in CNL is linear with respect to x; then $\epsilon^p\phi(x)$ must be also linear when $x - x_s \to +\infty$. This matching condition implies $c_1 = 0$. As $x - x_s \to +\infty$, the inner solution (A.7) admits the expansion

$$\epsilon^p\phi(x) \simeq \frac{A_2}{\mu_2}\left(-\epsilon^n x + \epsilon - \epsilon^n\frac{U_0}{\mu_2}\right) \tag{A.8}$$

Since $A_2 = \sqrt{\mu_A}$ and $\mu_2 = -2\mu_A$, expansion (A.8) represents exactly orders ϵ and ϵ^n of (A.4). Matching between CNL and TL^s is done.

The position of the maximum x_s must satisfy $d\phi/dx(x_s) = 0$. This condition determines the constant $c_2 = \epsilon^{n-p}A_2/\mu_2 k_-$. The complete solution (A.7) then reads:

$$\phi(x) = \epsilon^{n-p}\frac{A_2}{\mu_2 k_-}\,\mathrm{e}^{k_-(x-x_s)} + \frac{A_2}{\mu_2}\left(\epsilon^{1-p} - \epsilon^{n-p}\left(x + \frac{U_0}{\mu_2}\right)\right). \tag{A.9}$$

When $x - x_s \to -\infty$, the asymptotic behavior of $\phi(x)$ is determined by the exponential term. On differentiating Equation (A.9) and using again (A.9) in order to eliminate $\mathrm{e}^{k_-(x-x_s)}$, it follows that

$$\epsilon^p\frac{d\phi}{dx} = k_-\epsilon^p\phi + \epsilon^n x_s\frac{k_- A_2}{\mu_2} - \epsilon\frac{k_- A_2}{\mu_2} + \epsilon^n\frac{A_2}{\mu_2}\left(\frac{U_0 k_-}{\mu_2} - 1\right). \tag{A.10}$$

This exact relation will however be used as the asymptotic behavior of the solution (A.9) in the phase space as $x - x_s \to -\infty$. Moreover, the maximum amplitude verifies $A(x_s) = A_2 - \epsilon^p\phi(x_s)$ with

$$\epsilon^p\phi(x_s) = -\epsilon^n\frac{A_2}{\mu_2}x_s + \epsilon\frac{A_2}{\mu_2} + \epsilon^n\frac{A_2}{\mu_2}\left(\frac{1}{k_-} - \frac{U_0}{\mu_2}\right). \tag{A.11}$$

The solution is sought directly in the phase space in the form of a series representing $u(A) \equiv dA/dx$ and expanded into

$$u(A) = \frac{dA}{dx} = u_0(A) + \epsilon\, u_1(A) + \mu_1 u_2(x, A). \tag{A.12}$$

At the lowest order in ϵ, let us briefly recall how to compute $u_0(A)$ which is the same solution as the one obtained for saturated global modes [24], i.e. linking the origin of phase space $(A = 0, dA/dx = 0)$ to the point $(A = A_2(\mu_A), dA/dx = 0)$ and satisfying

$$u_0 u_0' - U_0\, u_0 + \mu_A A - A^3 = 0, \tag{A.13}$$

where a prime denotes differentiation with respect to A. This solution reads

$$u_0(A) = -\sum_{j=1}^{+\infty} \nu_j (A_2 - A)^j. \tag{A.14}$$

Introduction of (A.14) in (A.13) and identification of the powers of $(A_2 - A)$ yield equations for the recursive coefficients ν_j which may be numerically computed. [4]

$u_1(A)$ and $u_2(x, A)$ satisfy

$$u_0\, \partial_A u_1 + (\partial_A u_0 - U_0)\, u_1 = -A \tag{A.15}$$

$$u_0\, \partial_A u_2 + \partial_x u_2 + (\partial_A u_0 - U_0)\, u_2 = x\, A \tag{A.16}$$

and are also sought in the form of series expansions

$$u_1(A) = -\sum_{j=0}^{+\infty} \lambda_j (A_2 - A)^j, \tag{A.17}$$

$$u_2(x, A) = \sum_{j=0}^{+\infty} (\zeta_j + \eta_j\, x)(A_2 - A)^j. \tag{A.18}$$

[4] The first one at lowest order in $(A_2 - A)$ must be negative since (A.14) represents the stable manifold of A_2 and satisfies $\nu_1^2 - U_0 \nu_1 + \mu_2 = 0$. Thus $\nu_1 = U_0(1 - \sqrt{3})/2 \equiv k_-$.

The recurrent coefficients λ_j, ζ_j and η_j are numerically computed.[5] The asymptotic behavior of the solution (A.12) as $A \to A_2$ in the phase space reads

$$\frac{dA}{dx} \simeq -\nu_1(A_2 - A) + \mu_1\, x\, \eta_0 + \epsilon\, \lambda_0 + \mu_1\, \zeta_0 \tag{A.19}$$

Since we have verified that

$$k^- = \nu_1, \qquad \frac{k_- A_2}{\mu_2} = -\eta_0 = \lambda_0, \qquad \zeta_0 = \left(1 - \frac{U_0 k_-}{\mu_2}\right)\frac{A_2}{\mu_2},$$

expansions (A.19) and (A.10) are identical whatever p and solutions in TL^s and KF are now matched. In other words, the matching succeeds whatever the size of the transition layer TL^s.

When $A \to 0$, the asymptotic behavior of the solution reads

$$\begin{aligned} u_0(A) + \epsilon u_1(A) + \mu_1\, u_2(x,A) \simeq & -\sum_{j=1}^{+\infty} \nu_j A_2^j + \sum_{j=1}^{+\infty} j\nu_j A_2^{j-1} A \\ & + \mu_1\, x \sum_{j=0}^{+\infty} \eta_j A_2^j - \epsilon \sum_{j=0}^{+\infty} \lambda_j A_2^j + \mu_1 \sum_{j=0}^{+\infty} \zeta_j A_2^j. \end{aligned} \tag{A.20}$$

A.4 Transition layer TL^0 and outer layer OL

In the outer layer OL^+, $A(x)$ is small since it must vanish at infinity. Therefore, $A(x)$ is solution of the linear equation (15) and reads

$$A(x) = g(\mu_1) \exp\left(\frac{U_0}{2} x\right) \mathrm{Ai}\left((x - x_A)\mu_1{}^{\frac{1}{3}}\right) \tag{A.21}$$

where $g(\mu_1)$ is an integration constant (the coefficient of Bi must be zero in order to cancel the growing part of the general solution).

In the central nonlinear layer CNL, when $Z \to 0$, a singularity appears in the solution (A.3). The transition layer TL^0 has therefore been introduced to match

[5] The first equations allowing to initiate the computation read

$$\begin{aligned} (U_0 - \nu_1)\,\lambda_0 &= A_2, \quad \text{or} \quad \lambda_0 = (1+\sqrt{3})^{-1}, \\ (U_0 - \nu_1)\,\eta_0 &= -A_2, \quad \text{or} \quad \eta_0 = -(1+\sqrt{3})^{-1}, \\ (U_0 - \nu_1)\,\zeta_0 &= \eta_0, \quad \text{or} \quad \zeta_0 = -U_0^{-1}(2+\sqrt{3})^{-1}. \end{aligned}$$

solutions (A.3) and (A.21) when $Z \to 0$. In this layer, on using the change of variable $\tilde{Z} = Z/\mu_1^{1/2}$, $A(Z) = \mu_1^{1/4}\tilde{A}(\tilde{Z})$ in order to collect the nonlinear term, the advection term and the inhomogeneous term at the same order, $\tilde{A}(\tilde{Z})$ satisfies

$$U_0\tilde{A}' = -\tilde{Z}\tilde{A} - \tilde{A}^3. \tag{A.22}$$

The solution of Equation (A.22) reads

$$\tilde{A} = \tilde{A}_0 \left(1 + \frac{2\tilde{A}_0^2}{U_0}\int_0^{\tilde{Z}} \exp\left(-\frac{u^2}{U_0}\right) du\right)^{-1/2} \exp\left(-\frac{\tilde{Z}^2}{2U_0}\right) \tag{A.23}$$

where the integration constant $\tilde{A}_0$ is given by the matching with the CNL solution. Indeed, as $\tilde{Z} \to -\infty$, we obtain

$$\tilde{A} \simeq \sqrt{-\tilde{Z}}\left(1 + \frac{U_0}{4\tilde{Z}^2}\right) \tag{A.24}$$

if the choice $\tilde{A}_0 = (U_0/\pi)^{1/4}$ is done and solution (A.24) matches with (A.3).

When $\tilde{Z} \to +\infty$, the solution (A.23) admits the asymptotic expansion

$$\tilde{A} \simeq \frac{\tilde{A}_0}{\sqrt{2}} = \left(\frac{U_0}{4\pi}\right)^{\frac{1}{4}} \exp\left(-\frac{\tilde{Z}^2}{2U_0}\right) \tag{A.25}$$

and matches with the OL solution (A.21) once the following value of $g(\mu_1)$ is chosen:

$$g(\mu_1) = \pi^{1/4}U_0^{3/4} \exp\left(-\frac{U_0^3}{24\mu_1}\right). \tag{A.26}$$

References

[1] S. Goujon-Durand, P. Jenffer, J.E. Wesfreid, *Downstream evolution of the Bénard-von Kármán instability*, Phys,. Rev. E **50**, 308 (1994).

[2] B.J.A. Zielinska, J.E. Wesfreid, *On the spatial structure of global modes in wake flow*, Phys. Fluids **7**, 1418 (1995).

[3] C. Mathis, M. Provansal, L. Boyer *The Bénard-von Kármán instability: an experimental study near the threshold*, J. Phys. (paris) Lett. **45**, 483 (1984).

[4] K.R. Sreenivasan, S. Raghu, D. Kyle, *Absolute instability in variable density round jets.* Exp. Fluids **7**, 309 (1989).

[5] P.J. Strykowski, D.L. Niccum, *The influence of velocity and density ratio on the dynamics of spatially developing mixing layers*, Phys. Fluids A **4**, 770 (1992).

[6] H.W. Müller, M. Lücke, M. Kamps, *Convective Patterns in Horizontal flow*, Europhys. Lett. **10**, 451 (1989); *Transversal convection patterns in horizontal shear flow*, Phys. Rev. A **45**, 3714 (1992).

[7] P. Büchel, M. Lücke, D. Roth, R. Schmitz, *Pattern selection in the absolutely unstable regime as a nonlinear eigenvalue problem: Taylor vortices in axial flow*, Phys. Rev. E. **53**, 4764 (1996).

[8] W. Koch, *Local instability characteristics and frequency determination of self excited wake flows*, J. Sound Vib. **99**, 53 (1985).

[9] R.J. Briggs, *Electron-Stream Interaction with Plasmas* (MIT Press, Cambridge, MA, 1964).

[10] A. Bers, in *Physique des Plasmas*, edited by C. DeWitt and J. Peyraud (Gordon and Breach, New York, 1975).

[11] E.M. Lifshitz and L.P. Pitaevskii, *Physical kinetics* (Pergamon, London, 1981).

[12] D. Rockwell, E. Naudascher, *Self sustained oscillations of impinging free shear layers*, Annu. Rev. Fluid Mech. **11**, 67 (1979).

[13] E. Villermaux, Ph. D. thesis, Université de Grenoble (1992).

[14] P. Huerre, P.A. Monkewitz, *Local and global instabilities in spatially developing flows*, Annu. Rev. Fluid Mech. **22**, 473 (1990).

[15] P.A. Monkewitz, P. Huerre, J.M. Chomaz, *Global linear stability analysis of weakly non parallel shear flows*, J. Fluid Mech., **251**, 1 (1993).

[16] J.M. Chomaz, P. Huerre, L.G. Redekopp, *Bifurcations to local and global modes in spatially developing flows*, Phys. Rev. Lett., **60**, 25 (1988).

[17] J.M. Chomaz, P. Huerre, L.G. Redekopp, *A frequency selection criterion in spatially developing flows*, Stud. Appl. Math. **84**, 119 (1991).

[18] J.M. Chomaz, P. Huerre, L.G. Redekopp, *The effect of nonlinearity and forcing on global modes*, in *New Trends in Nonlinear Dynamics and Pattern-Forming Phenomena*, edited by P. Coullet and P. Huerre, (Plenum Press, New York, 1990).

[19] S. Le Dizès, P. Huerre, J.M. Chomaz, P.A. Monkewitz, Nonlinear stability analysis of slowly-diverging flows: Limitations of the weakly nonlinear approach. In *Proceedings of the IUTAM Symposium on Bluff-Body Wakes, Dynamics and Instabilities*, (Eds. H. Eckelmann, J.M.R. Graham, P. Huerre and P.A. Monkewitz) , 147-152, (Berlin : Springer-Verlag 1993).

[20] Y. Pomeau, S. Zaleski, P. Manneville, *Axisymmetric cellular structures revisited*, Journal of Applied Mathematics and Physics (ZAMP), **36**, 367 (1985).

[21] R.E. Hunt, *Spatially Varying Flows with Localized Forcing*, Ph. D. Thesis (1995).

[22] R.E. Hunt, D.G. Crighton, *Instability of flows in spatially developing media*, R. Soc. Lond. A **435**, 109 (1991).

[23] W. van Saarloos, P.C. Hohenberg, *Fronts, pulses, sources and sinks in generalized complex Ginzburg-Landau equations*, Physica **D56** 303 (1992).

[24] A. Couairon, J.M. Chomaz, *Absolute and convective instabilities, front velocities and global modes in nonlinear systems*, submitted to Physica **D**.

[25] A. Couairon, J.M. Chomaz, *Global Instability in fully nonlinear systems*, Phys. Rev. Lett. **77**, 4015 (1996).

[26] A. Couairon, J.M. Chomaz, *Pattern selection in the presence of a cross flow*, submitted to Phys. Rev. Lett.

[27] C.M. Ho, P. Huerre, *Perturbed free shear layers*, Ann. Rev. Fluid Mech. **16**, 365 (1984).

[28] P. Albarède, P.A. Monkewitz, *A model for the formation of oblique shedding and "chevron" patterns in cylinder wakes*, Phys. Fluids A **4**, 744.

[29] (a) D. Hammond, L.G. Redekopp, *Global Dynamics and flow vectoring in asymmetric wakes*, AIAA-94-2219. (1994); (b) submitted to J. Fluid Mech.

[30] A. Kolmogorov, I. Petrovsky, N. Piskunov, *Investigation of a diffusion equation connected to the growth of materials, and application to a problem in biology*, Bull. Univ. Moscow, Ser. Int. Sec. A **1**, 1 (1937).

[31] C.M. Bender, S.A. Orszag, *Advanced Mathematical Methods for Scientists and Engineers*, (Mc Graw Hill 1978).

[32] M. Abramowitz, I.A. Stegun, *Handbook of mathematical functions*, (Dover 1972).

Global modes in weakly inhomogeneous subcritical flows.

Arnaud Couairon and Jean–Marc Chomaz

LadHyX, CNRS UMR 156, Laboratoire d'Hydrodynamique,
École Polytechnique,
91 128 Palaiseau CEDEX, France

Abstract

We study the existence of nonlinear solutions of the real subcritical Ginzburg–Landau equation, with boundary condition at $x = 0$ and with a slowly varying bifurcation parameter. These solutions called nonlinear global (NG) modes are explicitly derived when nonlinear effects dominate the inhomogeneity. We derive scaling laws for the slope of NG modes and for the position of the maximum.

1 Introduction

Bluff body wakes are now well known to belong to a particular class of flows which behave like oscillators. But the relevant mechanism allowing to sustain the oscillations is yet not known. Several models have been proposed in the past decades to describe the behavior of this class of flows.

For wakes, one of the proposed mechanism relies on hydroacoustic resonances occurring when there is a second blunt body at a finite distance downstream [1]. A feedback loop dominates the dynamics of the flow with a downstream branch consisting of rotational instability waves rolling up into vortices and an upstream branch consisting of irrotational pressure disturbances generated by interaction between the vortical structures and the downstream body which are transformed back into vortical waves at the separation point of the boundary layer.

A second mechanism has been proposed by Villermaux [2] in the form of a nonlinear feedback which models direct reintroduction of vortical disturbances close to the bluff body by the recirculating region just behind it. But such a model is unable to predict the behavior of convection cells with throughflow or Taylor–Couette flow with crossflow in which no recirculation are present but which exhibit behavior and scaling laws similar to the wake instability

The possibility of a nonlinear self sustained resonance is a third possibility which

does not need any feedback loop by wave or advection of any kind and which has received growing attention over the last decade, especially since Mathis et al. [3] demonstrated that von Kármán vortex-shedding at low Reynolds number is the result of a linear global instability arising via a Hopf bifurcation. Zebib [4] and Jackson [5] confirmed this bifurcation to a global mode by determining the global oscillation frequency on computed non-parallel basic flows. Chomaz et al. [8], building on Koch [6] analysis, have proposed a model for the sequence of local and global transitions in the cylinder wake relying on the notions of absolute and convective instabilities initially developed in the context of plasmas physics [7]. These notions characterize the impulse response of a system with no streamwise variation (parallel flow). If localized disturbances are growing but swept away from the source, the basic state is said to be *convectively unstable.* In other words, the mean advection velocity is sufficiently high in comparison with the growth of perturbations to impose that the amplitude returns back to the basic state at a fixed location. By contrast, if disturbances spred and grow upstream and downstream and contaminate the whole medium the basic state is said to be *absolutely unstable.*

For wakes, the scenario [8] confirmed by the analysis of Monkewitz [9] predicts the following generic sequence while increasing the Reynolds number: first linear stability, then local convective instability, followed by apparition of a region of local absolute instability and finally the bifurcation to a self sustained global mode. But the next step which should describe how the global mode saturates has fiercely resisted till very recently. The case of homogeneous (parallel) flows achieved only in Taylor–Couette flow or Rayleigh–Bénard convection with throughflow has been solved first [12] and the scaling laws [10,11] previously obtained by numerical integration of Navier–Stokes equations for the growth size of the global modes have been found to agree remarkably well with the analytical scaling laws we derived using the complex Ginzburg–Landau equation. The problem of wakes is a little more complicated as the flow cannot be considered parallel and effect of the inhomogeneity has to be explicitly taken into account. In [13], we have shown how a simple nonlinear model equation, namely the real supercritical Ginzburg–Landau equation associated with a weakly varying parameter, is surprisingly well suited to describe bluff body wakes. Indeed, the spatial structure of numerically [14] or experimentally [15] measured wakes has been found to be in accordance with the analytically derived structure of solution of our model. We have derived scaling laws for the maximum amplitude and its position which compare satisfactorily with the one found experimentally by Goujon-Durand et al. [15] or numerically by Zielinska & Wesfreid [14].

In this previous study [13] dealing with the fully nonlinear and weakly inhomogeneous supercritical case, the scenario for the successive transitions described on a linear basis by Chomaz *et al.* [8] and leading to linear global modes concepts has been found to be also valid for the fully nonlinear system considered. A locally absolutely unstable region behind the bluff body is necessary to trigger the

global instability. However, we have demonstrated that this scenario is not universal when dealing homogeneous fully nonlinear systems [18], since addition of generic nonlinearity such as subcritical effect or nonlinear advection may promote the global instability of the flow for parameter values where it is convectively unstable or even stable. The aim of the present study is to extend to nonparallel subcritical systems the consideration that local absolute instability is only a sufficient condition to have destabilization of a nonlinear global mode (NG mode), *i.e.* that once triggered, a NG mode may sustain when the flow is only locally convectively unstable or stable at each station. This resonance through nonlinear effect is associated with much steeper front and therefore more abrupt variation of the rising part of the NG mode. As we will see, the particular scaling laws differ from those found in [13] Although the spatial structure of the corresponding NG modes has to our knowledge not been observed in wake flows, we obtain here quantitative laws which may easily be checked in a particular experimental configuration. We believe that slightly modified wake configurations, for example wake in a channel, or maybe Poiseuille or Couette flow or Görtler flow may lead to the emergence of these nonlinear NG modes.

2 The subcritical Ginzburg–Landau model

In this paper, we present the spatial structure of NG modes which are steady solutions of the real subcritical Ginzburg–Landau equation with a slowly varying coefficient $\mu(x)$

$$\frac{\partial A}{\partial t} + U_0 \frac{\partial A}{\partial x} = \frac{\partial^2 A}{\partial x^2} + \mu(x) A + A^3 - A^5, \tag{1}$$

with a positive advection velocity U_0, in a semi-infinite domain with an entrance condition

$$A(0) = 0, \tag{2}$$

and an asymptotic behavior at $x = +\infty$ dictated by the fact that we consider only solutions asymptotic to 0 at infinity as the system is supposed sufficiently stable there (*i.e.* such that $\mu(+\infty) < -1/4$).

$$A(+\infty) = 0. \tag{3}$$

For a more general variation, this condition may be relaxed and if $\mu(+\infty) = \text{Cst}$, the condition will be that A has reached at infinity a minimum of the potential (*i.e.* a fixed point).

The bifurcation parameter is assumed to depend linearly on the space variable x

$$\mu(x) = \mu_0 - \mu_1 x \tag{4}$$

where μ_0 and μ_1 are positive constants. Therefore, the system is similar to the one used in [8,13] but with a subcritical nonlinear potential. The choice of a linear dependence allows to give a concrete example but does not restrict the generality of the study which remains valid as long as $\mu(x)$ is any slowly decreasing function depending on x only through a slow space variable $X = x/L$; (L measures the inhomogeneity length scale and is equal to μ_1^{-1} in the present case).

In the parallel flow case ($\mu_1 = 0$ and $\mu = \mu_0$), we have determined in [18], for the same subcritical Ginzburg–Landau model, the transition to a global instability. In that case, a NG mode satisfy the boundary conditions $A(0) = 0$ and $A(+\infty) = A_2(\mu_0)$ with

$$A_2(\mu) = \left(\frac{1}{2} + \sqrt{\mu + 1/4}\right)^{\frac{1}{2}} \tag{5}$$

Throughout the study, this solution will be denoted "homogeneous" nonlinear global (NG) mode. It exists in the shaded region (Fig. 1) of parameter space (U_0, μ) limited by $\mu > \mu_A(U_0)$ with

$$\mu_A(U_0) = \frac{3}{16}U_0^2 + \frac{\sqrt{3}}{8}U_0 - \frac{3}{16} \quad \text{if} \quad U_0 < \sqrt{3} \tag{6}$$

$$\mu_A(U_0) = \frac{U_0^2}{4} \quad \text{if} \quad U_0 > \sqrt{3} \tag{7}$$

Only for the latter, the threshold for the existence of a global mode does correspond to the change in the linear instability of the basic solution $A = 0$ from convective to absolute. In this case, the transition has been called of Kolmogorov type as it corresponds to a Kolmogorov front [19] caught at the origin. At the opposite, the relation (6) is not linked to a change in the linear wave of infinitely small amplitude but from nonlinear effects that are able to withstand the advection. Therefore, the global modes obtained in that case have been called of nonlinear type (following classical differentiation made for front solutions). In [18],depending on whether (6) or (7) holds, we have determined two different scaling laws for the characteristic growth size[1] Δx of these homogeneous NG modes, versus the departure from global instability threshold $\epsilon = \mu - \mu_A$.

- When $U_0 > \sqrt{3}$, the homogeneous NG mode exists only when small amplitude waves are absolutely unstable (dark gray region of Fig. 1 limited by $\mu = U_0^2/4$)

[1] Δx is defined as the distance at which the solution reaches 99% of its maximum amplitude A_2.

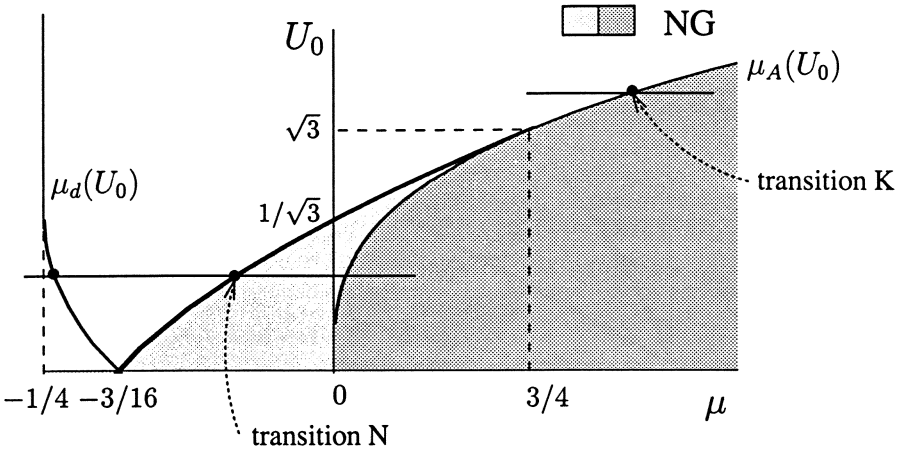

Fig. 1. Parameter space of the homogeneous problem. A homogeneous NG mode exists in the shadded regions. For $U_0 > \sqrt{3}$, the transition to global instability is of the Kolmogorov (K) type (simultaneous with the absolute convective transition). For $U_0 < \sqrt{3}$ the transition is of nonlinear type (N), occuring while the basic state is convectively unstable or stable.

and in that case, its characteristic growth size scales like $\epsilon^{-1/2}$.

$$\Delta x \simeq \frac{1}{\sqrt{\epsilon}} \quad \text{(Kolmogorov K type)} \tag{8}$$

A similar scaling in $\epsilon^{-1/2}$ for the growth size has been found in the study of the supercritical real or complex Ginzburg–Landau model [13], for which the transition to global instability is always of the Kolmogorov type.

- When $U_0 < \sqrt{3}$, a homogeneous NG mode exists while the system is convectively unstable or stable (light gray region of Fig. 1). For fixed U_0, when increasing μ, the global instability occurs before the absolute/convective transition (it is therefore called "nonlinear transition") and the characteristic growth size of the NG modes is much steeper than in the previous case and scales like.

$$\Delta x \simeq -\ln \epsilon \quad \text{(Nonlinear N type)} \tag{9}$$

In the non parallel flow case ($\mu_1 \neq 0$), we will restrict our presentation to the range $0 < U_0 < \sqrt{3}$ corresponding to a nonlinear transition of the parallel flow to global instability, since for $U_0 > \sqrt{3}$, the Kolmogorov transition occurs and the structure and the final results are strictly identical (except for numerical factors we have computed) to the supercritical model presented in [13]. As in [13], we face here a singular perturbation problem as the two limits $\mu_1 \to 0$ and $\epsilon \to 0$ cannot be taken at the same time and respective orders have to be specified (nonuniform limit) . The physical guideline for this ordering in small parameters relies on comparing the typical length scales associated with nonlinearity (departure from threshold ϵ) quantified by Δx and the length scale of the inhomogeneity μ_1^{-1}. Therefore, we will not only use a weakly nonparallel hypothesis ($\mu_1 \ll 1$), but also a stronger condition ensuring that nonlinearity "dominates" over nonparallelism in a sense

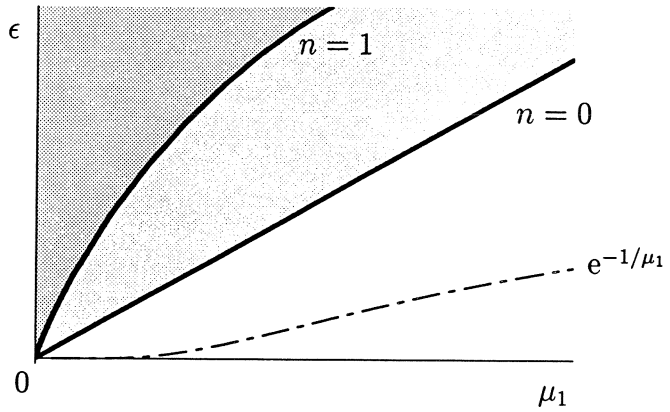

Fig. 2. Parameter space (μ_1, ϵ) for the model (10). In the gray regions, ϵ and μ_1 are linked by (14) with $n > 1$ in the dark gray region ($x_s \ll x_A$) and $0 < n < 1$ in the ligth gray region ($x_s \gg x_A$). In the white region, the hypothesis (11) breaks down and no NG mode can be sustained.

that we are going to precise. Let us assume that the growth size of homogeneous NG modes is sufficiently small in comparison with the inhomogeneity length scale. Under this hypothesis, we may describe the spatial structure of a NG mode of Eq. (1), rigorously defined as a solution of the equation

$$\frac{d^2A}{dx^2} - U_0\frac{dA}{dx} + (\mu_0 - \mu_1 x)A + A^3 - A^5 = 0, \tag{10}$$

vanishing at $x = 0$ and $x \to +\infty$, by interpreting its growing part as the leading edge of a homogeneous NG mode and its decreasing part as the adiabatic variation of the saturation amplitude $A_2(\mu)$ with respect to x through $\mu(x)$. As will be seen below, in some case, the NG mode drops off $A_2(\mu)$ and thus decreases faster in space than $\mu(x)$ but this do not alter the first steps of our analysis and modifies only the trailing edge of the NG modes. Using formula (9) for the growth size of homogeneous NG modes, the hypothesis that Δx is much smaller than the inhomogeneity length scale gives

$$\Delta x \ll \frac{1}{\mu_1} \Rightarrow \mu_1 \ll \frac{1}{\ln(1/\epsilon)} \tag{11}$$

This assumption is not extremely restrictive since under the assumption $\mu_1 \ll 1$ which accounts for the weak inhomogeneity of the medium, the condition (11) which excludes the exponentially small white region below the line e^{-1/μ_1} in Fig. 2 is verified even when the departure from global instability threshold ϵ is only algebraically small compared to μ_1.

Let us derive some intuitive guess for conditions that will turn to be important when the matching will actually be performed. Besides μ_1^{-1} just precises the scale of variation of μ. Several over length scales may be defined from simple consideration. In particular, Distance x_A from the origin at which $\mu(x_A) = \mu_A(U_0)$, or the

distance x_M at which the A_2 solution disappears (via a saddle node bifurcation, $\mu(x_M) = -1/4$) and others more subtil will have to be taken into account. At the origin of the semi-infinite domain, we assume that the bifurcation parameter μ_0 is greater than the NG instability threshold of homogeneous NG modes $\mu_A(U_0)$ (Eq. 6)

$$\mu_0 = \mu_A + \epsilon. \tag{12}$$

If ϵ is sufficiently large compared to μ_1, a NG mode may grow in space and saturate before the local bifurcation parameter $\mu(x)$ has become smaller than[2] μ_A. Let us recall that $x_A = \epsilon/\mu_1$ is the point at which the bifurcation parameter reaches the global instability threshold ($\mu(x_A) = \mu_A$). Let us also introduce x_s the location where the NG mode saturates and then decreases, *i.e.* the position of the maximum amplitude of the NG mode. When $x_s \ll x_A$, we may certainly describe the spatial growing part of the NG mode as the leading edge of the corresponding homogeneous NG mode (with the constant parameters μ_0 and U_0) and write $x_s \sim \Delta x \sim \ln(1/\epsilon)$. The condition $x_s \ll x_A$ implies $\mu_1 \ll \epsilon/\ln(1/\epsilon)$. However, the latter condition is misleading since the inhomogeneity brings in general a contribution to the maximum position x_s of the NG mode yet unknown, but which will be found positive and even larger than Δx the characteristic size of the homogeneous NG mode. Indeed, when $\mu_1 \ll \epsilon$, the NG mode is quasi homogeneous with a very long distance where the amplitude is only slightly below its maximum value. Hence, $x_s \geq \Delta x$ and the condition $x_s \ll x_A$ is more restrictive than $\Delta x \ll x_A$.

According to the respective values of x_s and x_A, we are led to distinguish two regions of the parameter space (μ_1, ϵ). At this stage, we must anticipate on the result which will be found for x_s in order to describe correctly (without the use of *ab initio* unknown jauge) the (μ_1, ϵ) plane (Fig. 2): x_s will be found to possess a dominant contribution which scales like $\ln(1/\mu_1)$, and therefore exceeds the expected contribution $\ln(1/\epsilon)$ coming from Δx (as if the NG mode was homogeneous). The condition $x_s \ll x_A$ then reads

$$\frac{\epsilon}{\mu_1} \gg \ln \frac{1}{\mu_1} \tag{13}$$

and corresponds to the dark gray region in Fig. 2. The condition $\mu_1 \ll \epsilon$ is valid in the gray regions. In the light gray region, $\epsilon \ll \mu_1 \ln(1/\mu_1)$ (or equivalently $x_s \gg x_A$) and in the white region, $\epsilon \ll \mu_1$. In order to cover the gray regions, we choose to connect ϵ and μ_1 by the relation

$$\epsilon = \mu_1 \left(\ln(1/\mu_1)\right)^n. \tag{14}$$

[2] For clarity we will no more mention the U_0 dependence of $\mu_A(U_0)$

with $n > 1$ in the dark gray region and $0 < n < 1$ in the light gray region. When n varies between $[0, +\infty)$, both gray regions are covered.

When $n > 1$, the NG mode spatial structure should be at first order, identical to the homogeneous NG mode, As we will see, inhomogeneity acts far downstream and comes into play at the maximum amplitude x_s.

When $0 < n < 1$, the inhomogeneity of the flow should act before the solution saturates. As a result, a NG mode grows in space less rapidly than for $n > 1$, since inhomogeneity counterbalances the departure from global instability threshold; the position of its maximum amplitude should be reached at a greater distance and have a different scaling than for $n > 1$.

Our goal is to describe the spatial structure of NG modes in the different regions of Fig. 2. In particular, we seek a scaling law for the position x_s of the maximum amplitude. Let us emphasize that x_s is expected to be at least greater than the characteristic size of homogeneous NG modes $\ln(1/\epsilon)$ and that a NG mode cannot be sustained in the white gray region of Fig. 2. We have to settle whether a NG mode may be sustained in the light gray region, and if so, what is the scaling law for its maximum amplitude position in this region.

3 Spatial structure of NG modes

An example of the ultimate state in a temporal numerical simulation of Eq. (1), with vanishing boundary conditions at the origin and at infinity, is displayed in Fig. 3. Initially the system is set in the uniform state $A = 0$. The amplitude grows and asymptotes a steady state for which the spatial structure will be described using the method of matched asymptotic expansions [20]. We distinguish seven subdomains in the original semi-infinite domain represented on Fig. 3.

The nonlinear front layers NF^i, $(i = s, d)$, the central nonlinear layer CNL and a linear outer layer OL are separated by transition layers (inner layers). The respective sizes of the layers are indicated on the figure. In the following, we indicate only briefly the nature of the solutions in each layers and we focus on the size of the different layers and on the description of the matching of the NG mode between the transition layer IL and NF^s which determines the existence of a NG mode and the associated scaling law for the position of the maximum amplitude x_s.

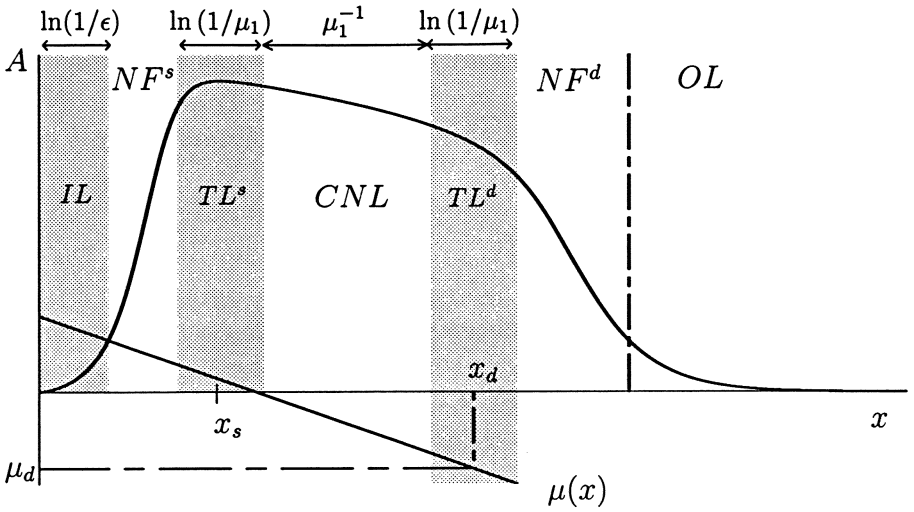

Fig. 3. A NG mode displays clearly four parts: In the nonlinear front layers NF^s, and NF^d, the solution respectively grows steep and decreases steep.In the central nonlinear layer CNL, the solutin decreases softly. OL is an outer linear region where the amplitude is small. An inner layer IL at the origin, and two transition layers (TL^s around the maximum amplitude, TL^d around the end of the weakly varying part of the solution) allow to connect linear and nonlinear regions; The straight line represents the bifurcation parameter $\mu(x)$.

3.1 Qualitative description of NG modes

In each subdomain, we must solve Eq. (10) and we need two boundary conditions in order to find the corresponding solution. We only know the boundary conditions at the origin and at infinity of the whole domain. Introduction of the transition layers IL at the origin, TL^s around x_s, TL^d around the point x_d which represents the right boundary of CNL and will be more precisely defined below, and matching between different layers will allow to determine all integration constants.

In IL, since the amplitude remains small, we use a solution of Eq. (10) linearized around zero, and the two integration constants are fixed by the boundary condition at the origin and the matching with the solution in NF^s, which is detailed below.

In the nonlinear front layer NF^s of size $\mathcal{O}(1)$, the solution is similar to the homogeneous global mode which grows in space till it reaches its maximum amplitude (Fig. 3) with an added small perturbation due to inhomogeneity. We assume that this rapidly growing solution allow to consider the bifurcation parameter as a constant (which equals $\mu_A(U_0)$, Eq. (6)) at leading order. We use the study of parallel model (10) to find the corresponding solution and compute the correction due to inhomogeneity.

At x_s the location of the maximum amplitude, the bifurcation parameter is close to the value $\mu_A(U_0)$ when neglecting ϵ and $\mu_1 \ln \epsilon$ terms. The matching between NF^s and TL^s is used as a boundary condition for the solution in NF^s. For this reason, the solution in NF^s can be computed unambiguously, only after the solution in TL^s is worked out.

In the transition layer TL_s of size $\ln(1/\mu_1)$, the amplitude has to match with the NF^s and therefore is close to $A_2(\mu_A)$ (Eq.(5)). It is represented by a linear solution of (10) around $A_2(\mu_A)$. The matching with CNL on the one hand, and the condition that $A(x)$ realizes a maximum at x_s on the other hand allow to determine the two integration constants. Again, the solution in TL^s can be only determined after the solution in the next layer CNL.

The central nonlinear layer (CNL) denotes the subdomain where the solution has bifurcated to the finite amplitude state $A_2(\mu)$ (Eq.(5)) and follows adiabatically the weak variation of the bifurcation parameter $\mu(x)$. The NG mode amplitude decreases slowly from $A_2(\mu(x_s))$ to $A_2(\mu(x_d))$, following approximately the slowly varying function $A_2(\mu(x)) = \left(1/2 + \sqrt{\mu_0 - \mu_1 x + 1/4}\right)^{1/2}$ and reflecting the interplay between nonlinearities and inhomogeneity. The boundaries of this region x_s and x_d actually determine the locations where the slope of the solution starts to steepen (with growing or decreasing amplitude). x_s has been defined as the position of the maximum amplitude, but the position x_d of the decreasing front, which represent the right boundary of CNL has to be precised.

The position of x_d is determined by the existence, in the homogeneous problem, of the decreasing front which links A_2 to zero. This occurs when the bifurcation parameter reaches a value $\mu_d(U_0)$ such that for the homogeneous system, the steady front solution may be computed in the phase space $(A, dA/dx)$ and corresponds to the existence of an heteroclinic orbit linking $A_2(\mu_d)$ to 0, *i.e.* for $\mu = \mu_d(U_0)$, the stable manifold of the origin of phase space intersects the unstable manifold of the point $A_2(\mu_d)$. In a previous study [18], we have determined the decreasing front transition value $\mu_d(U_0)$ which is plotted in Fig. 1 as a heavy continuous line of parametric equation

$$\mu = \mu_d(U_0) = \frac{3}{16}U_0^2 - \frac{\sqrt{3}}{8}U_0 - \frac{3}{16} \quad \text{if} \quad U_0 < \frac{1}{\sqrt{3}} \tag{15}$$

$$\mu = \mu_d(U_0) = -\frac{1}{4} \quad \text{if} \quad U_0 > \frac{1}{\sqrt{3}} \tag{16}$$

Returning to inhomogeneous problem, the position of the decreasing front is determined by $\mu(x_d) = \mu_d$.

The size of CNL is μ_1^{-1} at first order, since $x_d \sim \mu_1^{-1}(\mu_A(U_0) - \mu_d(U_0))$ and $x_s \ll \mu_1^{-1}$.

The transition layer TL^d of size $\ln(1/\mu_1)$ around x_d plays the same role than TL^s with A_2 replaced by $A_d = A_2(\mu_d)$ and the condition that $A(x)$ is maximum at x_s replaced by the condition that $A(x)$ exactly equals A_d at x_d.

In the nonlinear front layer NF^d of size $\mathcal{O}(1)$, the solution decreases back to a small amplitude, on a small length scale and we again consider that this rapidly decreasing solution is a backward facing nonlinear front with corrections due to inhomogeneity. The matching between TL^d and NF^d is used as a boundary condition to compute the solution in NF^d.

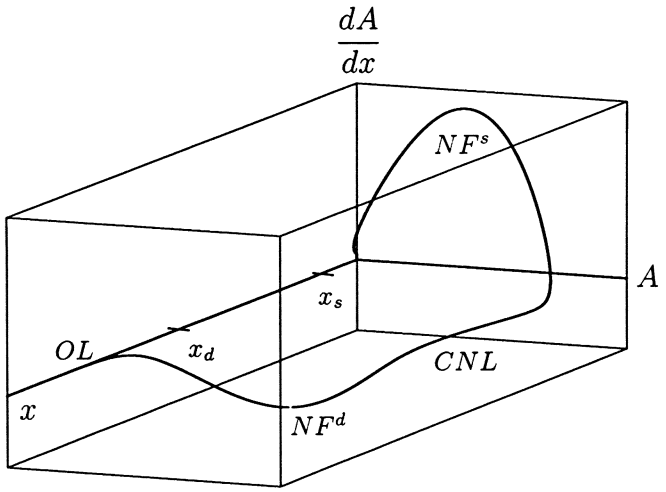

Fig. 4. The solution shown in Fig. 3 is plotted in the phase space $(A, x, dA/dx)$. The solution in NF^s and NF^d lay nearly in planes $(A, dA/dx)$, whereas in CNL, it lays nearly in the plane (A, x).

Let us point out that the whole structure of the NG mode has been pinned by the position of CNL between x_s and x_d. Actually, Fig. 3 may be viewed as the projection in the (A, x) plane of the three-dimensional phase space $(A, dA/dx, x)$. Fig. 4 show the structure of the solution in the phase space: The growing and decreasing fronts in NF^s and NF^d lay nearly in planes parallel to $(A, dA/dx)$, whereas the solution in CNL lay nearly in the (A, x) plane. The central nonlinear layer CNL whose left and right boundaries x_s and x_d are now precisely known from the variation of $\mu(x)$ allow to start this matching without applying the boundary conditions (2,3). The fact that solutions in NF^s and NF^d may be described in the plane $(A, dA/dx)$ allow to compute them by applying only one boundary condition given by the matching with CNL. Therefore, the whole solution is pinned by CNL. However, the whole matching must be done in order to know precisely the restrictions on μ_1 and ϵ the assumptions made imply and if the boundary conditions (2,3) may be applied but this do not alter the spatial structure of the solution described above.

In OL, the solution must vanish at infinity and hence, the amplitude remains small. We therefore use a solution of Eq. (10) linearized around zero, and fix the

remaining integration constant and the order of magnitude of the amplitude in OL by the matching with NF^d. This matching of the trailing edge in OL which is slave to the upstream structure of the NG mode is always possible and do not require an extra transition layer.

The complete spatial structure of NG modes represented on Fig. 3 for model (10) is detailed for each layer in Appendix A.

4 Matching $IL \to NF^s$ and scaling law for the position of the maximum

The inner solution in IL and the outer solution in NF^s are obtained in Appendix A. Denoting by ξ the inner variable for the amplitude in IL, the matching between these layers is done in a plane $(A, dA/dx)$ (Fig. 4), i.e. we match dA/dx considered as a function of A when $A \to 0$ with $d\xi/dx$ when $x \to +\infty$. When $x \to +\infty$, the asymptotic behavior of the $d\xi/dx$ (inner solution (A.34)) as a function of ξ reads

$$\frac{d\xi}{dx} \simeq r^+\xi + v_0^{1-r^-/r^+}\left(r^+ - r^-\right)^{r^-/r^+-1}\xi^{r^-/r^+} \tag{17}$$

where $r^+ = (U_0 + \sqrt{3})/4$, $r^- = (3U_0 - \sqrt{3})/4$. r^+ and r^- represent the spatial exponential growth (or decay) rates linked to possible ways to depart from (or arrive to) zero. v_0 represents the slope at the origin of the inner solution (which will be given by the matching). Multiplication of (17) by $\theta(\epsilon)$ (where $\theta(\epsilon) \to 0$ is the size in amplitude of the inner layer, to be precised below) and introduction of $A = \theta(\epsilon)\xi$ in (17) yields the following expansion (inner solution rewritten in outer variable)

$$\theta(\epsilon)\frac{d\xi}{dx} \simeq \frac{A_s^2}{\sqrt{3}}A + (v_0\theta(\epsilon))^{1-\lambda_1}\left(r^+ - r^-\right)^{\lambda_1}A^{\lambda_1}, \tag{18}$$

where $A_s \equiv A_2(\mu_A)$. The asymptotic behavior of the solution $u(A) \equiv dA/dx(A)$ in NF^s when $A \to 0$ is given by Eq. (A.32) of Appendix A. For the matching, we note that $\lambda_1 = r^-/r^+$ and $r^+ = A_s^2/\sqrt{3}$. Equation (18) is to be compared with expansion (A.32) in NF^s. The zeroth order terms are identical. At next order, we must identify $\theta(\epsilon)^{1-\lambda_1}$ with either ϵ or $\mu_1 \ln(1/\mu_1)$. When $n > 1$, (or $-\mu_1 \ln \mu_1 \ll \epsilon$), ϵ is the dominant term in (A.32) and the matching of solution (18) with solution (A.32) in NF^s yields

$$\theta(\epsilon) = \epsilon^\beta, \qquad \text{with} \qquad \beta = \frac{1}{1-\lambda_1}, \tag{19}$$

and

$$v_0 = \left(\frac{\sqrt{3} A_s^{2\lambda_2}}{(r^+ - r^-)^{\lambda_1}} \int_0^{A_s} a^{-\lambda_1} (A_s^2 - a^2)^{-\lambda_2 - 1} da \right)^{\beta}, \tag{20}$$

λ_2 being given by Eq. (A.28) of Appendix A. The position in x of the maximum is given by the sum of the contribution in IL found by Eq. (A.35) from $x = 0$ to x_i where $\xi = 1$:

$$x_i \simeq \frac{1}{r^+} \ln \frac{r^+ - r^-}{v_0}, \tag{21}$$

and the contribution in NF^s and TL^s found by Eq. (A.26) from x_i where $A = \theta(\epsilon)$ to x_s:

$$x_s - x_i \simeq \frac{1}{k_s^-} (2\beta \ln \epsilon + \ln \mu_1). \tag{22}$$

where $k_s^- = -2A_s^2/\sqrt{3}$. Since $\mu_1 \ll \epsilon \ll 1$, $\ln(1/\epsilon) \ll \ln(1/\mu_1)$ and when keeping only the dominant term, we find

$$x_s \simeq \frac{1}{|k_s^-|} \ln \left(\frac{1}{\mu_1} \right) \tag{23}$$

When $0 < n < 1$, (or $\mu_1 \ln(1/\mu_1) \gg \epsilon$) the same matching is possible. To obtain this result, let us compare the different orders in (A.32). The dominant second order term is either $\mu_1 \ln(1/\mu_1)$ or $\mu_1 x_s$.

- Firstly, x_s cannot dominate $\ln(1/\mu_1)$, as the term of order $\mu_1 x_s$ of negative sign in (A.32) cannot be matched with the order $\theta(\epsilon)^{1-\lambda_1}$ term of positive sign in (18).
- Secondly, the seek of a solution scaling like $x_s \sim s \ln(1/\mu_1)$ with the assumption $s + 1/k_s^- < 0$ leads again to the matching of the term of order $\mu_1 \ln(1/\mu_1)$ in (A.32) with the term of order $\theta(\epsilon)^{1-\lambda_1}$ in (18). By assumption, they have now the same sign and matching is achieved for $\theta(\epsilon) = (\mu_1 \ln(1/\mu_1))^{\beta}$. Then the contribution of NF^s and TL^s to x_s is evaluated as in Eq. (22) and is found to be $x_s - x_i = (2\ln(\theta(\epsilon)) + \ln \mu_1)/k_s^- \sim (2\beta + 1)/k_s^- \times \ln \mu_1$. It should correspond to $s \ln(1/\mu_1)$ and yields $s = -(2\beta+1)/k_s^-$, which is in contradiction with $s + 1/k_s^- < 0$.
- Finally, the only possible matching between IL and NF^s is achieved for (23) which cancels the $\mu_1 \ln(1/\mu_1)$ order in (A.32) and leaves the term of order ϵ as the dominant second order term. Therefore (19,20) established for $n > 1$ are also valid for $0 < n < 1$.

When $\mu_1 \gg \epsilon$, solutions (18) and (A.32) can no longer be matched, since the dominant terms to be compared, $\mu_1 x_s$ and $\theta(\epsilon)^{1-\lambda_1}$ in (A.32 and (18) are of opposite signs as previously.

Our analysis is therefore valid in the gray regions of Fig. 2, and whatever n, the dominant contribution to the position of the maximum x_s is given by (23), i.e. it scales like $\ln(1/\mu_1)$ when $\mu_1 \ll \epsilon$. Let us emphasize that the effect of the inhomogeneity differs in the light and dark gray regions although the scaling for x_s has been found to be the same. Indeed, in the dark gray region, NG modes are quasi homogeneous and inhomogeneity starts to play a role only in the transition layer TL^s. The distance needed to reach an arbitrary amplitude (smaller than the maximum by an order one quantity) scales like $\ln(1/\epsilon)$ as for the homogeneous problem. By contrast, in the light gray region, inhomogeneity starts to play a role in NF^s and the distance necessary to reach an arbitrary amplitude is here greater than $\ln(1/\epsilon)$. The fact that we find the same scaling for the maximum amplitude comes from the addition of the different contributions due to inhomogeneity in each layer. This result differs from the one found in the case of a Kolmogorov front transition to a nonlinear global instability, for which specific scalings have been found according to the distance at which inhomogeneity acts.

5 Discussion of results

The dominant part $\ln(1/\mu_1)$ of the scaling law for x_s has been shown to exceed the characteristic size of homogeneous NG modes ($\ln(1/\epsilon)$). The main part of the size of a homogeneous NG mode is the length it needs to grow out of the inner layer whereas for a NG mode, the main part of its size is used to reach the maximum. This difference comes from the definition as for a NG mode, we were using the distance at which the maximum amplitude is achieved whereas the size of a homogeneous NG mode is defined as the distance at which its amplitude reaches an arbitrary value, as it never reaches a maximum but asymptotes it at $+\infty$. In an inhomogeneous problem, the distance at which an arbitrary amplitude is reached scales as $\ln(1/\epsilon)$ in the dark gray region of Fig. 2, as for homogeneous NG modes. In the light gray region, it scales as $\ln(1/\mu_1)$. An extra length which is $\mathcal{O}(\ln(1/\mu_1))$ is needed to reach the maximum amplitude and brings the dominant contribution to the position of the maximum.

The fact that the inhomogeneity is sufficiently weak to play a role only in the decreasing part of the NG mode can be only determined by the measure of characteristic size of the NG mode close to threshold (used to reach an arbitrary amplitude) but not by the measure of the position of the maximum amplitude. Indeed, when the inhomogeneity is weak, the characteristic growth size of a NG mode is $\mathcal{O}(\ln(1/\epsilon))$ and depends on the departure from threshold ϵ. By contrast, when the inhomogeneity is stronger, it no longer depends on ϵ (scaling in

$\ln(1/\mu_1)$). Therefore the effect of inhomogeneity on the characteristic growth size is clear, whereas the position of the maximum never depends on the departure from threshold.

The same scaling is found when the maximum is reached before or when it is reached after the position x_A (such that $\mu(x_A) = \mu_A$ and which delineates the region where the flow would be globally unstable within a parallel flow approximation). By contrast, the study of the supercritical [13] model has shown two possible scaling according to the respective values of x_s and x_A, because in that case, the $\ln(1/\mu_1)$ terms coming from the TL^s was a third order effect cancelled by a lower order term due to nonlinear effect.

6 Conclusion

The present study has been restricted to advection velocities smaller than $\sqrt{3}$ since for $U_0 > \sqrt{3}$, the global instability occurs at the absolute/convective transition as for a purely supercritical bifurcating mode.

In an experimental setup in the parallel flow case, the nonlinear global instability may be either of the Kolmogorov type, *i.e.* occurring when the flow becomes absolutely unstable, or of the nonlinear type, *i.e.* occurring while the flow is still convectively unstable. This distinction is related to the advection velocity, but the nonlinear transition does not necessarily occur for small advection velocities. By contrast with the present study with a subcritical bifurcation model, [18] has shown that the addition of nonlinear advection terms in a supercritical model leads to a nonlinear transition for high advection velocities.

In the case of a Kolmogorov transition, the growth size of a NG mode has been shown [18] to scale like $\epsilon^{-1/2}$, where ϵ is the departure from threshold. This result is in good agreement with measurements of the size of NG modes obtained numerically by integration of Navier–Stokes equations for the Rayleigh–Bénard convection with throughflow by Müller *et al.* [11] and for Taylor–Couette rolls with throughflow by Büchel *et al.* [10]. In the case of a nonlinear transition the growth size of NG modes scales like $\ln(1/\epsilon)$.

In an experimental setup in the weakly nonparallel flow case, the nonlinear global instability may also be either of the Kolmogorov type or of the nonlinear type. The $\epsilon^{-1/2}$ scaling of the position of the maximum of NG modes pertaining for the case of a Kolmogorov transition is relevant to describe wakes when inhomogeneity is sufficiently weak as shown in [13]. This scaling derived theoretically is indeed in good agreement with the experimental measurements by Goujond-Durand *et al.* [15] and with the numerical computation by Zielinska and Wesfreid [14], for the wake of angular obstacles.

Concerning the case of a nonlinear transition in a weakly nonparallel flow, to our knowledge the scaling in $\ln(1/\mu_1)$ for the position of the maximum has not been observed experimentally. However, as we have shown in [18] that for parallel flows, a nonlinear global instability may occur while the system is still convectively unstable, the present analysis shows on an example that this result persists in the case of weakly nonparallel flows;

Therefore, according to the advection velocity, the same experimental setup may lead to two kind of global instability characterized by two kind of NG modes scaling: the $\ln(1/\mu_1)$ scaling for the maximum amplitude characterizes a transition to a global instability occurring while the system is still convectively unstable everywhere. The $\epsilon^{-1/2}$ scaling characterizes a transition to a global instability of the Kolmogorov type, occurring at the absolute/convective transition. These two scaling laws do not necessarily correspond to small ang large advection velocities as in the subcritical model. Indeed, the contrary may be possible as shown in [18] by the study of the "van der Pol–Duffing" system in the parallel flow case. We have shown that for the Rayleigh-Bénard problem and for the Taylor–Couette problem with small throughflow, the size of a NG mode exhibits a $\epsilon^{-1/2}$ scaling. The $\ln(1/\mu_1)$ scaling could be obtained in these systems for higher advection velocities. We conclude this paper by emphasizing again that an experiment known to display a subcritical behavior (which could be achieved by adding a Poiseuille flow) may lead to the observation of the specific scaling $\ln(1/\mu_1)$. Also Görtler flow seems to us a good candidate where these scaling for the NG modes could be observed.

A Detailed spatial structure of NG modes

Since the spatial structure of the solution is similar in NF^s and NF^d, and also in TL^s and TL^d, we will use the following notations throughout the appendices to avoid the double description of the layers.

$$\mu_s \equiv \mu_A, \quad A_s \equiv A_2(\mu_A), \tag{A.1}$$

$$A_d \equiv A_2(\mu_d) \tag{A.2}$$

A.1 Outer layer CNL

In this layer, the amplitude varies weakly with respect to the slow variable $X = \mu_1 x$. The change of variable $Z = \mu_1\, x - \mu_0$, where $\mu_0 = \mu_A + \epsilon$ leads to seek a solution of the equation

$$ZA - A^3 + A^5 + \mu_1 U_0 A'(Z) = 0. \tag{A.3}$$

where prime denotes differentiation with respect to the argument. Since the derivative $A'(Z)$ only appears at second order in μ_1, this equation possesses a solution which cannot satisfy boundary condition and which reads

$$A(Z) = A_0(Z) + \mu_1 A_1(Z). \tag{A.4}$$

with

$$A_0(Z) = \left(\frac{1}{2} + \frac{1}{2}\sqrt{1-4Z}\right)^{1/2} \qquad A_1(Z) = \frac{U_0}{4A_0^3(Z)(1-2A_0^2(Z))^2} \tag{A.5}$$

The position of CNL is fixed in space and delimited by the boundaries x_s at the left where $A(x)$ is maximum and x_d at the right where $\mu(x_d) = \mu_d(U_0)$. Solution (A.4–A.5) may be expanded near the boundaries of CNL which correspond to the values $Z = -\mu(x_i) + \mu_1(x - x_i)$, $i = s, d$. Please note that $\mu(x_s) = \mu_A + \epsilon - \mu_1 x_s$ whereas with $\mu(x_d) = \mu_d$. This leads to the following expansions, which are not totally symmetric due to the definition of the boundaries of CNL.

$$\text{when } x \to x_s \quad A(Z) \simeq A_0(-\mu_A) + (\mu_1 x - \epsilon)A_0'(-\mu_A) + \mu_1 A_1(-\mu_A) \tag{A.6}$$

$$\text{when } x \to x_d \quad A(Z) \simeq A_0(-\mu_d) + \mu_1 (x - x_d)A_0'(-\mu_d) + \mu_1 A_1(-\mu_d) \tag{A.7}$$

A.2 Transition layers TL^s and TL^d

In these two layers, the analysis is similar since we seek a solution of Eq. (10) linearized around one of the boundary x_i of CNL, which represents also the center of the layer TL^i $(i = s, d)$, and where the amplitude is close to a finite value A_i (see Eqs. (A.1,A.2)). We therefore introduce $A = A_i - \epsilon^{p_i}\phi_i(x)$ into Eq. (10) and expand it at first order in ϵ^{p_i} to find the equation satisfied by $\phi_i(x)$:

$$\frac{d^2\phi_i}{dx^2} - U_0 \frac{d\phi_i}{dx} + \tilde{\mu}_i \phi_i = \epsilon^{-p} A_i \psi_i(x), \tag{A.8}$$

where the second member $\psi_i(x)$ reads

$$\psi_2(x) = (\epsilon - \mu_1 x), \qquad \psi_3(x) = -\mu_1(x - x_d) \tag{A.9}$$

and $\tilde{\mu}_i = \mu_i + 3A_i^2 - 5A_i^4$, with the convention $\mu_s \equiv \mu_A$, Using the notations

$$k_s^- = -\frac{U_0 + \sqrt{3}}{2} \qquad k_s^+ = \frac{3U_0 + \sqrt{3}}{2}, \tag{A.10}$$

$$k_d^- = \frac{3U_0 - \sqrt{3}}{2} \qquad k_d^+ = \frac{-U_0 + \sqrt{3}}{2}, \tag{A.11}$$

the general solution of Eq. (A.8) then reads

$$\phi_i(x) = c_{1i}\, \mathrm{e}^{k_i^+(x-x_i)} + c_{2i}\, \mathrm{e}^{k_i^-(x-x_i)} + \epsilon^{-p_i}\frac{A_i}{\tilde{\mu}_i}\psi_i(x) - \mu_1\epsilon^{-p_i}\frac{U_0 A_i}{\tilde{\mu}_i^2} \tag{A.12}$$

where the last non-exponential term represents a particular solution of (A.8) and c_{1i}, c_{2i} are integration constants. A boundary condition will be imposed by the matching with the solution in CNL when $x - x_s \to +\infty$, and when $x - x_d \to -\infty$. The outer solution (A.6) in CNL is linear with respect to x; then $\epsilon^{p_i}\phi_i(x)$ must be also linear when $x - x_i \to \pm\infty$ (with the plus sign for $i = s$ and the minus sign for $i = d$). These two matching conditions imply $c_{1s} = 0$ and $c_{2d} = 0$. As $x - x_s \to +\infty$, or $x - x_d \to -\infty$, the inner solution (A.12) admits the expansion

$$\epsilon^{p_i}\phi_i(x) \simeq \frac{A_i}{\tilde{\mu}_i}\psi_i(x) - \mu_1\epsilon^{-p_i}\frac{U_0 A_i}{\tilde{\mu}_i^2} \tag{A.13}$$

Since $A_0(-\mu_i) = A_i$, $A_i/\tilde{\mu}_i = A_0'(-\mu_i)$ and $U_0 A_i/\tilde{\mu}_i^2 = A_1(-\mu_i)$, expansion (A.13) with $i = s, d$ represents exactly orders ϵ and μ_1 of (A.6) or (A.7). Hence, matching between CNL and TL^i is done.

The position of the maximum x_s must satisfy $d\phi_s/dx(x_s) = 0$ whereas x_d is defined by $\mu(x_d) = \mu_d$ and hence, $A(x_d) = A_d$ yields the condition $\phi_d(x_d) = 0$. these two conditions allow to determine the constants $c_{2s} = \mu_1\epsilon^{-p_s}A_s/\tilde{\mu}_s k_s^-$ and $c_{1d} = \mu_1\epsilon^{-p_d}A_d U_0/\tilde{\mu}_d^2$. The complete solutions (A.12) ($i = s, d$) are known and in order to match them with NF^i, we determine their asymptotic behavior when $x - x_s \to -\infty$ and $x - x_d \to +\infty$ (given by the exponential terms at leading order. Since the matching of these parts of solution will be done in the phase space, we differentiate Eq (A.12) and use again (A.12) to eliminate the exponential term which appears in the differentiated equation:

$$\epsilon^{p_s}\frac{d\phi_s}{dx} = k_s^-\epsilon^{p_s}\phi_s + \mu_1 x_s\frac{k_s^- A_s}{\tilde{\mu}_s} - \epsilon\frac{k_s^- A_s}{\tilde{\mu}_s} + \mu_1\frac{A_s}{\tilde{\mu}_s}\left(\frac{U_0 k_s^-}{\tilde{\mu}_s} - 1\right). \tag{A.14}$$

$$\epsilon^{p_d}\frac{d\phi_d}{dx} \simeq k_d^+\epsilon^{p_d}\phi_d \tag{A.15}$$

Equation (A.14) is an exact relation and will be used as the asymptotic behavior of the solution (A.12) in the phase space as $x - x_s \to -\infty$, whereas (A.15) is truncated at leading order which is sufficient to do the matching when $x - x_d \to +\infty$.

Moreover, the maximum amplitude verifies $A(x_s) = A_s - \epsilon^{p_s}\phi(x_s)$ with

$$\epsilon^{p_s}\phi(x_s) = -\mu_1\frac{A_s}{\tilde{\mu}_s}x_s + \epsilon\frac{A_s}{\tilde{\mu}_s} + \mu_1\frac{A_s}{\tilde{\mu}_s}\left(\frac{1}{k_s^-} - \frac{U_0}{\tilde{\mu}_s}\right). \tag{A.16}$$

A.3 Central nonlinear layer NF^s and NF^d

In these layers which posses one boundary at x_i, we consider that the solution grows (or decreases) sufficiently fast so that $\mu(x)$ is approximately constant and equal to μ_i. In other words, the size of these two layers is much smaller than μ_1. The seek of the solutions in NF^i is then equivalent to a problem that has been already solved [18]. Indeed, at leading order, the solution in NF^s represents an heteroclinic trajectory linking the point to the origin of phase space to the point $(A_s, dA/dx = 0)$ for the constant parameter value $\mu = \mu_A$ whereas in NF^d, the solution represents an heteroclinic trajectory linking the point $A_d, dA/dx = 0$ to the origin. At the next order, small corrections have to be added, due to the small variation of $\mu(x)$ on the size of NF^i

We therefore seek these solutions directly in the phase space in the form of Eq. (A.17),

$$u(A) = \frac{dA}{dx} = u_0(A) + \epsilon\, u_1(A) + \mu_1 u_2(A). \tag{A.17}$$

At the lowest order, $u_0(A)$ satisfies

$$u_0 u_0' - U_0 u_0 + \mu_i A + A^3 - A^5 = 0 \tag{A.18}$$

where a prime denotes differentiation with respect to A. For the value of the parameter μ_i previously defined and an advection velocity $U_0 < 1/\sqrt{3}$, both solutions $u_0(A)$ in NF^i, $(i = s, d)$ are polynomial. When $1/\sqrt{3} < U_0 < \sqrt{3}$, $u_0(A)$ is still polynomial in NF^s but not in NF^d. Since the trailing edge of the NG mode in NF^d and OL is slave of its spatial structure before these layers, we present here only the case $U_0 < 1/\sqrt{3}$ for simplicity, but this do not restrict the generality of the study. For each layer NF^i, the solution at leading order then reads

$$u_0(A) = \frac{\pm}{\sqrt{3}} A \left(A_i^2 - A^2\right), \tag{A.19}$$

with the plus sign if $i = s$ and the minus sign if $i = d$. This solution may be again integrated:

$$A = A_i \left(1 + A_{0i}^{-2}\, \mathrm{e}^{-\frac{\pm A_i^2}{\sqrt{3}} x}\right)^{-1/2} \tag{A.20}$$

where A_{0i} is an integration constant.

When $x \to x_i$, the asymptotic behavior of the solution reads

$$A = A_i - \frac{A_i}{2A_{0i}^2} \mathrm{e}^{-\frac{\pm 2A_i^2}{\sqrt{3}}x} \tag{A.21}$$

Since $k_s^- = -2A_s^2/\sqrt{3}$, and $k_d^+ = 2A_d^2/\sqrt{3}$, (A.21) matches with the solution (A.12) in TL^i. This determines the constants

$$A_{0s}^{-2} = \frac{2\mu_1}{\tilde{\mu}_s k_s^-} \mathrm{e}^{-k_s^- x_s}, \quad \text{and} \quad A_{0d}^{-2} = \frac{2\mu_1 U_0}{\tilde{\mu}_d^2} \mathrm{e}^{-k_d^+ x_d}. \tag{A.22}$$

When reporting these values in (A.20), we may find the asymptotic behavior of the solution in TL^d when $x - x_d \to +\infty$:

$$A \simeq A_d \frac{\tilde{\mu}_d}{\sqrt{2U_0\mu_1}} \exp(-k_d^+(x - x_d)/2) \tag{A.23}$$

In NF^d, this leading order is sufficient to do the matching with OL as will be seen below, but in NF^s, we have to compute the correction to the leading order. This next order to be taken into account may be either ϵ or $\mu_1 x$; We assume that they are separated; $u_1(A)$ and $u_2(x, A)$ satisfy

$$u_0\, u_1' + (u_0' - U_0)\, u_1 = -A \tag{A.24}$$
$$u_0\, u_2' + (u_0' - U_0)\, u_2 = x\, A \tag{A.25}$$

where x in (A.25) is at first order the function of A defined by (A.20), with the corresponding constant A_{0s}, which reads

$$x(A) = x_s - \frac{1}{k_s^-}\left(\ln\left(\frac{A^2}{A_s^2 - A^2}\right) - \ln\left(\frac{\tilde{\mu}_s k_s^-}{2\mu_1}\right)\right) \tag{A.26}$$

Introducing (A.18) in Eqs. (A.24,A.25) and (A.26) in (A.25) allows to compute u_1 and u_2 analytically, since $u_0(A)$ is a polynomial solution:

$$u_1(A) = -\sqrt{3}A^{\lambda_1}(A_s^2 - A^2)^{\lambda_2}\sqrt{3}\int_{A_s}^{A} a^{-\lambda_1}(A_s^2 - a^2)^{-\lambda_2 - 1} da \tag{A.27}$$

where

$$\lambda_1 = \frac{3U_0 - \sqrt{3}}{U_0 + \sqrt{3}}, \qquad \lambda_2 = -\frac{3U_0 + \sqrt{3}}{U_0 + \sqrt{3}}, \tag{A.28}$$

and

$$u_2(A) = \sqrt{3}A^{\lambda_1}(A_s^2 - A^2)^{\lambda_2} \int_{A_s}^{A} a^{-\lambda_1}(A_s^2 - a^2)^{-\lambda_2 - 1} x(a) da \tag{A.29}$$

where $x(a)$ is the function of a (A.26).

When $A \to A_s$, solution (A.18–A.29) may be expanded into

$$u_0(A) + \epsilon u_1(A) + \mu_1 u_2(x, A) \simeq -\frac{2A_s^2}{\sqrt{3}}(A_s - A) - \epsilon\frac{\sqrt{3}}{2A_s\lambda_2} + \mu_1\frac{\sqrt{3}}{2A_s\lambda_2}\left(x - \frac{\sqrt{3}}{2A_s^2\lambda_2}\right) \tag{A.30}$$

which is identical to expansion (A.14) since we verify that

$$k_s^- = -\frac{2A_s^2}{\sqrt{3}}, \quad \frac{k_s^- A_s}{\mu_s} = \frac{\sqrt{3}}{2A_s\lambda_2}, \quad \frac{A_s}{\mu_s}\left(\frac{U_0 k_s^-}{\mu_s} - 1\right) = -\frac{3}{4A_s^3\lambda_2^2}. \tag{A.31}$$

solutions in TL^s and NF^s are now matched. In other words, the matching succeeds whatever the size of the transition layer TL^s. When $A \to 0$, solution (A.18–A.29) expands into

$$\begin{aligned} u_0(A) + \epsilon u_1(A) + \mu_1 u_2(x, A) \simeq{}& \frac{A_s^2}{\sqrt{3}}A \\ &+ \left(\epsilon - \mu_1(x_s - \frac{1}{k_s^-}\ln\mu_1\right)\sqrt{3}A^{\lambda_1}A_s^{2\lambda_2}\int_0^{A_s} a^{-\lambda_1}(A_s^2 - a^2)^{-\lambda_2-1}da \\ &-\mu_1\sqrt{3}A^{\lambda_1}A_s^{2\lambda_2}\left(\frac{1}{k_s^-}\ln\frac{\tilde{\mu}_s k_s^-}{2}\right)\int_0^{A_s} a^{-\lambda_1}(A_s^2 - a^2)^{-\lambda_2-1}da \\ &+\mu_1\sqrt{3}A^{\lambda_1}A_s^{2\lambda_2}\frac{\sqrt{3}}{A_s^2}\int_0^{A_s} a^{-\lambda_1}(A_s^2 - a^2)^{-\lambda_2-1}\ln\frac{a}{\sqrt{A_s^2 - a^2}}da \end{aligned} \tag{A.32}$$

A.4 Transition layer IL

In this layer, the amplitude is small since A vanishes at $x = 0$. Denoting ξ the inner variable which is connected to the amplitude by the relation $A = \theta(\epsilon)\xi$ (where $\theta(\epsilon)$ denotes the size in amplitude of the inner layer and will be precised by the matching), ξ satisfies the linearized Eq. (10) around $A = 0$:

$$\xi'' - U_0\,\xi' + \mu(x)\xi = 0. \tag{A.33}$$

Since $\xi(x)$ must vanish at the origin, the solution of Eq. (A.33) may be written with one undetermined integration constant v_0, and using Airy functions [21]

$$\xi(x) = \frac{v_0 \pi}{\mu_1^{1/3}} \, \mathrm{e}^{\frac{U_0}{2}x} \left(a \, \mathrm{Bi}\left((x - x_K)\mu_1^{\frac{1}{3}} \right) - b \, \mathrm{Ai}\left((x - x_K)\mu_1^{\frac{1}{3}} \right) \right) \tag{A.34}$$

with $x_K = (\mu_A - U_0^2/4 + \epsilon)/\mu_1$, (the position at which $\mu(x)$ reaches $U_0^2/4$ here negative and therefore virtual), $a = \mathrm{Ai}\left(-x_K \mu_1^{1/3}\right)$ and $b = \mathrm{Bi}\left(-x_K \mu_1^{1/3}\right)$. The slope v_0 at the origin of the inner solution (A.34) will be fixed by the matching. Since $\mu_A(U_0) < U_0^2/4$, x_K is negative, and since $\mu_1 \ll 1$, we obtain $-x_K \mu_1^{1/3} \to +\infty$. Hence, Ai, Bi functions may be replaced by their asymptotic expansions at infinity since $\mu_1 \ll 1$. The same inner solution than for homogeneous NG mode [18] is found.

$$\xi(x) = \frac{v_0}{r^+ - r^-} \left(\mathrm{e}^{r^+ x} - \mathrm{e}^{r^- x} \right) \tag{A.35}$$

where $r^+ = (U_0 + \sqrt{3})/4$ and $r^- = (3U_0 - \sqrt{3})/4$.

A.5 outer layer OL

In the outer layer OL, $A(x)$ is small since it must vanish at infinity. Therefore, $A(x)$ is solution of the linear equation (A.33) and reads

$$A(x) = g(\mu_1) \exp\left(\frac{U_0}{2}x\right) \mathrm{Ai}\left((x - x_K)\mu_1^{\frac{1}{3}} \right) \tag{A.36}$$

where $g(\mu_1)$ is an integration constant (the coefficient of Bi must be zero in order to cancel the growing part of the general solution).

In order to do the matching between OL and NF^d, let us expand (A.36) when $x \to x_d$. Since $x - x_K = x_d - x_K + x - x_d$, and $x_d - x_K \sim (U_0 + \sqrt{3})^2/16\mu_1$, $x_d \sim (\mu_A - \mu_d)/\mu_1 = \sqrt{3}U_0/4\mu_1$, we may use the asymptotic behavior of Ai at infinity to find

$$A(x) \simeq g(\mu_1) \, \mathrm{e}^{\frac{U_0^2\sqrt{3}}{8\mu_1} - \frac{1}{96\mu_1}(U_0+\sqrt{3})^3} \frac{1}{4\sqrt{\pi}} \mu_1^{1/6} (U_0 + \sqrt{3})^{-1/2} \, \mathrm{e}^{-\frac{k_d^+}{2}(x - x_d)} \tag{A.37}$$

where we have used $-k_d^+/2 = U_0/2 - (\mu_1(x_d - x_K))^{1/2}$. The identification of (A.37) with (A.23) yields

$$g(\mu_1) = \mu_1^{-\frac{1}{3}} \, \mathrm{e}^{\left(-U_0^2\sqrt{3} + \frac{(U_0+\sqrt{3})^3}{12}\right)\frac{1}{8\mu_1}} \, f(U_0), \tag{A.38}$$

where

$$f(U_0) = (U_0 + \sqrt{3})^{1/2}(U_0 - \sqrt{3})^2 \left(U_0 - \frac{1}{\sqrt{3}}\right) \frac{3}{4} \left(\frac{3\pi}{2U_0}\right)^{\frac{1}{2}} \tag{A.39}$$

References

[1] D. Rockwell, E. Naudascher, *Self sustained oscillations of impinging free shear layers*, Annu. Rev. Fluid Mech. **11**, 67 (1979).

[2] E. Villermaux, Ph. D. Thesis, Université de Grenoble (1992).

[3] C. Mathis, M. Provansal, L. Boyer, *The Bénard von Kármán instability: an experimental study near the threshold*, J. Phys. (Paris) Lett. **45**, 483 (1984).

[4] A. Zebib, *Stability of viscous flow past a circular cylinder*, J. Eng. Math. **21**, 155, (1987).

[5] C.P. Jackson, *A finite-element study of the onset of vortex shedding in flow past variously shaped bodies*, J. Fluid Mech. **182**, 23 (1987).

[6] W. Koch, *Local instability characteristics and frequency determination of self excited wake flows*, J. Sound Vib. **99**, 53 (1985).

[7] (a) R.J. Briggs, *Electron-Stream Interaction with Plasmas* (MIT Press, Cambridge, MA, 1964). (b) A. Bers, in *Physique des Plasmas*, edited by C. DeWitt and J. Peyraud (Gordon and Breach, New York, 1975). (c) E.M. Lifshitz and L.P. Pitaevskii, *Physical kinetics* (Pergamon, London, 1981).

[8] J.M. Chomaz, P. Huerre, L.G. Redekopp, *Bifurcations to local and global modes in spatially developing flows*, Phys. Rev. Lett., **60**, 25 (1988).

[9] P.A. Monkewitz, *The absolute and convective nature of instability in two-dimensional wakes at low Reynolds numbers*, Phys. Fluids **31**, 999 (1988).

[10] P. Büchel, M. Lücke, D. Roth, R. Schmitz, *Pattern selection in the absolutely unstable regime as a nonlinear eigenvalue problem: Taylor vortices in axial flow*, Phys. Rev. E. **53**, 4764 (1996).

[11] H.W. Müller, M. Lücke, M. Kamps, *Convective Patterns in Horizontal flow*, Europhys. Lett. **10**, 451 (1989); *Transversal convection patterns in horizontal shear flow*, Phys. Rev. A **45**, 3714 (1992).

[12] A. Couairon, J.M. Chomaz, *Pattern selection in the presence of a cross flow*, submitted to Phys. Rev. Lett.,

[13] A. Couairon, J.M. Chomaz, *Nonlinear global modes in slowly varying flows*, submitted to Phys. Fluids.

[14] B.J.A. Zielinska, J.E. Wesfreid, *On the spatial structure of global modes in wake flow*, Phys. Fluids **7**, 1418 (1995).

[15] S. Goujon-Durand, P. Jenffer, J.E. Wesfreid, *Downstream evolution of the Bénard-von Kármán instability*, Phys,. Rev. E **50**, 308 (1994).

[16] P. Huerre, P.A. Monkewitz, *Local and global instabilities in spatially developing flows*, Annu. Rev. Fluid Mech. **22**, 473 (1990).

[17] Y. Pomeau, S. Zaleski, P. Manneville, *Axisymmetric cellular structures revisited*, Journal of Applied Mathematics and Physics (ZAMP), **36**, (1985), 367.

[18] A. Couairon, J. M. Chomaz, *Absolute and convective instabilities, front velocities and global modes in nonlinear systems*, submitted to Physica **D**.

[19] A. Kolmogorov, I. Petrovsky, N. Piskunov, *Investigation of a diffusion equation connected to the growth of materials, and application to a problem in biology*, Bull. Univ. Moscow, Ser. Int. Sec. A **1**, 1 (1937).

[20] C.M. Bender, S.A. Orszag, *Advanced Mathematical Methods for Scientists and Engineers*, (Mc Graw Hill, 1978).

[21] M. Abramowitz, I.A. Stegun, *Handbook of mathematical functions*, (Dover, 1972).

Conclusion

Dans cette dernière partie, nous synthétisons l'ensemble des résultats obtenus dans les trois chapitres de cette thèse et nous proposons certaines extensions possibles de ces résultats.

Dans le premier chapitre, nous avons décrit des modèles qui représentent la dynamique d'écoulements ouverts instables, supposée réduite près du seuil à celle des modes «actifs» au sens de Newell *et al.* [73], i.e. près du seuil, au mouvement du système sur sa variété centrale, et pour des écarts au seuil d'ordre un nous nous plaçons en aval de l'identification de ces modes actifs qui constitue un sujet encore ouvert. En ce sens, la structure transverse des écoulements est supposée rester passive dans le mécanisme de déstabilisation globale. L'évolution d'une amplitude spatialement variable a été étudiée en milieu semi-infini unidimensionnel. Dans toutes les équations d'amplitude utilisées dans ce premier chapitre, il existe un potentiel qui implique une dynamique relaxationnelle mais qui ne restreint pas la généralité des idées évoquées. Nous avons montré que le système bifurque vers une solution non triviale stationnaire et stable appelée mode global non linéaire, lorsqu'un paramètre de contrôle est augmenté au delà d'un certain seuil (le seuil non linéaire d'instabilité globale). Cette solution varie spatialement de l'état d'amplitude imposé par la condition limite à l'origine ($A = 0$ pour le cas «ideal») à un état d'amplitude fini qui dépend des non linéarités du système. Afin de caractériser la bifurcation vers ce mode global non linéaire, nous avons étudié l'influence de la vitesse d'advection sur le système et nous avons mis en évidence les liens entre cette instabilité globale non linéaire et les notions d'instabilités absolues et convectives linéaires, ou non linéaires. La notion d'instabilité absolue et convective *linéaires* a été définie initialement dans le contexte de la physique des plasmas [14, 12, 62] et appliquée avec succès pour décrire les instabilités de certains écoulements cisaillés ouverts [45, 46] ; elle repose sur la réponse impulsionnelle (en temps et en espace) d'un système spatialement infini. Les instabilités absolues et convectives *non linéaires* définies par Chomaz [18], caractérisent la réponse d'un milieu infini à des perturbations initiales d'extension finie et peuvent être déterminées grâce aux résultats obtenus sur la propagation de fronts [7, 10, 30, 92, 93].

Nous avons montré pour ces modèles d'équation d'amplitude réels de type Ginzburg--Landau que la notion de mode global non linéaire qui se rapporte typiquement

dans cette étude à un domaine semi-infini coïncide avec la notion d'instabilité absolue non linéaire, mais que de facon générale, un écoulement peut devenir non linéairement globalement instable alors que l'état de base constitué par la solution triviale est linéairement convectivement instable ou même stable. Ce résultat a priori surprenant n'est pas uniquement obtenu pour des systèmes sous-critiques : un exemple où ce résultat persite pour une bifurcation supercritique a été étudié. Cette situation parait générique dès lors que les non linéarités sont susceptibles d'accelérer le front du paquet d'onde généré par les perturbations initiales. Le seuil de bifurcation pour lequel un système évolue vers un mode global non linéaire, i.e. pour lequel une trajectoire relie $A = 0$ à la solution saturée, est déterminé par la stabilité structurelle de la variété stable de la solution saturée dans l'espace des phases. Au seuil de bifurcation, cette variété représente une hétérocline reliant le point fixe 0 au point fixe saturé. Elle est soit localement structurellement instable car le point fixe 0 change de nature et passe de nœud instable à spirale instable [79], soit globalement structurellement instable, lorsque la variété stable de la solution saturée est connectée à la variété la plus instable de 0. Dans le cas d'une instabilité structurelle locale, le seuil non linéaire d'instabilité globale correspond au seuil linéaire d'instabilité absolue. Ce résultat est similaire au «critère» de Kolmogorov [53, 92, 73] qui détermine la sélection de vitesse de front se propageant d'un état stable vers un état instable, et qui revient à étudier la nature absolue ou convective de l'instabilité linéaire. À l'inverse, lorsque le mode global non linéaire au seuil de bifurcation correspond à une trajectoire globalement structurellement instable dans l'espace des phase, le seuil ne peut être déterminé qu'en prenent en compte l'effet des non linearités du système dans tout l'espace et intervient pour des valeurs du paramètre de bifurcation plus basses que le seuil linéaire d'instabilité absolue.

L'étude de la réponse du système à un forçage localisé à l'origine a permis de montrer que lorsque les paramètres sont dans la région d'instabilité non linéaire globale, le système se comporte comme un oscillateur : il possède une dynamique intrinsèque et n'est que peu perturbé par un forçage modéré. À l'inverse, il se comporte comme un amplificateur spatial du forçage imposé à l'entrée de l'écoulement non seulement dans la région d'instabilité non linéaire convective, mais aussi dans une partie du domaine de stabilité non linéaire.

Des lois d'échelle pour la pente à l'origine et la taille de croissance des modes globaux ont été calculées par une analyse en perturbation singulière en fonction du paramètre de criticité ϵ qui mesure l'écart au seuil d'instabilité non linéaire globale. Ces lois sont caractéristiques du type de transition vers l'instabilité globale : la taille de croissance des modes globaux varie comme $\epsilon^{-1/2}$ lorsque le seuil linéaire d'instabilité absolue détermine le seuil non linéaire d'instabilité globale. En revanche, une croissance beaucoup plus rapide en $\ln(1/\epsilon)$ caractérise le cas non trivial où le seuil non linéaire d'instabilité globale est plus bas. Ces lois d'échelle peuvent être utilisées comme un critère pour déterminer le type de transition subie par un système expérimental.

Le chapitre 2 étend une partie de ces résultats au cas de systèmes non potentiels modélisés par une équation de Ginzburg–Landau complexe. Cette partie est focalisée sur le modèle de bifurcation supercritique dans le but de comparer les résultats obtenus avec des résultats récents publiés dans la littérature, notamment les analyses numériques de la convection de Rayleigh–Bénard avec écoulement de Poiseuille [71] ou du problème

de Taylor–Couette avec écoulement axial [15].

Pour le modèle de Ginzburg–Landau supercritique, l'instabilité non linéaire globale de l'écoulement se manifeste lorsque l'état de base du système devient linéairement instable absolu. Une analyse en perturbations singulières du même type que celle réalisée dans le premier chapitre a permis de montrer qu'au voisinage du seuil non linéaire d'instabilité globale, la taille de croissance des modes globaux est proportionnelle à $\epsilon^{-1/2}$ ou ϵ désigne toujours le paramètre de criticité ; seule la constante de proportionnalité change par rapport au cas réel et devient une fonction implicite des paramètres. La fréquence d'oscillation de l'écoulement peut être prédite uniquement par l'examen des portraits de phase des solutions asymptotiques à une onde propagative à l'infini. Parmi l'ensemble des variétés stables des ondes saturées, une seule croise le plan $A = 0$ quand l'instabilité de l'état de base est absolue et zéro quand l'écoulement est convectif. Pour des paramètres fixés, il n'y a pas de familles de modes globaux parametrée par la fréquence mais une unique solution. Au seuil non linéaire d'instabilité globale, nous obtenons analytiquement une prédiction au premier ordre (ordre 0 et pente) de cette fréquence en fonction du paramètre de criticité ainsi que la taille caractéristique du mode global. La comparaison des lois d'échelle obtenues est en bon accord avec les résultat numériques de Büchel *et al* [15] pour le système de Taylor–Couette avec écoulement axial et avec ceux de Müller *et al.* [71] pour le problème de Rayleigh–Bénard avec écoulement de Poiseuille. Pour des coefficients de diffusion et de variation de fréquence non linéaire différents pour lesquels nous ne connaissons pas de résultats expérimentaux ou numériques publiés dans la littérature, les simulations numériques valident également ces lois d'échelle. Ces simulations ont permis de tester la robustesse du modèle et de d'émettre une hypothèse sur la stabilité des mode globaux non linéaires : Nous avons montré que cette instabilité secondaire semble déterminée par la nature absolue ou convective de l'instabilité de «l'aile» du mode global non linéaire, qui désigne l'onde propagative vers laquelle il tend à grande distance. Pour le mode global obtenu au seuil de bifurcation primaire, cette région d'instabilité secondaire convective a été déterminée par l'analyse classique des points selles «pinçant» de la relation de dispersion.

Des simulations numériques ont confirmé que l'instabilité secondaire absolue de l'écoulement a lieu avec l'instabilité absolue de l'aile du mode global. Il est remarquable que pour certaines valeurs des coefficients du modèle de Ginzburg–Landau, l'instabilité secondaire est présente dès le seuil d'instabilité primaire. Dans ce cas, elle semble se développer en aval par rapport à l'instabilité primaire mais ceci n'est qu'une illusion car le lien avec l'instabilité absolue secondaire de l'onde saturée prouve que cette instabilité secondaire est elle même globale. Plus loin du seuil, une analyse plus complète de la transition convectif/absolu pour l'ensemble des ondes propagatives qui existent à paramètres fixés, associée a des simulations numériques a permis également de confirmer l'hypothèse d'une bifurcation secondaire liée a l'instabilité absolue de l'aile du mode global non linéaire. Cette idée nécessite de plus amples études pour déterminer si d'autres scénarios sont possibles. Par exemple l'étude de l'instabilité linéaire du trou de Nozaki-Bekki [75] peut être associée soit à une instabilité du cœur où l'amplitude est nulle, soit a l'instabilité des ailes [17]. Dans le cas des modes globaux non linéaires, il ne semble pas exister d'instabilité de cœur, celui ci étant fixé à l'origine par la condition aux limites. Cette observation pourrait être confirmée ou infirmée par une analyse plus poussée de la stabilité linéaire du mode global non linéaire, et pas seulement de son aile.

Notons que la détermination de l'instabilité linéaire absolue ou convective des ondes propagatives a une portée plus générale que celle d'avoir déterminé l'instabilité globale secondaire des modes globaux non linéaires : la méthode utilisée permet en fait de tester si l'instabilité secondaire d'un écoulement correspond à l'instabilité absolue d'une onde saturée, même lorsque la bifurcation primaire donne une solution asymptotique à une onde propagative qui n'est pas un mode global non linéaire (par exemple un trou de Nozaki–Bekki [75]). De plus, la méthode fournit une prédiction du seuil d'instabilité secondaire.

De façon analogue, une des perspectives de cette étude est l'extension des résultats du chapitre 2 au cas sous-critique (équation de Ginzburg–Landau complexe). Actuellement cette extension est en cours d'élaboration. Suivant la démarche effectuée au chapitre 2, il est apparu que les modes globaux non linéaires obtenus soit par l'examen de l'espace des phases, soit par simulations numériques, diffèrent de la solution de front non linéaire de van Saarloos et Hohenberg [92], «coincée» par le bord du domaine semi-infini. Dans ce cas sous-critique, les modes globaux non linéaires ne semblent donc pas pouvoir être décrits en perturbation par rapport au front non linéaire comme pour le modèle potentiel du chapitre 1, mais semblent plutôt «extraits» d'un ensemble plus général de fronts reliant deux ondes propagatives (une stable à une instable), et non plus l'état instable ou métastable d'amplitude nulle à une onde propagative stable. Ces observations préliminaires restent à confirmer.

Le chapitre 3 présente l'extension de l'analyse précédente au cas inhomogène. Des modèles simples d'équations d'amplitudes réelles de type Ginzburg–Landau avec coefficients variables ont été utilisés dans le but de montrer comment l'hypothèse de faible inhomogenéité du milieu se conjugue avec l'étude des modes globaux non linéaires homogènes, pour donner des solutions qui croissent spatialemnt comme si le milieu était homogène puis décroissent en suivant adiabatiquement l'amplitude de saturation. Nous avons montré que pour que cette analyse soit valable, il faut que le paramètre de criticité ϵ soit suffisamment (algébriquement) grand devant le paramètre d'inhomogénéité μ_1. Cette analyse a permis de décrire les modes globaux non linéaires et inhomogènes dans une portion de l'espace des paramètres (ϵ, μ_1) plus large que celle couverte par l'analyse de Le Dizès *et al.* [61]. Basée sur un développement WKBJ, leur analyse a montré que les modes globaux linéaires peuvent être correctement décrits lorsque le paramètre de criticité est exponentiellement petit devant le paramètre d'inhomogénéité. Des lois d'échelles pour la position du maximum d'amplitude ont été obtenues et sont en très bon accord avec l'ensemble des observations et en particulier avec les lois de puissance trouvées expérimentalement par Goujon-Durand *et al* [35] et numériquement par Zielinska et Wesfreid [97] pour les sillages.

L'extension de cette analyse des effets inhomogènes au cas d'une équation d'amplitude complexe permettrait de décrire les oscillations intrinsèques des écoulements inhomogènes par un modèle à la fois non potentiel et faiblement inhomogène. Le principe de l'analyse devrait rester identique à celui utilisé pour le cas réel inhomogène du chapitre 3 et la sélection de fréquence devrait être donnée au premier ordre par la solution obtenue dans le cas complexe homogène du chapitre 2. Les valeurs théoriques de cette fréquence en fonction du paramètre de bifurcation pourront alors être directement comparées à la célèbre courbe de bifurcation qui donne le Strouhal en fonction

du Reynolds pour les sillages, quitte à évaluer les coefficients de l'équation d'amplitude utilisée en fonction du nombre de Reynolds.

Rappelons pour terminer que dans toute cette étude, nous avons considéré que la structure transverse de l'écoulement est passive dans le mécanisme de déstabilisation globale. Une deuxième hypothèse sous-jacente à l'étude des milieux faiblement inhomogènes concerne l'ordre de grandeur du paramètre d'inhomogénéité qui doit être suffisament petit. En particulier dans un écoulement réel, ce paramètre est en général fixe et ne tend pas nécéssairement vers zéro avec la criticité. Même si ces modèles simples sont en bon accord avec les observations experimentales ou numériques, il convient de noter que les hypothèses utilisées peuvent n'être qu'approximativement satisfaites dans un écoulement réel. Dans le cas des écoulements de Rayleigh–Bénard et de Taylor–Couette, ces hypothèses semblent raisonnables, y compris celle de la direction transverse esclave car l'extension latérale de ces systèmes reste limitée. Considérer ces écoulements comme parallèles revient à dire que la taille caractéristique des modes globaux non linéaires reste grande devant l'échelle de diffusion dans la direction transverse. Pour les sillages confinés, les hypothèses sont justifiées a posteriori par le fait que nous retrouvons les observations numériques et expérimentales. Pour les sillages sans parois, les hypothèses sont certes plus discutables, surtout loin du seuil où l'écoulement n'est sans doute pas faiblement non parallèlle, ce qui limite l'approximation WKBJ. Néanmoins, un relativement bon accord entre théorie et expériences (réelles ou numériques) est obtenu. En élucider les raisons reste une question ouverte.

Bibliographie

[1] M. Abramowitz, I.A. Stegun, *Handbook of mathematical functions*, (Dover 1972).

[2] G. Ahlers, D.S. Cannel, *Vortex-front propagation in rotating Couette–Taylor flow*, Phys. Rev. Lett., **50**, 1583 (1983).

[3] G. Ahlers, D.S. Cannell, R. Heinrichs, *Convection in a binary mixture*, Phys. Rev. **A 35**, 2757 (1987).

[4] P. Albarède, P.A. Monkewitz, *A model for the formation of oblique shedding and "chevron" patterns in cylinder wakes*, Phys. Fluids A **4**, 744.

[5] V.I. Arnol'd, *Geometrical methods in the theory of ordinary differential equations*, (Springer, Heidelberg, 1983).

[6] D.G. Aronson, H.F. Weinberger, *1975 Nonlinear diffusion in population genetics, combustion, and nerve propagation*, in *Partial Differential Equations and Related Topics, Lecture Notes in Mathematics*, (Vol. 446, pp 5–49, Springer, New-York 1975).

[7] D.G. Aronson, H.F. Weinberger, *1978 Multidimensional nonlinear diffusion arising in population genetics*, Adv. Math. **30**, 33 (1978).

[8] K.L. Babcock, G. Ahlers, D.S. Cannel, *Noise-sustained structure in Taylor–Couette flow with through flow*, Phys. Rev. Lett. **67**, 3388 (1991); *Stability and noise in Taylor–Couette flow with through-flow*, Physica **61D**, 40 (1992).

[9] C.M. Bender, S.A. Orszag, *Advanced Mathematical Methods for Scientists and Engineers*, (Mc Graw Hill, 1978).

[10] E. Ben-Jacob, H. Brand, G. Dee, L. Kramer, J.S. Langer, *Pattern propagation in nonlinear dissipative systems*, Physica **14D**, 348 (1985).

[11] D. Bensimon, P. Kolodner, C.M. Surko, H. Williams, V. Croquette, *Competing and coexisting dynamical states of traveling-wave convection in an annulus*, J. Fluid Mech. **217**, 441 (1990).

[12] A. Bers, in *Physique des Plasmas*, edited by C. DeWitt and J. Peyraud (Gordon and Breach, New York, 1975).

[13] L. Brevdo, T.J. Bridges, *Absolute and convective instabilities of spatially periodic flows*, Phil. Trans. in print (1996).

[14] R.J. Briggs, *Electron-Stream Interaction with Plasmas* (MIT Press, Cambridge, MA, 1964).

[15] P. Büchel, M. Lücke, D. Roth, R. Schmitz, *Pattern selection in the absolutely unstable regime as a nonlinear eigenvalue problem: Taylor vortices in axial flow*, Phys. Rev. E. **53**, 4764 (1996).

[16] H. Chaté, P. Manneville, *Phase diagram of the two-dimensional complex Ginzburg--Landau equation* Physica **224A**, 348 (1996).

[17] H. Chaté, P. Manneville, *Stability of the Bekki–Nozaki hole solutions to the one-dimensional complex Ginzburg–Landau equation* Phys. Lett. **A 171**, 183 (1992).

[18] J.M. Chomaz, *Absolute and convective instabilities in nonlinear systems*, Phys. Rev. Lett., **69**, 1931 (1992).

[19] J.M. Chomaz, P. Huerre, L.G. Redekopp, *Bifurcations to local and global modes in spatially developing flows*, Phys. Rev. Lett., **60**, 25 (1988).

[20] J.M. Chomaz, P. Huerre, L.G. Redekopp, *The effect of nonlinearity and forcing on global modes*, in *New Trends in Nonlinear Dynamics and Pattern-Forming Phenomena*, edited by P. Coullet and P. Huerre, (Plenum Press, New York, 1990).

[21] J.M. Chomaz, P. Huerre, L.G. Redekopp, *A frequency selection criterion in spatially developing flows*, Stud. Appl. Math. **84**, 119 (1991).

[22] P. Collet, J.-P. Eckmann, *Instabilities and fronts in extended systems*, (Princeton, NJ: Princeton University Press 1990).

[23] A. Couairon, J.M. Chomaz, *Global Instability in fully nonlinear systems*, Phys. Rev. Lett. **77**, 4015 (1996).

[24] A. Couairon, J.M. Chomaz, *Absolute and convective instabilities, front velocities and global modes in nonlinear systems*, submitted to Physica **D**.

[25] A. Couairon, J.M. Chomaz, *Pattern selection in the presence of a cross flow*, submitted to Phys. Rev. Lett.

[26] P. Coullet, L. Gil, D. Repaux, *Defects and subcritical bifurcations*, Phys. Rev. Lett. **62**, 2957 (1989).

[27] P. Coullet, L. Gil, F. Rocca, *Optical vortices*, Opt. Commun. **73**, 403 (1989).

[28] M.C. Cross, P.C. Hohenberg, *Pattern formation outside of equilibrium*, Rev. Mod. Phys. **65**, 851 (1993).

[29] C. Cross, *Structure of nonlinear traveling wave states in finite geometries.* Phys. Rev. A, **38**, 3593 (1988).

[30] G. Dee, *Dynamical properties of propagating front solutions of the amplitude equations*, Physica **15D**, 295 (1985); *Propagation into an unstable state*, J. Stat. Phys. **39**, 705 (1985).

[31] R.J. Deissler, *Spatially growing waves, intermittency, and convective chaos in an open-flow system*, Physica **25D**, 233 (1987).

[32] S. Fauve, O. Thual, *Solitary waves generated by subcritical instabilities in dissipative systems*, Phys. Rev. Lett. **64**, 282 (1990).

[33] J. Fineberg, V. Steinberg, *Vortex-front propagation in Rayleigh–Bénard convection*, Phys. Rev. Lett., **58**, 1332 (1987).

[34] J.-P. Eckmann, T. Gallay, *Front solutions for the Ginzburg–Landau equation*, Commun. Math. Phys. **152**, 221, (1993).

[35] S. Goujon-Durand, P. Jenffer, J.E. Wesfreid, *Downstream evolution of the Bénard-von Kármán instability*, Phys. Rev. E, **50**, 308 (1994).

[36] J. Guckenheimer, P. Holmes, *Nonlinear Oscillations, Dynamical Systems, and Bifurcations of Vector Fields*, (Springer Verlag, 1983)

[37] J.D. Gunton, M. San Miguel, Paramdeep S. Sahni, *The dynamics of first-order phase transitions*, in *Phase transitions and critical phenomena*, edited by C. Domb and J.L. Lebowitz, (Vol. 8, Academic Press, 1983).

[38] E. Guyon, J.-P. Hulin, L. Petit, *Hydrodynamique physique*, (Interéditions / Éditions du CNRS, 1991).

[39] H. Haken, *Analogy between higher instabilities in fluids and lasers*, Phys. Lett. A **53**, 77 (1975).

[40] V. Hakim, in *Hydrodynamics and nonlinear instabilities*, Cambridge University Press, to be published.

[41] (a) D. Hammond, L. G. Redekopp, *Global Dynamics and flow vectoring in asymmetric wakes*, AIAA-94-2219. (1994); *Global dynamics of symmetric and asymmetric wakes*, submitted to J. Fluid Mech.

[42] K. Hannemann, H. Oertel Jr, *Numerical simulation of the absolutely and convectively unstable wake*, J. Fluid Mech. **199**, 55 (1989).

[43] A. Hanna, A. Saul, K. Showalter, *Detailed studies of propagating fronts in the iodate oxydation of arsenous acid*, J. Am. Chem. Soc. **104**, 3838 (1982).

[44] C.M. Ho, P. Huerre, *Perturbed free shear layers*, Annu. Rev. Fluid Mech. **16**, 365 (1984).

[45] P. Huerre, P.A. Monkewitz, *Absolute and convective instabilities in free shear layers.* J. Fluid Mech. **159**, 151 (1985).

[46] P. Huerre, P.A. Monkewitz, *Local and global instabilities in spatially developing flows*, Annu. Rev. Fluid Mech. **22**, 473 (1990).

[47] P. Huerre, M. Rossi, in *Hydrodynamics and nonlinear instabilities*, Cambridge University Press, to be published.

[48] R.E. Hunt, *Spatially Varying Flows with localized forcing*, Ph. D. Thesis (1995).

[49] R.E. Hunt, D.G. Crighton, *Instability of flows in spatially developing media*, R. Soc. Lond. A **435**, 109 (1991).

[50] C.P. Jackson, *A finite-element study of the onset of vortex shedding in flow past variously shaped bodies*, J. Fluid Mech. **182**, 23 (1987).

[51] C.K.R.T. Jones, T.M. Kapitula, J.A. Powell, *Nearly real fronts in a Ginzburg-Landau equation*, Proc. Roy. Soc. Edinburgh, **116A** 193, (1990).

[52] W. Koch, *Local instability characteristics and frequency determination of self excited wake flows*, J. Sound Vib. **99**, 53 (1985).

[53] A. Kolmogorov, I. Petrovsky, N. Piskunov, *Investigation of a diffusion equation connected to the growth of materials, and application to a problem in biology*, Bull. Univ. Moscow, Ser. Int. Sec. A **1**, 1 (1937), in *Selected works of A.N. Kolmogorov*, V.M. Tikhomirov (Ed.), (Kluwer Academic Publishers, 1991).

[54] P. Kolodner, J.A. Glazier, *Interaction of localized pulses of traveling-wave convection with propagating disturbances*, Phys. Rev. A, **42**, 7504 (1990).

[55] N. Koppel, L.N. Howard, *Plane wave solutions to reaction-diffusion equations*, Stud. Appl. Math. **56**, 291 (1973).

[56] Y. Kuramoto, *Chemical oscillation, wave and turbulence*, (Vol 19, Springer series in synergetics, Springer-Verlag, Haken H. edition, 1984).

[57] L.D. Landau, *On the problem of turbulence*, C.R. Acad. Sci. URSS **44**, 311 (1944).

[58] L.D. Landau, E.M. Lifshitz, *Fluid Mechanics*, (Pergamon, London, 1959).

[59] M.J. Landman, Solutions of the Ginzburg–Landau equation of interest in shear flow transition, Stud. Appl. Math. **76**, 187 (1987).

[60] S. Le Dizès, P. Huerre, J.M. Chomaz, P.A. Monkewitz, *Linear global modes in spatially-developing media*, Phil. Trans. R. Soc. Lond. A **354**, 169 (1996).

[61] S. Le Dizès, P. Huerre, J.M. Chomaz, P.A. Monkewitz, *Nonlinear stability analysis of slowly diverging flows: Limitations of the weakly nonlinear approach*, in *Proceedings of the IUTAM Symposium on bluff-body wakes, dynamics and instabilities* (ed. H. Eckelmann, J.M.R. Graham, P. Huerre, P.A. Monkewitz), 147-152 (Berlin: Springer-Verlag, 1993).

[62] E.M. Lifshitz, L.P. Pitaevskii, *Physical kinetics* (Pergamon, London, 1981).

[63] M. Lücke, M. Mihelcic, K. Wingerath, *Front propagation and pattern formation of Taylor vortices growing into unstable circular Couette flow*, Phys. Rev. A, **31**, 396 (1985).

[64] P. Manneville, *Dissipative structures and weak turbulence*, (Academic Press, Boston, 1990).

[65] C. Mathis, M. Provansal, L. Boyer, *The Bénard von Kármán instability: an experimental study near the threshold*, J. Phys. (Paris) Lett. **45**, 483 (1984).

[66] B.J. Matkowski, V. Volpert, *Stability of plane wave solutions of complex Ginzburg–Landau equations*, Quart. Appl. Math. **51**, 265 (1993).

[67] P.A. Monkewitz, *The absolute and convective nature of instability in two-dimensional wakes at low Reynolds numbers*, Phys. Fluids **31**, 999 (1988).

[68] P.A. Monkewitz, D.W. Bechert, B. Lehmann, B. Barsikow, *Self-excited oscillations and mixing in heated round jets*, J. Fluid Mech., **213**, 611 (1990).

[69] P.A. Monkewitz, P. Huerre, J.M. Chomaz, *Global linear stability analysis of weakly non parallel shear flows*, J. Fluid Mech., **251**, 1 (1993).

[70] J.V. Moloney, A.C. Newell, *Nonlinear optics*, Physica **44D**, 1 (1990) .

[71] H.W. Müller, M. Lücke, M. Kamps, *Convective Patterns in Horizontal flow*, Europhys. Lett. **10**, 451 (1989); *Transversal convection patterns in horizontal shear flow*, Phys. Rev. A **45**, 3714 (1992).

[72] A.C. Newell, J.A. Whitehead, *Finite bandwidth, finite amplitude convection*, J. Fluid. Mech. **38**, 279 (1969).

[73] A.C. Newell, T. Passot, J. Lega, *Order parameter equations for patterns*, Annu. Rev. Fluid Mech. **25**, 399 (1993).

[74] C.Z. Ning, H. Haken, *Detuned lasers and the complex lorentz equations: Subcritical and supercritical hopf bifurcations*, Phys. Rev. **A 41**, 3826 (1990).

[75] K. Nozaki, N. Bekki, (a) Phys. Rev. Lett. **51**, 2171 (1983); (b) J. Phys. Soc. Jpn. **53**, 1581 (1984).

[76] D.O. Olagunju, B.J. Matkowsky, *Burned stabilized cellular flames*, Quart. Appl. Math. **48**, 645 (1990).

[77] P. Palffy-Muhoray, H.J. Yuan, B.J. Frisken, W. van Saarloos, in *Nonlinear evolution of spatio-temporal structures in dissipative continuous systems*, edited by F.H. Busse and L. Kramer, (Plenum Press, New-York 1990).

[78] B. Pier, P. Huerre, *Fully Nonlinear Global Modes in Spatially Developing Media*, Physica **97D**, 206 (1996).

[79] F. Plaza, *Propagation des instabilités dans les systèmes étendus*, Thèse de doctorat, Université de Nice, Sophia Antipolis (1994).

[80] Y. Pomeau, S. Zaleski, P. Manneville, *Axisymmetric cellular structures revisited*, Journal of Applied Mathematics and Physics (ZAMP), **36**, 367 (1985).

[81] J.A. Powell, A.C. Newell, C.K.R.T. Jones, *Competition between generic and non-generic fronts in envelope equations*, Phys. Rev. A, **44**, 3636 (1991).

[82] A. Pumir, B.I. Shraiman, W. van Saarloos, P.C. Hohenberg, H. Chaté, M Holen, *Phase vs. defect turbulence in the 1-D complex Ginzburg–Landau equation*, in *Ordered and turbulent Patterns in Taylor–Couette flow* edited by C.D. Andereck and F. Hayot, (Plenum Press, New York 1992).

[83] D. Rockwell, E. Naudascher, *Self sustained oscillations of impinging free shear layers*, Annu. Rev. Fluid Mech. **11**, 67 (1979).

[84] M. Schumm, E. Berger, P.A. Monkewitz, *Self excited oscillations in the wake of two-dimensional bluff bodies and their control*, J. Fluid. Mech. **271**, 17 (1994).

[85] L.A. Segel, *Distance side-walls cause slow amplitude modulation of cellular convection*, J. Fluid. Mech. **38**, 203 (1969).

[86] A. Soward, *Thin disc kinematic $\alpha\omega$-dynamo models II. Short lenght scale modes*, Geophys. Astrophys. Fluid **64**, 201 (1992).

[87] K.R. Sreenivasan, S. Raghu, D. Kyle, *Absolute instability in variable density round jets*, Exp. Fluids **7**, 309 (1989).

[88] K. Stewartson, J.T. Stuart, *A nonlinear instability theory for a wave system in plane Poiseuille flow*, J. Fluid. Mech. **48**, 529 (1971).

[89] P.J. Strykowski, D.L. Niccum, *The influence of velocity and density ratio on the dynamics of spatially developing mixing layers*, Phys. Fluids A **4**, 770 (1992).

[90] G.S. Triantafyllou, M.S. Triantafyllou, C. Chryssostomidis, *on the formation of vortex streets behind stationnary cylinders*, J. Fluid. Mech. **170**, 461 (1986).

[91] M. van Hecke, W. van Saarloos, P.C. Hohenberg, Phys. Rev. Lett. **71**, 2162 (1993).

[92] W. van Saarloos and P.C. Hohenberg, *Fronts, pulses, sources and sinks in generalized complex Ginzburg-Landau equations*, Physica **56D**, 303 (1992).

[93] W. van Saarloos, *Front propagation into unstable states: Marginal stability as a dynamical mechanism for velocity selection*, Phys. Rev. A, **37**, 211 (1988); *Front propagation into unstable states. II. Linear versus nonlinear marginal stability and rate of convergence*, Phys. Rev. A, **39**, 6367 (1989).

[94] E. Villermaux, Ph. D. thesis, Université de Grenoble (1992).

[95] A. Weber, L. Kramer, I.S. Aranson L. Aranson, *Stability limits of traveling waves and the transition to spatiotemporal chaos in the complex Ginzburg–Landau equation*, Physica **61D**, 279 (1992); *Stability limits of spirals and traveling waves in nonequilibrium media*, Phys. Rev. A **46**, R2992 (1992).

[96] A. Zebib, *Stability of viscous flow past a circular cylinder*, J. Eng. Math. **21**, 155 (1987).

[97] B.J.A. Zielinska, J.E. Wesfreid, *On the spatial structure of global modes in wake flow*, Phys. Fluids **7**, 1418 (1995).

Modes globaux fortement non-linéaires dans les écoulements ouverts

Cette thèse s'intéresse à la dynamique de certains écoulements ouverts dont la propriété commune est d'osciller de façon auto-entretenue, comme par exemple les sillages, les jets chauds, la convection de Rayleigh–Bénard avec écoulement de Poiseuille ou le probleme de Taylor–Couette avec écoulement axial. Pour décrire l'amplitude des ondes d'instabilité, des modèles d'équation d'amplitude de type Ginzburg–Landau réels ou complexes sont utilisés. La prise en compte des non-linéarités et de l'advection moyenne permet la recherche de solutions non-linéaires appelées modes globaux qui représentent les modes d'oscillation autoentretenue saturée.

Le premier chapitre est consacré à la comparaison des notions d'instabilités absolues et convectives linéaires ou non-linéaires, et de modes globaux non-linéaires. Il montre que l'instabilité non-linéaire globale d'un écoulement peut avoir lieu soit au seuil d'instabilité linéaire absolu, soit en dessous de ce seuil ; dans ce dernier cas, le système devient globalement instable alors qu'il est encore linéairement convectivement instable ou même stable. Des lois d'échelle génériques, en particulier pour la taille de croissance des modes globaux en fonction du paramètre de criticité sont obtenues et diffèrent suivant que le seuil d'instabilité globale coïncide ou non avec le seuil d'instabilité linéaire absolue.

Le second chapitre étend une partie de ces résultats au cas non potentiel de l'équation de Ginzburg–Landau complexe et permet d'analyser avec succès quelques résultats numériques récents obtenus par Büchel *et al.* (problème de Taylor–Couette avec écoulement axial) ou par Müller *et al.* (convection de Rayleigh–Bénard avec écoulement de Poiseuille). Une expression de la fréquence globale selectionnée est obtenue au premier ordre (valeur et pente). Le domaine de stabilité d'un mode global non-linéaire est caracterisé simplement par la transition d'instable convectif à instable absolu de l'onde propagative qui lui est associée. Cette instabilité secondaire globale semble directement amener le système vers le désordre.

Le dernier chapitre est consacré aux écoulements faiblement inhomogènes et à l'analyse de la structure spatiale des modes globaux non-linéaires décrits comme leurs analogues en milieu homogène perturbés par l'inhomogénéité du milieu. Cette description donne lieu à des lois d'échelle pour la position du maximum d'amplitude du mode global en accord avec les observations expérimentales de Goujon-Durand *et al.* et numériques de Zielinska et Wesfreid pour les sillages.

Mots-clés : écoulements ouverts, instabilités absolues / convectives, modes globaux, équation de Ginzburg–Landau, non-linéarités fortes, systèmes dynamiques, développements asymptotiques raccordés.

Stongly nonlinear global modes in open flows

This dissertation describes some homogeneous and weakly non-parallel open flows which possess an intrinsic behaviour, such as wakes, hot jets, Rayleigh–Bénard convection with an added weak plane Poiseuille flow or Taylor–Couette problem with Poiseuille flow. The behaviour of hydrodynamical instability waves is described using real or complex amplitude equations of the Ginzburg–Landau type. The effect of strong nonlinearity and advection velocity is taken into account throughout this study in order to find the nonlinear global (NG) modes which represent the spatiotemporal streamwise distribution of fluctuations.

The first chapter is concerned with the comparison of the concepts of linear/nonlinear, absolute/convective instability and of NG modes. The onset of the NG instability is either simultaneous with the convective/absolute transition, or takes place when the flow is still convectively unstable or stable. Generic scaling laws characterising the kind of bifurcation toward a global instability are derived, in particular for the growth scale of the nonlinear global modes as a function of the departure from criticality.

The second chapter extends some of these results to the nonpotential case of the complex Ginzburg–Landau equation. Some numerical results by Büchel *et al.* (Taylor–Couette problem with throughflow) and by Müller *et al.* (Rayleigh–Bénard convection with throughflow) are succesfully analysed. A frequency selection criterion is obtained at first order (value and slope). The secondary instability of the flow is characterised by the transition from convectively unstable to absolutely unstable of the travelling waves to which the NG mode is asymptotic, and seems to drive the system directly toward disorder.

The last chapter is concerned with weakly inhomogeneous flows. The spatial structure of nonlinear global modes is described by perturbing their homogeneous counterpart with the inhomogeneity of the media. Scaling laws for the position of the maximum amplitude are obtained and compare satisfactorily with experimental observations by Goujon-Durand *et al.* and numerical results by Zielinska and Wesfreid for wakes.

Keywords: open shear flows, absolute / convective instability, global modes, Ginzburg–Landau equation, strong nonlinearity, dynamical systems, matched asymptotic expansions.